University of Strathclyde, Department of Physics

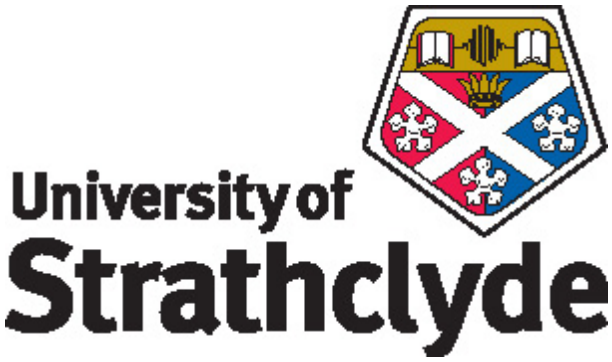

Diode Pumped Visible Vertical External Cavity Surface Emitting Lasers

By

Antony Smith

A thesis presented in fulfilment of the requirements
for the degree of Doctor of Philosophy.

2010

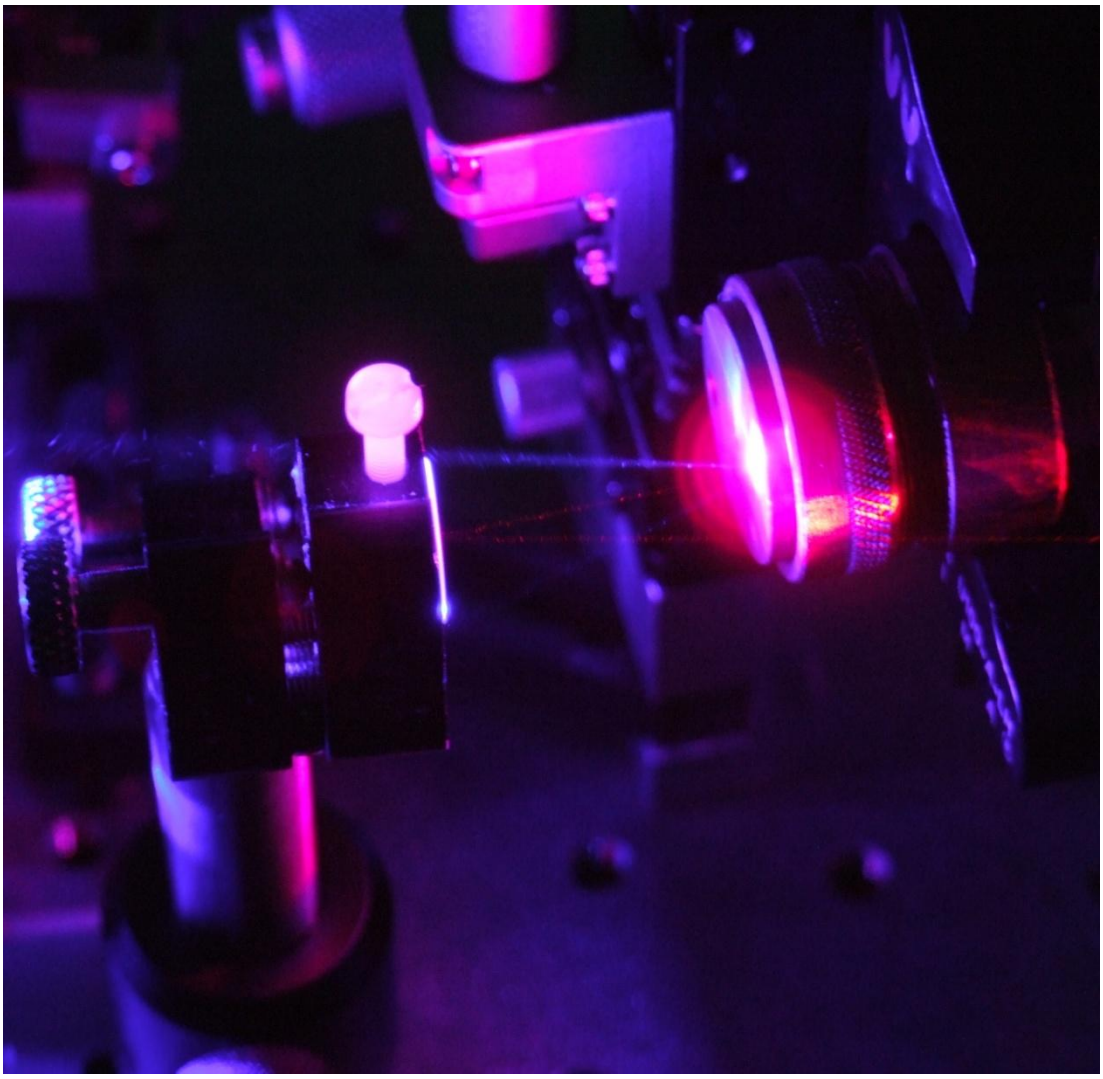

Dedicated to Kirsty, Janet and Jennifer for their support and encouragement.

Abstract

The Vertical External Cavity Surface Emitting Laser (VECSEL) is an optically pumped form of semiconductor laser. It offers high power and excellent beam quality combined with wavelength tuning capability and access to high-intracavity power through the external cavity for non-linear frequency conversion or single frequency work. The red emission VECSEL has been limited to the laboratory by the availability of suitable pump sources, but developments in GaN laser diode technology offer greater design flexibility.

This thesis reports on the development and demonstration of the first diode-pumped VECSEL with fundamental emission at visible wavelengths. Single transverse mode output power of 17mW at 670nm with a tuning range of 16nm was shown, limited by available pump power. The reasons for design changes made to allow diode-pumping and improve performance are explored. We investigate the cause of the VECSEL 'aging' effect evident in the permanent power decay.

Preliminary investigation of diode-pumped visible emission II-VI VECSELs is undertaken with a view to future development of the technology as a means to directly access the visible spectrum in a simple, compact and cost effective manner.

Contents

Abstract ..... **i**

Contents ..... **ii**

List of Figures ..... **vi**

CHAPTER 1 ..... **1**

Introduction **1**

1.1 VECSELs 1

1.2 Red Laser Technologies 6

1.2.1 Semiconductor Lasers 6

1.2.2 Gas Lasers 8

1.2.3 Crystal Lasers 8

1.2.4 Dye Lasers 9

1.3 II-VI VECSELs 9

1.4 Introduction to the work in this thesis 10

REFERENCES **12**

CHAPTER 2 ..... **17**

VECSEL Structure Design **17**

2.1 Structural Elements 17

2.1.1 Active Region 17

2.1.2 Quantum Wells 18

2.1.3 Gain Modelling 24

2.1.4 Resonant Periodic Gain 27

2.1.5 Resonant and Anti-Resonant cavity design 28

2.1.6 Wavelength Shift With Temperature 29

2.1.7 Distributed Bragg Reflector 30

2.2 Fabrication 32

2.3 Strain and Strain Compensation 35

2.4 III-V Red Emission VECSEL 38

2.4.1 AlGaInP Introduction 38

2.4.2 Material Considerations 40
2.5 II-VI Visible Emission VECSEL 41
2.6 Conclusion 43

REFERENCES 44

CHAPTER 3 48

Effects of Temperature on VECSELs 48
3.1 Mapping Different Growth Temperature VECSELs 48
3.1.1 Structure Used for Growth Test 48
3.1.2 Wafer mapping 49
3.1.2.1 Normal PL Measurement 50
3.1.2.2 Reflectivity Measurement 50
3.1.2.3 Edge PL 51
3.1.2.4 Individual Sample Characterisation 51
3.1.2.5 Results 51
3.2 Thermal Management in a VECSEL 55
3.3 Characterisation of Thermal Effects 58
3.3.1 Characterisation 58
3.3.2 Reflectivity 58
3.3.3 Photoluminescence 61
3.3.3.1 Edge PL 61
3.3.3.2 Normal PL 64
3.4 The Thermal Effects of Pump Wavelength 66
3.4.1 Experiment 66
3.4.2 Modelling the Effect of Pump Wavelength on Emission Wavelength 72
3.4.3 Finite Element Analysis 74
3.4.3.1 Modelling 76
3.4.3.2 Conclusions 80
3.5 Thermal Management by Peltier Element Only 81
3.5.1 Structure 82
3.5.2 Experiment 82
3.5.3 Results 83
3.5.4 Thermal Model 86
3.5.5 Discussion 87
3.6 Conclusion 88

REFERENCES 89

CHAPTER 4..... 91

Diode-Pumped AlGaInP VECSELs..... 91

4.1 Design Considerations..... 91

4.1.1 Absorption Length..... 91

4.1.2 Quantum Wells vs Threshold..... 94

4.2 Pumping at 405nm..... 97

4.2.1 Optical Pump Scheme..... 98

4.2.2 Structure..... 98

4.2.3 Experiment..... 99

4.3 Pumping at 445nm..... 101

4.3.1 Laser Diode Characterisation..... 101

4.3.2 Seven Quantum Well Structure..... 101

4.3.2.1 Experimental Set-Up..... 103

4.3.2.2 Results..... 105

4.3.2.3 Pumped with argon ion laser..... 107

4.3.3 Strain Compensated Seven Quantum Well Structure..... 108

4.3.3.1 Experimental Set-Up..... 109

4.3.3.2 Results..... 109

4.3.3.3 Pumped with Sabre..... 114

4.3.4 Comparison of strain-compensated and non-strain compensated structures..... 115

4.3.4.1 Lengthened Active Region..... 116

4.3.4.2 Rapid Thermal Annealing..... 116

4.3.4.3 Strain Compensation..... 117

4.4 Conclusion..... 117

REFERENCES 119

CHAPTER 5..... 121

Recombination Enhanced Defect Reactions..... 121

5.1 Laser Emission Decay..... 123

5.1.1 The Effect of Structural Degradation..... 124

5.2 How this relates to our structure..... 125

5.2.1 Experimental Results..... 127

5.2.1.1 Non-Strain Compensated Structure..... 127

5.2.1.2 Strain Compensated Structure 129
5.2.2 Conclusion 130

REFERENCES 131

CHAPTER 6 133

II-VI VECSELs 133
6.1 ZnSe/ZnCdSe VECSEL 133
6.1.1 Structure 133
6.1.2 Characterisation 134
6.1.2.1 Fused Silica Substrate 137
6.1.2.2 Diamond Substrate 140
6.2 ZnCdMgSe/ZnCdSe VECSEL 142
6.2.1 Structure 143
6.2.2 Characterisation 144
6.2.2.1 Edge PL Characterisation 150
6.3 Conclusion 152

REFERENCES 153

CHAPTER 7 155

Conclusions 155
7.1 VECSEL Thermal Issues 155
7.2 Diode-Pumped Visible VECSELs 156
7.3 Structural Degradation 157
7.4 II-VI VECSELs 158
7.5 Future Work 158

REFERENCES 166

List of Figures

Figure 1-1: III-V VECSEL Wavelength coverage 2
Figure 1-2: A red emission seven quantum well structure used in Chapter 4. 3
Figure 1-3: Schematic of a simple three mirror VECSEL cavity. 4
Figure 1-4: Schematic of a top emission VCSEL 6
Figure 1-5: Schematic drawing of the epitaxial layer structure for 850-nm bottom-emitting VCSEL 7
Figure 1-6: Bandgap energy vs Lattice constant diagram for II-VI binary compounds and common substrates 10
Figure 2-1: Schematic of simple VCSEL and VECSEL structures 17
Figure 2-2: Potential energy levels in a finite one dimensional square quantum well. V(z) is the potential energy level and L is the quantum well width. 19
Figure 2-3: Confined energy levels of a finite one dimensional square well 22
Figure 2-4: Energy levels and transitions in a $Ga_{0.5}In_{0.5}P/(Al_xGa_{1-x})_{0.5}In_{0.5}P$ quantum well 23
Figure 2-5: Modelled transition energy against quantum well width and composition 23
Figure 2-6: Displacement of sub-cavity standing waves for a)667nm, b)672nm and c)677nm in a 10 QW VECSEL 27
Figure 2-7: Illustration of temperature dependant shift of QW emission and sub-cavity resonance 30
Figure 2-8: Illustration of the principle of the DBR reflection with partial reflections of the incident beam (top). 31
Figure 2-9: Calculated reflectivity of an N=10, N=20, N=30 and N=40 $Al_{0.45}Ga_{0.55}As/AlAs$ DBR. 32
Figure 2-10: Schematic of an MBE growth set-up 33
Figure 2-11: Schematic of the MOCVD process 34
Figure 2-12: Compressive and tensile strain 36
Figure 2-13 : The effect of high compressive strain on the layer quality of AlGaInP quantum well lasers 37
Figure 2-14: Schematic diagram of the effect of biaxial strain on band structure 38
Figure 2-15: Bandgap energy v lattice constants for some common III-V alloys 39
Figure 2-16: Room temperature bandgap energies of unordered $(Al_xGa_{1-x})_{0.5}In_{0.5}P$ lattice matched to GaAs 40
Figure 3-1: Epi-side up wafer reference diagram 49
Figure 3-2: Contour map normal PL peak wavelength for the T_g=690°C 10QW structure. 52
Figure 3-3: Example characterisation graph 53
Figure 3-4: Normal and Edge PL from MR2331E. 54
Figure 3-5: Heatflow schematic for a)bare heatsink b)'thin device' approach and c) heatspreader approach. 56
Figure 3-6: Schematic of our DBR reflectivty measurement experimental set-up 59
Figure 3-7: Example of spectra of a) a tungsten lamp and b) a VESCEL structure. 60
Figure 3-8: Example VECSEL reflectivity 61
Figure 3-9: Schematic of an Edge PL experiment set-up 62
Figure 3-10: Typical edge PL measurements for a 20QW GaInP/AlGaInP VECSEL for a range of mount temperatures. Inset: Wavelength shift of edge PL peak with sample temperature. 63
Figure 3-11: Side-on view of edge emission polarisation from a VECSEL 64
Figure 3-12: Schematic of an Normal PL experiment set-up 65
Figure 3-13: Typical normal PL measurements for a 20QW GaInP/AlGaInP VECSEL for a range of mount temperatures. Inset: Wavelength shift of normal PL peak with sample temperature. 66
Figure 3-14: Slope efficiency variation with pump wavelength for different levels of output coupling a)1% b)2% and c)3% 69
Figure 3-15: Wavelength change per unit pump power for different levels of output coupling a)Hr b)1% and c) 2% 71
Figure 3-16: Absorption curves of various pump wavelengths in a 20QW VECSEL 73
Figure 3-17: Geometry of the FEA VECSEL model. The blue line is the constant temperature boundary and the red line is the line of radial symmetry. 76
Figure 3-18: Temperature change per unit pump power for various pump wavelengths (quantum defect heating). 78
Figure 3-19: Model results for slope efficiency heating for a)HR b) 1%OC and c)2%OC 79
Figure 3-20 COMSOL Multiphysics simulations of a red VECSEL structure pumped at (a) 445nm and (b) 532nm 80
Figure 3-21: Reflectivity (black) and Normal PL (blue) for sample MR2331K 82

Figure 3-22: Schematic of experimental set-up 83
Figure 3-23: Four power transfer curves for 7-8μm radius mode size heatspreaderless VECSEL taken under the same experimental conditions. 84
Figure 3-24: Power Transfer Curves for various mode sizes 85
Figure 3-25: Power Transfer v Pump Intensity for various mode sizes 86
Figure 3-26: FEA model of 670nm VECSEL pumped at 532nm with a 7μm pump radius 87
Figure 4-1: Modelled $(Al_{0.6}Ga_{0.4})_{0.51}In_{0.49}P$ absorption curve 92
Figure 4-2: Mathcad plot of pump absorption (at 405nm, 445 and 532nm) in active region of 10 quantum well red VECSEL designed for pumping at 532nm 93
Figure 4-3: Mathcad plot of the output power v number of quantum wells for ~600mW pump power (445nm) 95
Figure 4-4: Well and barrier set-up in model 96
Figure 4-5: Graph of quantum well radiative transition energy vs barrier thickness 96
Figure 4-6: Schematic of 405nm pumping set-up 100
Figure 4-7: Refractive index, pump absorption and standing wave of 7 quantum well structure 102
Figure 4-8: Reflectivity and Normal PL measurements 103
Figure 4-9: Slow and fast axis beam widths though pump optics 104
Figure 4-10:Schematic of experimental set-up for 445nm pumping 105
Figure 4-11: Power transfer curve of the 7 quantum well sample pumped at 445nm 105
Figure 4-12: Free running spectrum of K2138 pumped at 445nm, with inset mode profile and tuning curve. 106
Figure 4-13: Power transfer curve for strain compensated 7QW VECSEL 109
Figure 4-14: Free running spectrum for the strain compensated 7QW sample with inset mode profile. 110
Figure 4-15 Comparison of $|E|^2$ at Quantum Wells. 112
Figure 4-16: $|E|^2$ at centre of each well in 7QW diode-pumped strain compensated VECSEL 113
Figure 4-17: $|E|^2$ at centre of each well in 20QW 532nm pumped VECSEL 113
Figure 4-18: Power decay run with 2W 457.9nm and 1%OC for strain-comp structure 115
Figure 4-19: Normal photoluminescence over time: RTA and non-RTA sample comparison 117
Figure 5-1: Output power over time for the strain-compensated structure with 3% output coupling. 123
Figure 5-2: Output power over time with pump interruption for strain compensated structure with 3% output coupling 124
Figure 5-3: Normal PL measurements for two strain compensated diode-pumped red VECSEL samples 128
Figure 5-4: Normalised Output Power Decay Curve 128
Figure 5-5: Normalised power decay curves for K2208 129
Figure 6-1: Schematic of normal PL experiment for II-VI Heriot-Watt structure 135
Figure 6-2: PL decay for 130mW pump power 136
Figure 6-3: $Zn_{0.90}Cd_{0.10}Se$/ZnSe structure absorbance spectrum 138
Figure 6-4: Normal PL for a range of pump powers for sample HWA1959 139
Figure 6-5: Normal PL for a range of pump powers for sample HWA1960. 139
Figure 6-6: Variance of Normal PL at constant pump power for different temperatures Inset: Peak wavelength shift with temperature. 141
Figure 6-7: Spectra for constant temperature but varying pump power 141
Figure 6-8: Spectral coverage of ZnCdMgSe Lattice Matched to InP 142
Figure 6-9: Normal PL of two resonant II-VI VECSEL structures 145
Figure 6-10: Reflectivity measurements of resonant II-VI VECSEL structures 146
Figure 6-11: Normal PL of anti resonant II-VI VECSEL structures 148
Figure 6-12: Edge PL curves for resonant structure 149
Figure 6-13: Peak wavelength shift of a)Normal PL and b) Edge PL 149
Figure 6-14: Schematic of the experimental set-up for polarised edge PL measurements 150
Figure 6-15: EdgePL polarisation spectra for resonant sample A2796D 151
Figure 6-16: EdgePL polarisation spectra for anti-resonant sample A2802D 152
Figure 7-1: Schematic of a possible diode-pumped II-VI VECSEL floated onto a coated diamond heatspreader. 165

List of Tables

Table 3-1: 20QW structure used in pump wavelength experiment 67
Table 3-2: Wavelengths used and maximum available pump powers 68
Table 4-1: Absorption data for $(Al_{0.6}Ga_{0.4})_{0.51}In_{0.49}P$ 93
Table 4-2: Design for 670nm VECSEL pumped at 405nm 99
Table 4-3: 7 quantum well structure for pumping at 445nm 102
Table 4-4: Strain compensated 7 QW structure 108
Table 6-1: 5 quantum well ZnCdSe/ZeSe structure 134
Table 6-2: Time constants for three PL decay runs 136
Table 6-3: Resonant II-VI VECSEL Design 144
Table 7-1: AlAs/AlGaAs DBR with strain compensation layers in active region 161
Table 7-2: AlInP/AlGaInP DBR with strain compensation layers in active region 162
Table 7-3: AlInP/AlGaInP DBR without strain compensating layers in active region 163

Chapter 1

Introduction

1.1 VECSELs

VECSELs are an increasingly important and commercially relevant form of semiconductor laser. The technology combines the flexibility of a semiconductor gain medium with the external cavity access of the diode-pumped solid state laser. VECSELs take advantage of the mature growth technologies developed for more conventional laser formats such as laser diodes, and are now starting to replace diode-pumped solid-state lasers in some commercial products, such as Coherent's Verdi™ series which operates at 532nm and was previously a diode-pumped frequency-doubled Nd:YVO_4 laser.

They are capable of producing high-quality, multi-Watt, output at a wide range of wavelengths, with fundamental emission from 4-7 µm with PbSe or PbTe[1] and over 2µm with GaInAsSb[2,3], through the telecommunications bands (1.3-1.55µm) with InGaAs(N)/GaAs[4], InGaAsP[5] and InGaAlAs[6], down to the red VECSELs between 640 and 690nm[7], penetrating into the visible and ultraviolet with non-linear frequency conversion[4] and InGaN[8] (Figure 1-1[7,9-32,49-56]).

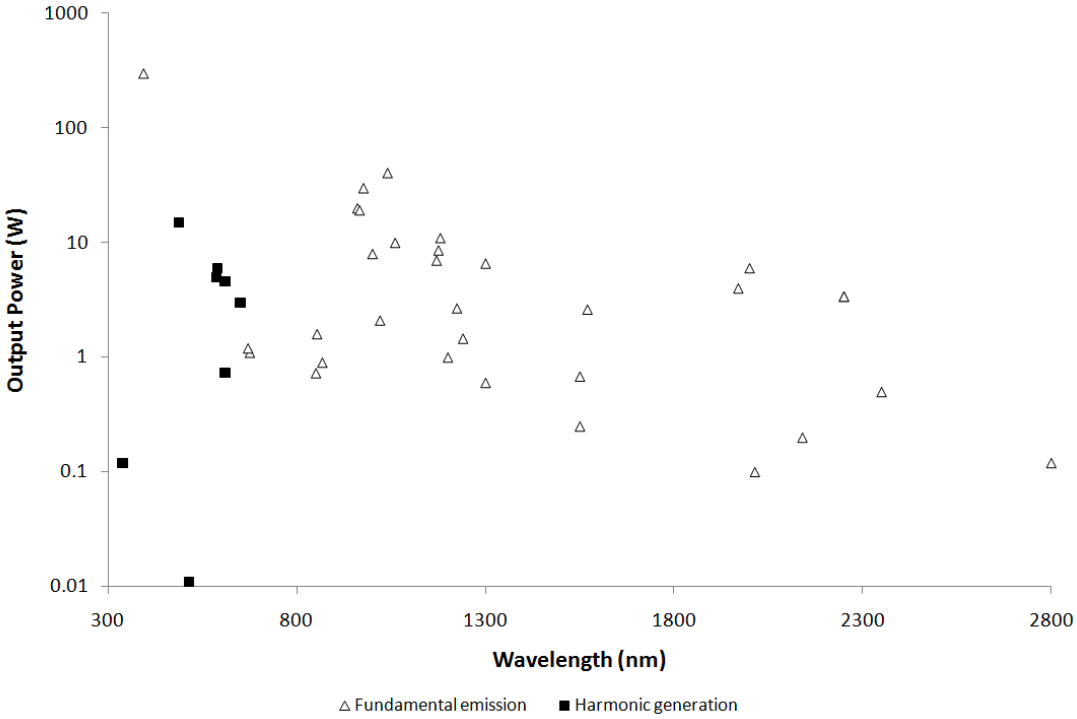

Figure 1-1: III-V VECSEL Wavelength coverage

VECSELs are commonly grown on binary semiconductor substrates and consist of three main parts: the active region, the semiconductor mirror and the external cavity.

The active region is optically pumped, with bulk material absorbing the pump photons and generating carriers which diffuse into thin layers of lower energy material (quantum wells) which confine the carriers and provide laser gain. Optical pumping removes the requirement to dope the structure with donor or acceptor atoms which simplifies growth. In addition it reduces post-processing as electrical contacts are not required.

The semiconductor mirror, known as a distributed bragg reflector (DBR), consists of layers of material of a quarter laser wavelength thick each of which partially reflects the laser beam in such a manner that the reflections constructively interfere. By growing a sufficient number of layers a reflectivity of greater than 99.99% can be achieved over a small range of wavelengths, known as the stopband. This level of reflectivity is necessary as VECSELs are relatively low gain devices and cannot

tolerate significant mirror losses. Growing the mirror as part of the device reduces the level of post-processing required.

An example of a VECSEL structure is shown in Figure 1-2. In addition to the elements just mentioned, it contains strain-compensation layers which will be discussed in Chapter 2.

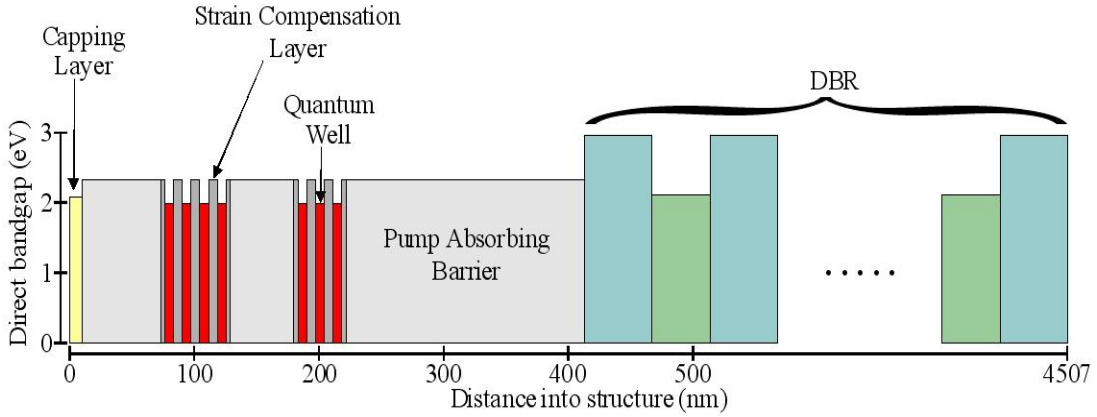

Figure 1-2: A red emission seven quantum well structure used in Chapter 4.

The active region and semiconductor mirror essentially form a 'mirror with gain' as part of the laser cavity. As the VECSEL does not have a top mirror grown onto it at least one external mirror is required to complete the cavity, meaning that the great majority of the laser cavity is 'in air' and accessible. The circulating intracavity power is significantly greater than the power coupled out of the cavity, making it the ideal place to site optical elements for non-linear frequency conversion as the conversion efficiency depends strongly on the intensity.

A simple three mirror cavity, typically used in this work, is shown in Figure 1-3. A VECSEL, such as the one shown in Figure 1-2 is used as one end mirror. The plane external end mirror is used to couple light out of the cavity. A curved mirror and the distance to the end mirrors are used to set a stable mode and match the size of the laser mode at the VECSEL surface to the pump spot size.

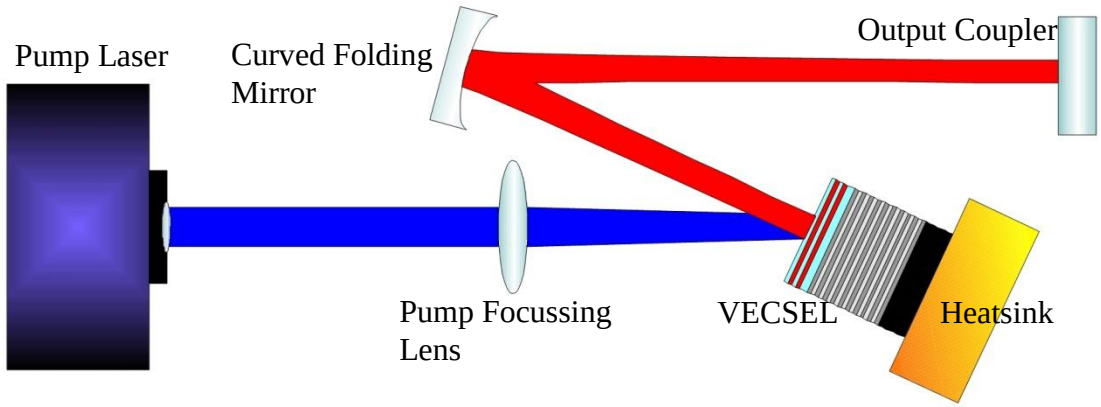

Figure 1-3: Schematic of a simple three mirror VECSEL cavity.

One of the advantages of the VECSEL design is that it has a very thin pump-absorbing region, ~1µm for the 532nm pumped red VECSELs, and so is effectively a planar absorber: the pump radius only needs to be matched to the intracavity beam mode radius in the plane of the active region. This is in contrast to volume absorber crystal-based lasers which can require the pump beam width be maintained over millimetres requiring more stringent optical design.

VECSELs are, in general, very tolerant of non-optimal pump arrangements. In addition to being a planar absorber, the pump-absorbing barriers will absorb, and generate carriers from, any pump photon energy above their bandgap. This has the significant advantage that not only can the same structure be pumped over a range of wavelengths (and so not require a wavelength-stabilised source) but, as will be seen in Chapter 4 the VECSEL design can be changed to cope with much shorter pump wavelengths through structural modification without requiring change in materials. Also, as the gain-providing quantum wells are populated by carriers diffusing into them from the pump-absorbing barriers rather than excited states in fixed atoms, there is no requirement for a high quality single longitudinal mode pump beam.

These qualities make the VECSEL ideally suited to diode-pumping. Laser diode emission is generally astigmatic and asymmetric, requiring additional optical components to manipulate the beam if high quality is required, often multimode in the slow-axis, and will shift in wavelength as the diode temperature changes. If used to pump a VECSEL, the beam merely needs to be circular at the VECSEL surface

and a variation of a few nanometres in pump wavelength will make little difference to device performance.

Laser diodes are an attractive pump source as they are compact and cost effective. They are ubiquitous, sold in their millions world-wide, and diode pumped solid state (DPSS) lasers are a common sight in laboratories. The first diode pumped VECSEL was demonstrated by Kuznetzov et al[33] in 1997 and diode pumped VECSELs now feature in commercial products such as the Verdi™ G series and Sapphire™ from Coherent®. However, prior to this work no diode pumped directly visible wavelength VECSEL had been demonstrated. Although commercial visible wavelength VECSELs are available they are based on longer wavelength VECSELs and use frequency doubling to achieve visible wavelengths which adds cost and complexity to the design as well as reducing efficiency.

A lack of short wavelength optical pump sources of sufficient power has restricted the choice of pump lasers to mainframe green lasers. Previous results[7] with red-emitting structures utilised a diode pumped frequency doubled Nd:YVO_4 laser emitting at 532nm. This reliance on relatively large, expensive and static lasers confined red VECSEL technology to the laboratory.

Diode pumping of VECSELs is routine at other wavelengths, however it is only recently that laser diodes of sufficient power and photon energy have become available. Prior to this work, our red VECSELs were pumped at 532nm using a diode-pumped frequency-doubled Nd:YVO_4 laser due to a lack of suitable short-wavelength diode pump sources[7]. The recent availability of GaN blue laser diodes of 0.5W and above has opened up the possibility of diode-pumping the red VECSEL. This is an attractive proposition as it frees the technology from the (relatively) large and expensive pump lasers which had restricted red VECSELs to the laboratory and potentially enables then to be commercially packaged like other diode-pumped solid-state lasers (DPSS). Rapid progress has been made in (In)GaN laser diode technology moving from the blue[34] through blue-green[35,36] into true green with 50mW CW at 515nm[37] and 524nm[38] and pulsed operation at 531nm[39]. Green GaN

Diode Pumped Visible Vertical External Cavity Surface Emitting Lasers

laser diodes are becoming commercially available, for instance Nichia have recently announced they are starting to ship sample 50mW GaN green laser diodes with an estimated lifetime of 10,000 hours[40].

1.2 Red Laser Technologies

Here we briefly review other red laser technologies, looking at their advantages and disadvantages compared to the red emission VECSEL.

1.2.1 Semiconductor Lasers

VCSELs are efficient electrically-pumped surface emitting semiconductor lasers resembling VECSELs but using a monolithically-grown top mirror to complete the laser cavity. Both the top and bottom mirror are doped to facilitate electrical pumping. A schematic of a top-emission VCSEL is shown in Figure 1-4[41].

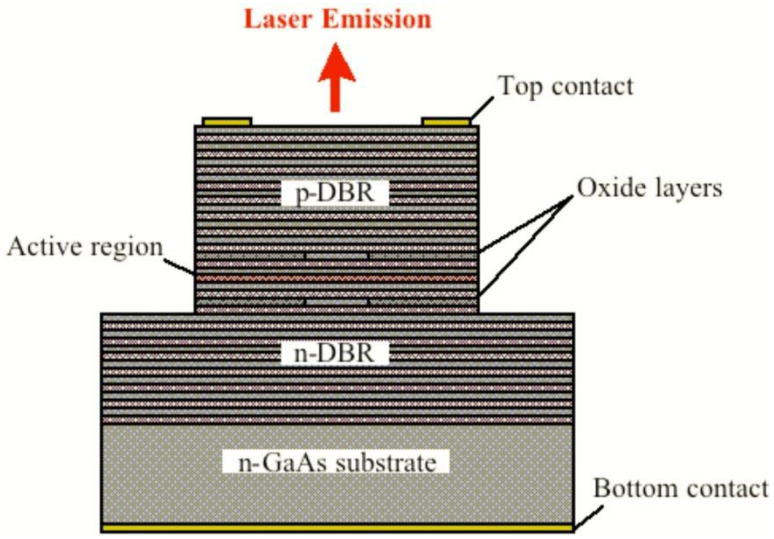

Figure 1-4: Schematic of a top emission VCSEL

VCSELs are compact, can produce high quality beams and do not require an external pump laser but are limited in output power and require significant post-growth processing. Top-emitting single-mode VCSELs are limited to output powers of a few mW. Up to 0.89W CW has been demonstrated from a single bottom-emitting device (Figure 1-5) at around 996nm and 1.55W from a VCSEL array[42].

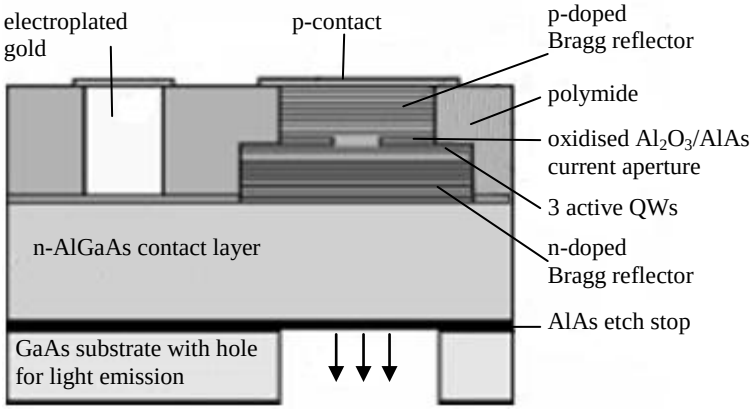

Figure 1-5: Schematic drawing of the epitaxial layer structure for 850-nm bottom-emitting VCSEL

Laser diodes are cheap, have the advantage of mature growth technology and production scale, and red laser diodes are readily available based on AlGaInP on GaAs substrates. However, laser diode output is naturally astigmatic and asymmetric due to the 'letterbox' shape of the gain region and transforming the output into a high quality circularly symmetric beam requires collimating the output with lenses and shaping using prisms both of which add cost and complexity. Laser diodes can be made single transverse mode by making the gain region more symmetric but that reduces the output power (as the gain volume is reduced). They can also be combined into a diode bar, an array of smaller laser diodes, offering very high power at the expense of beam quality.

Recently Sumpf et al[43] demonstrated a tapered laser diode emitting at 650nm at an output power of 690mW and an M^2=1.3. Greater output power of 1.05W was possible but with reduced beam quality. Whilst these devices have good power and beam quality, they cannot be simply power scaled to higher output.

It is possible to frequency-double a VECSEL operating between ~1250-1500nm, however VECSELs in that range offer no more power at their fundamental wavelength than red VECSELs, significantly less when frequency-doubled, and the tuning range is greatly reduced.

1.2.2 Gas Lasers

There are variety of lasers which use a gas as the gain medium. Typically electrically pumped they offer high beam quality but are not continuously tuneable.

For example, the Helium-Neon gas laser is a relatively simple and compact laser which can emit at 632.8nm. It consists of a glass tube containing the helium/neon gas mixture through which is passed a direct current. External mirrors complete the laser cavity, with the optional addition of intra-cavity Brewster windows if polarisation control is required. It produces good quality beams of a few tens of milliwatts, however they are not tuneable as laser emission is reliant on transition between specific energy levels.

1.2.3 Crystal Lasers

Crystal lasers are an excellent source of high quality high power red laser light, they are power scalable, can produce high quality output, offer high power and access to the external cavity. However they generally rely on discrete electronic transitions limiting them to specific emission wavelengths.

For instance, praseodymium ion (Pr^{3+}) doped $LiYF_4$ and $LiLuF_4$ has various visible wavelength transitions in addition to the red (~640nm). Richter et al[44] used a GaN laser diode at ~444nm with up to ~370mW to demonstrate 61mW from Pr:YLF and 76mW from Pr:LLF at 640nm. A frequency doubled VECSEL (to ~480nm) was used to match the strongest absorption line for both crystals and demonstrate 53mW from Pr:YLF and 66mW from Pr:LLF at 640nm. This result demonstrated high power and good efficiency, together with the cavity access enabling intracavity frequency doubling with LBO. The disadvantages are inherent to the fixed transitions of the laser medium: shifts in pump wavelength away from the absorption line decrease absorbed (and thus emitted) power, and the emission wavelength cannot be tuned.

Frequency-doubled Nd:YAG (656.5nm), Nd:YLF (671nm) or Nd:YVO_4 (671nm) are a way to obtain high power high beam quality red laser light. However, like the praseodymium doped crystal lasers they are not tuneable.

Vibronic lasers are a form of crystal laser which are wavelength tuneable. A common example is the titanium-sapphire laser. First demonstrated in 1982[45] Ti:sapphire lasers are popular research tools, in part due to their wide tuning range of 650-1100nm (although this requires changing mirror sets). A significant limitation to their use outside the laboratory has been the pump laser as it is typically pumped in the green (514-532nm), requiring an argon-ion or frequency-doubled Nd-doped laser, although recently Roth et al[46] demonstrated GaN laser diode-pumping of Ti:sapphire.

1.2.4 Dye Lasers

Dye lasers are optically pumped lasers which use solid or liquid dyes as the gain medium to produce tuneable laser output. Whilst they can access a wide range of wavelengths, they suffer from two major disadvantages: they are dependent on an external optical source such as a frequency-doubled solid-state laser, and they involve dangerous chemicals requiring careful handling and disposal.

Whilst VECSELs are not the only red laser technology, they offer a unique set of advantages: simple growth with minimal post-processing, high beam quality, high power, tuneable, an accessible external cavity and acceptance of a wide range of pumping conditions.

1.3 II-VI VECSELs

Fundamental emission at wavelengths below the red requires materials with greater direct bandgaps than are currently available in non-nitrile III-V materials. However, II-VI semiconductor compounds offer much wider bandgaps and may be able to extend VECSEL wavelength coverage through the whole of the visible spectrum. This has particular relevance to the display market where compact, efficient, cost-effective and long-lasting laser sources are required. Whilst, of course, the visible spectrum can be addressed with nonlinear frequency conversion this adds a level of complexity and cost whilst reducing efficiency.

Figure 1-6[47] shows a selection of II-VI semiconductor compounds and suitable substrates. Of particular interest is the ZnCd(Mg)Se which can be lattice-matched to

Diode Pumped Visible Vertical External Cavity Surface Emitting Lasers
the common III-V substrate InP and Zn(Mg)SSe material system which can be grown strained on GaAs, offering the possibility of VECSELs with fundamental emission ranging from the red into orange and through to blue. As VECSELs can be designed to emit at chosen wavelengths, the preferred RGB wavelengths[48] of 620nm, 532nm and 460nm are desirable targets for future exploitation of the technology.

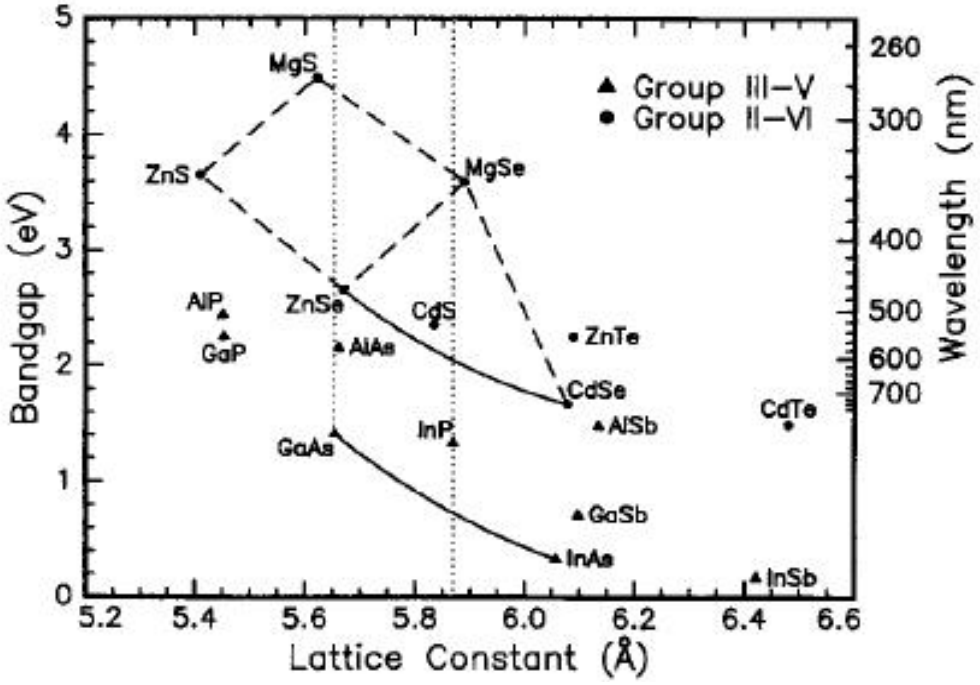

Figure 1-6: Bandgap energy vs Lattice constant diagram for II-VI binary compounds and common substrates

1.4 Introduction to the work in this thesis

This thesis describes the characterisation and development of diode-pumped red emission VECSELs. It builds on previous work on GaInP/AlGaInP VECSELs and utilises recent developments in GaN laser diode technologies to make the red VECSEL more compact and efficient. Further optimisation of the diode-pumped design is considered.

Chapter 2 discusses VECSEL design, looking at each element making up the structure. Overall design issues such as cavity resonance, threshold and efficiency,

structural strain and the effect of temperature on performance are considered. Factors specific to III-VI red emission and II-VI visible emission VECSELs are highlighted.

Chapter 3 examines more closely the effect of device temperature on laser performance. Thermal management techniques to improve temperature (and thus wavelength) stability are discussed. The effect on active region temperature of changing the pump wavelength is investigated. Characterisation of wafers of identical design but different growth temperatures is carried out.

Chapter 4 describes the development of new red VECSEL designs to utilise the shorter wavelength GaN laser diodes as the pump energy source. Both 405nm and 445nm pump wavelengths are used. Following the initial demonstration of the diode-pumped red emission VECSEL design alterations are made which improve output power and lifetime and the reasons for the improvement are examined.

Chapter 5 looks at the power decay and lifetime problems of the diode-pumped red VECSEL. Experimental results are presented which show a permanent degradation of performance and possible causes are discussed. Suggestions are made for future design change to improve device lifetime.

Chapter 6 introduces wide bandgap visible emission II-VI VECSELs through structures from collaborators at Heriot-Watt University and the City University of New York (CUNY). The structures and material systems are discussed and the structures characterised as the first step towards developing II-VI visible wavelength emission VECSELs.

Chapter 7 reviews the work contained in this thesis and looks forward to future research in diode-pumped red VECSELs and the next step in II-VI VECSEL design.

References

1 M. Rahim, A. Khiar, F. Felder, M. Fill, H. Zogg, and M. Sigrist, "5-μm vertical external-cavity surface-emitting laser (VECSEL) for spectroscopic applications," Applied Physics B: Lasers and Optics **100** (2), 261-264 (2010).

2 J. M. Hopkins, N. Hempler, B. Rosener, N. Schulz, M. Rattunde, C. Manz, K. Kohler, J. Wagner, and D. Burns, "High-power, (AlGaIn)(AsSb) semiconductor disk laser at 2.0 μm," Opt. Lett. **33** (2), 201-203 (2008).

3 N. Schulz, J. M. Hopkins, M. Rattunde, D. Burns, and J. Wagner, "High-brightness long-wavelength semiconductor disk lasers," Laser Photon. Rev. **2** (3), 160-181 (2008).

4 S. Calvez, J. E. Hastie, M. Guina, O. G. Okhotnikov, and M. D. Dawson, "Semiconductor disk lasers for the generation of visible and ultraviolet radiation," Laser Photon. Rev. **3** (5), 407-434 (2009).

5 Hans Lindberg, Anders Larsson, and Martin Strassner, "Single-frequency operation of a high-power, long-wavelength semiconductor disk laser," Opt. Lett. **30** (17), 2260-2262 (2005).

6 J. P. Tourrenc, S. Bouchoule, A. Khadour, J. Decobert, A. Miard, J. C. Haimand, and X. L. Oudar, "High power single-longitudinal-mode OP-VECSEL at 1.55 μm with hybrid metal-metamorphic Bragg mirror," Electronics Letters **43** (14), 754-755 (2007).

7 J. E. Hastie, S. Calvez, M. D. Dawson, T. Leinonen, A. Laakso, J. Lyytikainen, and M. Pessa, "High power CW red VECSEL with linearly polarized TEM_{00} output beam," Opt. Express **13** (1), 77-81 (2005).

8 R. Debusmann, N. Dhidah, V. Hoffmann, L. Weixelbaum, U. Brauch, T. Graf, M. Weyers, and M. Kneissl, "InGaN-GaN Disk Laser for Blue-Violet Emission Wavelengths," IEEE Photonics Technol. Lett. **22** (9), 652-654 (2010).

9 J. M. Hopkins, A. J. Maclean, D. Burns, E. Riis, N. Schulz, M. Rattunde, C. Manz, K. Kohler, and J. Wagner, "Tunable, single-frequency, diode-pumped 2.3 μm VECSEL," Opt. Express **15** (13), 8212-8217 (2007).

10 J. Chilla, S. Butterworth, A. Zeitschel, J. Charles, A. Caprara, M. Reed, and L. Spinelli, "High power optically pumped semiconductor lasers", *Solid State Lasers Xiii: Technology and Devices*, Vol. 5332, pp. 143-150.

11 B. Rudin, A. Rutz, M. Hoffmann, D. J. H. C. Maas, A. R. Bellancourt, E. Gini, T. Südmeyer, and U. Keller, "Highly efficient optically pumped vertical-emitting semiconductor laser with more than 20 W average output power in a fundamental transverse mode," Opt. Lett. **33** (22), 2719-2721 (2008).

12 Li Fan, Mahmoud Fallahi, Jörg Hader, Aramais R. Zakharian, Jerome V. Moloney, James T. Murray, Robert Bedford, Wolfgang Stolz, and Stephan W. Koch, "Multichip vertical-external-cavity surface-emitting lasers: a coherent power scaling scheme," Opt. Lett. **31** (24), 3612-3614 (2006).

13 S. S. Beyertt, U. Brauch, F. Demaria, N. Dhidah, A. Giesen, T. Kubler, S. Lorch, F. Rinaldi, and P. Unger, "Efficient Gallium-Arsenide Disk Laser," Quantum Electronics, IEEE Journal of **43** (10), 869-875 (2007).

14 J. E. Hastie, L. G. Morton, A. J. Kemp, M. D. Dawson, A. B. Krysa, and J. S. Roberts, "Tunable ultraviolet output from an intracavity frequency-doubled red vertical-external-cavity surface-emitting laser," Applied Physics Letters **89** (6), 061114 (2006).

15 J. M. Hopkins, S. A. Smith, C. W. Jeon, H. D. Sun, D. Burns, S. Calvez, M. D. Dawson, T. Jouhti, and M. Pessa, "0.6 W CW GaInNAs vertical external-cavity surface emitting laser operating at 1.32 μm," Electronics Letters **40** (1), 30-31 (2004).

16 J. Rautiainen, A. Härkönen, V. M. Korpijärvi, P. Tuomisto, M. Guina, and O. G. Okhotnikov, "2.7 W tunable orange-red GaInNAs semiconductor disk laser," Opt. Express **15** (26), 18345-18350 (2007).

17 H. Lindberg, M. Strassner, and A. Larsson, "Improved spectral properties of an optically pumped semiconductor disk laser using a thin diamond heat spreader as an intracavity filter," IEEE Photonics Technol. Lett. **17** (7), 1363-1365 (2005).

18 Jussi Rautiainen, Jari Lyytikäinen, Alexei Sirbu, Alexandru Mereuta, Andrei Caliman, Eli Kapon, and Oleg G. Okhotnikov, "2.6 W optically-pumped semiconductor disk laser operating at 1.57-μm using wafer fusion," Opt. Express **16** (26), 21881-21886 (2008).

19 S. J. McGinily, R. H. Abram, K. S. Gardner, Riis Erling, A. I. Ferguson, and J. S. Roberts, "Novel Gain Medium Design for Short-Wavelength Vertical-External-Cavity Surface-Emitting Laser," Quantum Electronics, IEEE Journal of **43** (6), 445-450 (2007).

20 S. Lutgen, T. Albrecht, P. Brick, W. Reill, J. Luft, and W. Spath, "8-W high-efficiency continuous-wave semiconductor disk laser at 1000 nm," Applied Physics Letters **82** (21), 3620-3622 (2003).

21 K. S. Kim, J. R. Yoo, S. H. Cho, S. M. Lee, S. J. Lim, J. Y. Kim, J. H. Lee, T. Kim, and Y. J. Park, "1060 nm vertical-external-cavity surface-emitting lasers with an optical-to-optical efficiency of 44% at room temperature," Applied Physics Letters **88** (9), 091107 (2006).

22 Li Fan, Chris Hessenius, Mahmoud Fallahi, Jorg Hader, Hongbo Li, Jerome V. Moloney, Wolfgang Stolz, Stephan W. Koch, James T. Murray, and Robert Bedford, "Highly strained InGaAs/GaAs multiwatt vertical-external-cavity surface-emitting laser emitting around 1170 nm," Applied Physics Letters **91** (13), 131114 (2007).

23 Jonna Paajaste, Soile Suomalainen, Riku Koskinen, Antti Härkönen, Mircea Guina, and Markus Pessa, "High-power and broadly tunable GaSb-based optically pumped VECSELs emitting near 2 μm," Journal of Crystal Growth **311** (7), 1917-1919 (2009).

24 S. L. Vetter, J. E. Hastie, V. M. Korpijarvi, J. Puustinen, M. Guina, O. Okhotnikov, S. Calvez, and M. D. Dawson, "Short-wavelength GaInNAs/GaAs semiconductor disk lasers," Electronics Letters **44** (18), 1069-1070 (2008).

25 J. Konttinen and et al., "High-power (>1 W) dilute nitride semiconductor disk laser emitting at 1240 nm," New Journal of Physics **9** (5), 140 (2007).

26 J.-M. Hopkins, R. D. Preston, A. J. Maclean, S. Calvez, H. Sun, J. Ng, M. Steer, M. Hopkinson, and D. Burns, "High performance 2.2 μm optically-

pumped vertical external-cavity surface-emitting laser," Journal of Modern Optics **54** (12), 1677 - 1683 (2007).

27 H. Lindberg, M. Strassner, J. Bengtsson, and A. Larsson, "High-power optically pumped 1550-nm VECSEL with a bonded silicon heat spreader," IEEE Photonics Technol. Lett. **16** (5), 1233-1235 (2004).

28 A. Laurain, M. Myara, G. Beaudoin, I. Sagnes, and A. Garnache, "Multiwatt-power highly-coherent compact single-frequency tunable Vertical-External-Cavity-Surface-Emitting-Semiconductor-Laser," Opt. Express **18** (14), 14627-14636 (2010).

29 M. Fallahi, L. Fan, Y. Kaneda, C. Hessenius, J. Hader, H. Li, J. V. Moloney, B. Kunert, W. Stolz, S. W. Koch, J. Murray, and R. Bedford, "5-W Yellow Laser by Intracavity Frequency Doubling of High-Power Vertical-External-Cavity Surface-Emitting Laser," IEEE Photonics Technol. Lett. **20** (17-20), 1700-1702 (2008).

30 B. Rosener, N. Schulz, M. Rattunde, C. Manz, K. Kohler, and J. Wagner, "High-power high-brightness operation of a 2.25-μm (AlGaIn)(AsSb)-based barrier-pumped vertical-external-cavity surface-emitting laser," IEEE Photonics Technol. Lett. **20** (5-8), 502-504 (2008).

31 Wang Tsuei-Lian, Y. Kaneda, J. M. Yarborough, J. Hader, J. V. Moloney, A. Chernikov, S. Chatterjee, S. W. Koch, B. Kunert, and W. Stolz, "High-Power Optically Pumped Semiconductor Laser at 1040 nm," IEEE Photonics Technol. Lett. **22** (9), 661-663 (2010).

32 D. Burns, J.-M. Hopkins, A. J. Kemp, B. Rösener, N. Schulz, C. Manz, K. Köhler, M. Rattunde, and J. Wagner, "Recent developments in high-power short-wave mid-infrared semiconductor disk lasers", *Solid State Lasers XVIII: Technology and Devices*, Vol. 719311 (SPIE), 2009.

33 M. Kuznetsov, F. Hakimi, R. Sprague, and A. Mooradian, "High-power (>0.5-W CW) diode-pumped vertical-external-cavity surface-emitting semiconductor lasers with circular TEM_{00} beams," IEEE Photonics Technol. Lett. **9** (8), 1063-1065 (1997).

34 Shuji Nakamura, Masayuki Senoh, Shin-ichi Nagahama, Naruhito Iwasa, Toshio Matsushita, and Takashi Mukai, "Blue InGaN-based laser diodes with an emission wavelength of 450 nm," Applied Physics Letters **76** (1), 22-24 (2000).

35 Kuniyoshi Okamoto, Junich Kashiwagi, Taketoshi Tanaka, and Masashi Kubota, "Nonpolar m-plane InGaN multiple quantum well laser diodes with a lasing wavelength of 499.8 nm," Applied Physics Letters **94** (7), 071105 (2009).

36 Desiree Queren, Adrian Avramescu, Georg Bruderl, Andreas Breidenassel, Marc Schillgalies, Stephan Lutgen, and Uwe Strauss, "500 nm electrically driven InGaN based laser diodes," Applied Physics Letters **94** (8), 081119 (2009).

37 Adrian Avramescu, Teresa Lermer, Jens Muller, Sonke Tautz, Desiree Queren, Stephan Lutgen, and Uwe Strauss, "InGaN laser diodes with 50 mW output power emitting at 515 nm," Applied Physics Letters **95** (7), 071103 (2009).

38 A. Avramescu, T. Lermer, J. Muller, C. Eichler, G. Bruederl, M. Sabathil, S. Lutgen, and U. Strauss, "True Green Laser Diodes at 524 nm with 50 mW

Continuous Wave Output Power on c-Plane GaN," Applied Physics Express **3** (6), 061003 (2010).

39 Yohei Enya, Yusuke Yoshizumi, Takashi Kyono, Katsushi Akita, Masaki Ueno, Masahiro Adachi, Takamichi Sumitomo, Shinji Tokuyama, Takatoshi Ikegami, Koji Katayama, and Takao Nakamura, "531 nm Green Lasing of InGaN Based Laser Diodes on Semi-Polar Free-Standing GaN Substrates," Applied Physics Express **2** (8), 082101 (2009).

40 Nichia press release, "Nichia starts sample shipments of green semiconductor laser", (7/7/2010). http://www.nichia.co.jp/en/about_nichia/2010/2010_070701.html

41 University of Illinois at Urbana-Champaign. http://vcsel.mntl.illinois.edu/VCSEL_fab_overview_files/slide0014_image031.png Photonic Device Research Group.

42 M. Miller, M. Grabherr, R. King, R. Jager, R. Michalzik, and K. J. Ebeling, "Improved output performance of high-power VCSELs," Selected Topics in Quantum Electronics, IEEE Journal of **7** (2), 210-216 (2001).

43 B. Sumpf, K. H. Hasler, P. Adamiec, F. Bugge, F. Dittmar, J. Fricke, H. Wenzel, M. Zorn, G. Erbert, and G. Trankle, "High-Brightness Quantum Well Tapered Lasers," IEEE J. Sel. Top. Quantum Electron. **15** (3), 1009-1020 (2009).

44 A. Richter, E Heumann, and G. Huber, "Power scaling of semiconductor laser pumped Praeseodymium lasers," Opt. Express **15** (8), 7 (2007).

45 P. F. Moulton, "Spectroscopic and laser characteristics of Ti:Al_2O_3," J. Opt. Soc. Am. B **3** (1), 125-133 (1986).

46 Peter W. Roth, Alexander J. Maclean, David Burns, and Alan J. Kemp, "Directly diode-laser-pumped Ti:sapphire laser," Opt. Lett. **34** (21), 3334-3336 (2009).

47 E. Snoeks, L. Zhao, B. Yang, A. Cavus, L. Zeng, and M. C. Tamargo, "Structural quality of pseudomorphic $Zn_{0.5}Cd_{0.5}Se$ layers grown on an InGaAs or InP buffer layer on (0 0 1) InP substrates," Journal of Crystal Growth **179** (1-2), 83-92 (1997).

48 A. Masters and C. Seaton, *Laser Focus World*, pp. S9-S11 (2006).

49 T. Schwarzback, M. Eichfelder, W.M. Schulz, R. Rossbach, M. Jetter, P. Michler, "Short wavelength red-emitting AlGaInP-VECSEL exceeds 1.2 W continuous-wave output power," Applied Physics B-Lasers and Optics **102** (4), 789-794 (2011).

50 B.Rosener, M. Rattunde, R. Moser, S. Kaspar, T. Topper, C. Manz, K. Kohler, J. Wagner, "Continuous-wave room-temperature operation of a 2.8 µm GaSb-based semiconductor disk laser." Opt. Lett. **36**(3), 319-321 (2011).

51 V.M. Korpijarvi, T. Leinonen, J. Puustinen, A. Harkonen, M.D. Guina,"11 W single gain-chip dilute nitride disk laser emitting around 1180 nm," Opt. Express **18** (25), 25633-25641 (2010).

52 A. Rantamaki, A. Sirbu, A. Mereuta, E. Kapon, O.G. Okhotnikov, "3 W of 650 nm red emission by frequency doubling of wafer-fused semiconductor disk laser," Opt. Express **18** (21), 21645-21650 (2010).

53 R, Debusmann, N. Dhidah, V. Hoffmann, L. Weixelbaum, U. Brauch, T. Graf, M. Weyers, M. Kneissl, "InGaN-GaN Disk Laser for Blue-Violet

Emission Wavelengths," IEEE Photonics Technol. Lett. **22** (9), 652-654 (2010).

54 Z.L. Li, Y.R. Song, P. Zhang, X.A. Zhang, "Intracavity Second Harmonic Generation Characteristics of Semiconductor Disk Laser," *Semiconductor Lasers and Applications IV*, Vol 7844 (SPIE) 2010.

55 J. Rautiainen, A. Harkonen, V. M. Korpijarvi, J. Puustinen, L. Orsila, M. Guina, O. G. Okhotnikov, *Red and UV Generation Using Frequency-Converted GaInNAs-Based Semiconductor Disk Laser*. (CLEO/QELS 2009), VOLS 1-5 (2009), pp.698.

56 J. Rautiainen, O. G. Okhotnikov, D. Eger, S. A. Zolotovskaya, K. A. Fedorova, and E. U. Rafailov, Electronics Letters **45** (3), 177 (2009).

Chapter 2

VECSEL Structure Design

2.1 Structural Elements

As discussed in Chapter 1, a VECSEL is an optically pumped layered semiconductor structure which resembles a VCSEL without the top mirror, as shown in Figure 2-1. Thus it consists of an active region, containing pump absorbing barriers and the quantum wells, a layered semiconductor mirror known as a distributed Bragg reflector (DBR) and an external mirror which completes the laser cavity.

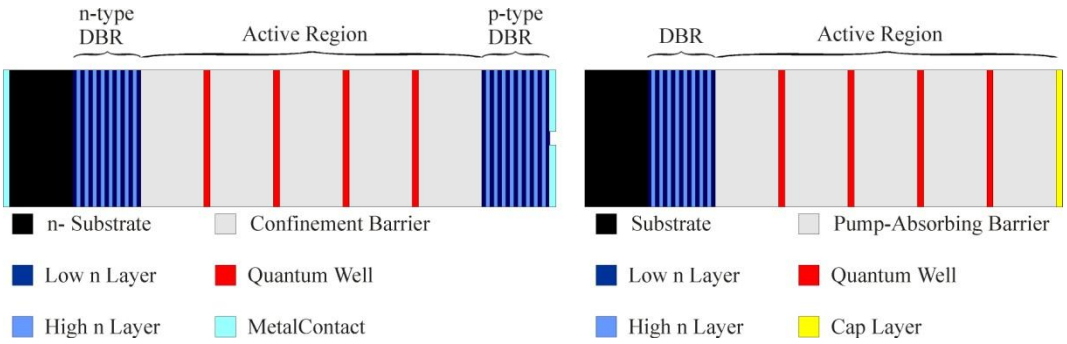

Figure 2-1: Schematic of simple VCSEL and VECSEL structures

Almost the entire laser cavity is in air and the laser mode is accessible for additional optical elements to effect single-mode operation or non-linear conversion.

2.1.1 Active Region

The active region is the critical element of the structure, setting the emission wavelength and strongly influencing the efficiency and threshold for laser operation.

The VECSEL is ideally suited to optical pumping as the thickness of the active region in a VECSEL is very small in comparison to other semiconductor lasers, a micron or less in the structures discussed here, compared to millimetres in laser diodes or crystals for instance. Thus the pump focus does not have to be maintained

over a macroscopic distance. Instead the VECSEL can be treated as a planar absorber and the pump focus is only required to be a suitable size and shape in the plane of the active region which simplifies the optical requirements of the pump scheme. Additionally, VECSELs are sufficiently strong absorbers that pump recycling is generally not required.

In designing the active region it is necessary to take into account:

- the desired lasing wavelength
- the pump wavelength
- the desired performance characteristics such as tuning range, threshold and output power.

The choice of pump absorbing barrier dictates the minimum pump photon energy and absorption length (the distance over which the pump photon intensity is reduced to 1/e of the initial value) of the pump photons in the active region. In turn this guides how long the active region should be so that all the quantum wells contribute to the laser gain. The width and composition of the quantum wells sets the emission wavelength and, with the barrier choice, affect how strongly the carriers are confined to the quantum wells. Stronger carrier confinement improves efficiency by reducing thermal emission of carriers from the quantum wells. The desired laser wavelength dictates the ideal placements of the quantum wells to minimise threshold using resonant periodic gain (section 2.1.4).

In addition there is a trade off between minimising the threshold and tuning range to be considered in choosing a cavity which is resonant at the laser wavelength, anti-resonant, or somewhere in between. Therefore we will now address each element in detail.

2.1.2 Quantum Wells

A quantum well consists of a thin layer of material of a lower bandgap than the surrounding material. The adjacent layers form energy barriers which confine the carrier in the direction normal to the well (remaining free in the other two directions)

and, when the thickness of the well is comparable to the de Broglie wavelength of the carriers, the carrier energy levels become quantised.

The de Broglie relation relates the wavelength of matter to its momentum and can be written as

$$\lambda = \frac{h}{p} \tag{2-1}$$

where h is Planck's constant and p the particle's momentum.

Confinement in two or even three dimensions (quantum wires and dots respectively) is possible but not addressed in this work.

If the carrier is confined in the z-direction of the simple ideal quantum well shown in Figure 2-2 then the time-independent Schrodinger equation (TISE) takes the form:

$$-\frac{\hbar}{2m^*}\frac{\partial^2\psi(z)}{\partial z^2} + V(z)\psi(z) = E\psi(z) \tag{2-2}$$

where m^* is the effective mass of the carrier (which is material dependant), $\psi(z)$ is the carrier wavefunction, E the carrier energy and V(z) the potential energy. The effective mass is used in place of the free carrier mass to allow the behaviour of carriers in the periodic electric potential of the crystal lattice to be treated as that of carriers in the free electron gas model.

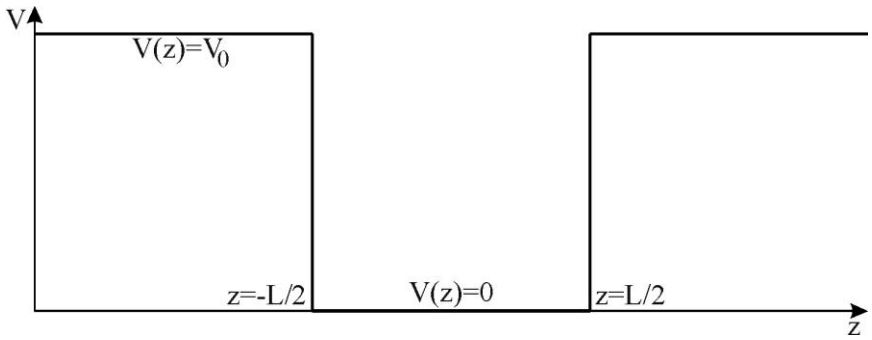

Figure 2-2: Potential energy levels in a finite one dimensional square quantum well. V(z) is the potential energy level and L is the quantum well width.

If we treat the potential energy of the well as 0 and the potential of the barrier as V_0, then:

$$V(z) = \begin{cases} 0, |z| < L/2 \\ V_0, |z| \geq L/2 \end{cases} \tag{2-3}$$

The simpler case of a particle in an infinite potential well can be obtained by setting $V_0=\infty$.

Rewriting the TISE as

$$-\frac{\hbar}{2m^*}\frac{\partial^2\psi(z)}{\partial z^2} = (E - V(z))\psi(z) \tag{2-4}$$

we can see that the solutions of this second order partial differential equation will differ for E>V and E<V i.e. in the quantum well and in the barrier.

Within the well, E>V so the TISE is satisfied by a solution of the form

$$\psi(z) = \begin{cases} \sqrt{\frac{2}{L}}cos(k_n z)\,, even\ n \\ \sqrt{\frac{2}{L}}sin(k_n z)\,, odd\ n \end{cases} \tag{2-5}$$

where $k_n=n\pi/L$ and n is a positive integer.
Outside the well, E<V and the TISE is satisfied by a solution of the form

$$\psi(z) = C_1 e^{-K_z z} + C_2 e^{-K_z z} \tag{2-6}$$

where $K_z^2 = \frac{2m}{\hbar^2}(V_0 - E)$.

However, the requirement that $\partial\psi(z)/\partial z$ is continuous and $\psi(z)\rightarrow 0$ as $|z|\rightarrow\infty$ restricts the solutions to

$$\psi(z) = \begin{cases} Ce^{-K_z z}, even\ n \\ -Ce^{-K_z z}, odd\ n \end{cases} \tag{2-7}$$

So the even states are given by

$$\psi(z) = \begin{cases} \sqrt{\frac{2}{L}} cos(k_n z), |z| < L/2 \\ Ce^{-K_z z}, |z| \geq L/2 \end{cases} \tag{2-8}$$

with the requirements that ψ(z) and ∂ψ(z)/ ∂z are continuous imposing the condition that

$$\sqrt{E} tan\left(\frac{\sqrt{mE}}{2\hbar^2} L\right) = \sqrt{V_0 - E} \tag{2-9}$$

whose solution gives the energy of the even states. The odd states are given by

$$\psi(z) = \begin{cases} \sqrt{\frac{2}{L}} sin(k_n z), |z| < L/2 \\ -Ce^{-K_z z}, |z| \geq L/2 \end{cases} \tag{2-10}$$

with the requirements that ψ(z) and ∂ψ(z)/ ∂z are continuous imposing the condition that

$$-\sqrt{E} cot\left(\frac{\sqrt{mE}}{2\hbar^2} L\right) = \sqrt{V_0 - E} \tag{2-11}$$

whose solution gives the energy of the odd states.

The first two energy levels in a one dimensional finite potential well are shown in Figure 2-3.

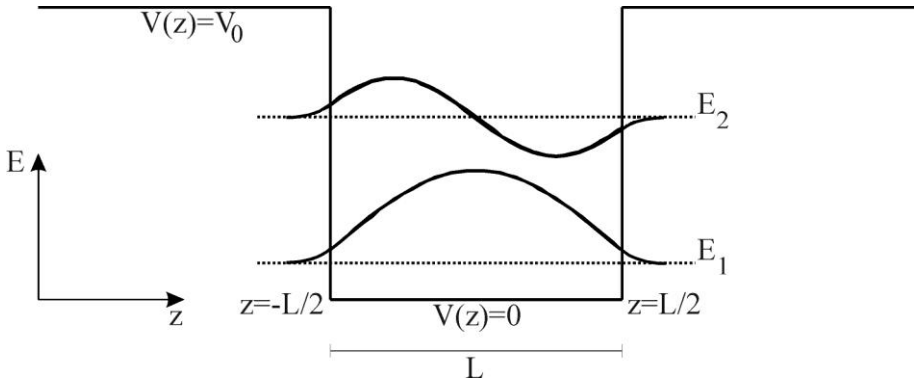

Figure 2-3: Confined energy levels of a finite one dimensional square well

There is always at least one solution to the previous equations within a quantum well, and therefore at least one confined energy level, however there can be many depending on the carrier effective mass and the depth of the potential well. The depth of the potential well will generally be different for holes and electrons as the difference in band minima for the barriers and well – conduction band offset (CBO) and valence band offset (VBO) - are usually different. For example, the direct bandgap CBO has been calculated as ~$0.65\Delta E_g$ for $Ga_{0.5}In_{0.5}P$ quantum wells in $(Al_xGa_{1-x})_{0.5}In_{0.5}P$ barriers by Zhang et al[1], where ΔE_g is the bandgap difference between the well and barrier. This is illustrated by Figure 2-4 which shows the direct bandgaps and band offsets for an $Ga_{0.5}In_{0.5}P$ quantum well in $(Al_xGa_{1-x})_{0.5}In_{0.5}P$ barriers.

The transition energy E_T can be changed by varying the quantum well layer thickness or material composition to set the desired quantum well emission wavelength. Based on work by Chuang[2] and Kolbas[3] we modelled the dependence of transition energy on the width of the quantum well. The results are illustrated in Figure 2-5 for four different quantum well $Ga_xIn_{1-x}P$ compositions in $(Al_{0.6}Ga_{0.4})_{0.5}In_{0.5}P$.

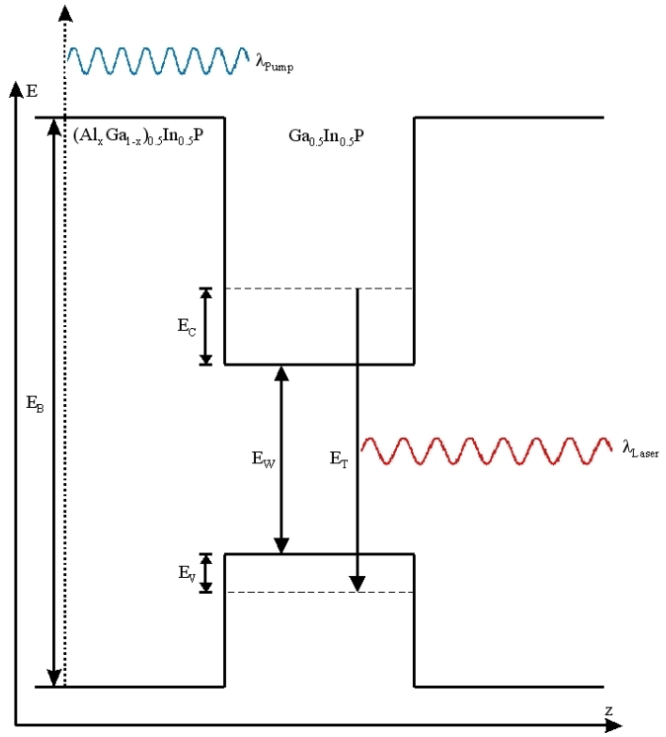

Figure 2-4: Energy levels and transitions in a $Ga_{0.5}In_{0.5}P/(Al_xGa_{1-x})_{0.5}In_{0.5}P$ quantum well

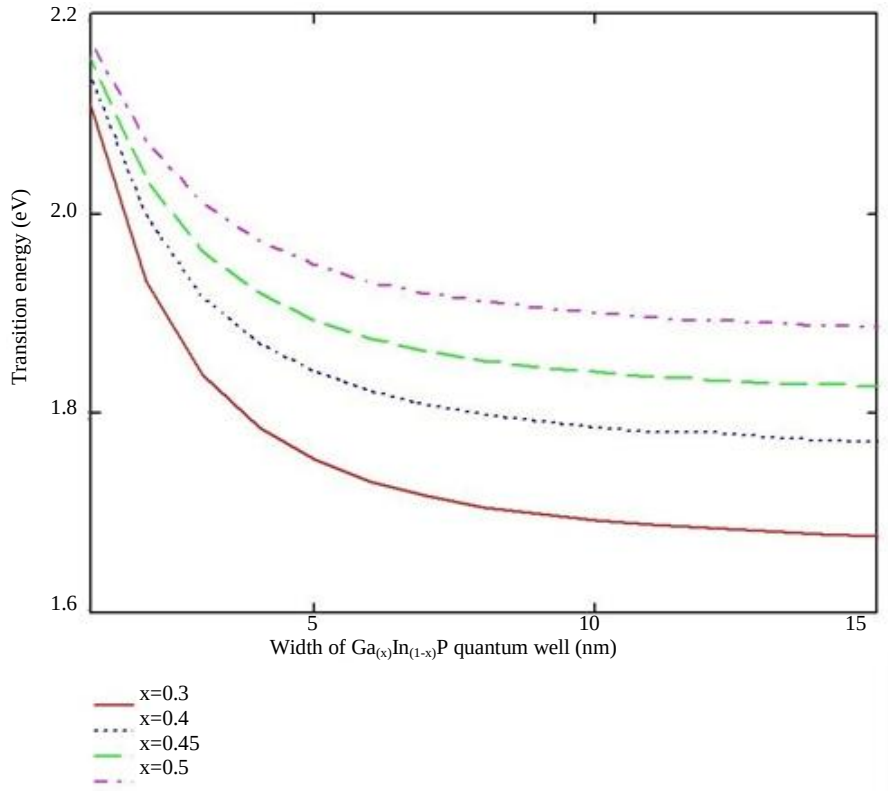

Figure 2-5: Modelled transition energy against quantum well width and composition

This ability to precisely tailor a structure to a desired emission wavelength with only minor alterations to existing proven designs shows the flexibility of the VECSEL technology.

2.1.3 Gain Modelling

Put simply, laser gain is the proportional increase in photons (of a specific energy) per unit distance. Understanding the level of gain and its dependence on factors such as wavelength is critical to designing VECSELs, predicting quantities such as threshold and enabling informed design decisions to be made on the number of quantum wells. We follow the model developed by Kuznetsov et al[4] as the basis for understanding the effect of gain on laser performance and design decisions. More detailed VECSEL models have been developed[5,6] which take into account additional factors, such as the change in the dependence of loss on carrier density with changing carrier density, and more accurately reflect VECSEL behaviour. However, the Kuznetsov model has the benefit of simplicity and is sufficient to provide a qualitative picture when developing a new structure, which we used when designing the VECSELs in Chapter 4.

The model uses a logarithmic dependence of quantum well gain g on carrier density:

$$g = g_0 ln(N/N_0) \tag{2-12}$$

g_0 is the material gain parameter, N the carrier density and N_0 the transparency carrier density.

The lasing threshold is reached when the level of gain from the quantum wells is sufficient to compensate for the round-trip losses due to output coupling and parasitic losses i.e.

$$Net\ Loss\ x\ Net\ Laser\ Gain = 1. \tag{2-13}$$

The Net Loss per round-trip is

$$NL = R_1 R_2 T_{loss} \tag{2-14}$$

and the Net Laser Gain is

$$NG = e^{2\Gamma g_{th} N_w L_w}. \tag{2-15}$$

where R_1 and R_2 are the end mirror reflectivities, T_{loss} is the proportional round-trip losses, N_w the number of quantum wells and L_w the width of each quantum well. Γ is the longitudinal confinement factor which expresses the overlap between the gain medium (quantum wells) and the $|E|^2$ standing field.

This can be expressed as the round-trip condition:

$$NL\ x\ NG = R_1 R_2 T_{loss} e^{2\Gamma g_{th} N_w L_w} = 1 \tag{2-16}$$

The round-trip condition shows simply that increasing the level of output coupling (i.e. decreasing R_2) increases the level of gain needed to reach threshold and increases the pump intensity (and so pump threshold) needed to provide the extra gain.

The threshold carrier density N_{th} can be expressed as

$$N_{th} = N_0 \left(\frac{1}{NL}\right)^{(\ln NG)^{-1}} \tag{2-17}$$

and the threshold pump power as

$$P_{th} = N_{th} \frac{h\nu N_w L_w A_p}{\eta_{abs} \tau(N_{th})} \tag{2-18}$$

where hν is the pump photon energy, A_p the area of the pump spot, η_{abs} the pump absorption efficiency and $\tau(N_{th})$ the carrier lifetime.

The overall differential efficiency of the device η_{diff} is

$$\eta_{diff} = \eta_{abs}\eta_{quant}\eta_{out} \tag{2-19}$$

The quantum efficiency

$$\eta_{quant} = \frac{\lambda_{pump}}{\lambda_{laser}} \tag{2-20}$$

reflects how much of the pump photon energy is lost producing a laser photon and also sets the lower bound on the heat loading of the device as will be seen in the section on thermal modelling.

The output efficiency

$$\eta_{out} = \frac{\ln(R_2)}{ln(R_1 R_2 T_{loss})} \tag{2-21}$$

reflects how much of the round-trip loss is usefully output coupled through R_2.

This leads to an expression for the output power of the VECSEL

$$P_{las} = (P_p - P_{th})\eta_{diff} \tag{2-22}$$

which is a combination of the pump power above threshold (P_p-P_{th}) and the differential efficiency of the device η_{diff}.

The Kuznetsov model assumes the quantum wells have been arranged in a particular manner within the structure which reduces threshold known as resonant periodic gain (RPG).

2.1.4 Resonant Periodic Gain

In 1988 Raja et al[7] proposed a novel method of placing the quantum wells in a multiple quantum well gain medium to both increase efficiency and wavelength selectivity. The level of effective gain is proportional to the $|E|^2$ field[8], which implies that the locations of the anti-nodes of the $|E|^2$ field at the lasing wavelength would be the best place to site the quantum wells. Placing the quantum wells in this way has the additional advantage of enhancing the wavelength selectivity of the design, as the anti-nodes of the $|E|^2$ field shift farther from the quantum wells as the wavelength shifts away from the design. This is illustrated in Figure 2-6 for a ten quantum well structure designed to be resonant at 672nm.

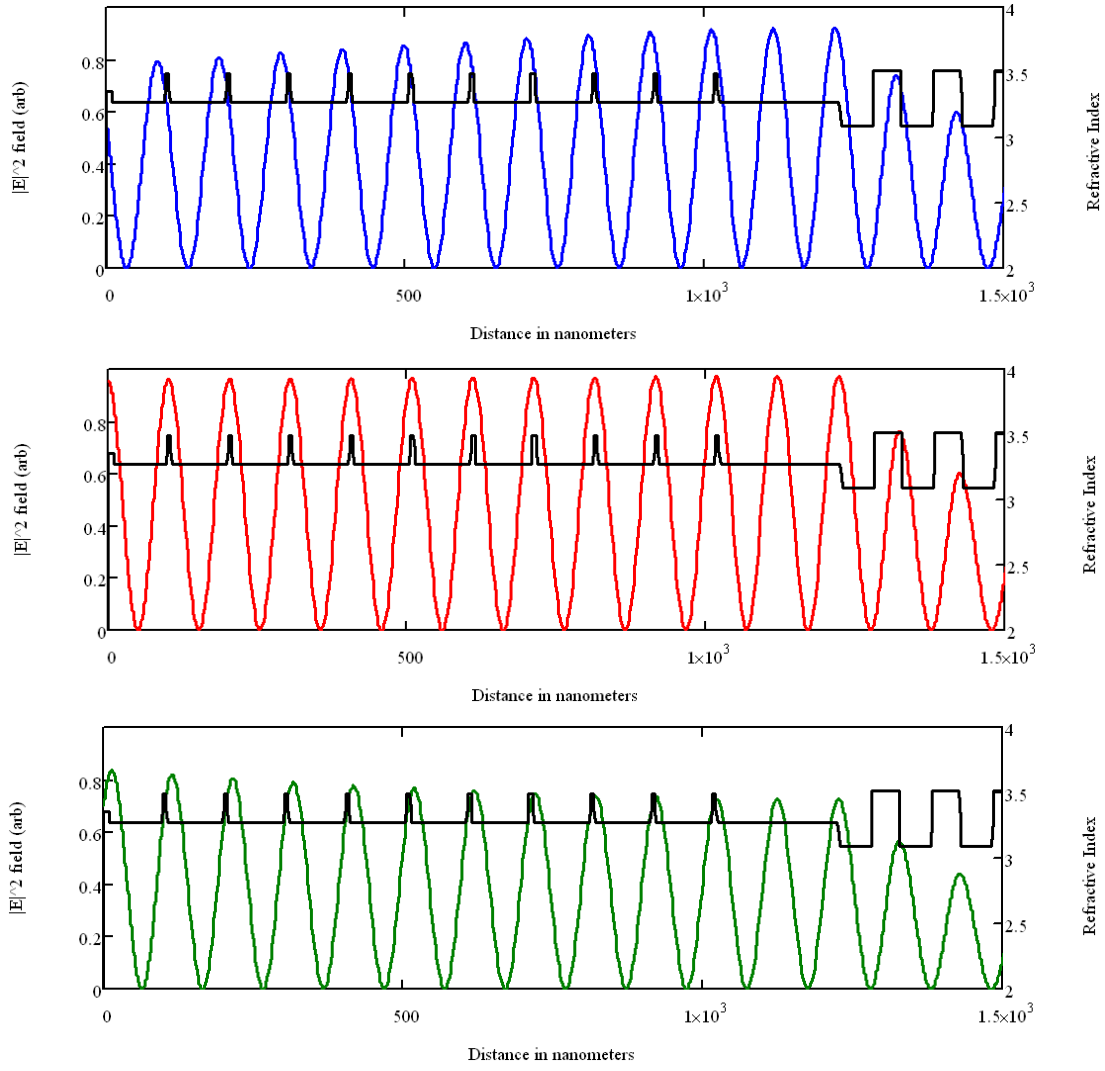

Figure 2-6: Displacement of sub-cavity standing waves for a)667nm, b)672nm and c)677nm in a 10 QW VECSEL

Spatial hole burning, the depletion of carriers by the standing wave causing gain to be seen at other wavelengths, is avoided as the anti-nodes of the standing wave overlap very thin gain layers and thus effective gain is enhanced only for very specific longitudinal modes where the anti-nodes of the standing wave coincide with the gain layers[9-12].

Also amplified spontaneous emission (ASE) is reduced as the gain is strongly wavelength dependant because the gain medium layers coincide with the peaks of the electric field at the laser wavelength only. Amplified spontaneous emission is caused by a spontaneously emitted photon (with random phase) encountering a region with population inversion (and gain) and stimulating emission.

VECSELs are low gain devices, the gain element being the thin quantum wells, and taking advantage of resonant periodic gain is vital in obtaining good performance. In the red emission diode-pumped structure demonstrated in Chapter 4 the total thickness of the gain elements is only 49nm.

2.1.5 Resonant and Anti-Resonant cavity design

A resonant cavity is one designed so that an anti-node of the laser standing wave appears at the semiconductor-air interface (when the cavity is resonant at the laser wavelength), maximising the magnitude of the anti-nodes of the standing electric field at the designed operating wavelength at the quantum wells. The structure will likely be designed so that the resonant wavelength matches the quantum well gain peak, producing maximum effective gain (a combination of the material gain and electric field intensity) at the designed laser wavelength. This ensures the maximum gain and lowest threshold. However the effective gain due to the overlap between the material gain and electric field is sensitive to wavelength change and as the quantum well peak gain moves away from the resonance wavelength both the material gain *and* $|E|^2$ field at the wells decline, making the effective gain strongly wavelength dependant so restricting the tuning range.

An approach first introduced by Holm et al[13] to reduce the sensitivity to temperature and increase the tuning range is to design the cavity to have a node of the laser standing wave at the semiconductor-air interface. This reduces the magnitude of the electric field at the RPG wavelength but significantly broadens the effective gain peak because the $|E|^2$ field at the quantum wells actually increases as the laser wavelength shifts away from the RPG wavelength which broadens the effective gain. This effect is analysed in Garnache et al[8] for resonant and anti-resonant VECSEL cavities. Whilst an anti-resonant design will have a higher threshold than the corresponding resonant design the broadening of the gain makes it less sensitive to the cavity changes caused by temperature or deliberate tuning. The length of the part of the active region containing the quantum wells also plays a role in determining the sensitivity of the laser gain to changes in the laser wavelength, which we examine in section 4.3.3.2 in the context of the experimental performance of the diode-pumped red VECSEL.

2.1.6 Wavelength Shift With Temperature

Often a structure will be designed with the quantum well emission at a shorter wavelength than the cavity resonance. As the active region heats up[14] both the quantum well emission and cavity resonance shift to longer wavelengths but at different rates[15,16] as shown in Figure 2-7. To compensate for the larger shift of the quantum well emission the quantum well design wavelength can be made shorter than the cavity resonance so that, for the anticipated rise in temperature, the emission and resonance peaks coincide during laser operation. Although the quantum well emission efficiency decreases with temperature due to increased non-radiative recombination and thermal emission of carriers from the wells, observed PL can increase with temperature as the emission and resonance wavelengths overlap.

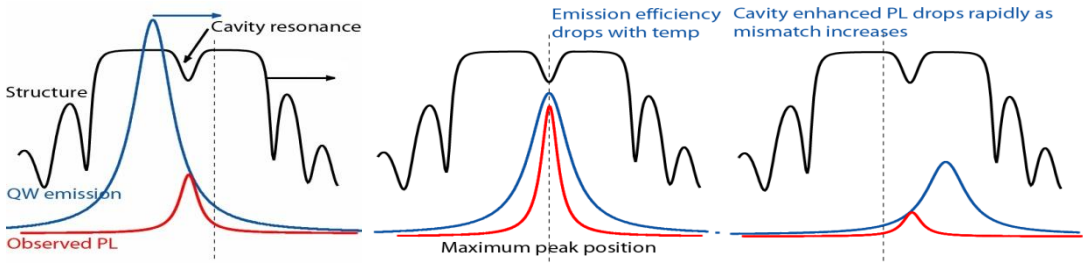

Figure 2-7: Illustration of temperature dependant shift of QW emission and sub-cavity resonance

For high enough pump power the loss of emission efficiency due to heating can be more significant than the additional carrier density and output power will actually decrease. This is known as 'thermal rollover'. The management of thermal effects in a VECSEL to minimise the output wavelength shift for changes in pump power will be discussed in section 3.2.

2.1.7 Distributed Bragg Reflector

Being low gain devices, VECSELs are sensitive to the quality of the laser cavity and require high quality laser cavity mirrors in order to minimise round trip losses and function successfully.

Rather than use mirror-coatings applied during post-processing, a high quality mirror (R>99.9%) known as a distributed Bragg reflector (DBR) can be grown as part of the VECSEL structure. This consists of alternating layers of high and low refractive index material where the constructive interference of the partial reflections at each layer results in a high level of reflectivity for a range of wavelengths known as the stopband. The extent of the stopband provides an upper and lower wavelength limit to the tuning which can be achieved as the reflectivity drops sharply outside the stopband causing high losses.

The reflectivity of the DBR depends partly on the refractive index contrast of the materials and partly on the layer thicknesses. Each layer of the DBR has a thickness of a quarter of the design wavelength (in the medium), so each layer interface is $\lambda/4$ apart and the light changes phase by $\pi/2$. At each interface partial reflection takes place, with reflection at the low to high refractive index interface shifting the phase

by π but without phase shift at the high to low interface. The result of this is that the light reflected at each interface constructively interferes and the cumulative effect is that of a highly reflective mirror. The reflectivity is wavelength dependent and can be tailored for reflectivity centred on the laser wavelength. This principle is illustrated in Figure 2-8.

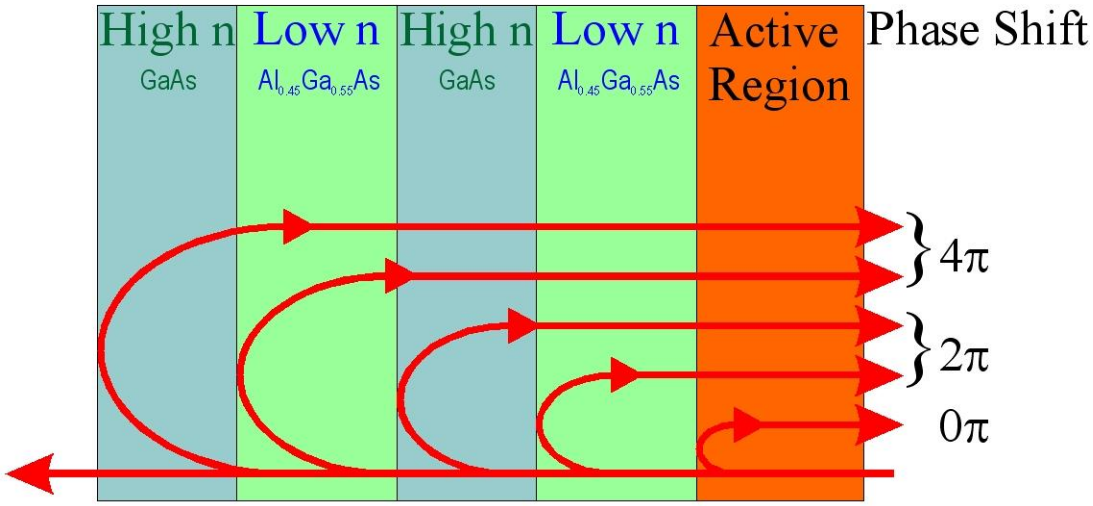

Figure 2-8: Illustration of the principle of the DBR reflection with partial reflections of the incident beam (top).

The level (and wavelength spread) of reflectivity is set by the refractive index contrast and the number of layers used. The reflectivity of a DBR with N pairs of alternating layers is given by

$$R_N = \left(\frac{n_0 - n_s \left(\frac{n_1}{n_2}\right)^{2N}}{n_0 - n_s \left(\frac{n_1}{n_2}\right)^{2N}} \right)^2 \qquad (2\text{-}23)$$

where n_0, n_1, n_2 and n_s are the respective refractive indices of the surrounding medium, the two alternating materials, and the substrate. It is desirable to keep the number of layers to the minimum necessary as additional layers add growth complexity and thermal resistance. There is also a diminishing return on the number of layers and once a sufficiently broad stopband of high reflectivity has been established there is little benefit to adding more. A good stopband is required for the laser to operate over a range of wavelengths. The reflectivity of an

Diode Pumped Visible Vertical External Cavity Surface Emitting Lasers $Al_{0.45}Ga_{0.55}As$/AlAs DBR for different values of N is shown in Figure 2-9, calculated using the calculation of Bragg stack reflection from Born and Wolf[17] and various material parameters for AlGaAs[18,19] (AlGa)InP[20] and GaInP[21,22].

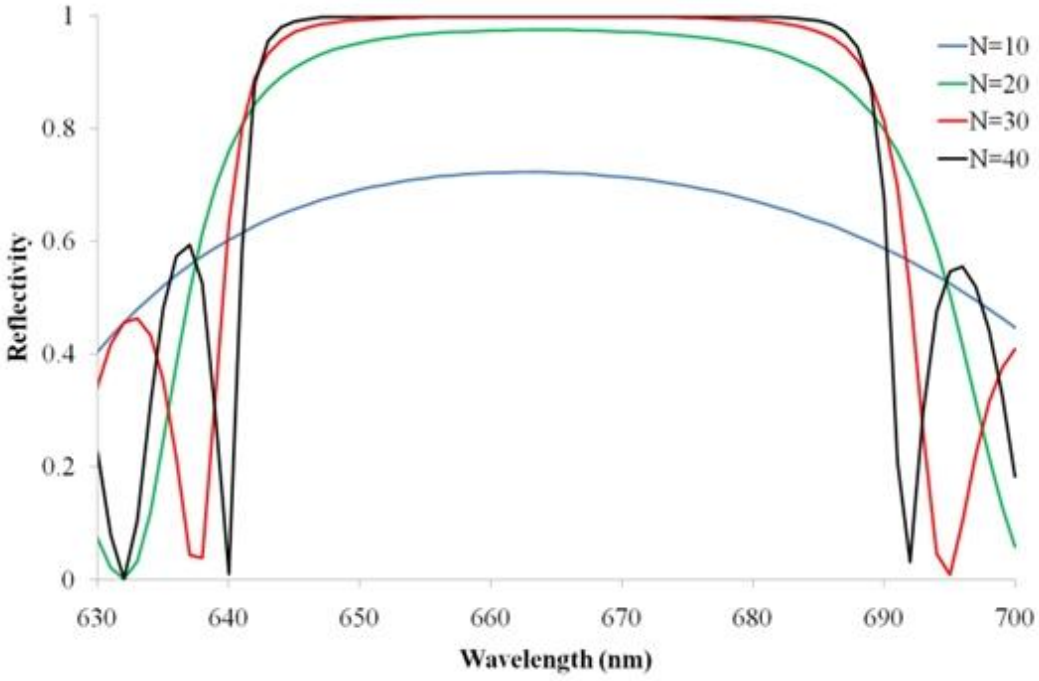

Figure 2-9: Calculated reflectivity of an N=10, N=20, N=30 and N=40 $Al_{0.45}Ga_{0.55}As$/AlAs DBR.

2.2 Fabrication

The AlGaInP VECSEL structures used for the diode-pumped VECSEL were grown by our collaborators at the Optoelectronics Research Centre, Tampere University of Technology, Finland. They were grown by molecular beam epitaxy (MBE) on a GaAs substrate. In this technique, one or more solid sources of materials are evaporated in effusion cells and fired into an ultra-high vacuum chamber to condense onto the substrate (where they may react with each other), illustrated schematically in Figure 2-10[23]. The beams do not interact until they reach the wafer.

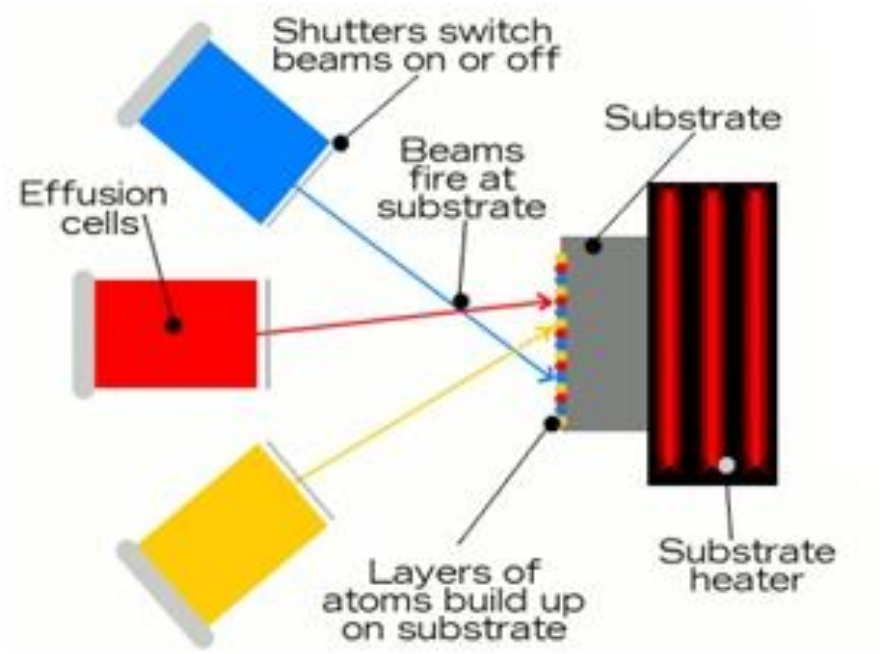

Figure 2-10: Schematic of an MBE growth set-up

The slow rate of deposition, typically around 1 micron per hour, allows the structure of the films to grow epitaxially. Precise control over the growth is maintained using monitoring techniques such as reflection high energy electron diffraction (RHEED) and computer controlled shutters on the effusion cells.

The structures used for characterisation in Chapter 3 were grown by metal organic chemical vapour epitaxy (MOCVD) by the EPSRC National Centre for III-V Technologies at the University of Sheffield. In this technique, metal-organic precursors containing the required elements are passed over the heated substrate which causes them to chemically decompose, depositing the desired substance on the surface, as shown Figure 2-11[24]. Hydrogen is often used as a carrier gas.

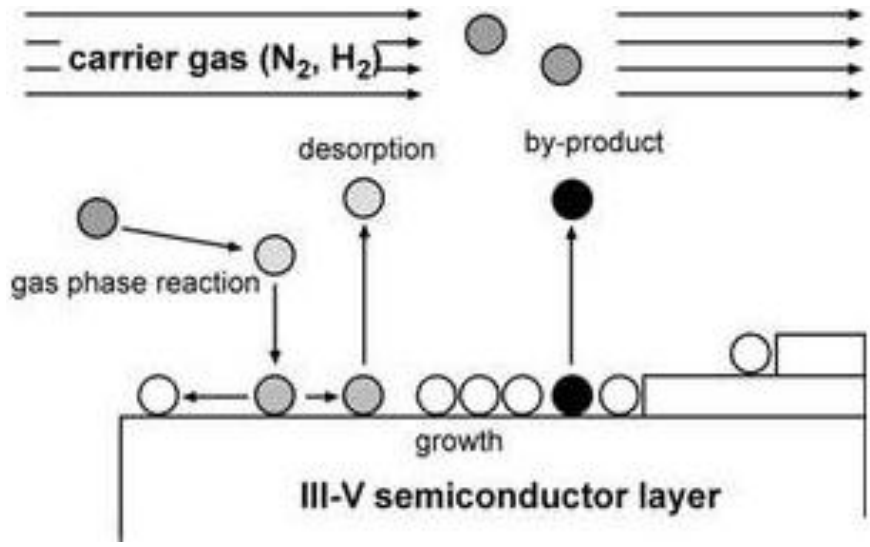

Figure 2-11: Schematic of the MOCVD process

It is possible to grow structures 'top down' or 'top up. In 'top down' growth the structure is grown in reverse order, with the epitaxial surface grown first and the DBR is the last element grown. An etch-stop may be grown between the substrate and active region to facilitate substrate removal. Disadvantages of this method are that it requires post-processing to remove the substrate before the wafer is usable and substrate removal can leave the epitaxial surface damaged if, for instance, the etchant is not perfectly selective. The structure may also 'relax' after substrate removal if under net strain. 'Top down' growth is useful where the DBR is intended to be bonded onto a heatsink as that gives the structural rigidity to facilitate substrate removal. This is particularly relevant for 'thin disk' devices which remove heat directly through the substrate. VECSEL thermal issues will be covered in Chapter 3.

In 'top up' growth the DBR is grown onto the substrate first, with the epitaxial-layer of the device the last layer grown. Post-processing is not required as the substrate serves the useful purpose of providing rigidity for the structure and, if the heatspreader approach to thermal management is used, does not significantly influence heat build up. All the structures used in this work were grown 'top up'. Some of the structures used here were heated to high temperature (800°C) for one second in a process known as rapid thermal annealing (RTA). This encourages the diffusion of mobile point defects within the structure which may annihilate with their

opposite, say an interstitial atom with a vacancy in the lattice, to reduce the deep level recombination defect density[25] and improve performance.

Annealing can also occur at room temperature during pumping of the device which will be noted in Chapters 4 and 5.

2.3 Strain and Strain Compensation

Strain is a result of the difference between the natural lattice constant of a material and that of the material on which it is grown, with the new layer forced to adopt a different biaxial lattice spacing. A consequence of growing different materials layered on top of one another is that there may be a mismatch between the lattice constant of the layers resulting in strain.

In the layered semiconductor structure of a VECSEL this is set by the lattice constant of the substrate. The elastic strain ε is a measure of the proportional distortion of the lattice in the epi-plane and can be defined as $\varepsilon = (a_s - a_0)/a_0$ where a_s is the unstrained lattice constant of the substrate and a_0 the unstrained lattice constant of the material layer.

A layer is said to be compressively strained if its unstrained lattice constant is larger than that of the material on which it is grown, and tensile strained if its unstrained lattice constant is smaller. This is illustrated in Figure 2-12[21]. Bi-axial compressive strain will cause uni-axial tensile strain in the growth direction and vice versa for a tensile strained layer, deforming the unit cell. A crystal structure can be thought of as made up of a ‘cell’ of atoms repeated over and over again like stacked boxes. The smallest possible cell is called the unit cell.

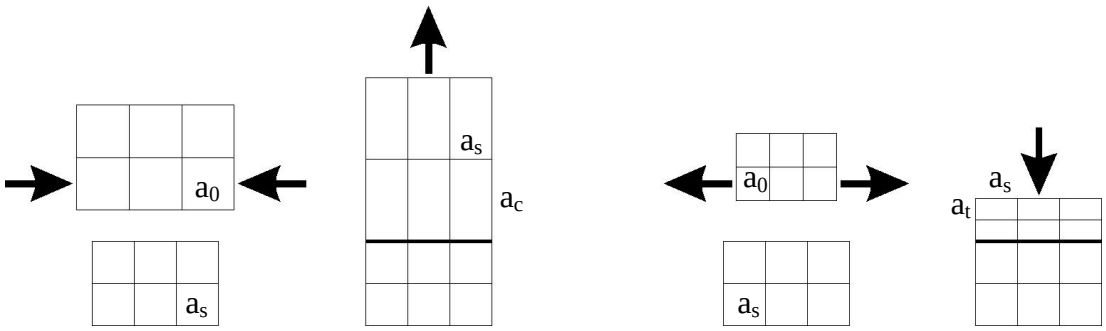

Figure 2-12: Compressive and tensile strain

Small levels of elastic strain can be accommodated without inducing damage in the strained layer, however as more of a lattice mismatch is introduced defects begin to appear to relieve some of the strain. Eventually no more elastic strain can be tolerated and additional strain is wholly relieved by misfit dislocations. Olsen et al[26] suggest that for an elastic strain $|\varepsilon| \leq 0.01\%$ no misfit dislocations occur (they use the term misfit strain ε_{mf} for what we have called elastic strain). Dislocations provide an additional non-radiative recombination channel, reducing device performance and lifetime.

It is not only the lattice mismatch of the material which needs careful consideration but the accumulation of stress in the structure as the thickness of strained layers increase. Beyond a certain level of cumulative strain, misfit dislocations form to relieve the strain. The Mathews-Blakeslee critical thickness[27] can reasonably be taken as the limit beyond which misfit dislocations must appear, although Morgensen et al[28] observe degradation in the performance of high compressively strained AlGaInP laser for levels below the Matthews-Blakeslee critical thickness (10nm QW 1% compressive strain), as shown in Figure 2-13.

We can reasonably utilise a simple "thickness-weighted method" [29] to calculate the overall strain, where the cumulative strain is the sum of the strain-thickness product for each layer: $\sum_i t_i \varepsilon_i$. Although other, possibly more accurate, methods have been proposed, for example Ekins-Daukes et al[29], for the low levels of strain in the structures used in our experiments the difference is negligible.

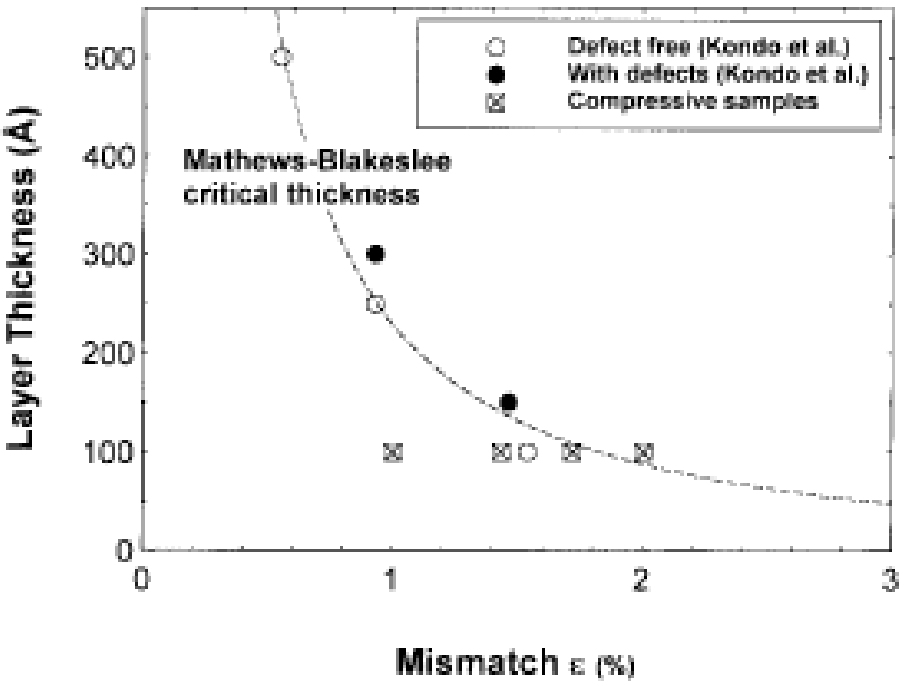

Figure 2-13 : The effect of high compressive strain on the layer quality of AlGaInP quantum well lasers

Strain can be an unavoidable consequence of the material used to achieve the desired emission wavelength but it is common to use strained quantum wells even where lattice matching is possible because of desirable changes in the well material band structure. For an unstrained quantum well of $Ga_xIn_{1-x}P$, the 1st heavy hole band edge and 1st light hole band edge are (nearly) degenerate, with subband mixing between them. This is undesirable as the 1e-1hh transition is utilised in our surface-emitting device to provide gain for light polarised in the plane of the quantum wells whereas the 1e-1lh transition emission is polarised perpendicular to plane of the quantum wells and only utilised in edge-emitting devices. Increasing the Indium proportion introduces compressive strain into the quantum well which shifts the hh subbands to higher energies and the lh subbands to lower energies[30,31] as shown in Figure 2-14. In addition it increases the curvature of the 1hh subband at k=0 which decreases the density of states and so decreases the threshold carrier density.

Compressive strain also reduces the size of the unit cell causing an increase in the bandgap. Tensile strain has the opposite effect, causing an increase in unit cell volume and a decrease in bandgap[31].

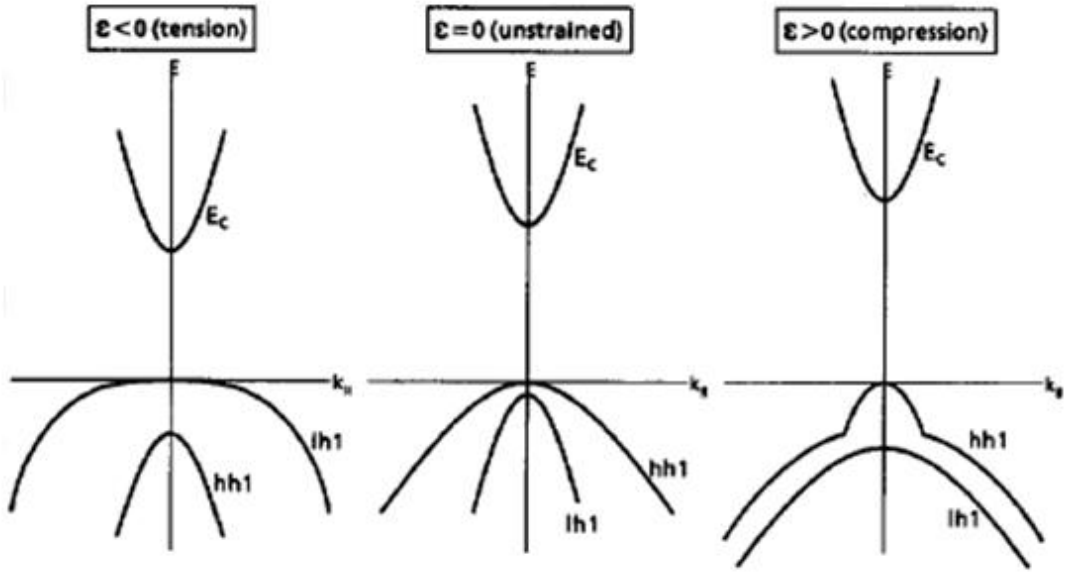

Figure 2-14: Schematic diagram of the effect of biaxial strain on band structure

For a surface emitting structure such as VECSEL it is necessary that the quantum well emission is polarised in the plane of the quantum wells. The 1e-1hh transition emission has the desired polarisation but the 1e-1lh transition emission is polarised in the growth direction. Hence introducing compressive strain, breaking 1hh-1lh valence band degeneracy and making the 1hh the ground state improves the TE gain and has been utilised in the quantum wells of the (AlGa)InP red emission quantum well VECSELs used in this work.

2.4 III-V Red Emission VECSEL

2.4.1 AlGaInP Introduction

All the red emission wavelength VECSELs in this work are based on the AlGaInP material system which can be lattice matched to GaAs [Figure 2-15[32]]. $(Al_xGa_{1-x})_yIn_{1-y}P$ is a versatile material system as the lattice constant and bandgap can be varied almost independently by changing the indium and aluminium fractions respectively. This enables us to use the same material system for the pump absorbing barriers and quantum wells, simplifying growth.

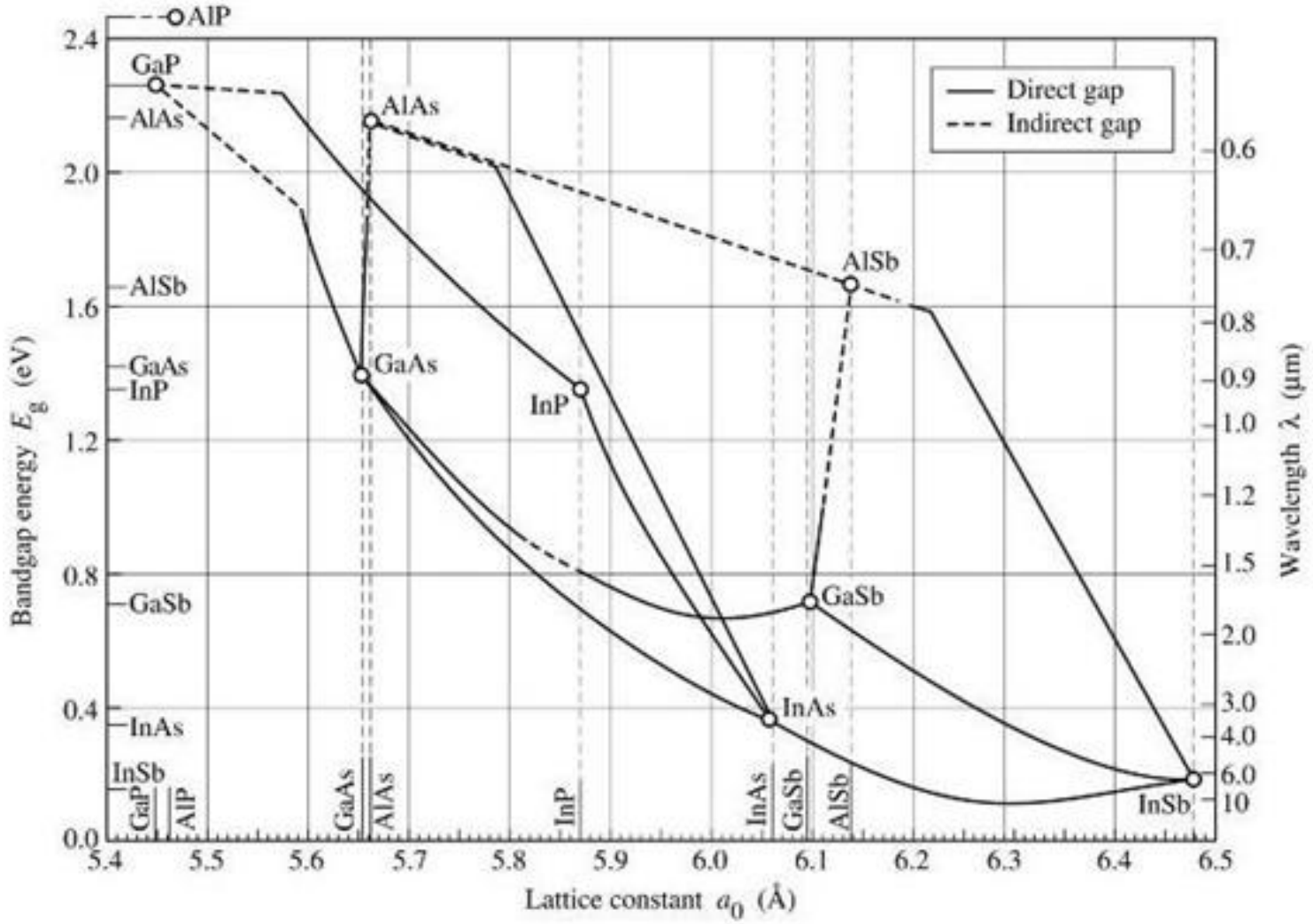

Figure 2-15: Bandgap energy v lattice constants for some common III-V alloys

2.4.2 Material Considerations

The quantum well material $Ga_xIn_{1-x}P$ is a direct bandgap semiconductor for $x<0.7$[33] and is lattice matched to GaAs at $x=0.51$[33]. By reducing the gallium proportion below the lattice-matched value we can compressively strain the quantum wells, with benefits to laser gain which were discussed in section 2.3.

The barrier material $(Al_xGa_{1-x})_{0.51}In_{0.49}P$ is lattice matched to GaAs and a direct bandgap semiconductor for $x<0.52$[33] at room temperature. An aluminium content of $x=0.6$ is used in all the pump absorbing barriers to maximise the difference between the lowest quantum well and barrier energy levels and so maximise carrier confinement. For the composition $(Al_{0.6}Ga_{0.4})_{0.51}In_{0.49}P$ the Γ and X conduction band minima have the same energy[1,31,34,35], as illustrated in Figure 2-16 for the near-identical $(Al_xGa_{1-x})In_{0.5}P$ lattice-matched to GaAs[32]. Higher aluminium content would increase the Γ bandgap but a carrier escape route would be provided by carrier scattering into the X-band, reducing radiative carrier lifetime. $(Al_{0.6}Ga_{0.4})_xIn_{1-x}P$ can also be used as a strain compensation layer by slightly increasing or decreasing the indium proportion from the lattice-matched value.

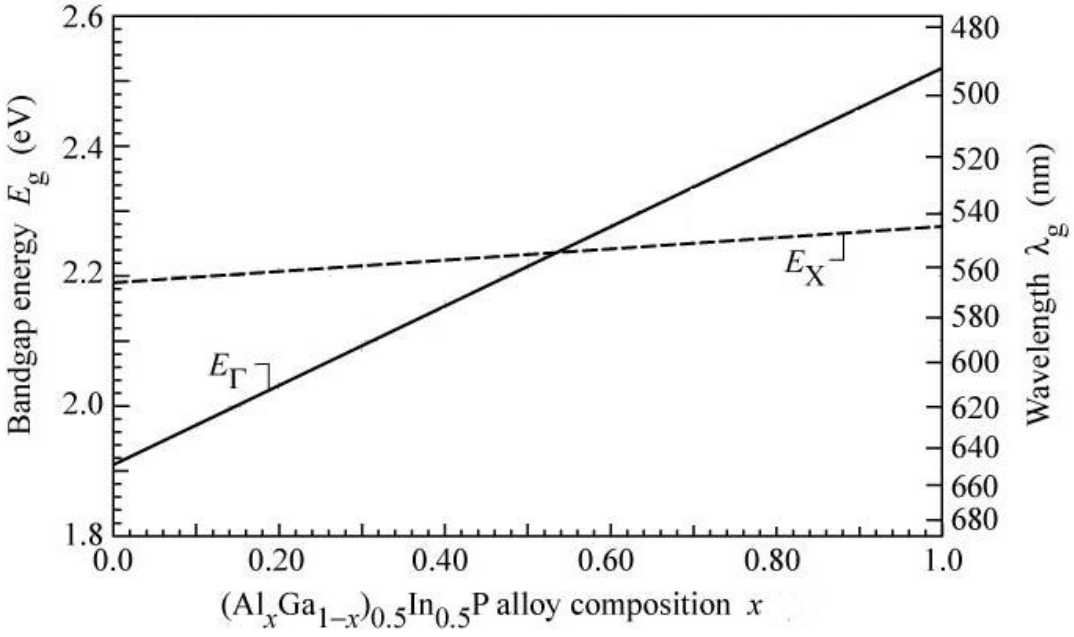

Figure 2-16: Room temperature bandgap energies of unordered $(Al_xGa_{1-x})_{0.5}In_{0.5}P$ lattice matched to GaAs

An $Al_xGa_{1-x}As$ based DBR deposited on the GaAs substrate fulfils the high reflectivity requirement of an end mirror and the active region of the VECSEL is then grown on the DBR. For the red VECSEL structures used here the high refractive index material is $Al_{0.45}Ga_{0.55}As$ (n=3.51)[18,19] and the low refractive index material is AlAs (n=3.09). A greater refractive index contrast could be achieved with a lower aluminium proportion in the high refractive index layer (GaAs has a refractive index of n=3.80) but it is impractical for our structures as it would absorb at the laser design wavelength. To achieve a reflectivity of >99.9% at 670nm using $Al_{0.45}Ga_{0.55}As$/AlAs, N=40 pairs were used (compared to around N=24 for GaAs/AlAs if there were no absorption).

One issue with the (AlGa)InP material system is that aluminium oxidises, resulting in non-radiative areas, and it also expands when oxidised, so we use a thin GaInP layer as the epi-surface of the structure to present a barrier to oxidisation.

It is desirable to use a layer of high bandgap material near the epitaxial surface as a barrier to prevent carriers diffusing onto the epi-surface and recombining uselessly. Unfortunately, no lattice-matched III-V material of a high enough bandgap to be non-absorbing is available for the pump wavelengths used in optically pumping the red emission VECSEL. It would be possible to insert an AlAs barrier between the GaInP barrier at the epi-surface and the (AlGa)InP pump-absorbing barrier material as a confinement barrier to prevent carriers diffusing onto the surface of the VECSEL, however AlAs will absorb the pump wavelength, and so generate carriers, and there is risk of damage due to oxidisation so we have not used a confinement window in our designs.

2.5 II-VI Visible Emission VECSEL

II-VI VECSELs are an exciting prospective area of research because the technology offers the possibility of VECSELs addressing the whole of the visible spectrum. Non-nitrile III-V VECSELs can only natively reach the red part of the visible spectrum without non-linear frequency conversion. InGaN VECSELs are capable of reaching the near-UV, Debusemann et al[35] having recently demonstrated pulsed

Diode Pumped Visible Vertical External Cavity Surface Emitting Lasers operation at 337nm but growth difficulties resulted in too high a threshold to allow CW operation.

II-VI material systems offer access to direct wide bandgaps. For example, as shown in Figure 1-6, ZnMgCdSe lattice matched to InP can cover the wavelength range from orange to blue and ZnMgSSe[37] lattice matched to GaAs extends into the UV.

If VECSELs could natively cover the visible spectrum it would make them more attractive for commercial use in display technologies[38,39] where it would be advantageous to be able to fabricate multiple wavelength sources on the same substrate.

VECSEL technology is an attractive way to develop a II-VI laser as doping is not required. There have been difficulties in obtaining high quality growth of p-doped II-VI material for electrical injection[40,41] making optical pumping more desirable than in III-V devices. It is worth noting that these II-VI devices were grown on III-V substrates. A problem in the development of II-VI materials has been the lack of suitable high quality II-VI substrates, which has led to the utilisation of the better developed and higher quality III-V substrates such as InP and GaAs. Growing the II-VI active region directly onto the III-V substrate can cause a significant defect density, which can be addressed by growing a buffer layer between the substrate and active region. The growth quality of lattice matched ZnCdSe[42] and ZnMgCdSe[43] on an InP substrate is substantially improved by using a III-V buffer[44] such as InP[45] or InGaAs[46].

A difficulty in the development of the II-VI VECSEL is the necessity to grow a sufficiently high quality DBR. Whilst DBRs lattice matched to GaAs[47,48] and InP[49,50], have been grown, they have not had a high enough reflectivity (>99.9%) with a wide enough stopband to be suitable. Binary compound low refractive index layers have proven problematical as MgS grown on ZnSe[51] takes on a rocksalt structure for layers more than a few nanometres thick. It is possible to grow ZnMgSSe as a superlattice of binary compounds[52] however this somewhat complicates growth. A

solution may be to eliminate the DBR altogether. An approach to this is to use the II-VI structure as a gain element within a laser cavity, either by etching a via-hole in the substrate or removing it altogether using the epitaxial lift-off technique developed at Heriot-Watt. The structure can also be used as a cavity end mirror with gain by applying a highly reflectivity coating to a heatspreader and bonding it to the structure.

2.6 Conclusion

We have discussed the elements which make up a VESCEL and the design considerations. One of the advantages of the VECSEL format is the ability to vary the emission wavelength and tuning range by small alterations in layer thicknesses which gives great flexibility in design.

We have discussed the issues specific to the AlGaInP material system used for the red VECSEL. Results for this structure will be presented in Chapters 3 to 5.

The II-VI material systems ZnMgCdSe and ZnMgSSe were introduced as prospective VECSEL candidates for extending direct VECSEL emission across the whole of the visible spectrum. Characterisation results of structures based on these will be presented in Chapter 6.

References

1 X. H. Zhang, S. J. Chua, and W. J. Fan, "Band offsets at GaInP/AlGaInP(001) heterostructures lattice matched to GaAs," Applied Physics Letters **73** (8), 1098-1100 (1998).

2 Shun Lien Chuang, *Basic Quantum Mechanics*. (John Wiley & Sons Inc, 1995).

3 R. M. Kolbas, N. G. Anderson, W. D. Laidig, Y. Sin, Y. C. Lo, K. Y. Hsieh, and Y. J. Yang, "Strained-layer InGaAs-GaAs-AlGaAs photopumped and current injection lasers," Quantum Electronics, IEEE Journal of **24** (8), 1605-1613 (1988).

4 M. Kuznetsov, F. Hakimi, R. Sprague, and A. Mooradian, "Design and characteristics of high-power (> 0.5-W CW) diode-pumped vertical-external-cavity surface-emitting semiconductor lasers with circular TEM_{00} beams," IEEE J. Sel. Top. Quantum Electron. **5** (3), 561-573 (1999).

5 J. Hader, G. Hardesty, Wang Tsuei-Lian, M. J. Yarborough, Y. Kaneda, J. V. Moloney, B. Kunert, W. Stolz, and S. W. Koch, "Predictive Microscopic Modeling of VECSELs," Quantum Electronics, IEEE Journal of **46** (5), 810-817 (2010).

6 Christina Bückers, Eckhard Kühn, Christoph Schlichenmaier, Sebastian Imhof, Angela Thränhardt, Jörg Hader, Jerome V. Moloney, Oleg Rubel, Wei Zhang, Thorsten Ackemann, and Stephan W. Koch, "Quantum modeling of semiconductor gain materials and vertical-external-cavity surface-emitting laser systems," physica status solidi (b) **247** (4), 789-808 (2010).

7 M. Y. A. Raja, S. R. J. Brueck, M. Osinski, C. F. Schaus, J. G. McInerney, T. M. Brennan, and B. E. Hammons, "Surface-emitting, multiple quantum well GaAs/AlGaAs laser with wavelength-resonant periodic gain medium," Applied Physics Letters **53** (18), 1678-1680 (1988).

8 A. Garnache, A. A. Kachanov, F. Stoeckel, and R. Houdré, "Diode-pumped broadband vertical-external-cavity surface-emitting semiconductor laser applied to high-sensitivity intracavity absorption spectroscopy," J. Opt. Soc. Am. B **17** (9), 1589-1598 (2000).

9 C. H. Chong and J. Sarma, "Lasing mode selection in vertical-cavity surface emitting-laser diodes," IEEE Photonics Technol. Lett. **5** (7), 761-764 (1993).

10 G. C. Wilson, D. M. Kuchta, J. D. Walker, and J. S. Smith, "Spatial hole burning and self-focusing in vertical-cavity surface-emitting laser diodes," Applied Physics Letters **64** (5), 542-544 (1994).

11 V. N. Morozov, J. A. Neff, and Zhou Haijun, "Analysis of vertical-cavity surface-emitting laser multimode behavior," Quantum Electronics, IEEE Journal of **33** (6), 980-988 (1997).

12 J. W. Scott, R. S. Geels, S. W. Corzine, and L. A. Coldren, "Modeling temperature effects and spatial hole burning to optimize vertical-cavity surface-emitting laser performance," Quantum Electronics, IEEE Journal of **29** (5), 1295-1308 (1993).

13 Mark A. Holm, David Burns, Pasquale Cusumano, Allister I. Ferguson, and Martin D. Dawson, "High-Power Diode-Pumped AlGaAs Surface-Emitting Laser," Appl. Opt. **38** (27), 5781-5784 (1999).

14 A. J. Kemp, G. J. Valentine, J. M. Hopkins, J. E. Hastie, S. A. Smith, S. Calvez, M. D. Dawson, and D. Burns, "Thermal management in vertical-external-cavity surface-emitting lasers: finite-element analysis of a heatspreader approach," Quantum Electronics, IEEE Journal of **41** (2), 148-155 (2005).

15 A. C. Tropper, H. D. Foreman, A. Garnache, K. G. Wilcox, and S. H. Hoogland, "Vertical-external-cavity semiconductor lasers," Journal Of Physics D-Applied Physics **37** (9), R75-R85 (2004).

16 N. Schulz, M. Rattunde, C. Ritzenthaler, B. Rosener, C. Manz, K. Kohler, and J. Wagner, "Effect of the Cavity Resonance-Gain Offset on the Output Power Characteristics of GaSb-Based VECSELs," IEEE Photonics Technol. Lett. **19** (21), 1741-1743 (2007).

17 M.Born, E.Wolf, *Principles of Optics*, (Pergamon Press, 1985)

18 S. Adachi, "GaAs, AlAs, And $Al_xGa_{1-x}As$ - Material Parameters For Use In Research And Device Applications," Journal Of Applied Physics **58** (3), R1-R29 (1985).

19 A. B. Djurisic, A. D. Rakic, P. C. K. Kwok, E. H. Li, M. L. Majewski, and J. M. Elazar, "Modeling the optical constants of $Al_xGa_{1-x}As$ alloys," Journal Of Applied Physics **86** (1), 445-451 (1999).

20 M. Schubert, J. A. Woollam, G. Leibiger, B. Rheinlander, I. Pietzonka, T. Sass, and V. Gottschalch, "Isotropic dielectric functions of highly disordered $Al_xGa_{1-x}InP$ ($0 <= x <= 1$) lattice matched to GaAs," Journal of Applied Physics **86** (4), 2025-2033 (1999).

21 Sadao Adachi, *Optical Constants of Crystalline and Amorphous Semiconductors*. (Kluwer Academic Publishers, 1999).

22 H. Tanaka, Y. Kawamura, H. Asahi, "Refractive indices of $In_{0.49}Ga_{0.51-x}Al_xP$", Journal of Applied Physics **59** (3), 985-986 (1986)

23 "http://www.explainthatstuff.com/molecular-beam-epitaxy-introduction.html".

24 "HZB - Solar Energy Research - MOCVD Preparation of III-V materials (http://www.helmholtz-berlin.de/forschung/enma/materialforschung-pv/se4/arbeitsgebiete/solarzellenstrukturen/mocvd_en.html)".

25 A. Tukiainen, J. Dekker, T. Leinonen, and M. Pessa, "Characterization of deep levels in rapid-thermal-annealed AlGaInP," Materials Science and Engineering B **91**, 389-392 (2002).

26 G. H. Olsen, C. J. Nuese, and R. T. Smith, "Effect of Elastic Strain on Energy-Band Gap and Lattice-Parameter in III-V-Compounds," Journal of Applied Physics **49** (11), 5523-5529 (1978).

27 J. W. Matthews and A. E. Blakeslee, "Defects in epitaxial multilayers: I. Misfit dislocations," Journal of Crystal Growth **27** (DEC), 118-125 (1974).

28 P. C. Mogensen, S. A. Hall, P. M. Smowton, U. Bangert, P. Blood, and P. Dawson, "The effect of high compressive strain on the operation of AlGaInP quantum-well lasers," Quantum Electronics, IEEE Journal of **34** (9), 1652-1659 (1998).

29 N. J. Ekins-Daukes, K. Kawaguchi, and J. Zhang, "Strain-balanced criteria for multiple quantum well structures and its signature in X-ray rocking curves," Crystal Growth & Design **2** (4), 287-292 (2002).

30 S. Kamiyama, T. Uenoyama, M. Mannoh, Y. Ban, and K. Ohnaka, "Analysis of GaInP/AlGaInP compressive strained multiple-quantum-well laser," Quantum Electronics, IEEE Journal of **30** (6), 1363-1369 (1994).

31 D. P. Bour, R. S. Geels, D. W. Treat, T. L. Paoli, F. Ponce, R. L. Thornton, B. S. Krusor, R. D. Bringans, and D. F. Welch, "Strained $Ga_xIn_{1-x}P/(AlGa)_{0.5}In_{0.5}P$ heterostructures and quantum-well laser diodes," Quantum Electronics, IEEE Journal of **30** (2), 593-607 (1994).

32 E.F.Schubert, *Light Emitting Diodes, Second edition* (Cambridge University Press, 2006)

33 I. Vurgaftman, J. R. Meyer, and L. R. Ram-Mohan, "Band parameters for III-V compound semiconductors and their alloys," Journal of Applied Physics **89** (11), 5815-5875 (2001).

34 D. J. Mowbray, O. P. Kowalski, M. Hopkinson, M. S. Skolnick, and J. P. R. David, "Electronic band structure of AlGaInP grown by solid-source molecular-beam epitaxy," Applied Physics Letters **65** (2), 213-215 (1994).

35 U. Dorr, W. Schwarz, A. Worner, R. Westphaling, A. Dinger, H. Kalt, D. J. Mowbray, M. Hopkinson, and W. Langbein, "Optical properties of $(Al_xGa_{1-x})_{0.52}In_{0.48}P$ at the crossover from a direct-gap to an indirect-gap semiconductor," Journal of Applied Physics **83** (4), 2241-2249 (1998).

36 R. Debusmann, N. Dhidah, V. Hoffmann, L. Weixelbaum, U. Brauch, T. Graf, M. Weyers, and M. Kneissl, "InGaN-GaN Disk Laser for Blue-Violet Emission Wavelengths," IEEE Photonics Technol. Lett. **22** (9), 652-654 (2010).

37 Hiroyuki Okuyama, Kazushi Nakano, Takao Miyajima, and Katsuhiro Akimoto, "Epitaxial Growth of ZnMgSSe on GaAs Substrate by Molecular Beam Epitaxy," Jpn. J. Appl. Phys **30**, L1620 (1991).

38 A. Cavus, L. Zeng, M. C. Tamargo, N. Bambha, F. Semendy, and A. Gray, "ZnCdSe/ZnCdMgSe quantum wells on InP substrates for visible emitters," Applied Physics Letters **68** (24), 3446-3448 (1996).

39 Maria Tamargo, Abdullah Cavus, Linfei Zeng, Ning Dai, Neil Bambha, A. Gray, Fred Semendy, Wocjiech Krystek, and Fred Pollark, "MBE Growth of lattice-matched ZnCdMgSe quaternaries and ZnCdMgSe/ZnCdSe quantum wells on InP substrates," Journal of Electronic Materials **25** (2), 259-262 (1996).

40 U. Ozgur, I. Alivov Ya, C. Liu, A. Teke, M. A. Reshchikov, S. Dogan, V. Avrutin, S. J. Cho, and H. Morkoc, "A comprehensive review of ZnO materials and devices," Journal of Applied Physics **98** (4), 041301 (2005).

41 S. B. Zhang, S. H. Wei, and A. Zunger, "Elements of doping engineering in semiconductors", *Ncpv Photovoltaics Program Review - Proceedings of the 15th Conference*, Vol. 462, pp. 62-69 (1999).

42 E. Snoeks, L. Zhao, B. Yang, A. Cavus, L. Zeng, and M. C. Tamargo, "Structural quality of pseudomorphic $Zn_{0.5}Cd_{0.5}Se$ layers grown on an InGaAs or InP buffer layer on (0 0 1) InP substrates," Journal of Crystal Growth **179** (1-2), 83-92 (1997).

43 L. Zeng, A. Cavus, B. X. Yang, M. C. Tamargo, N. Bambha, A. Gray, and F. Semendy, "Molecular beam epitaxial growth of lattice-matched $Zn_xCd_yMg_{1-x-y}Se$ quaternaries on InP substrates," Journal of Crystal Growth **175-176** (Part 1), 541-545 (1997).

44 A. Cavus, L. Zeng, B. X. Yang, N. Dai, M. C. Tamargo, N. Bambha, and F. Semendy, "Optimized growth of lattice-matched ZnCdSe epilayers on InP substrates," Journal of Crystal Growth **175-176** (Part 1), 558-563 (1997).

45 E. Snoeks, S. Herko, L. Zhao, B. Yang, A. Cavus, L. Zeng, and M. C. Tamargo, "Improvement in quality of epitaxial $Zn_{0.5}Cd_{0.5}Se$ layers grown on (001) InP substrates by using an InP buffer layer," Applied Physics Letters **70** (17), 2259-2261 (1997).

46 Koichi Naniwae, Hiroshi Iwata, Naotaka Kuroda, Kenichiro Yashiki, Masaru Kuramoto, and Tohru Suzuki, "MBE growth of ZnCdSe and MgZnCdSe alloys on InP substrates with a GaInAs buffer-layer," Journal of Crystal Growth **159** (1-4), 36-40 (1996).

47 C. Kruse, S. M. Ulrich, G. Alexe, E. Roventa, R. Kröger, B. Brendemühl, P. Michler, J. Gutowski, and D. Hommel, "Green monolithic II-VI vertical-cavity surface-emitting laser operating at room temperature," physica status solidi (b) **241** (3), 731-738 (2004).

48 K. Sebald, C. Kruse, and J. Wiersig, "Properties and prospects of blue-green emitting II-VI-based monolithic microcavities," physica status solidi (b) **246** (2), 255-271 (2009).

49 S. P. Guo, O. Maksimov, M. C. Tamargo, F. C. Peiris, and J. K. Furdyna, "Distributed Bragg reflectors for visible range applications based on (Zn,Cd,Mg)Se lattice matched to InP," Applied Physics Letters **77** (25), 4107-4109 (2000).

50 Maria C. Tamargo, Shiping Guo, Oleg Maksimov, Ying-Chih Chen, Frank C. Peiris, and Jacek K. Furdyna, "Red-green-blue light emitting diodes and distributed Bragg reflectors based on ZnCdMgSe lattice-matched to InP," Journal Of Crystal Growth **227**, 710-716 (2001).

51 N. Teraguchi, H. Mouri, Y. Tomomura, A. Suzuki, H. Taniguchi, J. Rorison, and G. Duggan, "Growth of ZnSe/MgS strained-layer superlattices by molecular beam epitaxy," Applied Physics Letters **67** (20), 2945-2947 (1995).

52 C. Kruse, G. Alexe, M. Klude, H. Heinke, and D. Hommel, "High Reflectivity p-Type Doped Distributed Bragg Reflectors Using ZnSe/MgS Superlattices," physica status solidi (b) **229** (1), 111-115 (2002).

Chapter 3

Effects of Temperature on VECSELs

Temperature plays a significant role in the development and use of VECSELs., from design decisions accounting for temperature-dependant effects through the choice of growth temperature and the choice of thermal management technique and practical effects of changing pump wavelength. In this chapter we look at some of the areas in which heat impacts on VECSELs.

3.1 Mapping Different Growth Temperature VECSELs

Previous red emission VECSEL structures were GaInP/AlGaInP on GaAs structures grown at Sheffield at 690°C, as it is the temperature which had been used to produce doped growths in this material system, however there was a lack of evidence to indicate that it produced the best results or the effect on growth of using other temperatures. These were used to produce our highest performing VECSEL structure[5] (1.1W at 674nm). To investigate this, identical structures were grown by MOCVD at Sheffield at different temperatures: T_g=690°C (MR2331), T_g=710°C (MR2329+MR2335) and T_g=730°C (MR2330) on 2" GaAs[100] wafers. By characterising the wafers we hoped to gain some idea about the effect of growth temperature on device performance and whether the usual growth temperature is the best.

3.1.1 Structure Used for Growth Test

The structure used consisted of ten 7nm thick compressively strained $Ga_{0.46}In_{0.54}P$ quantum wells, arranged with one at each of the first ten antinodes of the laser standing wave in the VECSEL sub-cavity to take advantage of resonant periodic gain (RPG)[6], with $(Al_{0.6}Ga_{0.4})_{0.51}In_{0.49}P$ pump-absorbing barriers. A $Ga_{0.52}In_{0.48}P$ capping layer prevented oxidisation of the aluminium containing layers. The DBR consisted

of 40.5 pairs of $Al_{0.45}Ga_{0.55}As$/AlAs designed for a reflectivity stopband centred at 670nm.

The wafers were not rotated during growth and some variability of layer thickness (and thus behaviour) due to growth variation was expected. This variability allows potentially high performance areas of the wafer to be "cherry-picked" for further investigation but also reduces the consistency of performance. Hence, in order to understand the effect of growth temperature on device characteristics the whole wafer was mapped using normal PL and reflectivity techniques.

3.1.2 Wafer mapping

The wafer was placed epi-side up on a brass platform maintained at ~25°C by a peltier element underneath it. The platform was translated along the x- and y-axis to position the wafer. The platform was marked with lines along the x- and y-axis to facilitate alignment. The major flat was lined up with the line parallel to the y-axis and the minor flat lined up with the line parallel to the x-axis. The position of the top corner of the major flat was used as a reference point and designated as (0,0) so all the wafer maps would share a common co-ordinate system.

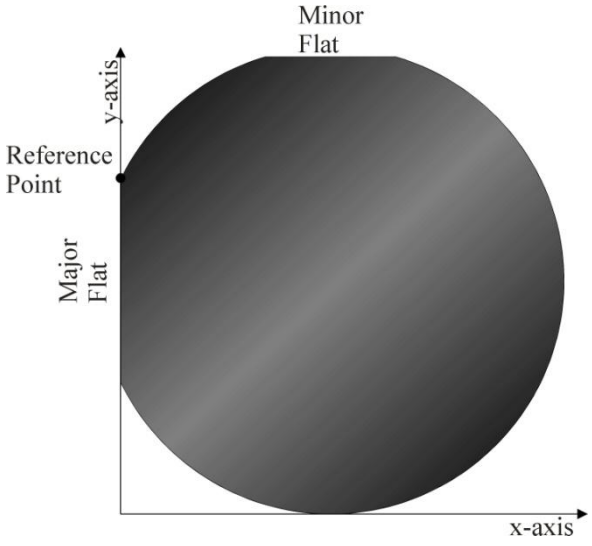

Figure 3-1: Epi-side up wafer reference diagram

3.1.2.1 Normal PL Measurement

For the whole wafer maps, a laser beam of ~100mW at 532nm was focussed onto the wafer using an f=50mm bi-convex lens placed above the sample. The fluorescence was collected by another lens (f=25mm) placed above the wafer and steered to another lens to collimate before focussing into the fibre-tip of a spectrum analyser. Measurements were taken at 5mm intervals across the surface of the wafer for a spectral range of 570-700nm with 0.25nm resolution. The brass platform was maintained at 23-25°C.

Individual cleaved samples were secured with silver heat conducting paint to a peltier element which was used to vary the sample temperature. The sample was irradiated with 500mW at 532nm focussed onto the sample by an f=250mm lens The sample mount was moved into the beam so that the edge of the sample, which had been attached so that one edge of the sample coincided with a vertical edge of the TEC, only just intercepted the pump beam. The PL was collected and collimated with a series of lenses and directed by mirrors through an f=250mm plano-convex lens into the spectrometer. A chopper rotating at 240Hz was placed before the final focussing lens and synched up to the lock-in amplifier to reduce background noise.

3.1.2.2 Reflectivity Measurement

For the whole wafer maps the reflectivity measurements were taken using a similar set-up to the normal PL. The output of a tungsten lamp was focussed onto the wafer using an f=25mm bi-convex lens placed above the sample. The reflected light was collected by the same lens and steered to another lens to collimate before focussing into the fibre-tip of a spectrum analyser. Measurements were taken at 5mm intervals across the surface of the wafer for a spectral range of 570-750nm with 0.25nm resolution. The spectral range was extended beyond that of the normal PL measurements to fully capture the long wavelength side of the DBR reflectivity. The brass platform was maintained at 23-25°C.

3.1.2.3 Edge PL

The pump arrangement for measuring edge PL of individual samples was the same as for the normal PL measurement. The PL was collected and collimated with a 10x microscope objective and directed by mirrors through an f=250mm plano-convex lens into the spectrometer. The microscope objective was aligned ~10-15° from the plane of the sample to make sure the light collected was direct quantum well emission and not PL which had been waveguided by the quantum well layer. A chopper rotating at 240Hz was placed before the final focussing lens and synched up to the lock-in amplifier to reduce background noise.

3.1.2.4 Individual Sample Characterisation

Two 4mm square samples were cleaved from each of the wafers grown at 690°C and 710°C for further characterisation based on the wafer maps aiming for an offset between the PL and subcavity resonance. In laser operation the active part of the sample will increase in temperature and the quantum well emission will increase in wavelength faster than the sub-cavity resonance. If the sample is chosen well, the quantum well peak gain wavelength should coincide with the sub-cavity resonance during laser operation ensuring greater efficiency. Measurements were taken for a range of temperatures to measure the wavelength shift with temperature of the samples.

3.1.2.5 Results

The Normal PL measurements clearly show the effect of the non-uniform material growth as shown on the contour map of the 690°C wafer [Figure 3-2]. On the bubble plot maps, the position of the bubble corresponds to the position of the measurement on the wafer, the size of the bubble the magnitude of the fluorescence, with the intensity and peak wavelength displayed next to it. Note that MR2330 grown at 730°C was supplied as a part-wafer, a part of the wafer already having been cleaved off and retained by Sheffield.

An Excel VBA program was written to graph the normal PL and reflectivity for each of the measured points on the sample. An example plot for is shown in Figure 3-3 The wafer maps indicated little difference in normal Pl between the wafers grown at different temperatures, although they do illustrate the benefit and drawback of non-uniform growth: there is a small range of wavelengths for which good samples can be obtained but there are also areas of the wafer which appear undesirable.

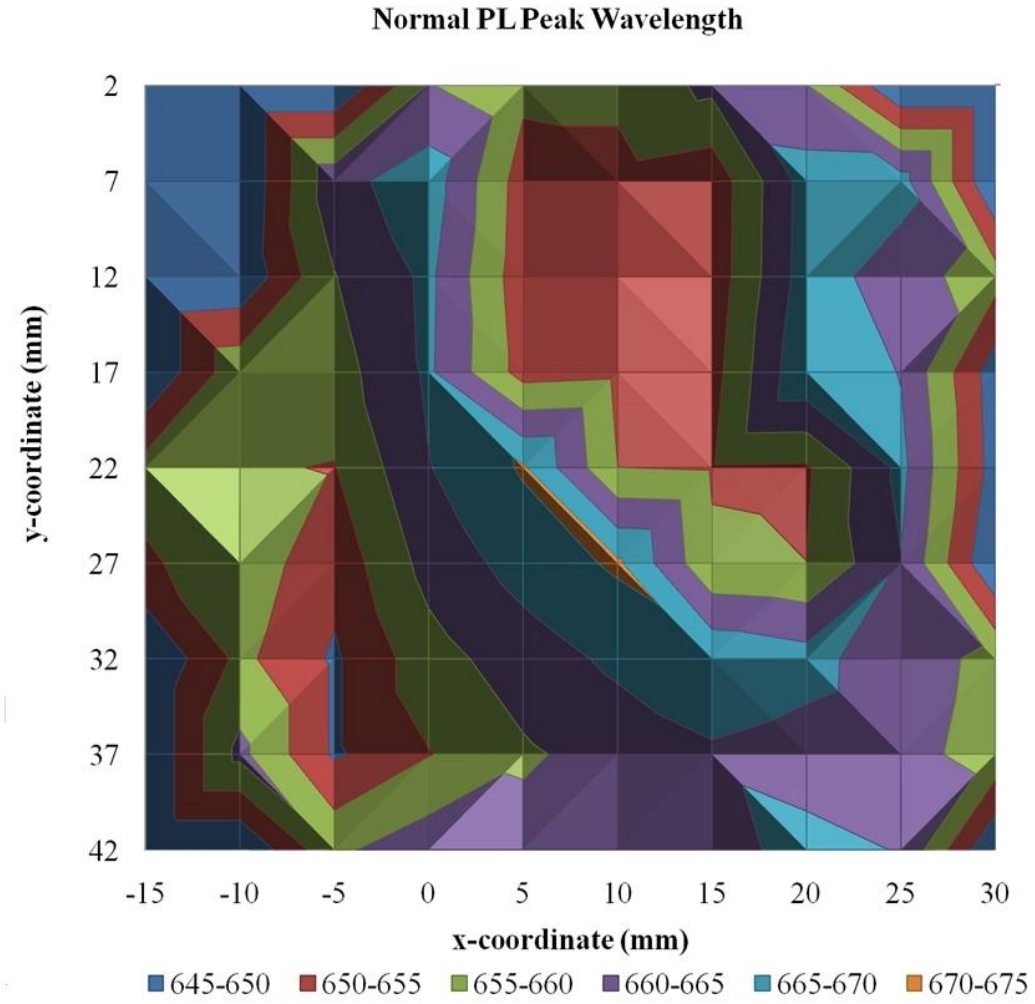

Figure 3-2: Contour map normal PL peak wavelength for the T_g=690°C 10QW structure.

Samples MR2329E and MR2331D were cleaved because the normal PL response appeared to be of the same or slightly shorter wavelength than the absorption dip in the reflectivity spectrum. MR2329G and MR2331E were chosen because the normal

PL response appeared somewhat shorter than the sub-cavity resonance in the DBR stopband.

It was not possible to collect edge PL readings below 12°C due to condensation build-up on the sample. High temperature edge PL readings were averaged over a number of scans to reduce the noise in the data as the PL was very faint.

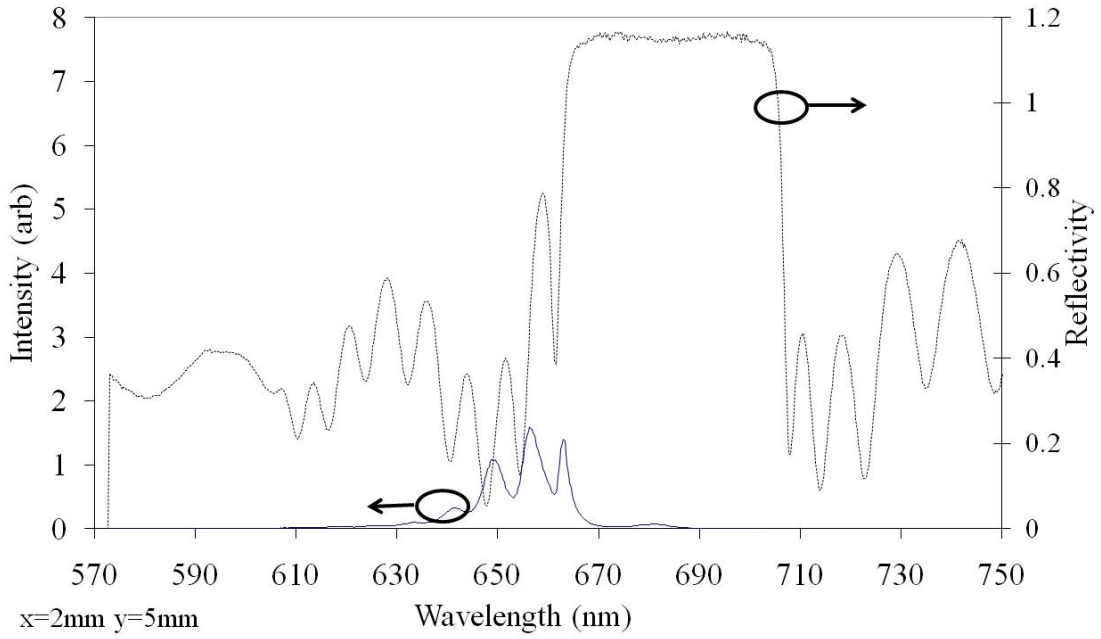

Figure 3-3: Example characterisation graph

The wavelength shift with temperature of MR2329E was 0.14nm/K for edge PL and 0.10nm/K for normal PL. The wavelength shift with temperature of MR2331D was 0.19nm/K for edge PL and 0.09nm/K for normal PL.

The effect of sub-cavity resonances other than the designed one was clear in the normal PL spectra for all samples, but particularly in MR2329G and MR2331E because the quantum well emission was closer to the wavelength of the shorter wavelength sub-cavity resonances. The effect of the quantum well emission moving into and then through the desired resonance can be seen as the temperature increases. Although the increased temperature reduces the intensity of the quantum well

emission the normal PL intensity actually increases due to the effect of the resonance as the quantum well emission moves into alignment. Figure 3-4 illustrates this effect in MR2331E.

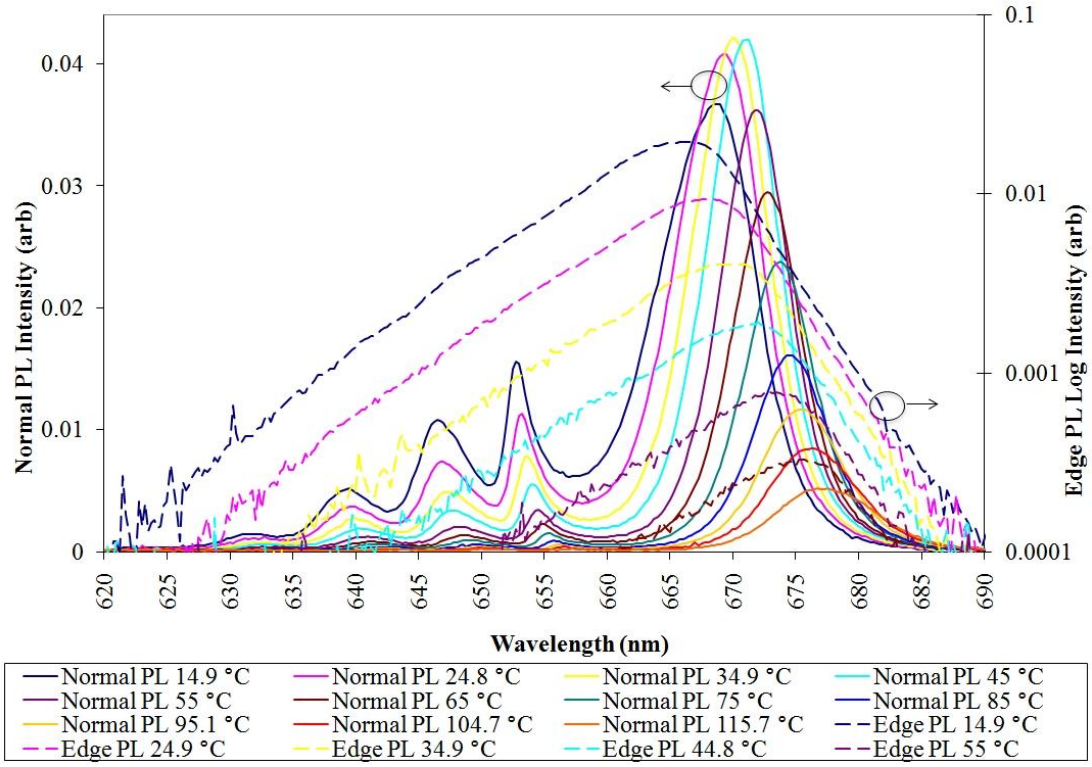

Figure 3-4: Normal and Edge PL from MR2331E.

The wavelength shift with temperature of MR2329G was 0.17nm/K for edge PL and 0.07nm/K for normal PL. The wavelength shift with temperature of MR2331E was 0.19nm/K for edge PL and 0.09nm/K for normal PL.

The expected values for the temperature dependant emission wavelength shift for this material system are roughly 0.3nm/K for edge PL and 0.1nm/K for normal PL. The observed values for edge PL were ~0.14-0.19nm/K and normal PL ~0.07-0.10nm/K for the four samples. The normal PL shift was in line with expectations but the edge PL shift slower than expected

3.2 Thermal Management in a VECSEL

As noted in section 2.1.6, temperature has a strong effect on VECSEL performance, with heating affecting not only the output power through increased Auger recombination[3,4] and thermionic emission of carriers[5] but also peak gain wavelength. Therefore, managing the active region temperature to minimise its effect is critical for the viability of the technology and its practical deployment.

In single pump pass structures, pumped through the top surface, there are two main areas where heat will be generated: the active region and the DBR. Pump photons are primarily absorbed in the active region, generating carriers which lose energy to the crystal lattice by emitting phonons, as they descend to the bottom of the valance band of the barrier or quantum well or when they recombine non-radiatively. Pump photons not absorbed in the active region will be absorbed in the DBR. Without thermal management, heat will spread axially and radially, with the centre of the pumped area having the greatest difficulty in exporting heat, causing thermal lensing due to the increase of refractive index with increasing temperature. This is exacerbated if the pump beam has a Gaussian profile (rather than a 'top hat' profile). Thermal lensing strongly limits the ability to reach high output powers through power scaling[6]: increasing the pumped area in step with the pump power to maintain a constant pump intensity. Thermal management techniques generally extract heat through the non-emitting surface of the device (‘bottom’) or emitting surface (‘top’), as shown in Figure 3-5. These approaches aim to make the heatflow effectively one dimensional, reducing the lateral spread of heat which would reduce the scope for power scaling.

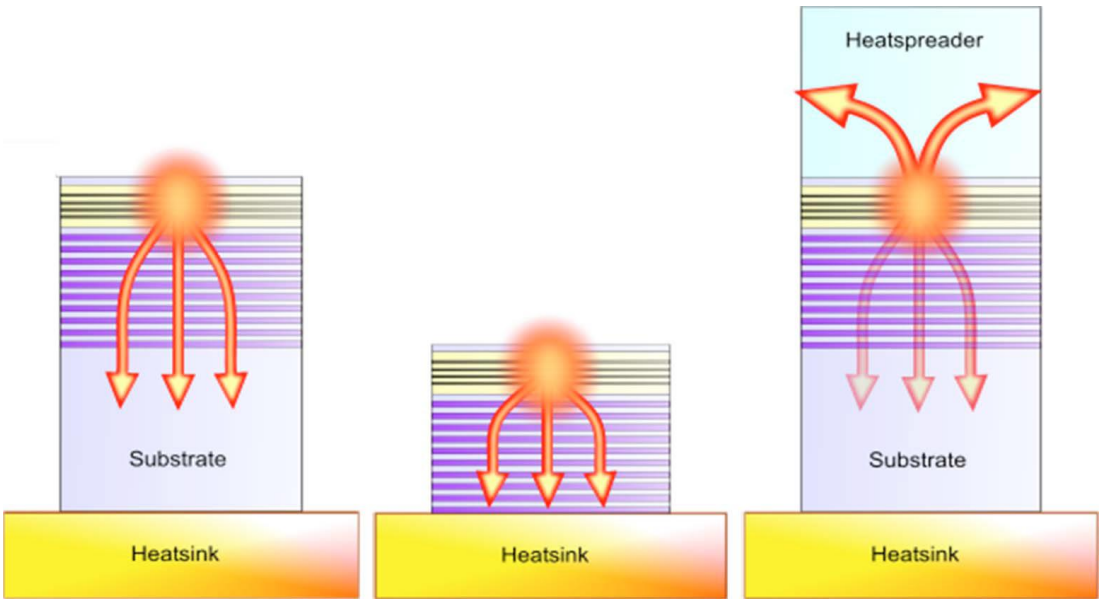

Figure 3-5: Heatflow schematic for a)bare heatsink b)'thin device' approach and c) heatspreader approach.

Thin Disk

In order to remove heat through the bottom of the structure to a cooled mount, the thermal resistance of all layers below the active region must be overcome. An obvious first step is to remove the substrate[7] (the 'thin disk' approach) by mechanical polishing and/or chemical etching and bond the structure to a heatsink. In this case, many devices are grown in reverse order with the DBR being the final layer. The thermal resistance of the DBR is only partly due to the bulk material thermal conductivity: additional axial thermal resistance is caused by the number of interfaces within it. The thin disk approach works best when the DBR has a small number of layer pairs of (relatively) good thermal. The material system and pump spot size largely dictate the effectiveness of this approach, partly due to a) the thermal conductivity of the active region and b) the thermal resistance of the DBR. The efficacy of this approach for large spot sizes at wavelengths around 1µm is shown by Maclean et al[6] modelled using finite element analysis for a range of wavelengths, and thus material systems, and pump spot sizes. Output powers of tens of watts, such as 30W at 980nm by Chilla et al[8] and 40.7W at 1040nm by Wang et al[9], have been demonstrated for InGaAs VECSELs.

Heatspreader

Another approach, and the one we have used, is to remove heat through the top of the structure by bonding a heatspreader to the epitaxial surface, demonstrated initially by Alford et al[10] using sapphire. Heat flows from the active region into the heatspreader where it is dissipated into a wider and cooler area before flowing through the structure into the heatsink. Because the DBR is effectively bypassed, its thermal resistance is much less significant meaning this approach is applicable for a much larger wavelength range than 'thin disk'. This approach is effective for the AlGaInP VECSELs operating in the red because, as noted in section 2.4.2, 40 pairs of $Al_{0.45}Ga_{0.55}As$/AlAs are required which has a higher bulk thermal conductivity than a GaAs/AlAs DBR (κ=~11 $Wm^{-1}K^{-1}$ for $Al_{0.45}Ga_{0.55}As$, ~90 $Wm^{-1}K^{-1}$ for AlAs, ~45 $Wm^{-1}K^{-1}$ for GaAs) and requires almost twice as many layers which further decreases the axial thermal conductivity.

Sapphire was used as the heatspreader crystal in early demonstrations κ=~44 $Wm^{-1}K^{-1}$ and later silicon carbide[11,12] and diamond[12-15] were introduced which have order of magnitude better thermal conductivities (κ=~490 $Wm^{-1}K^{-1}$ and κ=~1600 $Wm^{-1}K^{-1}$ respectively).

Liquid Capillary Bonding

To be effective the interface between the heatspreader and device must not provide a thermal barrier. The solution we have used, which requires only simple post processing and material, is liquid capillary bonding. This technique, analysed by Liau[16], utilises the surface tension of a liquid sandwiched between the heatspreader and semiconductor wafer to pull the two layers into sufficiently close contact as it evaporates that they are then held together by Van der Waals' force. The bond strength is reliant on the closeness of the two surfaces so it is very important that the surfaces be clean, smooth and flat. No mechanical pressure is required and common liquids such as methanol or distilled water may be used which makes this a very simple and useful method.

3.3 Characterisation of Thermal Effects

Here we characterise structures to determine how closely important qualities such as reflectivity, resonances and peak gain wavelength match the design and how these vary with device temperature.

3.3.1 Characterisation

It is important to know how the wafer properties match up to the design; actual wafer characteristics can be quite different from the "ideal" designed ones. The characteristics of the wafer can vary considerably across the wafer due to layer thickness variation, the extent depending on the growth technique and whether or not the wafer was rotated during growth. Of the samples used in this work, those grown by MOCVD were not rotated during growth, which can be clearly seen in the wafer maps, but the MBE samples were rotated during growth.

Although a lack of uniformity can reduce the amount of wafer with desirable characteristics, it also makes it possible to "cherry pick" parts of the wafer based on experimental observations from characterisation. We have measured the characteristics of the wafers using a combination of reflectivity, normal and edge photoluminescence techniques.

3.3.2 Reflectivity

As the DBR forms an end mirror of the laser cavity its quality and high reflectivity wavelength range strongly affect device performance. Fortunately characterisation of the reflectivity of grown VECSEL structures can be carried out relatively simply using an experimental set-up illustrated in Figure 3-6.

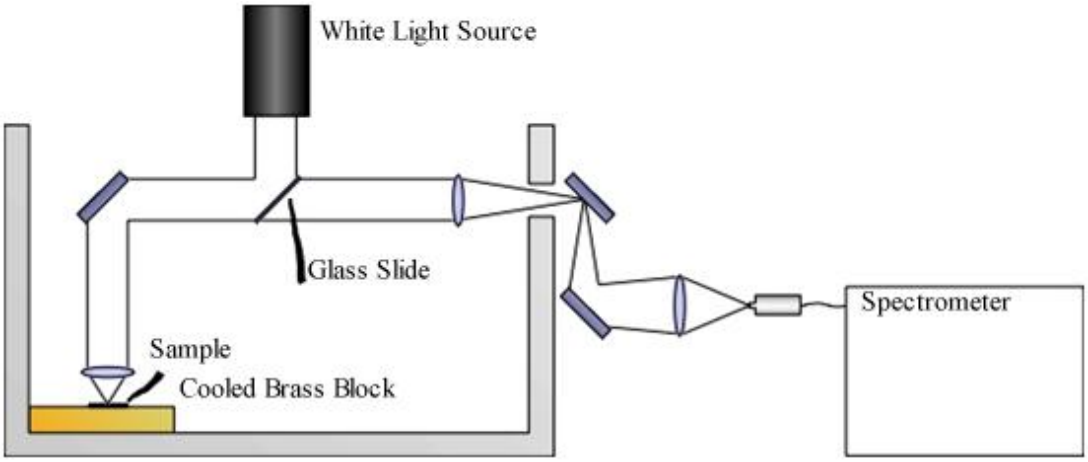

Figure 3-6: Schematic of our DBR reflectivty measurement experimental set-up

The emission from the light source will not be uniform across the wavelength range and the intensity across the range must be measured in order to provide a context for the DBR reflectivity measurement. In this experimental set-up the emission profile of the broad spectrum light source, for instance a tungsten lamp, is measured by focussing the light onto a silver mirror, which has a broad reflectivity at visible wavelengths. The reflected spectrum is measured and used as a reference. An example of this is shown in Figure 3-7(a) and illustrates why a spectrum of the light source is needed.

The mirror is then replaced with the VECSEL and the measurement repeated, an example of which is given in Figure 3-7(b).

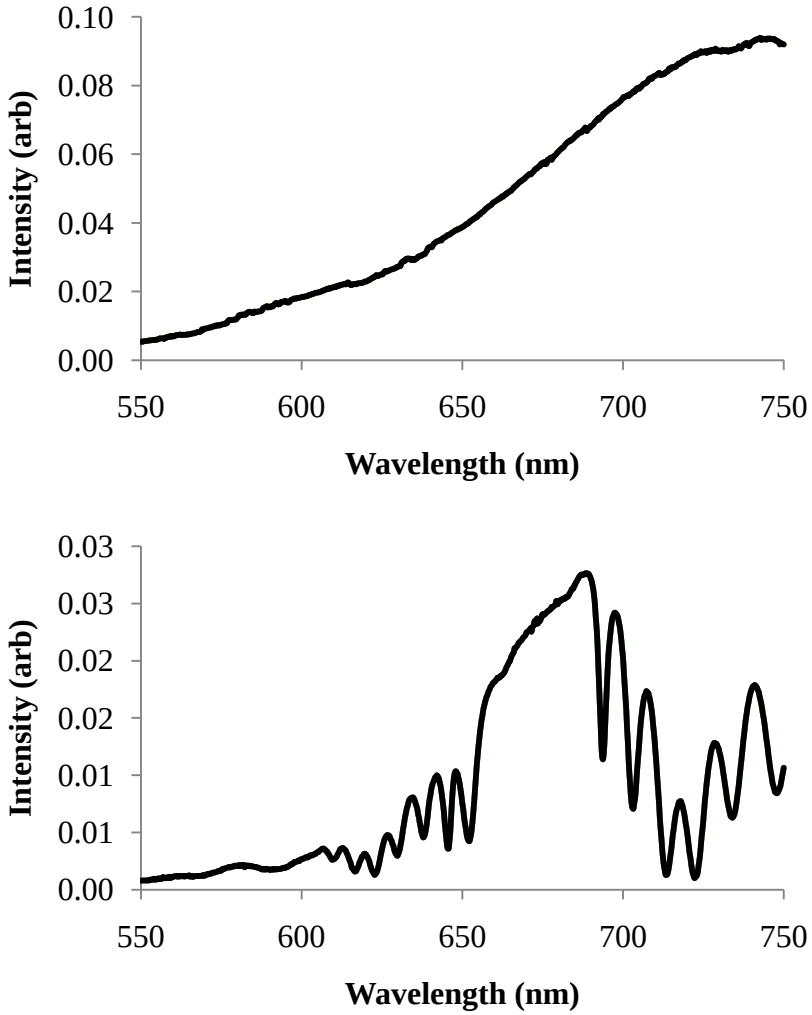

Figure 3-7: Example of spectra of a) a tungsten lamp and b) a VESCEL structure.

Dividing the intensity of the VECSEL reflectivity by the silver mirror reflectivity at each wavelength measured gives a good picture of the DBR reflectivity. If the focussed light spot on the VECSEL is not roughly the same size the magnitude of the relative reflectivity may be distorted, as illustrated by Figure 3-8 which shows the reflectivity of the same structure used above.

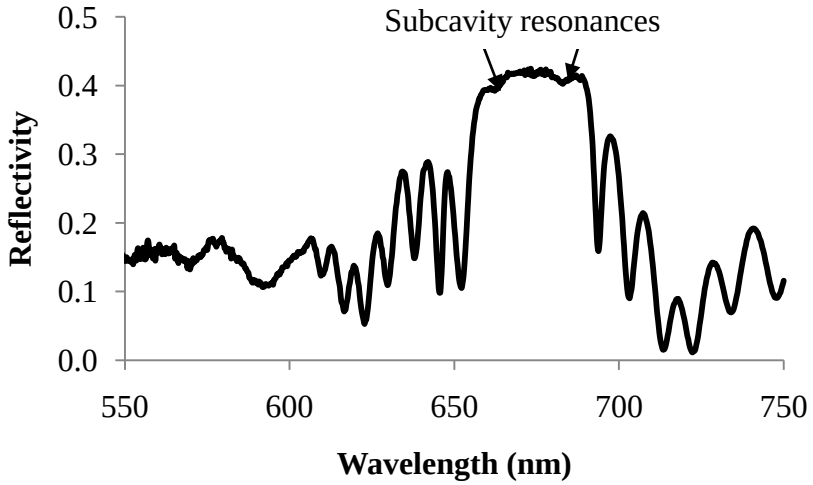

Figure 3-8: Example VECSEL reflectivity

Additionally, in some reflectivity spectra, a dip in reflectivity in the stopband may be observed due to increased absorption of light caused by a subcavity resonance. This can be used in conjunction with photoluminescence measurements to determine the offset between the quantum well emission and cavity resonance and provide an indication of likely lasing wavelength (see section 2.1.6).

3.3.3 Photoluminescence

3.3.3.1 Edge PL

Edge photoluminescence is a useful technique for determining the emission wavelength of the quantum wells by measuring the light emitted directly from the wells without the interference of intervening dielectric layers. Pumping the VECSEL structure at its edge ensures some direct quantum well emission can be captured, using a set-up such as Figure 3-9.

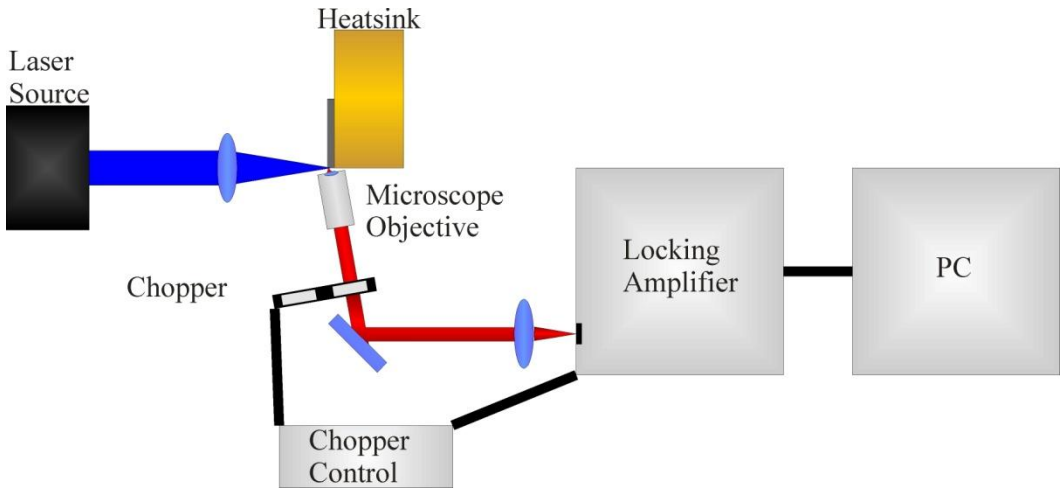

Figure 3-9: Schematic of an Edge PL experiment set-up

The sample is optically pumped at a wavelength short enough to be absorbed in the barrier. Although a longer wavelength for in-well pumping could be used, the quantum wells are very thin and much less pump light would be absorbed resulting in less emission. The pump intensity should be sufficient to produce detectable emission but not so much as to substantially change the quantum well temperature.

The PL gathering optics must be placed at an angle to the plane of the quantum wells to avoid collecting light waveguided by the quantum well material which has a higher refractive index than the surrounding barrier layers.

This technique can be used to determine the shift in quantum well emission wavelength with temperature by varying the sample mount temperature, taking a spectrum at each temperature point, and plotting the change of emission peak wavelength against temperature. Typically for an AlGaInP VECSEL a combination of mechanical expansion and reduction of the bandgap with increasing temperature causes the quantum well emission to shift to longer wavelength[17] at ~0.3nm/K, and mechanical expansion causes the cavity resonance to shift to longer wavelengths at ~0.1nm/K. Clearly reducing the build up of heat will decrease the sensitivity of the emission wavelength, and thermal management techniques will be discussed in section 3.2. A typical set of Edge PL measurements is shown in Figure 3-10.

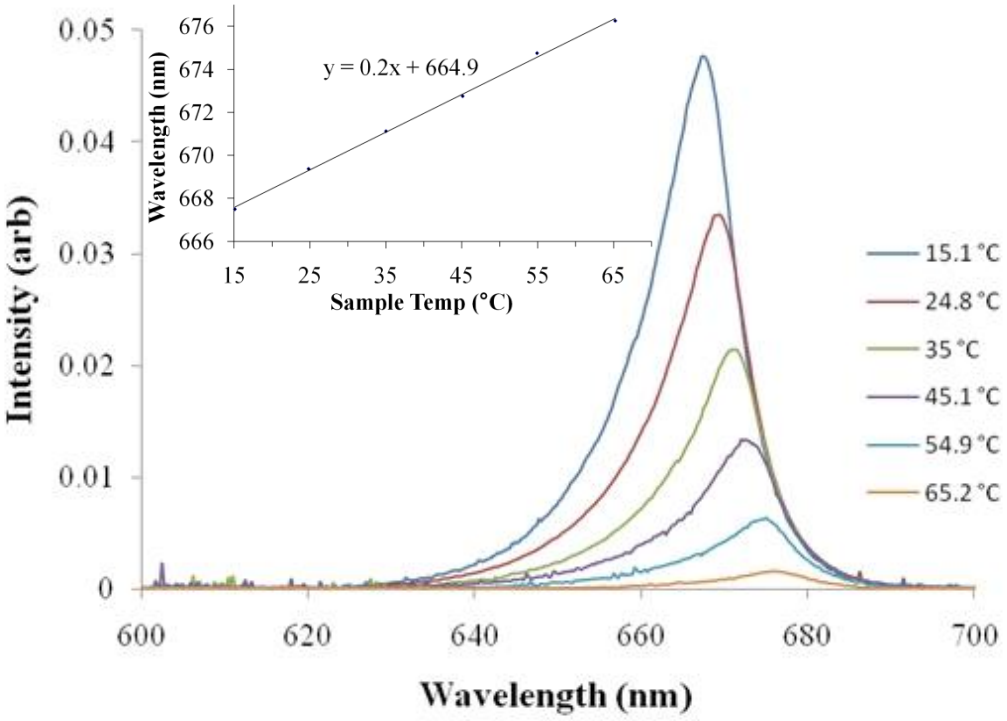

Figure 3-10: Typical edge PL measurements for a 20QW GaInP/AlGaInP VECSEL for a range of mount temperatures. Inset: Wavelength shift of edge PL peak with sample temperature.

In addition to showing the quantum well emission wavelength, the polarisation of the edge emission gives information about the relative gain of TE and TM polarised light and the energy separation of the light and heavy hole levels.

In order for a surface emitting structure, such as a VECSEL, to function there needs to be sufficient gain for photons polarised in the plane of the quantum well. So, the quantum well edge emission should ideally be TE polarised (see Figure 3-11). The ground state is deduced from the polarisation of the longest wavelength emission, and the difference in wavelength between the TE and TM polarisations gives the energy separation of the 1hh and 1lh energy levels. The ratio of the intensity of the two polarisations shows the relative transition probabilities.

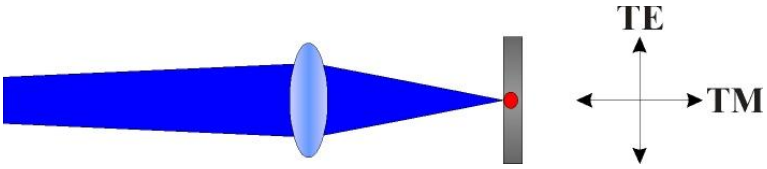

Figure 3-11: Side-on view of edge emission polarisation from a VECSEL

Measuring the intensity and wavelength of the two polarisations can provide valuable information in understanding device performance. For instance, we compare the relative intensity of TE and TM edge PL of II-VI samples in section 6.2.2.1 to determine if the grown quantum wells are unstrained as had been specified in the design.

3.3.3.2 Normal PL

We have seen with Edge PL that we can learn the emission wavelength of the quantum wells without the interference of the surrounding layers. However in laser operation light will pass through the layered structure and the spectrum will be altered by the subcavity resonances, strongly influencing the laser behaviour. We can gain data about this effect and the subcavity resonances through normal PL measurements.

As Figure 3-12 shows normal PL measurements can be taken using a very similar experimental set-up to edge PL, the biggest difference being that photoluminescence collected is emitted (and collected) normal to the surface.

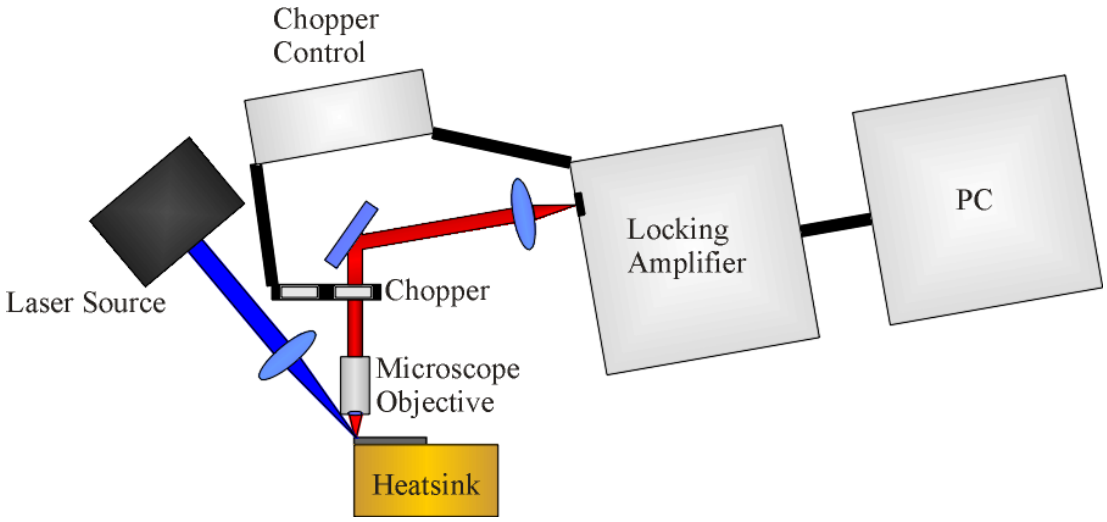

Figure 3-12: Schematic of an Normal PL experiment set-up

As with the edge PL measurements, the structure is optically pumped at a wavelength short enough to be absorbed in the barriers rather than the wells. However, unlike edge PL, there is no restriction on where on the sample measurements can be taken. It is therefore possible to map a wafer without cleaving.

A typical set of normal PL measurements, for the same sample used for the previous edge PL measurements, is shown in Figure 3-13. This shows the effect of resonances on surface normal emission, the main emission peak is narrower and shifts to longer wavelengths at ~0.1nm/K, in line with the expected cavity resonance shift. Several smaller emission peaks are visible at shorter wavelengths due to off-stopband reflectivity peaks. Unlike in the edge PL measurements, there is a substantial drop in relative emission intensity only when the sample mount temperature is increased beyond 24.9°C, indicating that the cavity resonance at 15.1°C was at a slightly longer wavelength than the quantum well emission peak.

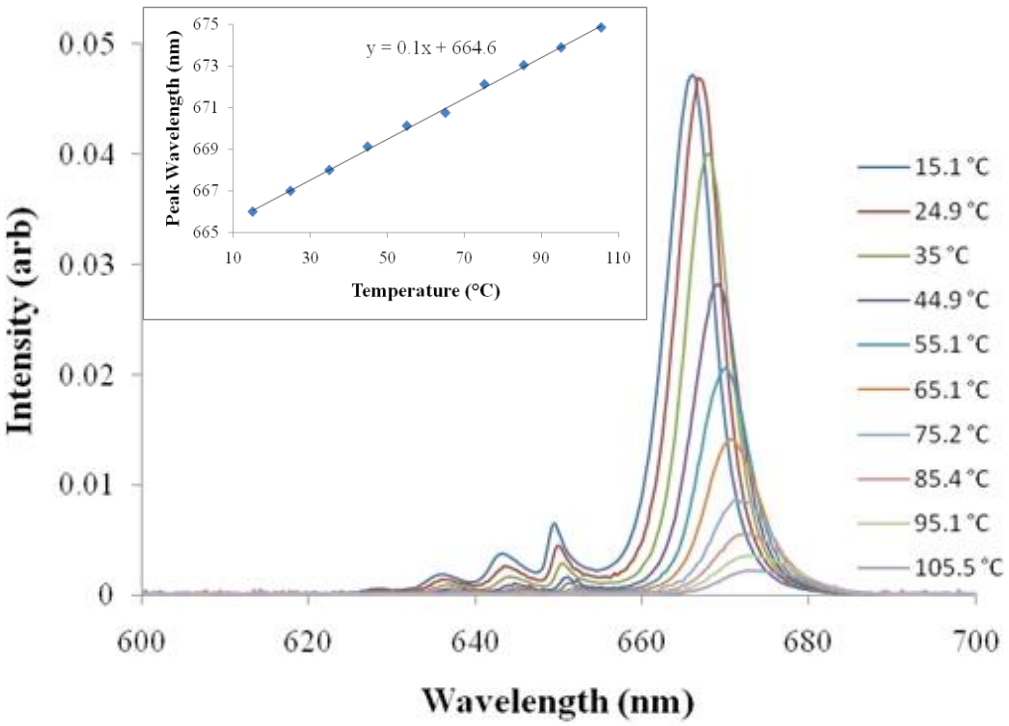

Figure 3-13: Typical normal PL measurements for a 20QW GaInP/AlGaInP VECSEL for a range of mount temperatures. Inset: Wavelength shift of normal PL peak with sample temperature.

3.4 The Thermal Effects of Pump Wavelength

In the earlier section on characterisation we saw the effect of temperature on photoluminescence wavelength and overlap with the subcavity resonances. Heat build up in the active region is not only determined by the pump intensity and mount temperature but also by the pump wavelength. Here we examine data from pumping a VECSEL at different wavelengths while keeping the rest of the experimental set-up unchanged and then use a finite element analysis (FEA) model to try to understand the results.

3.4.1 Experiment

The structure used consisted of twenty 7nm thick compressively strained $Ga_{0.46}In_{0.54}P$ quantum wells, arranged in pairs at the antinodes of the laser standing wave in the VECSEL sub-cavity to take advantage of resonant periodic gain $(RPG)^2$, with $(Al_{0.6}Ga_{0.4})_{0.51}In_{0.49}P$ pump-absorbing barriers, as shown in Table 3-1. A

$Ga_{0.52}In_{0.48}P$ capping layer prevented oxidisation of the aluminium containing layers. The DBR consisted of 40.5 pairs of $Al_{0.45}Ga_{0.55}As$/AlAs designed for a reflectivity stopband centred at 670nm. The active region was 1.161µm in length which ensured no more than 5% of 532nm pump light would reach the DBR.

$Ga_{0.52}In_{0.48}P$	**10 nm**	**Cap**	
$(Al_{0.60}Ga_{0.40})_{0.51}In_{0.49}P$	**60 nm**	**Barrier**	
$(Al_{0.60}Ga_{0.40})_{0.51}In_{0.49}P$	**81 nm**	**Barrier**	} x10
$Ga_{0.60}In_{0.40}P$	**6 nm**	**Quantum Well**	
$(Al_{0.60}Ga_{0.40})_{0.51}In_{0.49}P$	**7 nm**	**Barrier**	
$Ga_{0.60}In_{0.40}P$	**6 nm**	**Quantum Well**	
$(Al_{0.60}Ga_{0.40})_{0.51}In_{0.49}P$	**91 nm**	**Barrier**	
AlAs	**54 nm**	**DBR**	
$Al_{0.45}Ga_{0.55}As$	**47 nm**	**DBR**	} x40
AlAs	**54 nm**	**DBR**	
GaAs (10° towards 1[111])	**500 nm**	**Substrate**	

Table 3-1: 20QW structure used in pump wavelength experiment

A 500µm thick diamond heatspreader was bonded by liquid capillary action to the epitaxial surface of the VECSEL.

The VECSEL was placed as an end mirror of a v-cavity, with a plane mirror output coupler and a curved folding mirror. The pump beam was focussed onto the sample using a f=200mm lens giving a 30.4µm radius pump spot. The laser cavity was designed to match the laser mode size to the pump spot at the VECSEL.

In order to quantify the variation of temperature with pump wavelength, we used an argon-ion laser to optically pump a VECSEL structure at five different wavelengths (shown in Table 3-2) and over a range of powers to measure the change in output wavelength per unit pump power, from which we determined the temperature rise in the device, and slope efficiency.

Pump Wavelength (λ_p) /nm	Maximum Pump Power /W
514	13
501	1.75
496	5
476	5
457	2.38

Table 3-2: Wavelengths used and maximum available pump powers

All pump wavelengths used were shorter than the absorption edge of the pump-absorbing barriers. Whilst in-well pumping would reduce the thermal effects[18], due to the decreased quantum defect, multi-pass pumping would be required which would make the pump set-up more complicated.

Power transfer curves [Figure 3-14] were taken for each of the five pump wavelengths with different output coupling (highly reflecting (HR) end mirror, 1% and 2%). The increase in slope efficiency with increasing pump wavelength is not surprising if we consider that the each pump photon produces only one carrier pair, and thus at most one photon at the laser wavelength. As the laser wavelength is largely constant this means that as the pump wavelength becomes shorter more of the pump energy is wasted producing energetic carriers (which lose the excess energy to the lattice) and so is less efficient.

As expected, initially the slope efficiency increases as the output coupling increases. However there is an optimum level of output coupling (between 2% and 3%) after which the slope efficiency declines. Data are not available for 2% and 3% output coupling at 457nm as threshold was not reached.

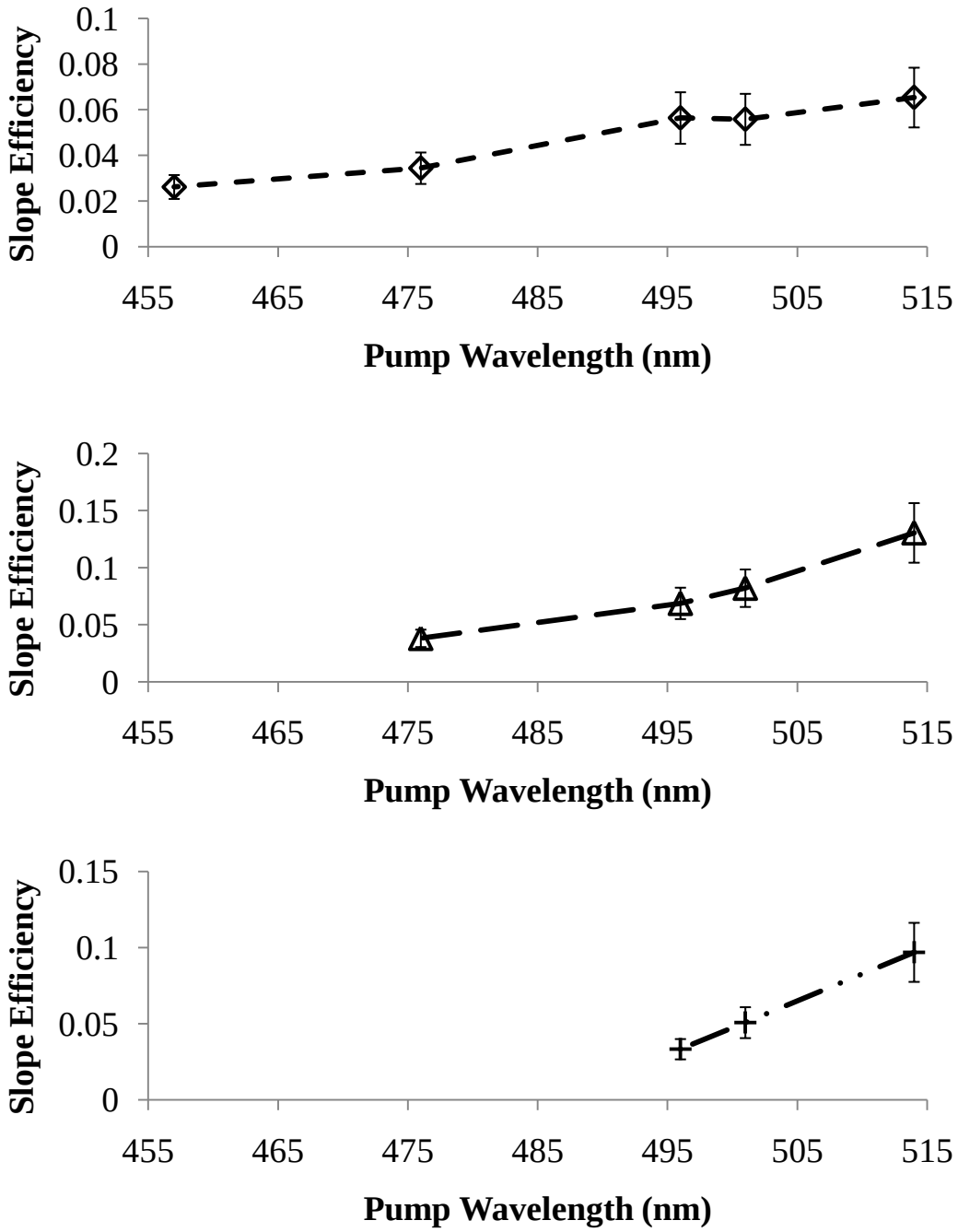

Figure 3-14: Slope efficiency variation with pump wavelength for different levels of output coupling a)1% b)2% and c)3%

Measurements were made of the output wavelength around threshold and at maximum power (the highest power at which the VECSEL would function or the maximum pump power) for different wavelengths to determine the extent of the wavelength change (and thus temperature change in the active region) of the

VECSEL output [Figure 3-15]. Whilst there is some variability in the data, there is a noticeable trend for the wavelength shift per unit pump power to increase as the pump wavelength increases, implying the device temperature increases as the pump wavelength increases in spite of the reduction in quantum defect.

Maclean et al[6] found that a higher level of output coupling than optimum was shown to decrease slope efficiency and hence cause additional heating. However given the variation in our data we are hesitant to draw any conclusions about the relationship between the level of output coupling used and device temperature.

We have determined experimentally that the VECSEL active region temperature actually increases with increasing wavelength. This is counter-intuitive as it would be expected that the reduced quantum defect which reduces the heat deposition in the structure would lead to a decrease in device temperature and is discussed in the next sections.

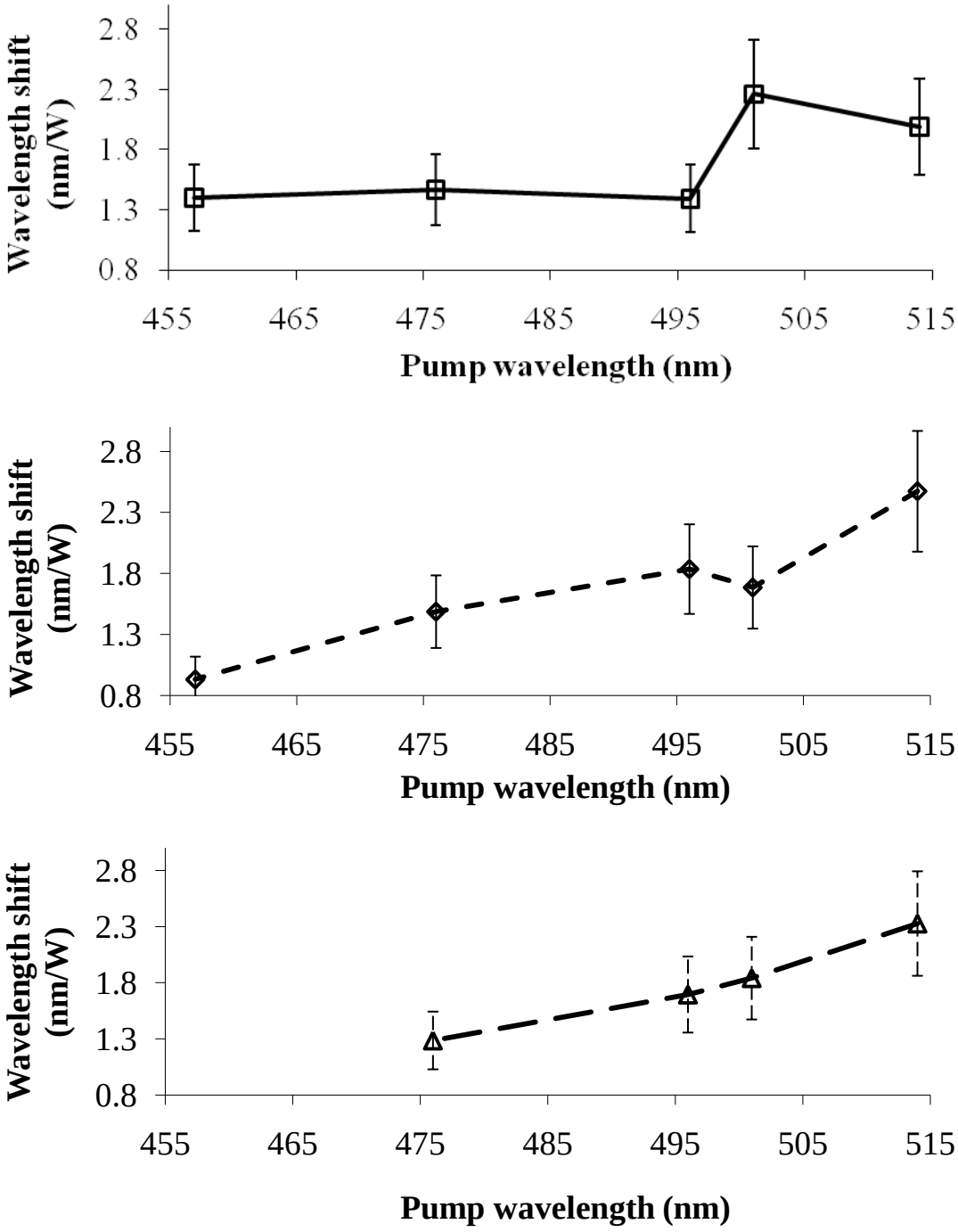

Figure 3-15: Wavelength change per unit pump power for different levels of output coupling a)Hr b)1% and c) 2%

3.4.2 Modelling the Effect of Pump Wavelength on Emission Wavelength

To explore the relationship between pump wavelength and active region temperature, a 10 quantum well GaInP/AlGaInP red emission VECSEL was pumped at a variety of wavelengths.

Decreasing the pump wavelength increases the quantum defect, which is a measure of the proportion of pump photon energy 'lost' when producing a laser photon, and is defined as

$$q_{defect} = 1 - \frac{\lambda_{pump}}{\lambda_{laser}} \quad (3\text{-}1)$$

where λ_{laser} is the VECSEL emission wavelength and λ_{pump} the pump wavelength. An increase in quantum defect means more energy is lost to the crystal lattice as heat.

In the AlGaInP material system, decreasing the pump wavelength increases the absorption coefficient, calculated from Schubert et al[19], thus decreasing the absorption length (the distance in which pump intensity falls to $1/e^2$ of its initial strength). Absorption curves in the 20QW structure (used in the earlier experiment) for a range of wavelengths are shown in the Figure 3-16. In addition, a shorter pump wavelength increases the amount of pump energy wasted as heat due to the quantum defect. The combination of these effects results in more heat being deposited, in a smaller volume, as the pump wavelength is decreased. Intuitively one would expect this to cause greater heat build up in the device and so the emission wavelength to increase as outlined in section 2.1.6.

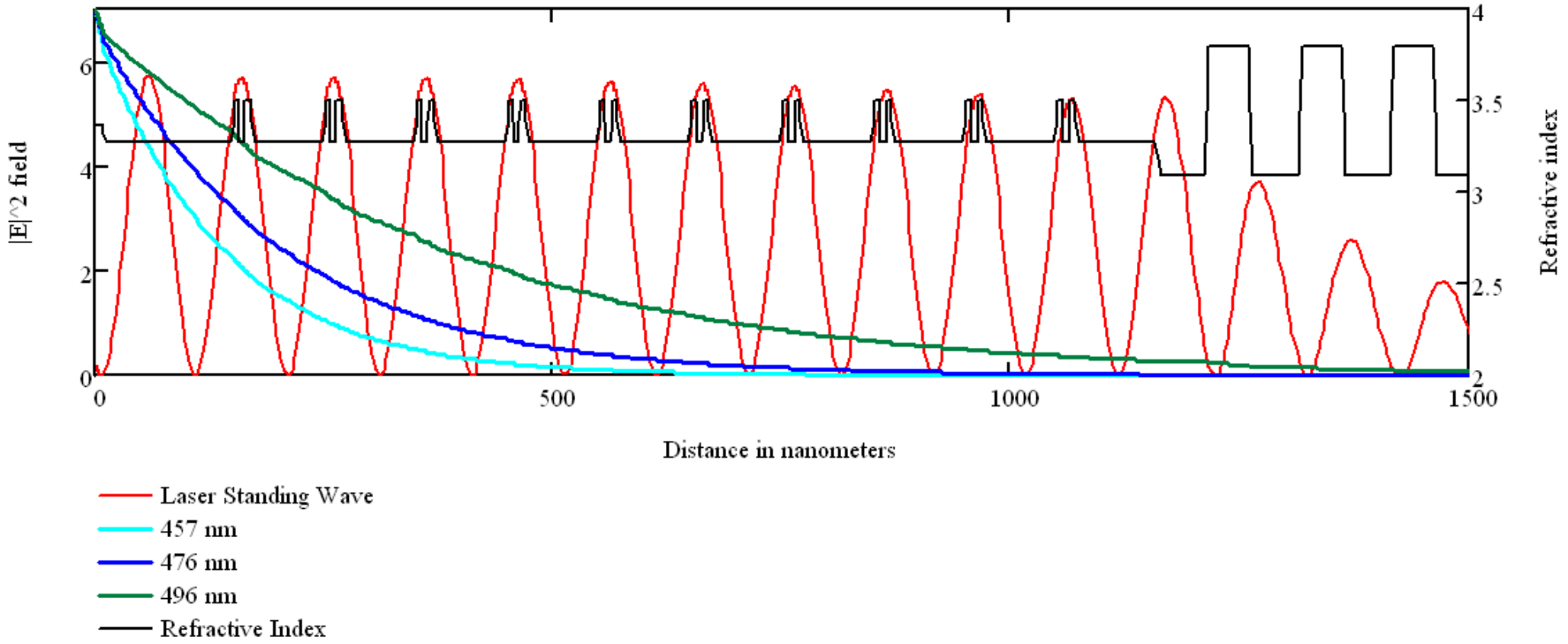

Figure 3-16: Absorption curves of various pump wavelengths in a 20QW VECSEL

3.4.3 Finite Element Analysis

Heat in semiconductor structures is a complex problem with no analytical solution except in very simple cases[20] and needs to be addressed using numerical methods. Finite Element Analysis (FEA) breaks structures down into a network of linked points or nodes which form triangular elements (called a mesh) and are assigned material properties such as thermal conductivity. The application of Fourier's equation to the nodes and surrounding elements yields a set of coupled equations which can be solved by computer. The mesh density can be increased in critical areas to improve accuracy and decreased in non-critical areas to decrease processor time. The calculations were carried out using a standard desktop PC and Comsol Multiphysics using a model developed by Dr Alan Kemp of the Institute of Photonics, University of Strathclyde which I adapted for our particular geometry.

The basis of the model is Fourier's Equation which describes the rate of heat flow:

$$-\nabla \cdot (k\nabla T) = Q \tag{3-2}$$

where k is the thermal conductivity, T the temperature and Q the heat loading density.

Heat is generated when pump photons are absorbed and the generated carriers lose energy to the lattice. Non-radiative transitions also contribute heat energy. Heat is generated throughout the region where the pump is absorbed and is strongest towards the top of the structure where the pump light enters.

A fine mesh is used in the immediate region of the pumped area and in the thin cap and gain region layers where the heat loading and temperature gradient are greatest and a coarser mesh in other regions.

It is assumed the pump beam is circularly symmetric and perfectly Gaussian. The pump spot is small compared to the dimensions of the sample and is assumed to be

pumped near the centre. This leads to the simplifying assumption of radial symmetry which makes the model two-dimensional, greatly reducing computation.

Calculation is further reduced by treating the comparatively large gain region and DBR as single homogeneous layers. In the case of the gain region, the quantum wells are thin compared to the bulk pump-absorbing layers and are of very similar thermal conductivity. The radial (k_r) and axial (k_z) thermal conductivities for these composite layers are calculated as follows[21].

$$k_r = \frac{\sum_i t_i}{\sum_i \frac{t_i}{k_i}} \tag{3-3}$$

$$k_z = \frac{\sum_i k_i t_i}{\sum_i t_i} \tag{3-4}$$

where k_i is the thermal conductivity and t_i the thickness of layer i.

The pump absorption coefficient α is calculated in a similar manner[21].

$$\alpha = \frac{\sum_i \alpha_i t_i}{\sum_i t_i} \tag{3-5}$$

However, for the DBR, the axial thermal conductivity is lower due to phonon reflection at the many DBR interfaces between $Al_{0.45}Ga_{0.55}As$ and AlAs[22].

The geometry of the model is shown in Figure 3-17. A thin layer (~ 100 μm) of indium is used to improve thermal contact between the substrate and brass mount. The thermal conductivity of the chip to mount interface has little effect on temperature[22] provided it is above ~0.1$Wmm^{-2}K^{-1}$. A 100μm thick layer of indium has a thermal conductivity of ~0.8 $Wmm^{-2}K^{-1}$. There is little heatflow between the heatspreader and mount and this interface is not critical.

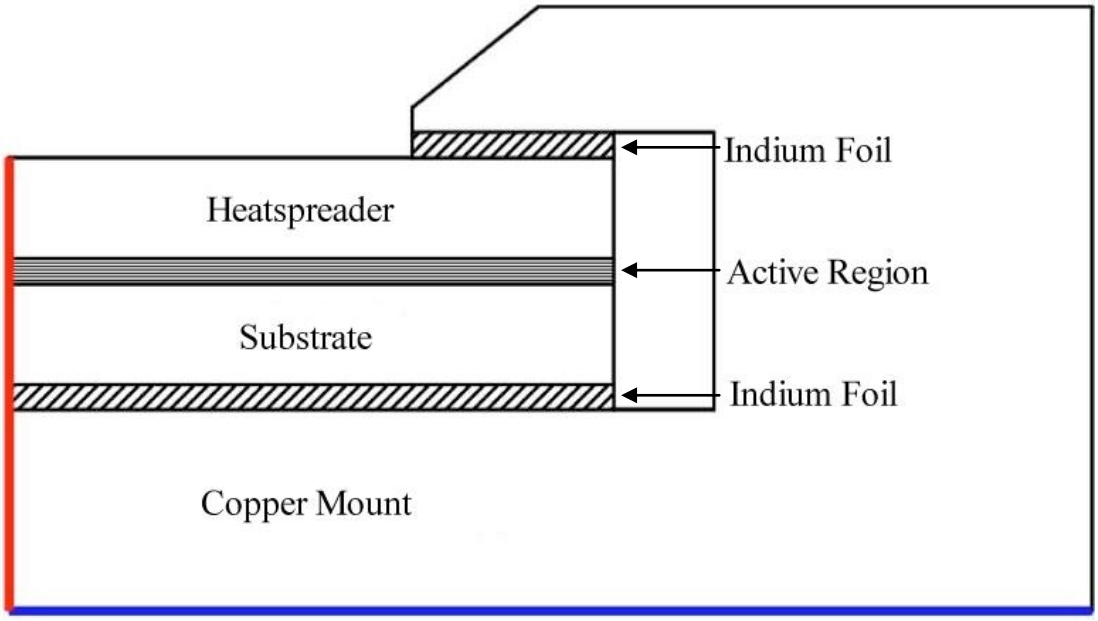

Figure 3-17: Geometry of the FEA VECSEL model. The blue line is the constant temperature boundary and the red line is the line of radial symmetry.

The solutions of the set of equations are constrained by the chosen boundary conditions. A constant temperature boundary condition is imposed in the Indium/Copper mount interface.

This model was used by Kemp et al[21] to explore the comparative effectiveness of the 'thin disk' and heatspreader approaches and the relative importance of the interfaces between the semiconductor structure and external materials.

To investigate the experimental findings we used the FEA model, specifying a pump power of 1W, pump spot radius of 30.4μm and a Gaussian beam profile. As the model was used to show the temperature change rather than absolute temperature the results are for 1W of pump energy absorbed above threshold.

3.4.3.1 Modelling

Three measures of temperature are plotted against experimental results: the maximum temperature (ΔT) in the gain region and two radially averaged temperatures: the radial average (ΔT_r) is weighted to account for the Gaussian distribution of the pump, the radial and axial average ($\Delta T_{r,z}$) is additionally weighted

to take into account the pump absorption. The radial average is expected to reflect the changes in the subcavity resonance while the radial and axial average may better reflect the change in quantum well gain[21].

Heat loading is the fraction of the pump energy absorbed in a volume element which becomes heat. It is assumed that any pump energy absorbed in the DBR becomes heat.

Quantum Defect Heating

One assumption that can be made for the heat load in the gain region is that of quantum defect heating. It assumes that every pump photon absorbed in the structure produces one emission photon and the difference in energies becomes heat. The heat loading in the gain region is

$$\eta_G = 1 - \lambda_{pump}/\lambda_{emission} \quad (3\text{-}6)$$

This can be regarded as a lower bound to the device heat loading as it underestimates the heat loading, ignoring non-radiative recombination and output coupling is not taken into account. We modelled the temperature increase in a twenty quantum well red VECSEL, comparing the model results with experimental data for the case of a high reflectivity end mirror/output coupler. It is clear from in Figure 3-18 that quantum defect heating fails to show a significant increase in temperature per unit pump power with increasing pump wavelength until pump light starts to penetrate into the DBR, unlike the experimental results.

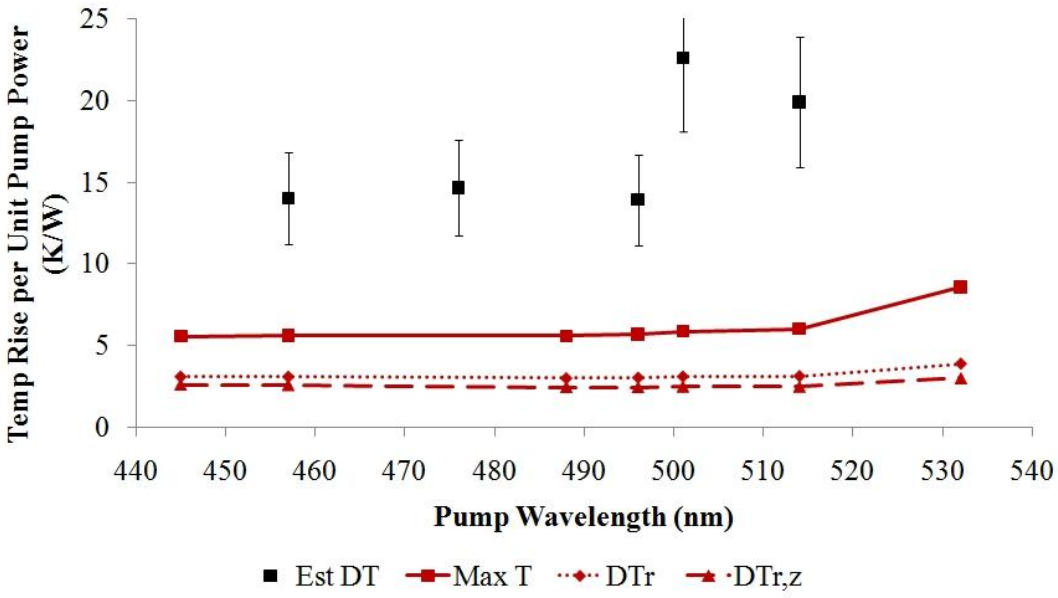

Figure 3-18: Temperature change per unit pump power for various pump wavelengths (quantum defect heating).
Est DT is the inferred actual temperature rise, Max T the modelled temperature at the hottest point, DTr the modelled weighted average radial temperature and Dtr,z the modelled weighted average axial&radial temperature.

Slope Efficiency Heating

Alternatively, one can assume that any energy not extracted from the system by output coupling becomes heat. As the slope efficiency is the proportion of pump energy (above threshold) which is extracted as output, this sets the gain region heat loading as

$$\eta_G = 1 - \text{Slope Efficiency} \qquad (3\text{-}7)$$

and so its value is derived from experiment. Slope efficiency figures for wavelengths not measured have been interpolated/extrapolated from experimental figures. Slope efficiency heating can be regarded as an upper bound to the heat loading, it overestimates the heat loading as it ignores laser cavity losses and fluorescence which do not contribute to heating. We modelled the increase in temperature in a twenty quantum well red VECSEL for the cases of a highly reflecting, 1% and 2% output coupler and compared the predictions to experimental results. It can be seen from Figure 3-19 that slope efficiency heating better reflects experimental

observations than quantum defect heating, however only the maximum temperature in the device (ΔT) shows a significant increase in temperature per unit pump power.

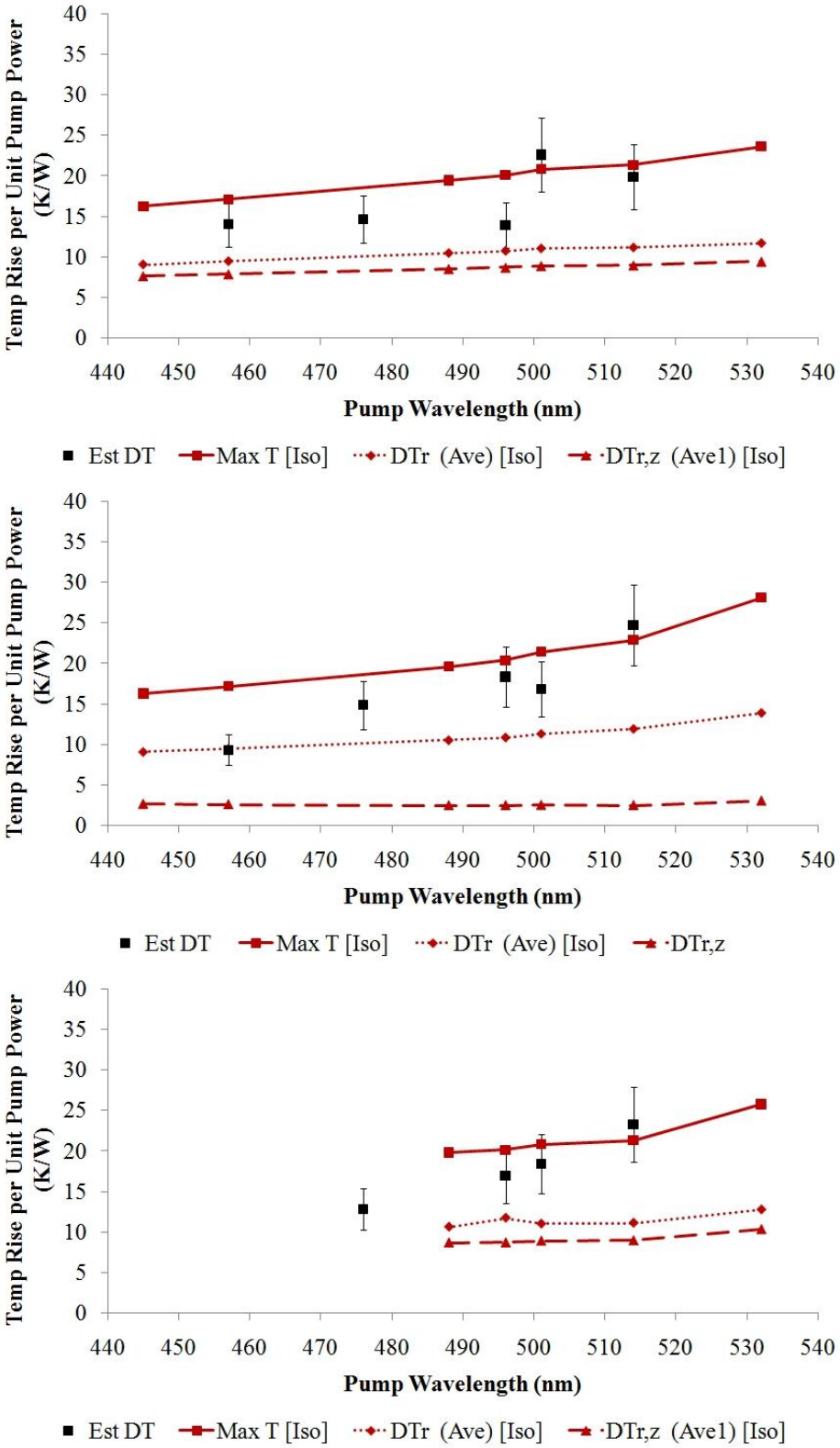

Figure 3-19: Model results for slope efficiency heating for a)HR b) 1%OC and c)2%OC

3.4.3.2 Conclusions

Experimental results show an increase in emission wavelength, and thus temperature, at wavelengths below that at which significant pump light penetrates into the DBR. It appears from the model and experimental results that the additional heat generation at shorter pump wavelengths is counteracted by the reduced thermal resistance due to it being generated closer to the diamond heatspreader and thus experiencing less thermal resistance. This causes the counterintuitive situation of a longer pump wavelength, and thus lower quantum defect, resulting in higher active region temperatures. This is illustrated by Figure 3-20 showing the modelled temperature rise in a twenty quantum well structure with a liquid-capillary bonded[16,18] 500µm diamond heatspreader for pump wavelengths of 445nm and 532nm.

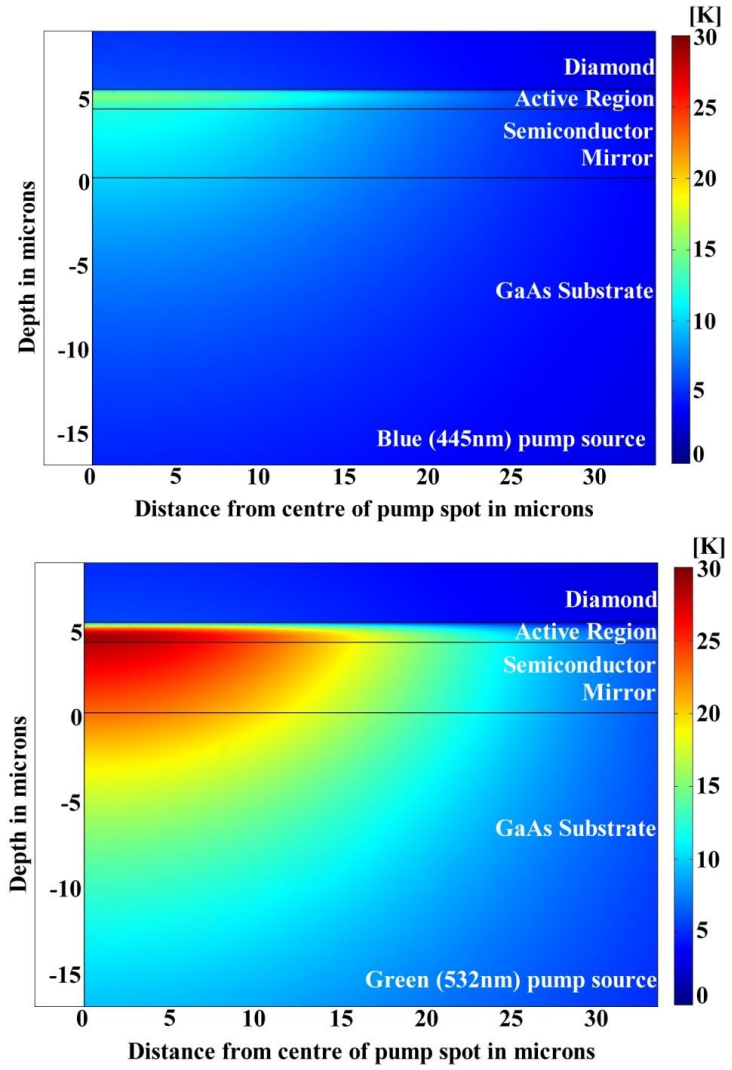

Figure 3-20 COMSOL Multiphysics simulations of a red VECSEL structure pumped at (a) 445nm and (b) 532nm

Two assumptions were tested regarding heat loading in the structure: *quantum defect heating* which only demonstrated active region temperature rises after pump light penetrated into the DBR and underestimated the heat loading; and *slope efficiency heating* which showed a temperature increase as the pump wavelength increased but overestimated the heat loading at short pump wavelengths. Although there is some qualitative agreement between the model and experiment there is quantitative disagreement. There are a few possible reasons for this:

- the absorption coefficient at the different pump wavelengths is based on models and not actual experimental data. Small changes in absorption change how deep into the structure pump light penetrates and thus how much thermal resistance it encounters.
- the heat loading assumptions were deliberately simple and do not present an accurate picture of how and where heat is generated within the VECSEL.
- Heatflow within a complex layered semiconductor structure is not well understood and the assumptions made in the model regarding heatflow may not be valid.

The benefit of using a heatspreader when using shorter pump wavelength will be seen in Chapter 4 where 445nm GaN laser diodes are used to pump a GaInP/AlGaInP VECSEL.

3.5 Thermal Management by Peltier Element Only

Typically significant thermal management is employed when using a VECSEL in order to reduce the heat-loading in the device and thus the temperature dependant effect on wavelength and efficiency, for example previous red VECSEL results were all achieved using a diamond heatspreader. However the low output power required by applications such as gas-sensing may avoid the need for the usual thermal management techniques, allowing the VECSEL to be cooled by peltier element with no thinning or post-processing (other than cleaving the sample).

3.5.1 Structure

The structure used was the ten quantum well design grown at 690°C examined in section 3.1 and a 4mm square sample was cleaved from wafer MR2331 on the basis of the wafer mapping. The normal PL and reflectivity for this sample is shown in Figure 3-21. It was expected that, due to the lack of thermal management, the device would only operate at very low power and the sample was chosen to have its quantum well emission peak, inferred from the reflectivity and normal PL data, close to the sub-cavity resonance to minimise the threshold.

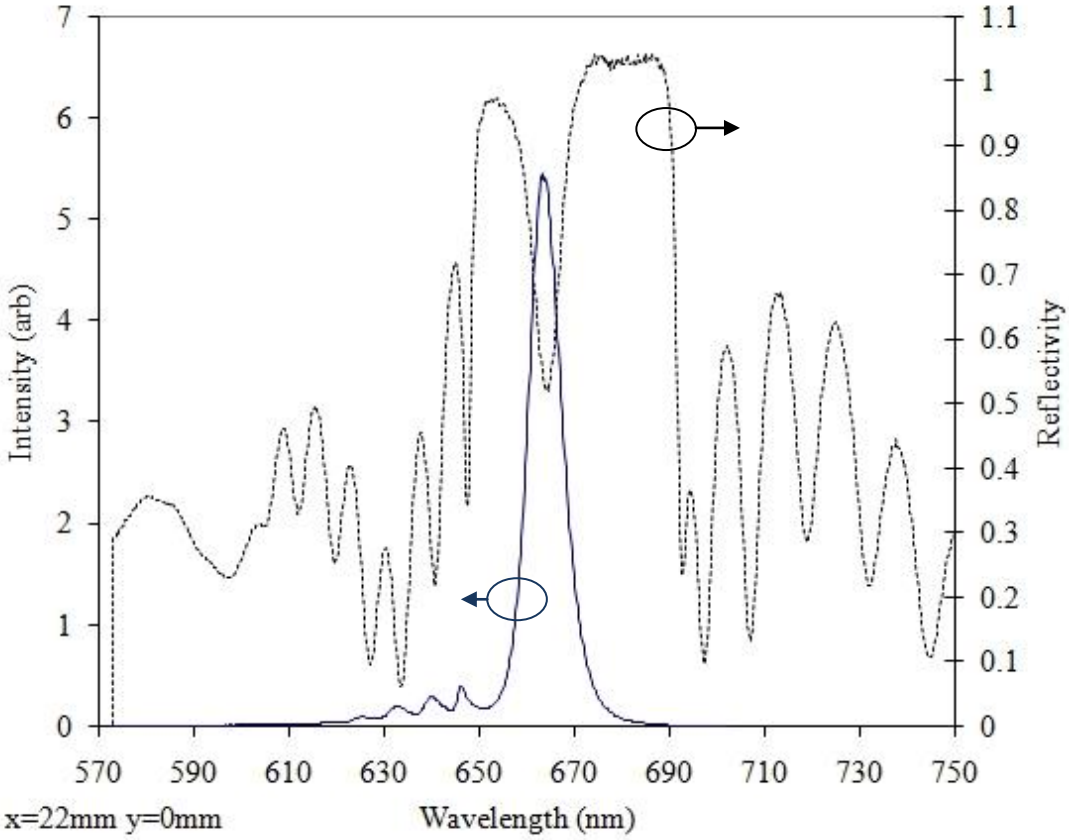

Figure 3-21: Reflectivity (black) and Normal PL (blue) for sample MR2331K

3.5.2 Experiment

The sample was attached, using silver heat conducting paste, to a peltier element which was in turn attached in the same way to a water-cooled brass mount. The peltier element was maintained at ~10°. In order to minimise the angle of the cavity

mode on the folding mirror, the sample and peltier element were attached as close to the edge of the brass mount as possible. The sample was placed as the end mirror of a three mirror cavity with a curved folding mirror and highly reflecting plane end mirror. A 532nm single transverse mode pump source was used. The experimental set-up is shown in Figure 3-22.

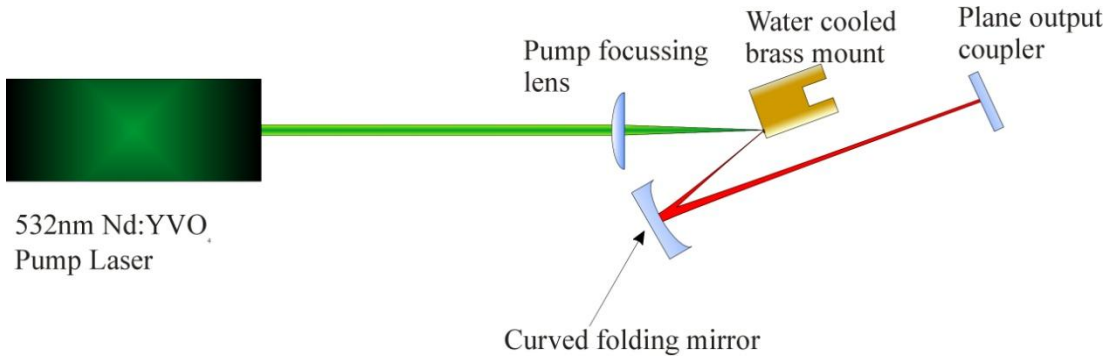

Figure 3-22: Schematic of experimental set-up

The lack of thermal management would severely limit power scaling so the initial demonstration was designed for the smallest pump spot, and hence lowest threshold, we could reasonably attain with a mode-matched cavity.

3.5.3 Results

To achieve the small pump spot an f=8mm lens was used to focus the pump beam onto the sample. In order to accommodate all the equipment a pumping angle of ~59° was necessary which increased reflection losses compared to the more usual pump angle of ~20°. The short cavity arm was 12.5mm and the long arm 315mm. The concave folding mirror had a radius of curvature of r=-25mm. The arm lengths were adjusted to give best single transverse mode performance, with a mode size on the sample surface of 7-8μm radius calculated using WinLase^{TM}. Laser action was observed at ~8.7mW absorbed pump power with a threshold of ~6.5mW. A maximum of 214μW was obtained through the HR end mirror with a slope efficiency of 2%

Although a smaller mode radius should be possible the cavity became increasingly sensitive to small changes as the mode size decreased which made a further reduction in mode size impractical. This was the first time the red emission VECSEL had been observed to lase without a heatspreader or substrate thinning.

Power transfer curves are shown in Figure 3-23 for the lowest threshold points on the sample. Several power transfer curves were taken because of the variability of performance across the sample.

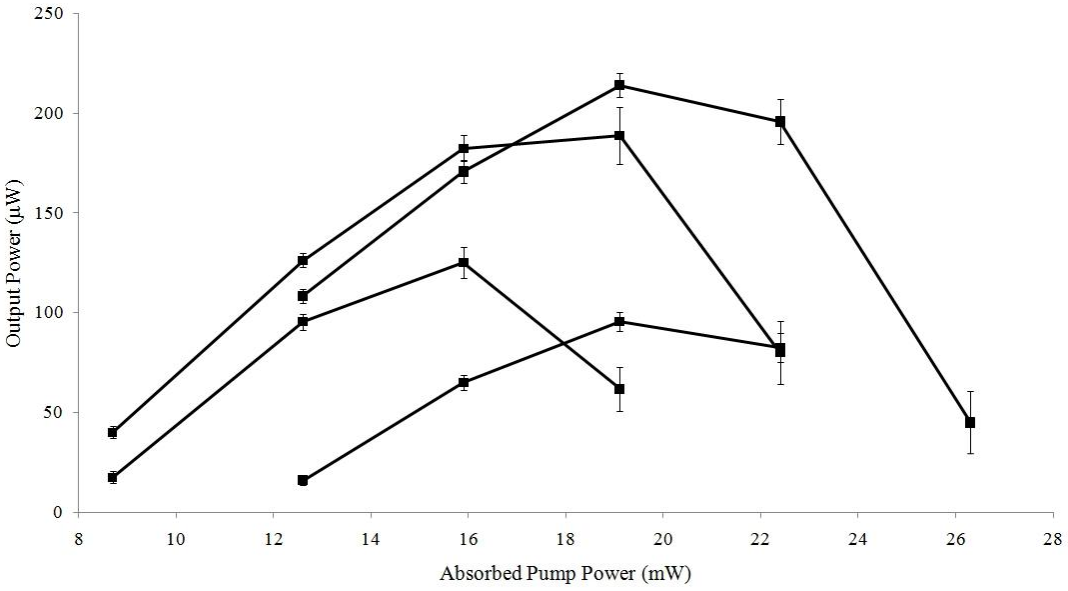

Figure 3-23: Four power transfer curves for 7-8µm radius mode size heatspreaderless VECSEL taken under the same experimental conditions.

The experimental set-up was varied to see if, and how much, the system could be power scaled. Cavities with mode sizes (on VECSEL surface) of 12µm, 17µm and 20µm radius were created by adjusting cavity arm lengths and the pump spot size changed by varying the pump focussing lens (f=88.3mm, f=125mm and f=150mm respectively) and distance from pump focussing lens to sample with the mode size and pump spot matched to give the best single transverse mode performance. Power transfer curves were taken with an HR end mirror. Power transfer curves for mode sizes are shown in Figure 3-24. Note the significantly greater power of the multimode output for the 12µm radius pump spot. In all cases the VECSEL

performed better multimode, the larger and less concentrated mode ensuring less concentrated heating. Also, the smaller the mode size the smaller the range of pump powers over which the laser would operate.

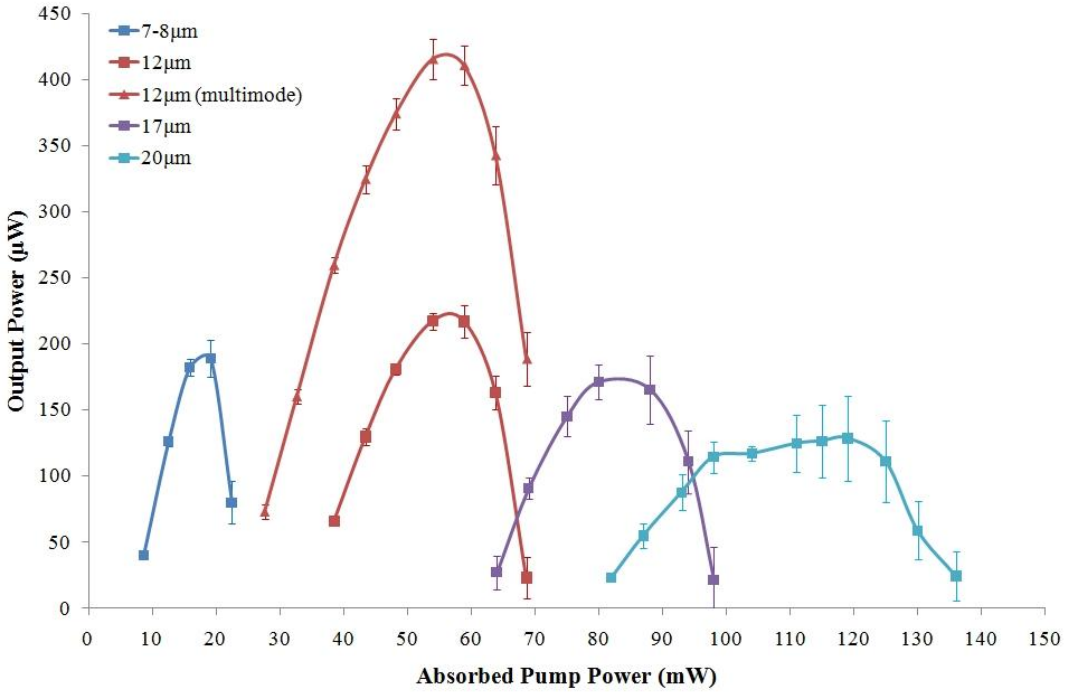

Figure 3-24: Power Transfer Curves for various mode sizes

We can compare the output through the high reflector end mirror against the absorbed average pump intensity for different pump spot sizes. Figure 3-25 suggests that the rollover point occurs for similar absorbed average pump intensity for the range of mode sizes tested. The 12µm radius multi mode output has a higher pump intensity rollover point. The 12µm radius output which was believed to be single mode shares this rollover intensity and has a higher output power than the other single mode cavities which suggests that it was wrongly identified as single mode.

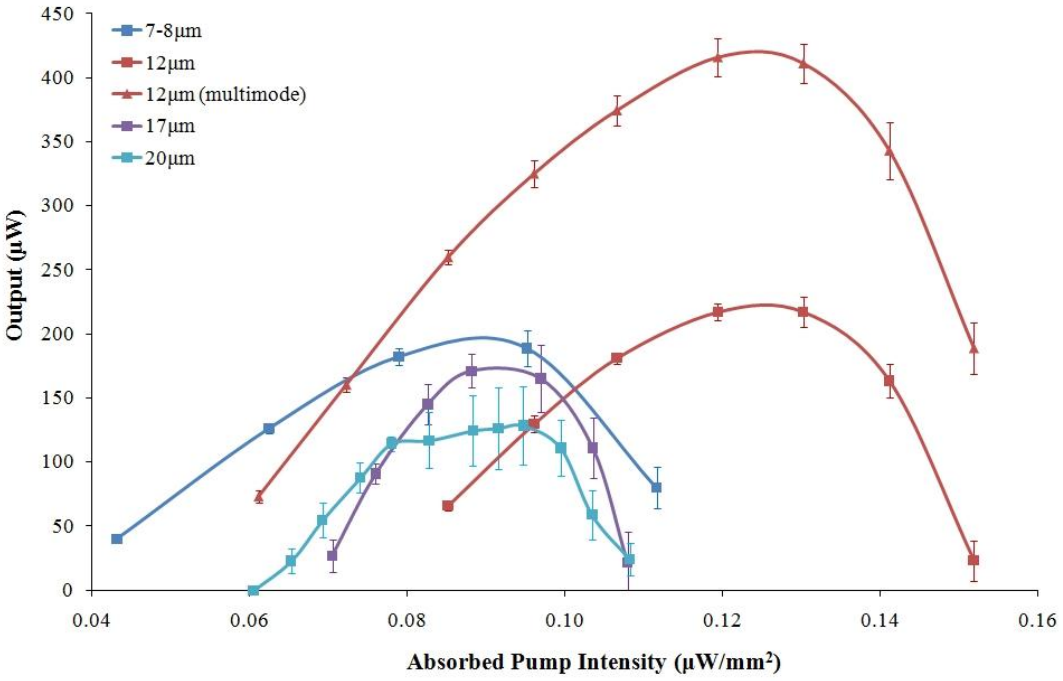

Figure 3-25: Power Transfer v Pump Intensity for various mode sizes

We swapped the HR end mirror for a plane 1% output coupler in the 20µm mode radius set-up but were unable to achieve laser action.

3.5.4 Thermal Model

The thermal effects for the optimal absorbed pump power of 18mW for a 7µm radius Gaussian pump spot were modelled using the FEA model of section 3.4.2. A maximum temperature rise of 4.7K was calculated, as shown in Figure 3-26

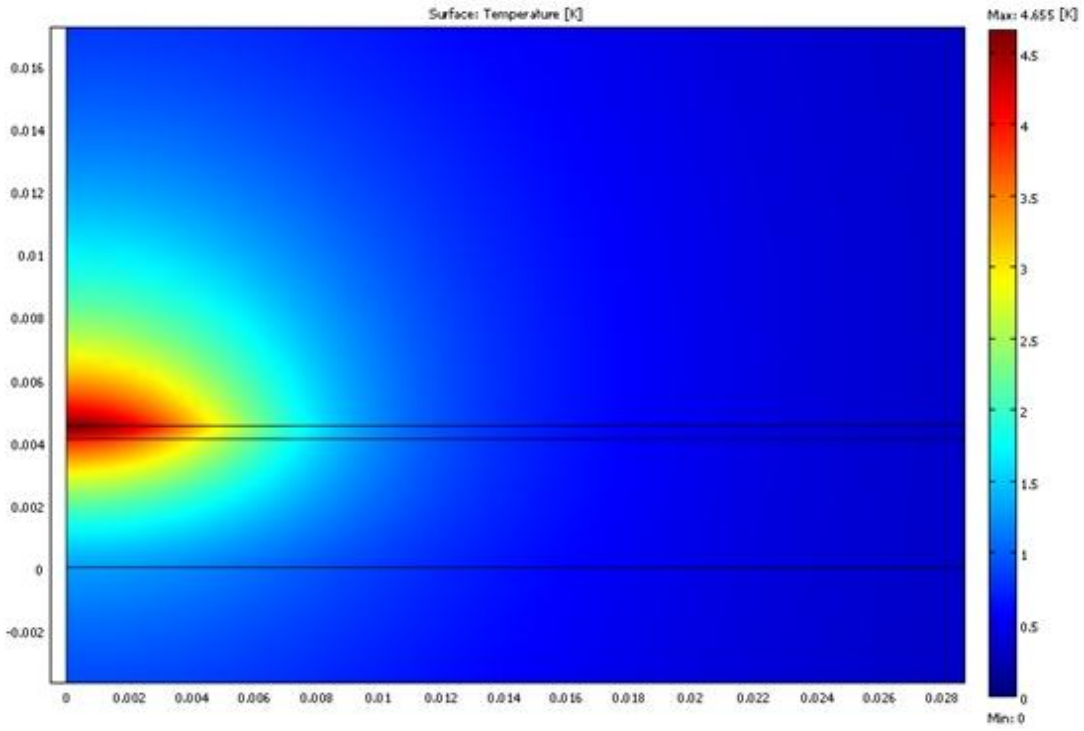

Figure 3-26: FEA model of 670nm VECSEL pumped at 532nm with a 7µm pump radius

3.5.5 Discussion

We demonstrated for the first time laser action in a red VECSEL without heatspreader or 'thin disk' thermal management methods. We were motivated to examine the performance of a VECSEL without a heatspreader by a previous attempt to demonstrate a fibre-coupled AlGaInP 670nm VECSEL using a 4µm diameter single mode fibre with a 532nm pump. The plane fibre-tip was HR coated for the 670nm and formed one end mirror of a plane-plane cavity with length of the order of microns and the VECSEL as the other end mirror (with gain). Despite seeing good etalon effects we were unable to induce laser action.

For the range of single transverse mode sizes the thermal rollover point occurred for similar pump power intensities, the smaller modes giving greater output power but also smaller operational pump power ranges. The results suggest that a 4-5µm diameter mode (allowing for beam expansion after exiting the fibre) would have a very small pump power operating range. For a stable laser mode to exist in the plane-

plane cavity a thermal lens of suitable focal length would need to be produced in the VECSEL. Given the small operating range of a VECSEL without a heatspreader it seems likely that the pump power range needed to also produce the correct thermal lens was too small and we were not able to match it.

3.6 Conclusion

We have looked at the characterisation of AlGaInP/GaInP red VECSEL structures, utilising photoluminescence and reflectivity measurements to map the growth variation of the 2" wafers grown at different temperatures, showing little difference between the wafers. We then characterised four samples in greater detail. The shift in normal- and edge-emission photoluminescence wavelength with temperature was measured, being broadly in line with expectations.

We discussed two different approaches to thermal management of VECSELs. The thermal effect of pumping a red VECSEL structure with a diamond heatspreader at different wavelengths was examined, with both the experimental results and modelling suggesting that reducing the pump photon energy increased active region temperature.

Finally, a red VECSEL structure, cooled only by a peltier element, was pumped at different pump spot sizes and powers. Laser output without significant thermal management, with output powers of up to a few hundred microwatts, was demonstrated. This was the first time one of our red VECSELs had been used without a heatspreader, showing suitability for low power applications.

References

1 J. E. Hastie, L. G. Morton, A. J. Kemp, M. D. Dawson, A. B. Krysa, and J. S. Roberts, "Tunable ultraviolet output from an intracavity frequency-doubled red vertical-external-cavity surface-emitting laser," Applied Physics Letters **89** (6), 061114 (2006).

2 M. Y. A. Raja, S. R. J. Brueck, M. Osinski, C. F. Schaus, J. G. McInerney, T. M. Brennan, and B. E. Hammons, "Surface-emitting, multiple quantum well GaAs/AlGaAs laser with wavelength-resonant periodic gain medium," Applied Physics Letters **53** (18), 1678-1680 (1988).

3 N. K. Dutta, "Calculation of Auger rates in a quantum well structure and its application to InGaAsP quantum well lasers," Journal of Applied Physics **54** (3), 1236-1245 (1983).

4 J. Hader, J. V. Moloney, and S. W. Koch, "Temperature Dependence of Radiative and Auger Losses in Quantum Wells," Quantum Electronics, IEEE Journal of **44** (2), 185-191 (2008).

5 J. W. Scott, R. S. Geels, S. W. Corzine, and L. A. Coldren, "Modeling temperature effects and spatial hole burning to optimize vertical-cavity surface-emitting laser performance," Quantum Electronics, IEEE Journal of **29** (5), 1295-1308 (1993).

6 A. J. Maclean, R. B. Birch, P. W. Roth, A. J. Kemp, and D. Burns, "Limits on efficiency and power scaling in semiconductor disk lasers with diamond heatspreaders," J. Opt. Soc. Am. B **26** (12), 2228-2236 (2009).

7 M. Kuznetsov, F. Hakimi, R. Sprague, and A. Mooradian, "Design and characteristics of high-power (> 0.5-W CW) diode-pumped vertical-external-cavity surface-emitting semiconductor lasers with circular TEM_{00} beams," IEEE J. Sel. Top. Quantum Electron. **5** (3), 561 (1999).

8 J. Chilla, S. Butterworth, A. Zeitschel, J. Charles, A. Caprara, M. Reed, and L. Spinelli, "High power optically pumped semiconductor lasers", *Solid State Lasers Xiii: Technology and Devices*, Vol. 5332, pp. 143-150 (2004).

9 Wang Tsuei-Lian, Y. Kaneda, J. M. Yarborough, J. Hader, J. V. Moloney, A. Chernikov, S. Chatterjee, S. W. Koch, B. Kunert, and W. Stolz, "High-Power Optically Pumped Semiconductor Laser at 1040 nm," IEEE Photonics Technol. Lett. **22** (9), 661-663 (2010).

10 W. J. Alford, T. D. Raymond, and A. A. Allerman, "High power and good beam quality at 980 nm from a vertical external-cavity surface-emitting laser," J. Opt. Soc. Am. B - Optical Physics **19** (4), 663-666 (2002).

11 J. E. Hastie, J. M. Hopkins, S. Calvez, C. W. Jeon, D. Burns, R. Abram, E. Riis, A. I. Ferguson, and M. D. Dawson, "0.5-W single transverse-mode operation of an 850-nm diode-pumped surface-emitting semiconductor laser," IEEE Photonics Technol. Lett. **15** (7), 894 (2003).

12 Jennifer Hastie, Lynne Morton, Stephane Calvez, Martin Dawson, Tomi Leinonen, Markus Pessa, Graham Gibson, and Miles Padgett, "Red microchip VECSEL array," Opt. Express **13** (18), 7209-7214 (2005).

13 J. E. Hastie, S. Calvez, M. D. Dawson, T. Leinonen, A. Laakso, J. Lyytikainen, and M. Pessa, "High power CW red VECSEL with linearly polarized TEM_{00} output beam," Opt. Express **13** (1), 77-81 (2005).

14 J. M. Hopkins, S. A. Smith, C. W. Jeon, H. D. Sun, D. Burns, S. Calvez, M. D. Dawson, T. Jouhti, and M. Pessa, "0.6 W CW GaInNAs vertical external-cavity surface emitting laser operating at 1.32 μm," Electronics Letters **40** (1), 30-31 (2004).

15 H. Lindberg, M. Strassner, E. Gerster, and A. Larsson, "0.8 W optically pumped vertical external cavity surface emitting laser operating CW at 1550 nm," Electronics Letters **40** (10), 601-602 (2004).

16 Z. L. Liau, "Semiconductor wafer bonding via liquid capillarity," Applied Physics Letters **77** (5), 651-653 (2000).

17 A. C. Tropper, H. D. Foreman, A. Garnache, K. G. Wilcox, and S. H. Hoogland, "Vertical-external-cavity semiconductor lasers," Journal Of Physics D-Applied Physics **37** (9), R75 (2004).

18 A. J. Kemp, G. J. Valentine, J. M. Hopkins, J. E. Hastie, S. A. Smith, S. Calvez, M. D. Dawson, and D. Burns, "Thermal management in vertical-external-cavity surface-emitting lasers: finite-element analysis of a heatspreader approach," Quantum Electronics, IEEE Journal of **41** (2), 148-155 (2005).

19 M. Schubert, J. A. Woollam, G. Leibiger, B. Rheinlander, I. Pietzonka, T. Sass, and V. Gottschalch, "Isotropic dielectric functions of highly disordered $Al_xGa_{1-x}InP$ ($0 <= x <= 1$) lattice matched to GaAs," Journal of Applied Physics **86** (4), 2025-2033 (1999).

20 A. C. Tropper and S. Hoogland, "Extended cavity surface-emitting semiconductor lasers," Progress in Quantum Electronics **30** (1), 1-43 (2006).

21 A. J. Kemp, J. M. Hopkins, A. J. Maclean, N. Schulz, M. Rattunde, J. Wagner, and D. Burns, "Thermal management in 2.3-μm semiconductor disk lasers: A finite element analysis," Quantum Electronics, IEEE Journal of **44** (1-2), 125-135 (2008).

22 H. Lindberg, M. Strassner, J. Bengtsson, and A. Larsson, "Optically pumped VECSEL operating at 1550 nm", *Vertical-Cavity Surface-Emitting Lasers Viii*, Vol. 5364, pp. 25-33 (2004).

Chapter 4

Diode-Pumped AlGaInP VECSELs

In this chapter we design a GaInP/AlGaInP red-emitting VECSEL for short wavelength optical pumping by GaN laser diodes, examining the factors impacted by the change of pump wavelength and the motivation for each modification. We demonstrate the first visible wavelength diode pumped VECSEL, producing 12mW[1] with excellent beam quality. Further iteration of the design improves performance to a pump power limited 17mW[2].

4.1 Design Considerations

The red-emission VECSELs used in previous work by Hastie et al[3,4] were designed to be pumped at 532nm. Changing pump source to GaN laser diodes required redesign of the active region to take into account the effect of using the shorter pump wavelengths. The DBR design was preserved as the emission wavelength was unchanged.

4.1.1 Absorption Length

Laser diodes of sufficient power were available to us initially at 405nm and later 445nm. These, more energetic, pump wavelengths are absorbed more strongly[5] by (AlGa)InP than the 532nm wavelength used to pump earlier structures. The absorption curve of the barrier material $(Al_{0.6}Ga_{0.4})_{0.51}In_{0.49}P$ was modelled according to Schubert et al[5] (shown in Figure 4-1).

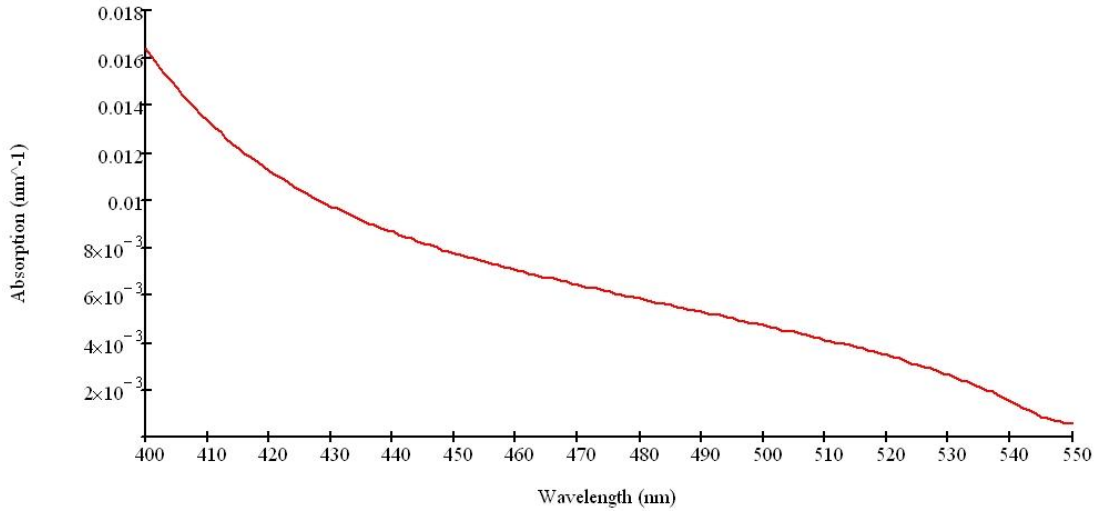

Figure 4-1: Modelled $(Al_{0.6}Ga_{0.4})_{0.51}In_{0.49}P$ absorption curve

In order to provide gain, quantum wells require sufficient carrier generation in their vicinity to achieve a carrier density above transparency. The active region was designed to ensure that quantum wells were placed only where a reasonable level of pump intensity remained; we used a guideline of 5% remaining pump energy.

The absorption length (the distance in which the pump intensity drops to 1/e of its initial value) of 405nm and 445nm is significantly shorter in the $(Al_{0.6}Ga_{0.4})_{0.51}In_{0.49}P$ barriers than at 532nm. For the purposes of calculating the absorption length of the active region, the quantum wells have been neglected as they are thin compared to the $(Al_{0.6}Ga_{0.4})_{0.51}In_{0.49}P$ pump absorbing layers.

According to Beer's Law, the proportion of pump intensity remaining after the pump light has passed a distance x (nm) through a material with an absorption constant α (nm^{-1}) is

$$T = e^{-\alpha x} \tag{4-1}$$

Therefore the absorption length L_{abs} is the value of x for which T=1/e i.e.

$$L_{abs} = {}^{1}/_{\alpha} \tag{4-2}$$

The absorption constants were calculated from Schubert[5] et al and the absorption constants and length for the relevant wavelengths are presented in Table 4-1.

Pump Wavelength (nm)	Absorption Constant α (nm^{-1})	Absorption Length L_{abs} (nm)
532	$2.416x10^{-3}$	413.9
445	$8.161x10^{-3}$	122.5
405	$14.721x10^{-3}$	67.9

Table 4-1: Absorption data for $(Al_{0.6}Ga_{0.4})_{0.51}In_{0.49}P$

Absorption of 405, 445 and 532nm light in a 670nm emission structure designed for pumping at 532nm was modelled[5-8] the results of which are presented in Figure 4-2. This showed that it would not be possible to use existing structures as the pump light would be depleted too quickly.

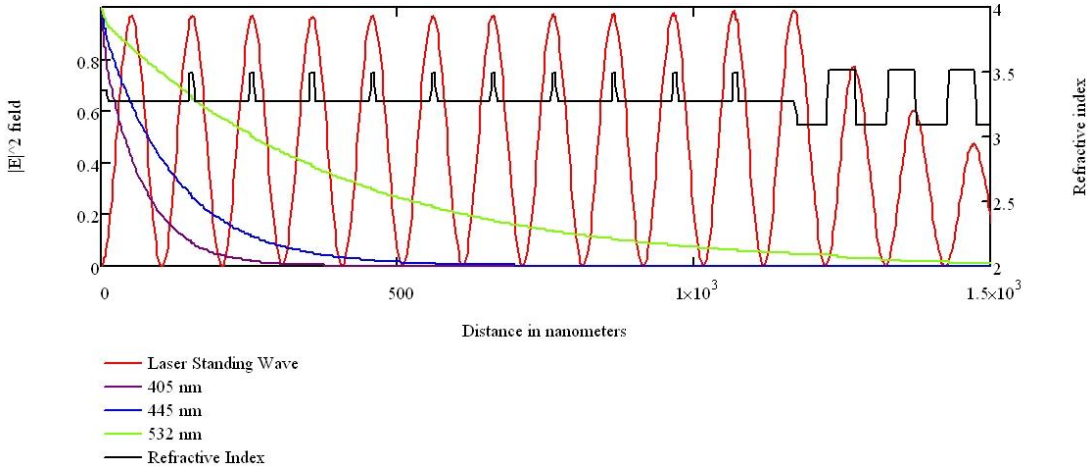

Figure 4-2: Mathcad plot of pump absorption (at 405nm, 445 and 532nm) in active region of 10 quantum well red VECSEL designed for pumping at 532nm

To avoid laser wavelength absorption from under-pumped quantum wells it was decided to position quantum wells at the first two anti-nodes of the cavity standing wave only. The next design parameter to be considered is how many quantum wells should be placed at each anti-node.

4.1.2 Quantum Wells vs Threshold

Kuznetsov et al[9] developed a simple model of an InGaAs/AlGaAs VECSEL, elements of which were highlighted in section 2.1.6, which allowed important design issues to be examined such as the effect of varying the number of quantum wells on threshold and output power.

The threshold carrier density N_{th} has a dependence on the number of quantum wells N_w of the form:

$$N_{th} \propto a^{1/N_w} \tag{4-3}$$

So the threshold carrier density is high for few quantum wells but decreases sharply for greater numbers of wells. The threshold pump power

$$P_{th} \propto N_{th} N_W (A + B N_{th} + C {N_{th}}^2) \tag{4-4}$$

(A, B and C are the non-radiative, radiative and Auger recombination coefficients) and consequently for few wells the pump power threshold is very high but as N_{th} becomes smaller and changes less with N_w, the N_w term dominates.

A Mathcad program based on Kuznetzov et al[9] was used to explore the model for our GaInP/AlGaInP VECSELs, which illustrates the effect of the number of quantum wells on output power for a fixed level of output coupling and pump power (Figure 4-3).

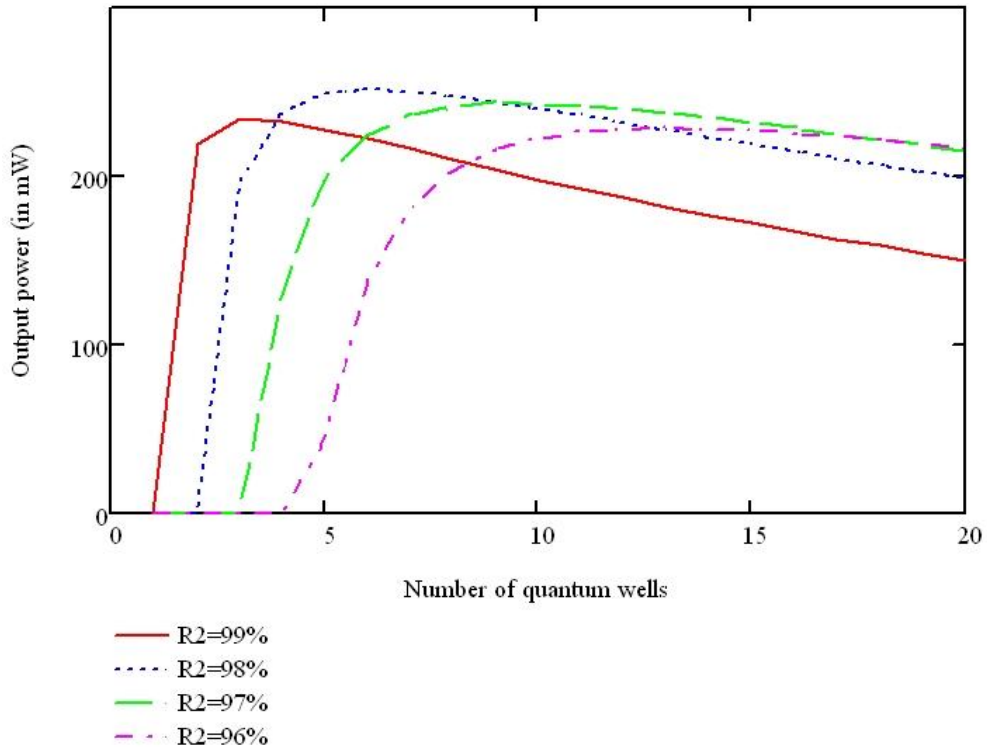

Figure 4-3: Mathcad plot of the output power v number of quantum wells for ~600mW pump power (445nm)

Based on this modelling, for ~600mW of absorbed pump power, >5 quantum wells are required for efficient operation, and therefore multiple quantum wells at each anti-node. Although the magnitude of the laser standing wave at quantum wells not centred at the anti-nodes is reduced, it was preferable to accept this small drawback rather than risk having too few quantum wells in the structure and we decided to employ 7 quantum wells, 4 at the first anti-node and 3 at the second. In order to maximise the intensity of the standing wave at the quantum wells the barriers between them were designed to be as thin as possible without coupling between the wells significantly reducing the energy levels.

A Mathcad program based on the work of Yuh[10], Kolbas[11] and Chuang-[12] was used to determine the emission wavelength of a pair of 7nm $Ga_{0.45}In_{0.55}P$ quantum wells in $(Al_{0.6}Ga_{0.4})_{0.51}In_{0.49}P$ barrier material with the barrier between the wells of variable thickness (Figure 4-4). It was assumed that if two quantum wells separated by a barrier of a given thickness were not significantly coupled then neither would three or more quantum wells separated by the same thickness barriers.

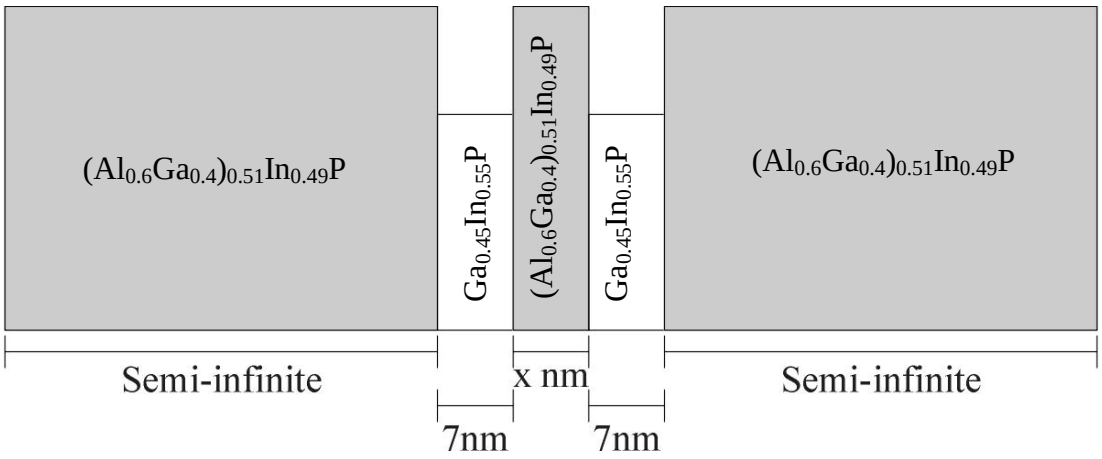

Figure 4-4: Well and barrier set-up in model

The model suggested that a barrier width of 6nm would be just sufficient to avoid affecting the emission wavelength of each well (Figure 4-5). However it was decided to use a barrier thickness of 7nm for structure design to allow a safety margin for thickness variation in growth.

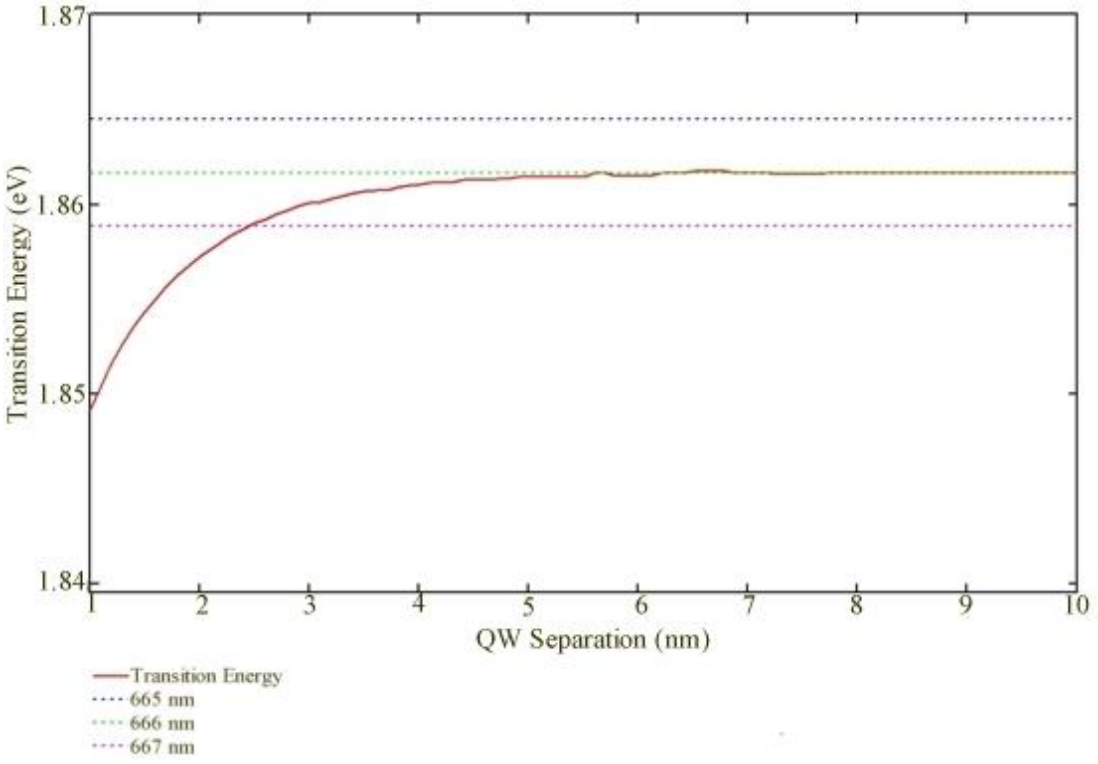

Figure 4-5: Graph of quantum well radiative transition energy vs barrier thickness

4.2 Pumping at 405nm

Four engineering sample Nichia laser diodes were used for optical pumping with a combined output power of 1.57W and peak wavelength of ~406nm at low power and ~408nm at full power.

Beam profiles were taken of two of the (fast-axis collimated) laser diode beams at a number of positions along the direction of beam propagation. The profiles were taken with a BeamMaster model BM-7 which uses seven individual knife-edges on a rotating drum to scan the beam through seven different axes in a single rotation. The beam widths in the tangential and sagittal planes were taken from the saved beam profiles.

The beam propagation ratio, or M^2 value, is a commonly used measure of the quality of a laser beam. An ideal Gaussian beam is diffraction-limited and has an M^2 of 1. Equation 4-8 describes the evolution of the beam radius as the beam propagates in the z-direction:

$$w = \sqrt{{w_0}^2 + \left((M^2)^2 \left(\frac{\lambda}{\pi w_0} \right) (z - z_0) \right)^2} \qquad (4\text{-}5)$$

where w is the beam radius (the radius at which the beam profile intensity drops to $1/e^2$), z the position along the direction of beam propagation, w_0 is the beam waist (the smallest beam radius), z_0 the position of the beam waist and λ is the wavelength. The M^2 value of the experimentally measured beam is calculated by fitting a curve of the above equation to the data points with M^2, w_0 and z_0 as fitting parameters for the least squares fit.

If the beam is circularly symmetric it can be described using one value of M^2, however beams from laser diodes are notably asymmetric and require separate M^2 value for the fast and slow axis.

Beam width measurements were made of two of the (fast-axis collimated) laser diode beams using a BeamMaster™ and the M^2 calculated as 1.86 x 8.24 (fast axis x slow axis) and 1.60 x 9.36 (fast axis x slow axis). It was assumed the beams from the other two laser diodes were similar to those measured.

4.2.1 Optical Pump Scheme

To solve the problem of focussing two pairs of beams to the same (circular) spot, two of the laser diodes were raised so that the four beams formed a rectangle, with the first two beams passing underneath the mirrors for the second two beams, as shown in Figure 4-6. The beams were spaced 2mm apart horizontally and 6mm vertically. We used two cylindrical lenses as a slow-axis beam expansion telescope to give more control over the shape of the pump spot by varying the position of the focal point of the slow axis and so the point at which the beam dimensions in the slow and fast axis were equal. As noted in section 2.1.1 VECSEL can be treated as a planar absorber, being relatively thin and having strong absorption, and so we could place it where the beam became circular giving good control over the pump spot size.

4.2.2 Structure

The 6 quantum well structure was designed to be resonant at the laser wavelength, with room temperature quantum well emission at 665nm with a DBR stopband centred at 670nm ± 3nm at room temperature and grown on a 2” GaAs wafer by MBE at the ORC, Tampere University of Technology. The composition of the structure is shown in Table 4-2

Material	Thickness (nm)	Purpose
$Ga_{0.52}In_{0.48}P$	10	Cap
AlAs	60	Confinement
$(Al_{0.6}Ga_{0.4})_{0.51}In_{0.49}P$	10	Barrier
$Ga_{0.46}In_{0.54}P$	6	QW
$(Al_{0.6}Ga_{0.4})_{0.51}In_{0.49}P$	7	Barrier
$Ga_{0.46}In_{0.54}P$	6	QW
$(Al_{0.6}Ga_{0.4})_{0.51}In_{0.49}P$	7	Barrier
$Ga_{0.46}In_{0.54}P$	6	QW
$(Al_{0.6}Ga_{0.4})_{0.51}In_{0.49}P$	10	Barrier
AlAs	50	Spacer
$(Al_{0.6}Ga_{0.4})_{0.51}In_{0.49}P$	10	Barrier
$Ga_{0.46}In_{0.54}P$	6	QW
$(Al_{0.6}Ga_{0.4})_{0.51}In_{0.49}P$	7	Barrier
$Ga_{0.46}In_{0.54}P$	6	QW
$(Al_{0.6}Ga_{0.4})_{0.51}In_{0.49}P$	7	Barrier
$Ga_{0.46}In_{0.54}P$	6	QW
$(Al_{0.6}Ga_{0.4})_{0.51}In_{0.49}P$	10	Barrier
AlAs	25	Spacer
$Al_{0.45}Ga_{0.55}As$	47	DBR (x40)
AlAs	54	DBR (x40)
GaAs (10° towards [111])	500	Buffer

Table 4-2: Design for 670nm VECSEL pumped at 405nm

4.2.3 Experiment

We combined the pump set-up from section 4.2.1 with a three mirror cavity to give the experimental set-up shown in Figure 4-6.

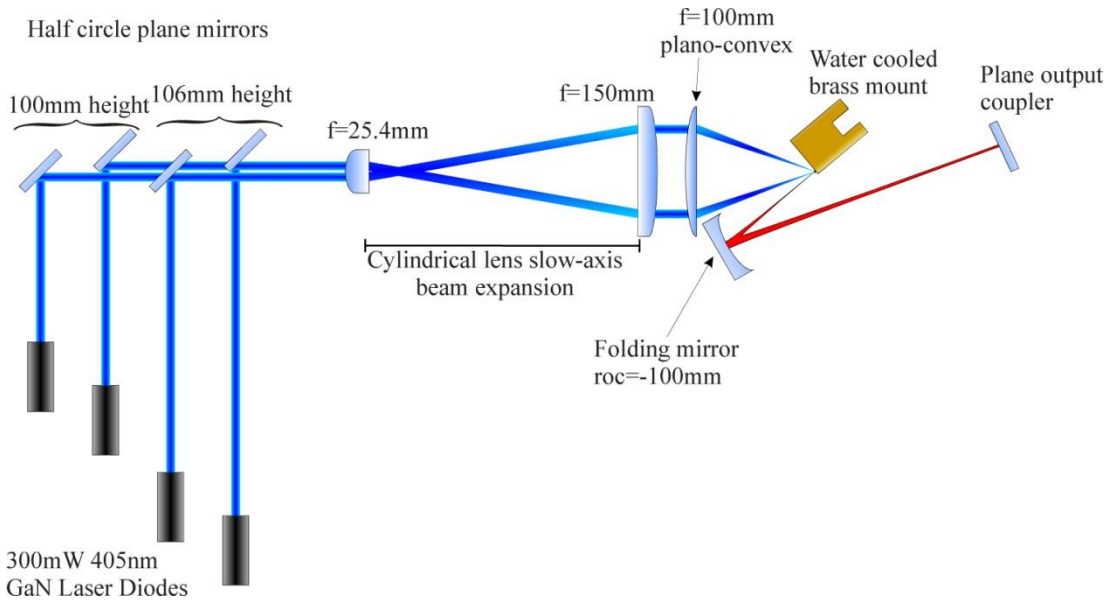

Figure 4-6: Schematic of 405nm pumping set-up

With this set-up and an f=100mm pump focussing lens we obtained a circular pump spot of ~51µm diameter. It should be noted that although the BeamMaster™ showed a combined circular pump spot, the individual pump beams could vary considerably and each beam had to be checked individually to ensure they were of roughly the same dimensions.

A diamond heatspreader, anti-reflection coated for 405nm, was bonded to a 4mm square sample by liquid capillary action[13] and the cavity set up with a folding mirror to sample length (short arm) of ~53mm, folding mirror to output coupler (long arm) of ~450mm and a designed mode diameter of ~51µm. We also tried an uncoated diamond heatspreader bonded to a 4mm square sample by liquid capillary action and similar cavity arm lengths.

In both cases the cavity arm lengths were adjusted to vary the mode size to match the pump spot on the sample to try to achieve laser action but without success. A monolithic design with a sample bonded using liquid capillary action to a diamond heatspreader coated for 0.5% transmission was also tried.

Initial characterisation had achieved very brief laser action using 1.5W of pump power at 457.9nm. It was calculated that ~68% of the pump light was absorbed in the active region. The structure performed poorly, lasing only briefly with a longer than designed pump wavelength. It may be that there were too few quantum wells, driving up the threshold beyond the power available at 405nm. The strong absorption of the 405nm pump wavelength would also have contributed to a high threshold by reducing the carrier generation near the quantum wells at the second anti-node.

Optically pumping the structure at a longer wavelength would increase the carrier generation in the vicinity of the second set of quantum wells, decreasing the pump power needed for them to reach transparency.

4.3 Pumping at 445nm

4.3.1 Laser Diode Characterisation

Two 500mW 445nm engineering sample Nichia laser diodes were characterised. Although the laser diodes were rated up to a forward current of 650mA our laser diode drivers were limited to 500mA. The laser diodes produced a combined power of 966mW once cooled to 10°C. An aspheric lens was inserted into each mount and adjusted to collimate the fast axis. At full power the peak wavelengths were 444 and 447 nm. Beam width measurements were made of one of the two laser diode beams using a BeamMaster™ and the M^2 calculated as 1.88 x 1.93 (Fast axis x Slow axis).

4.3.2 Seven Quantum Well Structure

The structure designed for pumping at 405nm experiment was modified in the following ways:

- An additional quantum well was placed the first anti-node of the active region, where the pump intensity absorbed is strongest, to try to minimise the threshold and increase maximum power.
- The AlAs spacer layers were removed to reduce the amount of aluminium in the structure and reduce its vulnerability to oxidisation damage.

- The pump-absorbing barrier of the active region was extended after the second set of quantum wells to reduce the amount of pump light absorbed by the DBR and so reduce the heat build-up.

The composition of the structure is shown in Table 4-3 and the cavity standing wave and pump absorption in Figure 4-7.

Layer	Material	Mole Fraction	Thickness (nm)	Purpose
12	$Ga_xIn_{1-x}P$	0.52	10	Cap
11	$(Al_xGa_{1-x})_{0.51}In_{0.49}P$	0.6	59	Barrier
10 x 4	$(Al_xGa_{1-x})_{0.51}In_{0.49}P$	0.6	7	Barrier
9 x 4	$Ga_xIn_{1-x}P$	0.45	7	QW
8	$(Al_xGa_{1-x})_{0.51}In_{0.49}P$	0.6	50	Barrier
7 x 3	$(Al_xGa_{1-x})_{0.51}In_{0.49}P$	0.6	7	Barrier
6 x 3	$Ga_xIn_{1-x}P$	0.45	7	QW
5	$(Al_xGa_{1-x})_{0.51}In_{0.49}P$	0.6	190	Barrier
4	AlAs		54	DBR
3 x 40	$Al_xGa_{1-x}As$	0.45	47	DBR
2 x 40	AlAs		54	DBR
1	GaAs [100]		500	Buffer

Table 4-3: 7 quantum well structure for pumping at 445nm

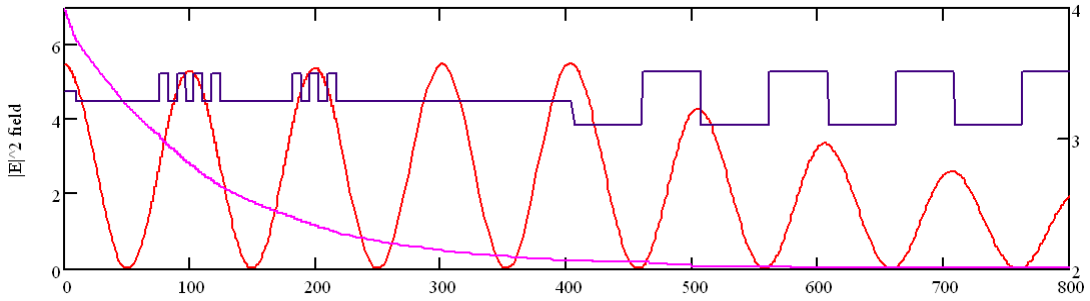

Figure 4-7: Refractive index, pump absorption and standing wave of 7 quantum well structure

The structure was designed for quantum well emission at 665nm with a DBR stopband centred at 670nm ± 3nm at room temperature and grown on a 2" GaAs wafer by MBE. Measurements from the grower indicated that the DBR stopband was centered at ~670nm with an absorption dip due to the cavity resonance at 663nm [Figure 4-8].

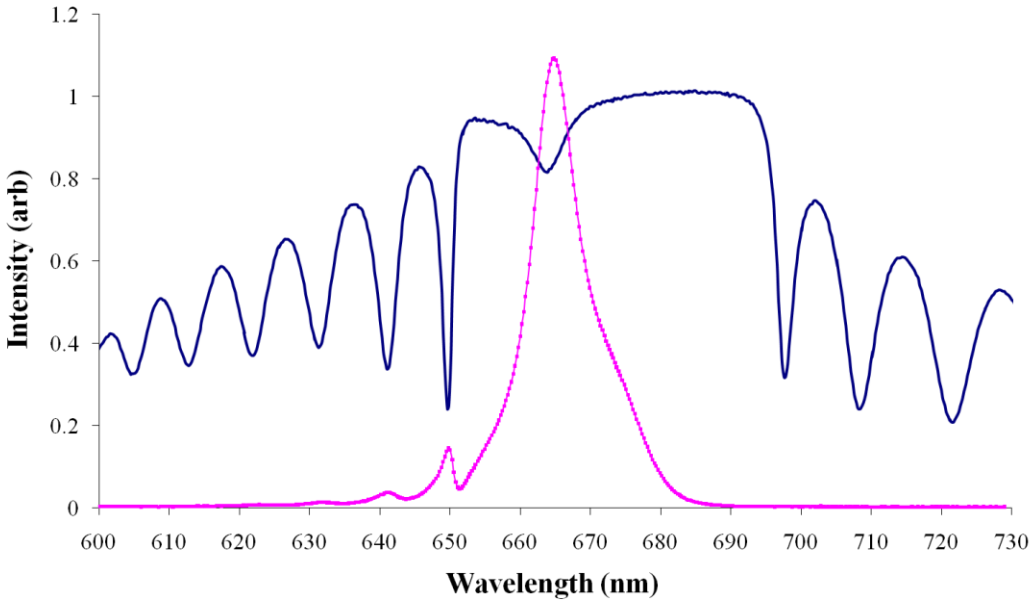

Figure 4-8: Reflectivity and Normal PL measurements

4.3.2.1 Experimental Set-Up

The Nichia laser diodes used a non-standard pin configuration which was not compatible with the Thorlabs laser diode mounts which had to be rewired, plus other modifications to make the mounts compatible with the Arroyo laser diode drivers. The mounts were further modified to increase heat dissipation from the rear by removing some of the cooling fins and replacing them with a water-cooled block. Spherical lenses were fitted to the front of each mount and adjusted to collimate the fast axis.

A 250µm thick uncoated diamond heatspreader was bonded to the sample using liquid capillary[13] action and it was placed in a water-cooled brass mount cooled to -5°C.

A low-order 440nm half waveplate was used to rotate the polarisation of the first laser diode output by 90° so that it would be reflected by the polarisation beamsplitter cube. The beams were polarisation coupled to ensure that we would effectively be dealing with a single pump beam after the polarisation beamsplitter cube. Beam steering mirrors were used to steer the original polarisation beam to

Diode Pumped Visible Vertical External Cavity Surface Emitting Lasers

ensure the beams would be co-incident after passing through the polarisation beamsplitter cube. A schematic of the experimental set-up is given in Figure 4-10.

A pair of cylindrical lenses (f=25.4 and 100mm) were used as a beam telescope to expand the slow-axis of the combined pump beam [Figure 4-9] and so move the focal point of the slow-axis. The beam was then focussed using an f=88.3mm plano-convex lens.

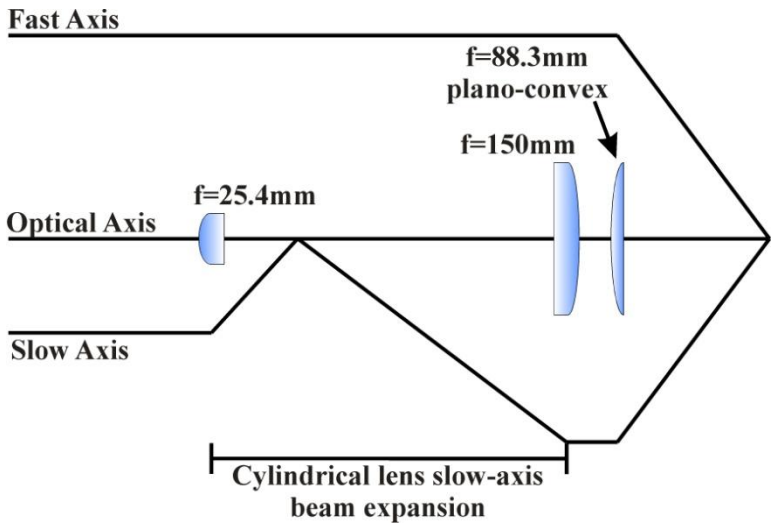

Figure 4-9: Slow and fast axis beam widths though pump optics

The distance between the cylindrical lenses was adjusted to achieve a circular pump spot of ~38μm diameter. The incident power absorbed by the sample was ~586mW. Although we had 1W of pump power available, the laser diode peak wavelength fell outside the acceptance band of the low-order λ/2 waveplate resulting in an elliptically polarised beam which reduced the power reflected by the 445nm polarisation beamsplitter cube and reduced the overall pump power available. Further loss was incurred due to pump reflection from the uncoated diamond heatspreader.

The sample formed the end mirror of a v-cavity with a folding mirror of radius of curvature 50mm and a plane end mirror as an output coupler [Figure 4-10].

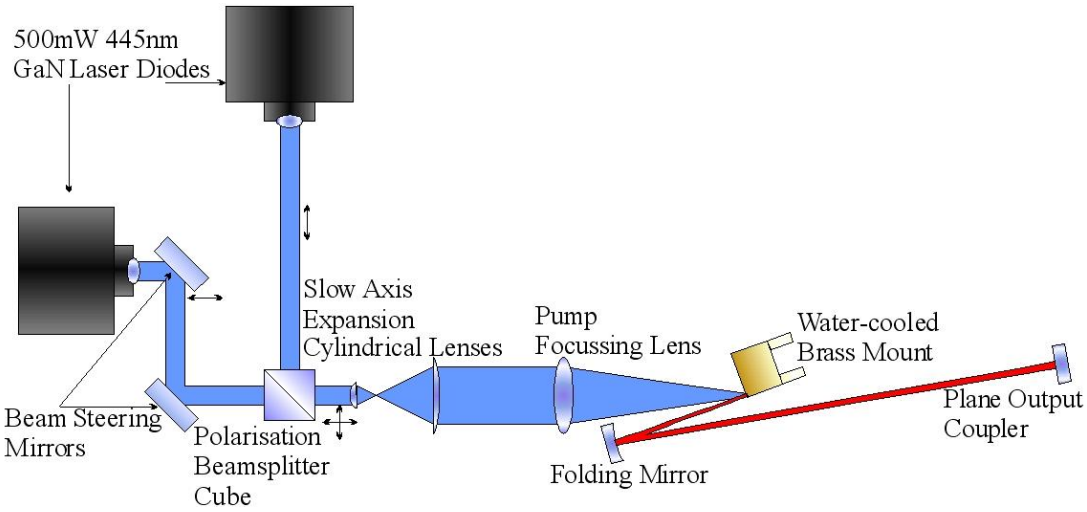

Figure 4-10:Schematic of experimental set-up for 445nm pumping

4.3.2.2 Results

In the set-up shown in Figure 4-10 the sample position to folding mirror and folding mirror to output coupler distances were adjusted to optimise the output power and achieve stable single transverse mode output. The power transfer curve using a 2% output coupling plane end mirror in Figure 4-11 shows a threshold of ~260mw and a slope efficiency of 3.8%. The maximum output power was 12mW, limited by available pump power. Although higher output power was obtained, it was fleeting and could not be sustained for long enough to take a power transfer curve or be reliably reproduced. Performance varied significantly across the sample.

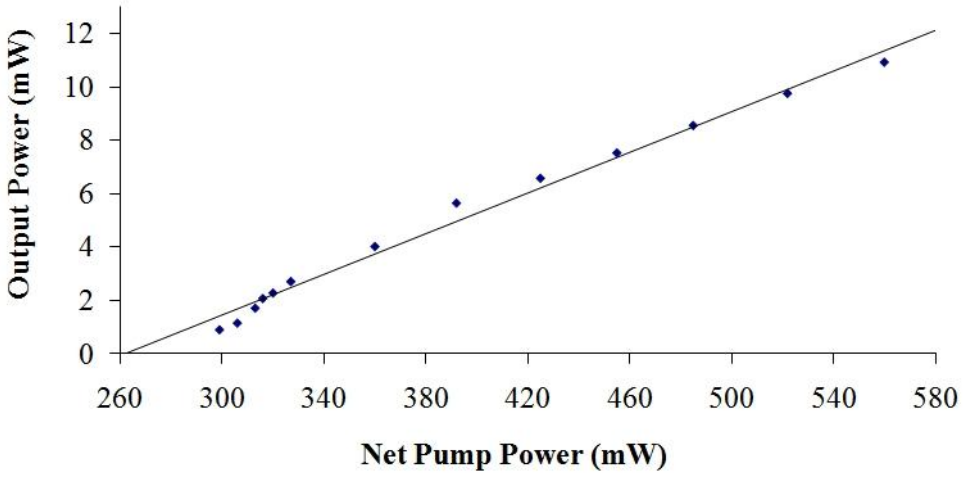

Figure 4-11: Power transfer curve of the 7 quantum well sample pumped at 445nm

The free running spectrum of the laser operating at maximum power is shown in Figure 4-12 taken using an optical spectrum analyser (OSA) with a spectral resolution of 0.8nm. The output peak wavelength is ~673nm with a FWHM of ~1nm. A tuning curve was taken using a 2mm birefringent filter inserted into the laser cavity at Brewster's angle[14-16] between the folding mirror and high reflectance output coupler. A tuning range of 11nm was obtained, which was broader than expected for a resonant cavity with only 7 quantum wells and less than a watt of pump power.

Tuning the output away from the designed wavelength offsets the peaks of the standing wave inside the sub-cavity from the desired position (centred on the quantum wells) which reduces gain. With multiple quantum wells grouped at the first two anti-nodes the effect is minimised. Although the short active region of the structure reduces the maximum number of quantum wells which can be included, it contributes to the width of the tuning range[17]. This will be discussed further in section 4.3.3 on the strain-compensated structure.

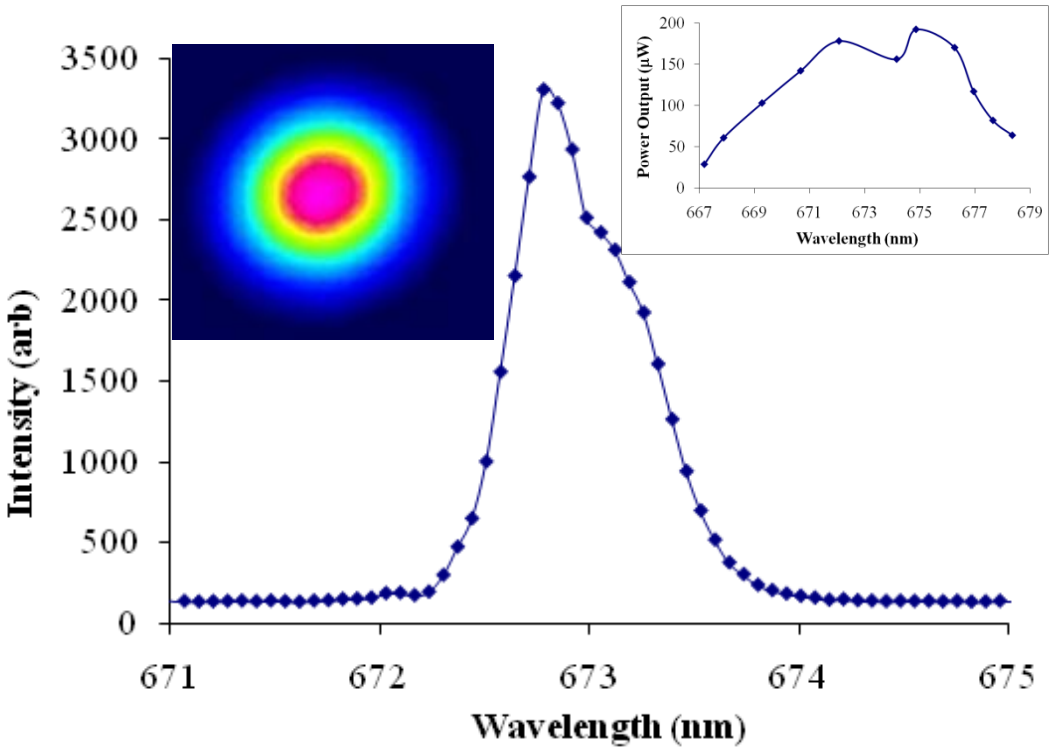

Figure 4-12: Free running spectrum of K2138 pumped at 445nm, with inset mode profile and tuning curve.

An f=88.3mm biconvex lens was placed after the output coupler and a series of beam profiles taken with a BeamMaster^{TM}. An M^2 of <1.2 was calculated in both axes indicating single transverse mode output.

It was observed that the output power of the laser decayed over time, dropping quickly initially and then more steadily. Lasing would not resume at that spot on the sample indicating permanent damage. Typical elapsed time between commencing and ceasing laser action was around 40 minutes although there was considerable variability across the sample. This degradation is not unique to VECSELs and has also been seen in red-emitting AlGaInP laser diode bars[20,21]

Degradation of the diode-pumped structure will be discussed in Chapter 5.

4.3.2.3 Pumped with argon ion laser

The results obtained with the 445nm laser diodes were limited by the available pump power of 1W. We used argon ion laser which could supply 2.42W at 457.9nm to investigate if more output power could be obtained. The longer pump wavelength would be less strongly absorbed, with an absorption length of 418nm against 367nm for 445nm and ~4.4% absorbed in the DBR compared to~ 2.8% but it was hoped that the additional power might be enough to overcome these negative aspects. A sample was liquid-capillary bonded to a diamond heatspreader anti reflection coated for 405nm. The sample was placed in a water cooled brass block in a standard v-cavity with short arm~54mm, long arm~340mm, and roc=100mm folding mirror with a mode size at the VECSEL surface of ~30μm radius. The pump beam was focussed onto the sample with an f=200mm plano-convex lens.

Single transverse mode output of over 1mW, which is comparable to that obtained with the 445nm pump, was obtained through an HR end mirror using 2W pump power, however the output power decayed quickly with similar behaviour to pumping at 445nm.

4.3.3 Strain Compensated Seven Quantum Well Structure

To address the possibility that strain was driving the previous structure's permanent degradation when optically pumped it was decided to design another structure utilising strain compensation layers next to the quantum wells. The pump-absorbing barrier after the second set of quantum wells was also lengthened to further decrease pump absorption in the DBR. The composition of the structure is shown Table 4-4.

Layer	Material	Mole Fraction	Thickness (nm)	Purpose
18	$Ga_xIn_{1-x}P$	0.52	10	Cap
17	$(Al_xGa_{1-x})_{0.51}In_{0.49}P$	0.60	63	Barrier
16	$(Al_xGa_{1-x})_{0.6}In_{0.4}P$	0.60	3.5	Barrier (Strain Comp)
15	$Ga_xIn_{1-x}P$	0.45	7	QW
14 x 3	$(Al_xGa_{1-x})_{0.6}In_{0.4}P$	0.60	7	Barrier (Strain Comp)
13 x 3	$Ga_xIn_{1-x}P$	0.45	7	QW
12	$(Al_xGa_{1-x})_{0.6}In_{0.4}P$	0.60	3.5	Barrier (Strain Comp)
11	$(Al_xGa_{1-x})_{0.51}In_{0.49}P$	0.60	51	Barrier
10	$(Al_xGa_{1-x})_{0.6}In_{0.4}P$	0.60	3.5	Barrier (Strain Comp)
9	$Ga_xIn_{1-x}P$	0.45	7	QW
8 x 2	$(Al_xGa_{1-x})_{0.6}In_{0.4}P$	0.60	7	Barrier (Strain Comp)
7 x 2	$Ga_xIn_{1-x}P$	0.45	7	QW
6	$(Al_xGa_{1-x})_{0.6}In_{0.4}P$	0.60	3.5	Barrier (Strain Comp)
5	$(Al_xGa_{1-x})_{0.51}In_{0.49}P$	0.60	191	Barrier
4	AlAs		54	DBR
3 x 40	$Al_xGa_{1-x}As$	0.45	47	DBR
2 x 40	AlAs		54	DBR
1	GaAs [100]		500	Buffer

Table 4-4: Strain compensated 7 QW structure

The structure was designed for quantum well emission at 665nm with a DBR stopband centred at 670nm ± 3nm at room temperature. The cavity resonance was specified as 674nm as previous structures had shorter wavelength resonance than ideal. It was grown on a 2" GaAs wafer by MBE.

4.3.3.1 Experimental Set-Up

A 4mm square sample was bonded to a 250μm thick uncoated square diamond by liquid capillary action[13]. The experimental set-up was very similar to that used for the non strain-compensated structure (shown in Figure 4-10) with the position of the second cylindrical lens and pump focussing lens adjusted to give a 32μm diameter pump spot.

4.3.3.2 Results

The folding mirror-sample and folding mirror-output coupler distances were adjusted to optimise the output power and achieve stable single transverse mode output. The power transfer curve using a 3% output coupling plane end mirror in Figure 4-13 shows a threshold of ~341mw and a slope efficiency of 6.4%, almost double that achieved with the previous structure. The maximum output power was 17mW, limited by available pump power. Although output power of up to 30mW was obtained, it was fleeting and could not be sustained for long enough to take a power transfer curve or reliably reproduced.

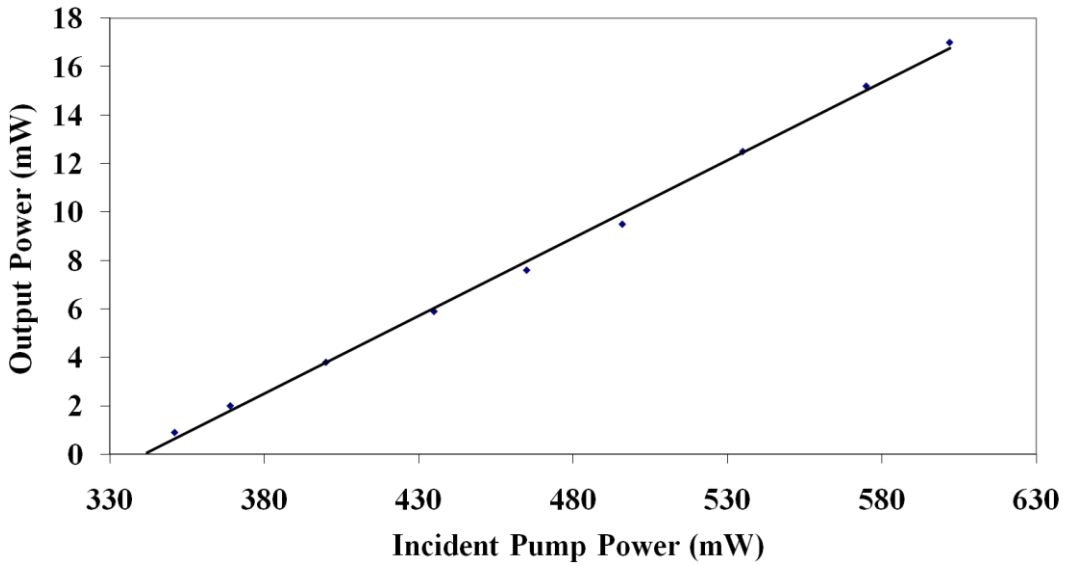

Figure 4-13: Power transfer curve for strain compensated 7QW VECSEL

The free running spectrum of the laser operating at maximum power is shown in Figure 4-14, taken using the OSA. The output peak wavelength is 670nm with a FWHM of ~3nm. A tuning curve was taken using a 1mm birefringent filter inserted into the laser cavity at Brewster's angle between the folding mirror and high reflectance output coupler. A thinner BRF than that used for the previous structure was necessary as the tuning range of the laser output exceeded the free spectral range of the 2mm BRF. A tuning range of 16nm was obtained. This compares well with the tuning range obtained in the 532nm pumped 20 quantum well VECSEL[3,18] which was pumped many more times above threshold.

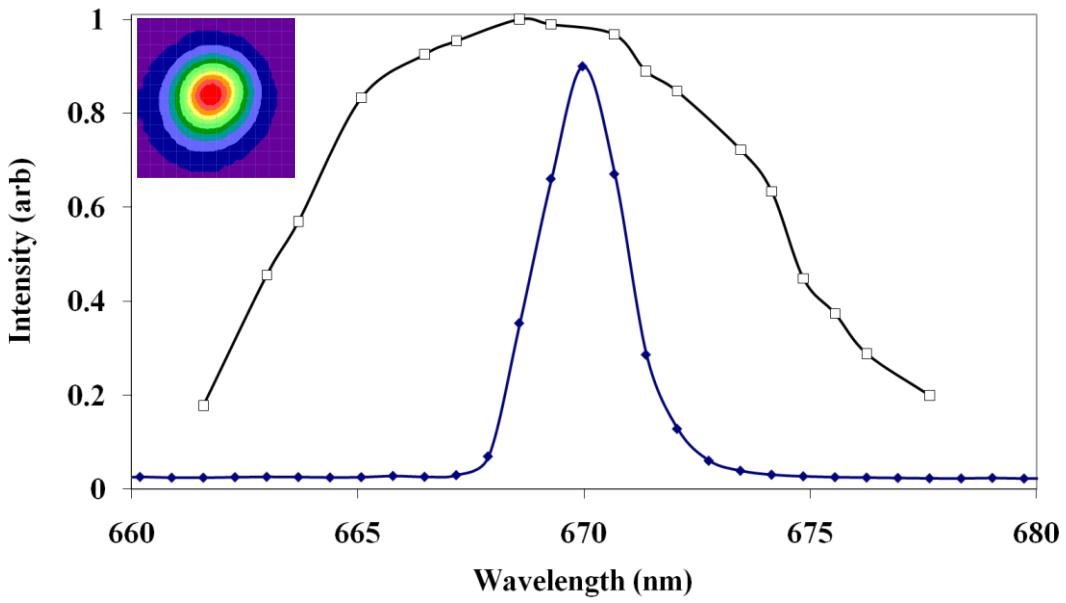

Figure 4-14: Free running spectrum for the strain compensated 7QW sample with inset mode profile.

An f=25.4mm plano-convex lens was placed after the output coupler and a series of beam profiles taken with a BeamMaster™. An M^2 of ~1.1 was calculated for both axes indicating single transverse mode output.

The output power of the laser decayed over time, again dropping quickly initially and then more steadily. Lasing would not resume at that spot on the sample indicating the damage was permanent. However typical elapsed time between commencing and

ceasing laser action had increased from 40 minutes for the previous structure to around 100 minutes.

The output power through a high reflector output coupler was measured over time for several spots on the sample. Power decay readings were also taken where the pump was interrupted and again output power resumed at the level it was when interrupted, ruling out heat build-up as the cause. This will be discussed in more detail in chapter 5.

The relatively broad tuning range can be explained using a model of the standing wave in the VECSEL[5-8] to track the magnitude of the $|E|^2$ field at the centre of each well. To summarise the differences in the structures:

20QW structure

- 670nm emission design
- Resonant cavity
- Active region of 1.161µm
- Two 6nm quantum wells at each of the first ten standing wave anti-nodes.

7QW structure

- 670nm emission design
- Resonant cavity
- Active region of 413nm
- Four 7nm quantum wells grouped at the first anti-node of the standing wave and three at the second. 7nm barriers between the quantum wells within each group.

The structures differed only in their active regions and were both modelled as having a diamond heatspreader and identical DBR.

The cavity standing wave was calculated for a range of wavelengths from 620nm to 720nm in steps of 1nm and the magnitude of the $|E|^2$ field at the centre of each well used to obtain an average of the magnitude of the $|E|^2$ field across the quantum wells. Because the wells are thin compared to the half-wavelength of the standing wave the

Diode Pumped Visible Vertical External Cavity Surface Emitting Lasers

change in $|E|^2$ is small across a given well and the value at the centre point is virtually the same as the average taken over the whole width of the quantum well. The $|E|^2$ average of the diode-pumped seven quantum well structure closely resembles the wavelength dependence of the $|E|^2$ in the wells calculated in Garnache et al[17] for a VECSEL working at the subcavity resonant wavelength. However, the $|E|^2$ average of the twenty quantum well structure shows its overall $|E|^2$ profile is more typical of an anti-resonant structure being broader and lower magnitude as the comparison in Figure 4-15 shows.

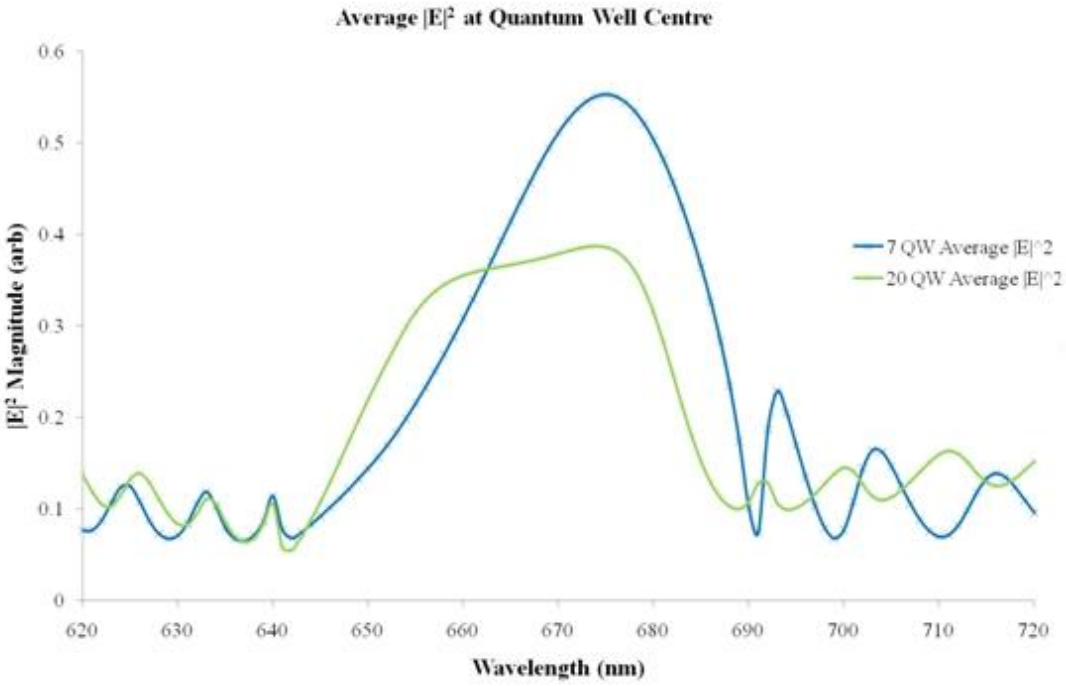

Figure 4-15 Comparison of $|E|^2$ at Quantum Wells.

Breaking the $|E|^2$ profile down to the level of individual wells for the diode-pumped design (Figure 4-16) and 532nm pumped structure (Figure 4-17) shows that the broader profile of the 20 quantum well is the sum of two sets of peaks with the $|E|^2$ field aligning symmetrically across each pair of quantum wells at ~667nm.

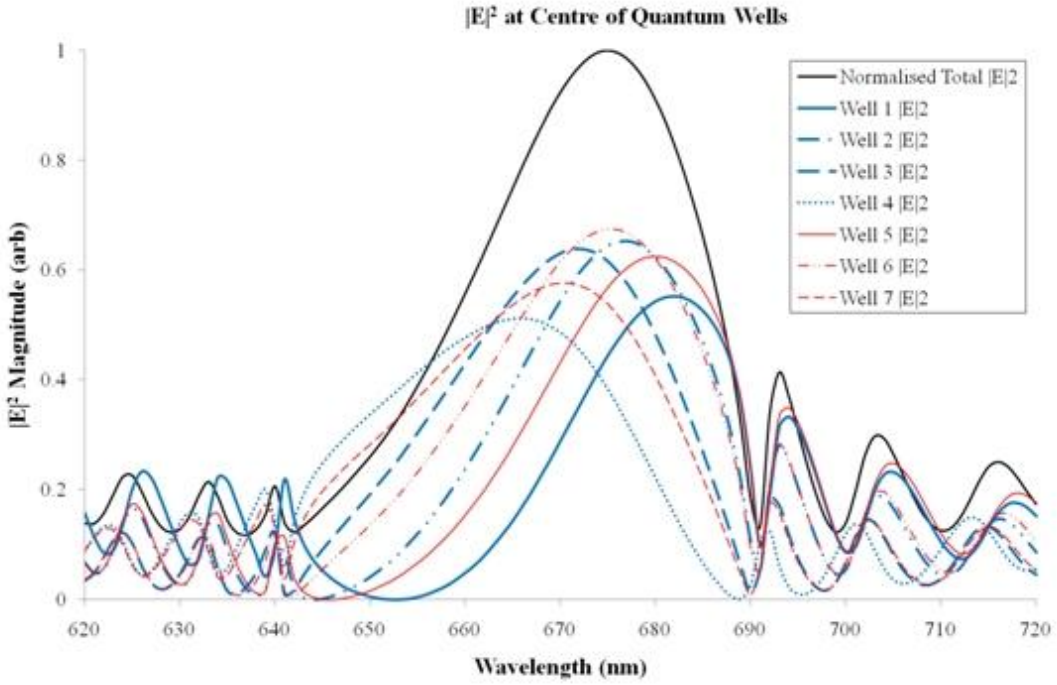

Figure 4-16: $|E|^2$ at centre of each well in 7QW diode-pumped strain compensated VECSEL

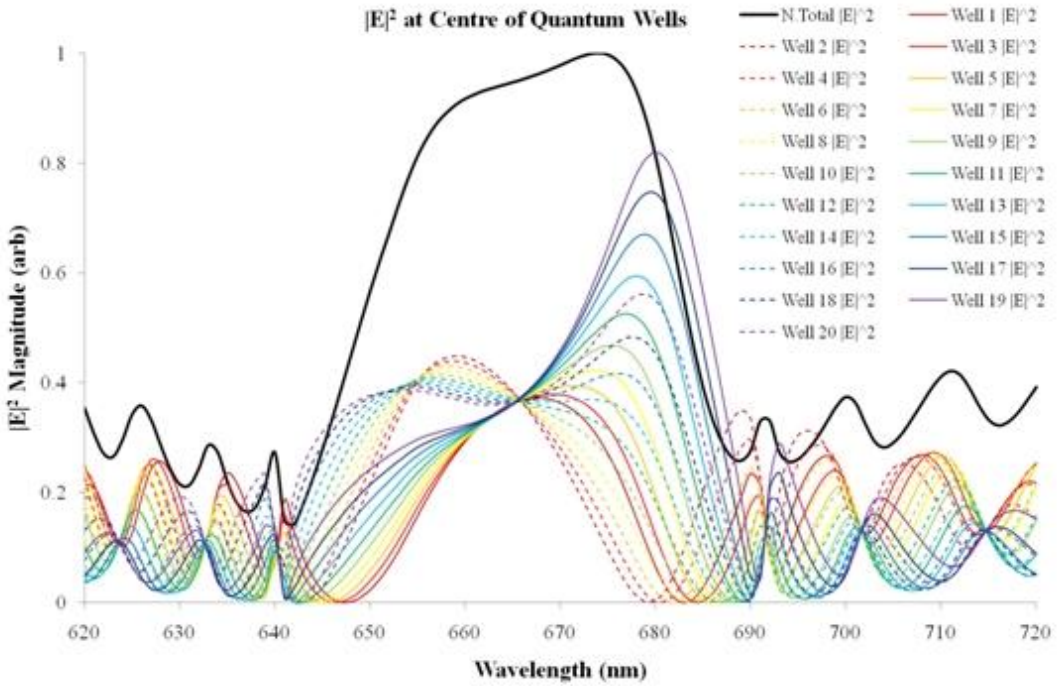

Figure 4-17: $|E|^2$ at centre of each well in 20QW 532nm pumped VECSEL

The broad $|E|^2$ profile of the twenty quantum well anti-resonant cavity showed a broad tuning range due to the stable magnitude of $|E|^2$ at the quantum wells as the emission wavelength changed. Although the resonant nature of the seven quantum well cavity would be expected to greatly increase the dependence of the magnitude of $|E|^2$ at the quantum wells on emission wavelength this was compensated by the much shorter gain region causing a much smaller shift in the position of the anti-nodes $|E|^2$.

4.3.3.3 Pumped with Sabre

As with the non strain compensated structure we tried pumping the structure at 457.9nm with the argon ion laser. The sample was liquid-capillary bonded to a diamond heatspreader anti reflection coated for 405nm. The sample was placed in a water cooled brass block in a standard v-cavity with short arm~54mm long arm~340mm and roc=100mm folding mirror with a mode size of ~30µm radius. The pump beam was focussed onto the sample with an f=200mm plano-convex lens.

Single transverse mode output of 1.4mW was obtained through the HR end mirror using 2W pump power. Output power of upto 37mW with a 1% output coupler was achieved for a gross pump power of 2.42W, with a threshold of 1.26W.An output power decay run was completed with the 1% output coupler and 2W of pump power [Figure 4-18].

This is similar to degradation at the designed pump wavelength, which will be examined in chapter 5.

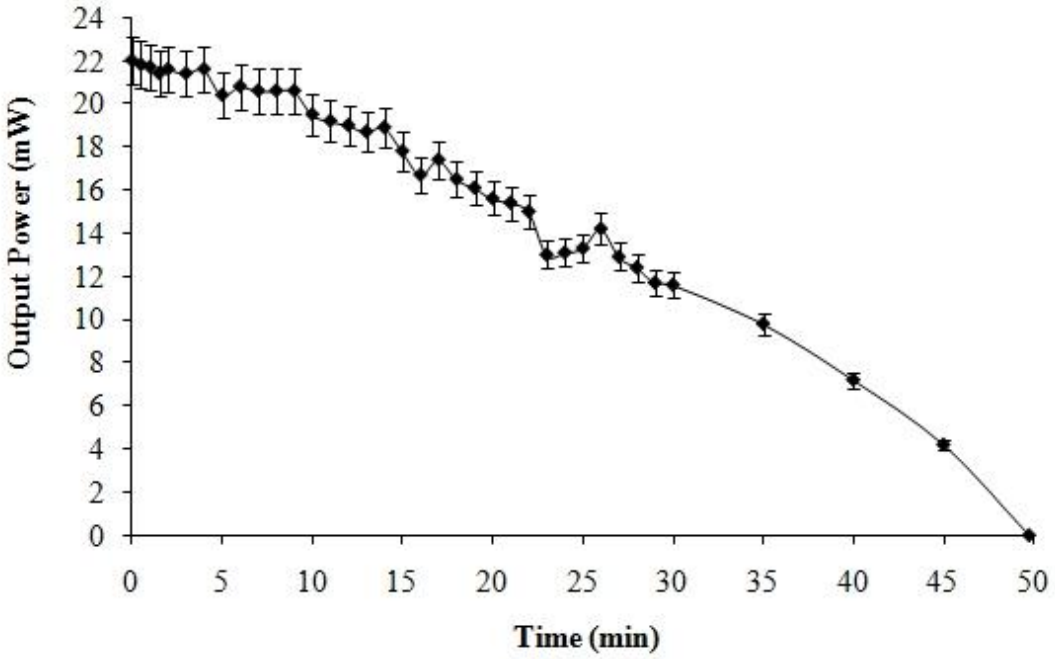

Figure 4-18: Power decay run with 2W 457.9nm and 1%OC for strain-comp structure

4.3.4 Comparison of strain-compensated and non-strain compensated structures.

The strain compensated structure exhibited a longer lifetime, 100 minutes against 40minutes, and was more efficient with a greater slope efficiency (6.4% v 3.8%) and higher optimum output coupling (3% v 2%), as well as a greater tuning range (16nm v 11nm).

To summarise, there were three main differences in the design of the strain-compensated and non strain-compensated samples used in the experiments:

a) Longer active region to reduce pump absorption in the DBR.
b) The strain compensated sample had undergone rapid thermal annealing (RTA) at 800°C for 1 second but the non strain-compensated structure had not.
c) Strain compensation layers interleaved with the quantum wells to balance out the strain of the compressively strained wells.

These differences will be examined in order in the next sections.

4.3.4.1 Lengthened Active Region

Whilst reducing the amount of pump light absorbed in the DBR will provide some benefit, as the pump energy absorbed in the DBR does not generate usable carriers, is wasted as heat and noticeably affects device temperature, it seems unlikely that the small difference in active region length between the structures would be sufficient to make such a difference to device performance.

4.3.4.2 Rapid Thermal Annealing

Fluorescence over time measurements were made for the non-RTA and RTA strain-compensated structures.

A sample of each of the structures was attached to a peltier element with silver heat conducting paint. The peltier element was attached to a water-cooled brass mount with silver heat conducting paint. This arrangement enabled the sample being pumped to be changed by translating the mount and without altering the experimental set-up. The peltier element was maintained at 10°C ± 0.5°C. The fluorescence was collected by an f=49mm 2" plano-convex lens, pump light filtered out with a 530nm long-pass filter before being focussed by an f=25.4mm plano-convex lens onto the power meter detector head.

Two fluorescence time-decay measurement runs were made for each sample plus one where the pump beam was interrupted several times for 5-10 minutes to establish there was no thermal effect. Readings were taken every ten seconds.

All the PL time-decay measurement runs [Figure 4-19] show an initial increase in PL intensity before remaining roughly constant. The PL decay runs are very similar, the PL levels from the RTA sample reached the maximum faster but this could be due to sample variance and both the RTA and non-RTA samples show an initial increase in PL. The step increase in the second RTA's sample near the three hour mark is similar to the step changes in PL observed in Vogelgesang et al[19] where the quantum well PL

intensity abruptly changes and site specific, possibly caused by sample inhomogeneities, rather than general behaviour.

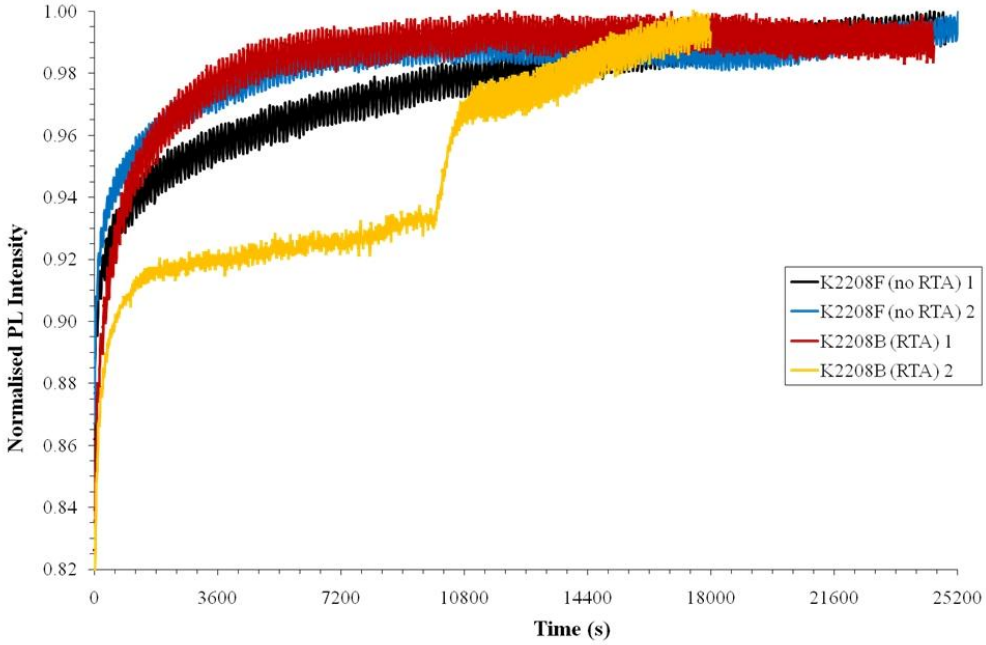

Figure 4-19: Normal photoluminescence over time: RTA and non-RTA sample comparison

4.3.4.3 Strain Compensation

The 7nm $Ga_{0.45}In_{0.55}P$ quantum wells are 0.49% compressively strained in both structures. In the strain-compensated structure this is roughly balanced by the same level of tensile strain in the strain compensation layers. Strain has been identified as a contributing factor to semiconductor laser degradation[20-26] and decreasing the strain in a device is an area in which improvements in device lifetime can be achieved. With the other changes in the structure eliminated as possible causes for the improvement in performance it seems likely that the reduction in strain due to the compensation layers is responsible. This will be explored in the next chapter.

4.4 Conclusion

We have demonstrated the first diode-pumped visible wavelength VECSEL. Output power of 17mW and a 16nm tuning range were achieved. Output power was limited by available pump power, with no evidence of thermal rollover, suggesting that

output power could be improved using power scaling as advances in blue laser diode technology produce more powerful sources.

Permanent degradation of the diode-pumped AlGaInP VECSEL material is a cause of some concern and needs to be addressed if the technology is to be taken further.

References

1 A. Smith, J. E. Hastie, H. D. Foreman, T. Leinonen, M. Guina, and M. D. Dawson, "GaN diode-pumping of red semiconductor disk laser," Electronics Letters **44** (20), 1195-1196 (2008).

2 A. Smith, J. E. Hastie, A.J. Kemp, H. D. Foreman, M. D. Dawson, Tomi Leinonen, and M. Guina, "GaN diode-pumping of a red semiconductor disk laser", *21st Annual Meeting of the IEEE Lasers and Electro-Optics Society*, 404-405 (2008).

3 J. E. Hastie, S. Calvez, M. D. Dawson, T. Leinonen, A. Laakso, J. Lyytikainen, and M. Pessa, "High power CW red VECSEL with linearly polarized TEM_{00} output beam," Opt. Express **13** (1), 77-81 (2005).

4 Jennifer Hastie, Lynne Morton, Stephane Calvez, Martin Dawson, Tomi Leinonen, Markus Pessa, Graham Gibson, and Miles Padgett, "Red microchip VECSEL array," Opt. Express **13** (18), 7209-7214 (2005).

5 M. Schubert, J. A. Woollam, G. Leibiger, B. Rheinlander, I. Pietzonka, T. Sass, and V. Gottschalch, "Isotropic dielectric functions of highly disordered $Al_xGa_{1-x}InP$ ($0 <= x <= 1$) lattice matched to GaAs," Journal of Applied Physics **86** (4), 2025-2033 (1999).

6 S. Adachi, "GaAs, AlAs, And $Al_xGa_{1-x}As$ - Material Parameters For Use In Research And Device Applications," Journal Of Applied Physics **58** (3), R1-R29 (1985).

7 A. B. Djurisic, A. D. Rakic, P. C. K. Kwok, E. H. Li, M. L. Majewski, and J. M. Elazar, "Modeling the optical constants of $Al_xGa_{1-x}As$ alloys," Journal Of Applied Physics **86** (1), 445 (1999).

8 M Born and E Wolf, *Principles of optics*. (Pergamon press, 1985).

9 M. Kuznetsov, F. Hakimi, R. Sprague, and A. Mooradian, "Design and characteristics of high-power (> 0.5-W CW) diode-pumped vertical-external-cavity surface-emitting semiconductor lasers with circular TEM_{00} beams," IEEE J. Sel. Top. Quantum Electron. **5** (3), 561 (1999).

10 P. F. Yuh and K. L. Wang, "Formalism of the Kronig-Penney Model for Superlattices of Variable Basis," Physical Review B **38** (18), 13307-13315 (1988).

11 R. M. Kolbas, N. G. Anderson, W. D. Laidig, Y. Sin, Y. C. Lo, K. Y. Hsieh, and Y. J. Yang, "Strained-layer InGaAs-GaAs-AlGaAs photopumped and current injection lasers," Quantum Electronics, IEEE Journal of **24** (8), 1605-1613 (1988).

12 Shun Lien Chuang, *Basic Quantum Mechanics*. (John Wiley & Sons Inc, 1995).

13 Z. L. Liau, "Semiconductor wafer bonding via liquid capillarity," Applied Physics Letters **77** (5), 651-653 (2000).

14 M. A. Holm, D. Ferguson, and M. D. Dawson, "Actively stabilized single-frequency vertical-external-cavity AlGaAs laser," IEEE Photonics Technol. Lett. **11** (12), 1551-1553 (1999).

15 K. Gardner, R. Abram, and E. Riis, "A birefringent etalon as single-mode selector in a laser cavity," Opt. Express **12** (11), 2365-2370 (2004).

16 Fan Li, Fallahi Mahmoud, T. Murray James, Bedford Robert, Kaneda Yushi, R. Zakharian Aramis, Hader Jorg, V. Moloney Jerome, Stolz Wolfgang, and W. Koch Stephan, "Tunable high-power high-brightness linearly polarized vertical-external-cavity surface-emitting lasers," Applied Physics Letters **88** (2), 021105 (2006).

17 A. Garnache, A. A. Kachanov, F. Stoeckel, and R. Houdré, "Diode-pumped broadband vertical-external-cavity surface-emitting semiconductor laser applied to high-sensitivity intracavity absorption spectroscopy," J. Opt. Soc. Am. B **17** (9), 1589-1598 (2000).

18 J. E. Hastie, L. G. Morton, A. J. Kemp, M. D. Dawson, A. B. Krysa, and J. S. Roberts, "Tunable ultraviolet output from an intracavity frequency-doubled red vertical-external-cavity surface-emitting laser," Applied Physics Letters **89** (6), 061114 (2006).

19 R. Vogelgesang, J. J. Liang, V. Wagner, H. J. Lugauer, J. Geurts, A. Waag, and G. Landwehr, "Wavelength-dependent optical degradation of green II--VI laser diodes," Applied Physics Letters **75** (10), 1351-1353 (1999).

20 S. K. Choi, M. Mihara, and T. Ninomiya, "Dislocation Velocities in GaAs," Jpn. J. Appl. Phys **16** (5), 737 (1977).

21 S. K. Choi, M. Mihara, and T. Ninomiya, "Dislocation Velocities in InAs and GaSb," Jpn. J. Appl. Phys **17** (2), 329 (1977).

22 Kishino Seigo, Chinone Naoki, Nakashima Hisao, and Ito Ryoichi, "Dark-line defects induced by mechanical bending in GaAs-$Ga_{1-x}Al_xAs$ double-heterostructure wafers," Applied Physics Letters **29** (8), 488-490 (1976).

23 Mathias Ziegler, Tran Quoc Tien, Sandy Schwirzke-Schaaf, Jens W. Tomm, Bernd Sumpf, Gotz Erbert, Myriam Oudart, and Julien Nagle, "Gradual degradation of red-emitting high-power diode laser bars," Applied Physics Letters **90** (17), 171113 (2007).

24 A. Tukiainen, J. Dekker, T. Leinonen, and M. Pessa, "Characterization of deep levels in rapid-thermal-annealed AlGaInP," Materials Science and Engineering B **91-92**, 389-392 (2002).

25 V. Celli, M. Kabler, T. Ninomiya, and R. Thomson, "Theory of Dislocation Mobility in Semiconductors," Physical Review **131** (1), 58 (1963).

26 Lisa Sugiura, "Comparison of degradation caused by dislocation motion in compound semiconductor light-emitting devices," Applied Physics Letters **70** (10), 1317-1319 (1997).

Chapter 5

Recombination Enhanced Defect Reactions

As we saw in the previous chapter, the diode-pumped red VECSEL structure suffers from a rapid decline in output power and permanent structural damage. In this section we will look at how and why this might occur and what, if anything, can be done about it.

Recombination enhanced defect reactions have been linked to degradation in both III-V[1,2] and II-VI[3] optoelectronic devices such as laser diodes and LEDs.

Semiconductor devices such as VECSELs and laser diodes are composed of a number of different layers of different composition and lattice constant which causes strain in the device, and particularly shear strain at the interfaces between different layers, which is accommodated elastically[4] by defects or, for large strain, microcracks. Additionally, defects are created in the growth process through the introduction of impurities, imperfect growth or strain introduced by differing thermal expansion constants. Kumar and Sastry[5] calculated the fractional increase in length per Kelvin of temperature change (linear thermal coefficient), of $\alpha_L=3.81\text{x}10^{-6}$ K^{-1} for AlAs, $\alpha_L=5.316$ $\text{x}10^{-6}$ K^{-1} for GaAs at 300K, which, for a growth temperature of 730°C, would give a relative change of length (lattice constant) of ~0.065%. The linear thermal coefficient does change with temperature but not dramatically, for instance Kaye & Laby[6] give for GaAs $\alpha_L=5.7$ $\text{x}10^{-6}$ K^{-1} at 293K and $\alpha_L=7.1$ $\text{x}10^{-6}$ K^{-1} at 800K.

Defect movement, formation or growth requires an input of energy, known as the activation energy. This energy is affected by a number of factors, such as strain or temperature, which can serve to enhance defect reactions. Defect movement is a process of bond breaking and reforming so energy stored in the lattice in the form of strain can reduce the activation energy or even provide sufficient energy to cause

movement.[7,8] Higher bandgap materials demonstrate greater resistance to dislocation motion as the bandgap increases with the bond strength and the higher bond strength reduces dislocation mobility[8,9].

Stress has been induced in samples by mechanical bending to cause dark line defects[10] (a high density dislocation network) as well as to study the relationship between strain and defect movement velocity. Experiments by Choi et al[7,8] on GaAs, InAs and GaSb demonstrated that increasing levels of shear stress caused increased defect velocity for two simple types of defects. Even very small levels of stress ~0.05% caused by packaging strain[11] have been linked to reduced device lifetime in laser diodes by acting as the source for gradual degradation of the active region.

Thermal energy is often used productively in annealing[12] to encourage existing defects to diffuse and annihilate with other defects, such as an interstitial atom diffusing into a suitable vacancy in the lattice. However, it can also have a negative effect in causing defects to move during device operation. The impact of stress and temperature on defect motion can be seen in Eqn 5-1 for the dislocation velocity of semiconductors[13,14]

$$v_d = \left(\frac{\tau}{\tau_0}\right) v_0 e^{\left(-\frac{E_d}{kT}\right)} \tag{5-1}$$

where v_d is the dislocation velocity, τ is the applied shear stress, E_d the activation energy of motion, T the temperature, v_0 and τ_0 pre-exponential factors which depend on the material.

Non-radiative recombination enhances the motion of dislocations by supplying energy to the lattice through phonon emission. Comparison of the dislocation velocity in InP[15], GaP[16] and GaAs[17] in the dark and under electron beam irradiation and laser light illumination over a range of applied strain demonstrates a clear increase in the dislocation velocity of Eqn 5-1 below a material dependant temperature T due to a reduction in the activation energy of the dislocation.

Additionally, more intense irradiation was shown to increase the dislocation velocity[17].

In order to try to understand the output power decay seen in the previous chapter we ran extended laser and spontaneous emission measurements.

5.1 Laser Emission Decay

Under the experimental conditions detailed in Chapter 4, laser performance showed a sharp decrease in output power followed by a gentler decline until output ceased. Two typical power versus time plots are shown in Figure 5-1.

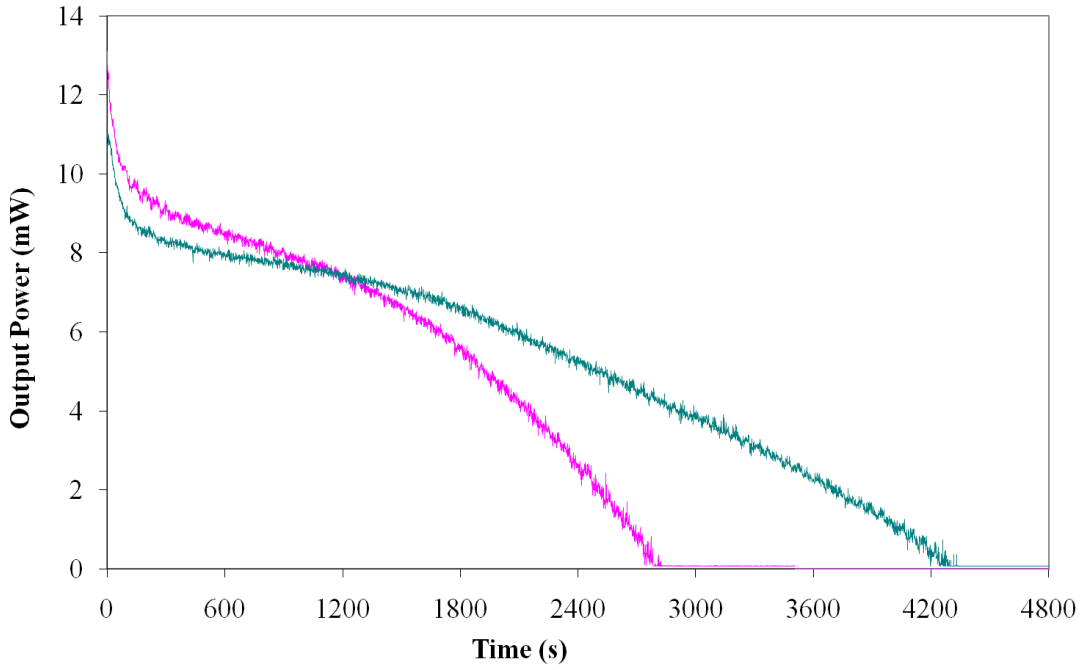

Figure 5-1: Output power over time for the strain-compensated structure with 3% output coupling

To rule out the possibility of the decline in performance being due to thermal build up in the device, the pump beam was interrupted during an output power measurement. If the power decline was due to heat build up then the output power should resume at its initial level; if it is due to structural damage then it should resume at the same level as when it was interrupted. As Figure 5-2 shows, the output

power did not recover after pump beam interruption, implying permanent damage. Also, samples which were left overnight had not recovered the next day.

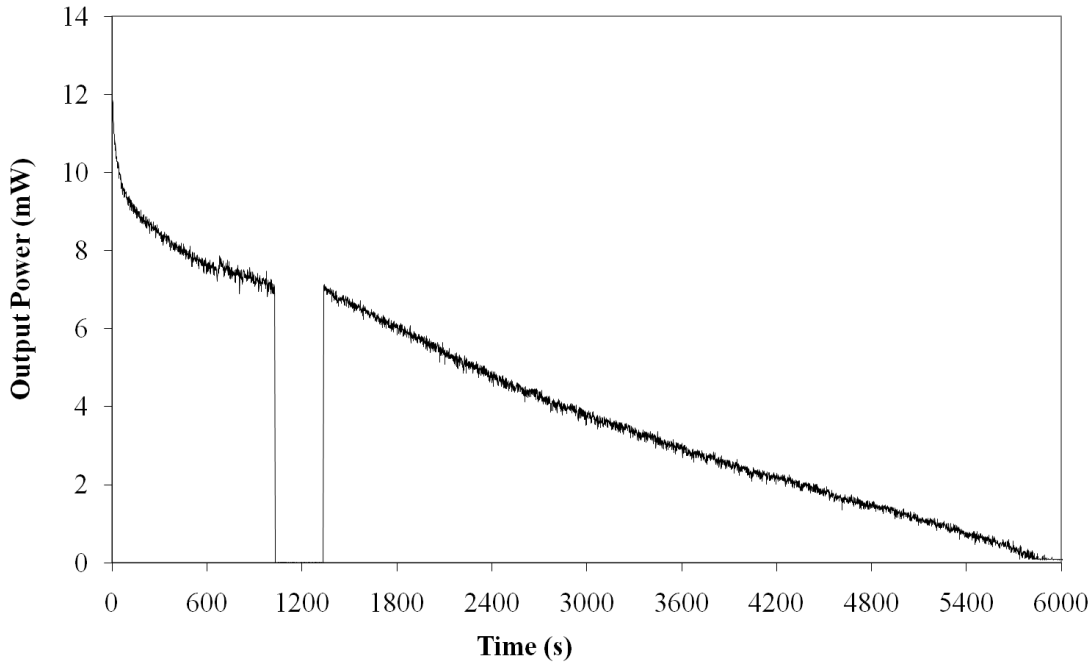

Figure 5-2: Output power over time with pump interruption for strain compensated structure with 3% output coupling

5.1.1 The Effect of Structural Degradation

A reasonable place to start investigation into the effect on laser performance of the structural damage and power decay is the Kuznetsov[18] model used in earlier chapters (where many of the terms were defined) to describe VECSEL output characteristics..

According to this model, the output power is given by

$$P_{las} = (P_p - P_{th})\eta_{out}\eta_{quant}\eta_{abs} \quad (5\text{-}2)$$

where P_p is the pump power and P_{th} the threshold pump power.

The quantum efficiency $\eta_{quant}=\lambda_{pump}/\lambda_{laser}$ is constant (neglecting small λ_{laser} change due to by strain relaxation), and we assume that the pump absorption efficiency η_{abs} does not change. The output efficiency

$$\eta_{out} = \frac{ln(R_2)}{ln(R_1 R_2 T_{loss})} \tag{5-3}$$

will decrease, decreasing the output power P_{las}, if structural damage compromises the reflectivity or causes additional round trip losses.

The threshold pump power P_{th} is affected not only by changes in reflectivity and round trip losses but also by changes in material gain:

$$P_{th} = N_{th} \frac{h\nu N_w L_w A_p}{\eta_{abs} \tau(N_{th})} \tag{5-4}$$

where the threshold carrier density N_{th} is given by:

$$N_{th} = N_0 \left(\frac{1}{R_1 R_2 T_{loss}}\right)^{(2\Gamma g_0 N_w L_w)^{-1}} \tag{5-5}$$

hυ is the pump photon energy, N_w the number or quantum wells.

The DBR reflectivity R_1 and round trip loss transmission factor T_{loss} in the above equations cannot be uncoupled in the model but physical considerations enable the decoupling of degradation of DBR reflectivity and increased round trip losses. Less than 3% of the absorbed ~600mW 445nm pump power penetrates to the DBR in the strain-compensated structure which even in a pump spot as small as 32μm diameter should not have sufficient intensity to cause damage. Therefore it is likely that the culprit is damage in the active region.

5.2 How this relates to our structure

Having ruled out damage to the DBR in section 5.1.1, we are left with the possibilities of damage to the pump-absorbing material causing round trip losses and damage to the quantum wells causing increased round trip losses..

Vogelgesang et al[19] used a range of pump wavelengths, from below the quantum well transition energy to above the cladding layer bandgap, to investigate the source of degradation in a BeMgZnSe laser diode. At low levels of illumination the quantum well photoluminescence decreased only when the pump photon energy was at least that of the quantum well transition. No damage was found in the cladding layers, implying the quantum well was degrading. Similarly, in an electrically pumped red-emitting AlGaInP laser diode[20] damage was confined to the quantum well region supplied with carriers. Raja et al[21] noted that degradation was only observed when above bandgap radiation was used i.e. when carriers were generated in the material.

Defects in the quantum wells can act as non-radiative recombination centres as well as interacting with photons[20]. By introducing mid-bandgap energy levels in the quantum well material, the defect can capture both holes and electrons efficiently[22,12] and provide a non-radiative recombination channel which competes strongly with the desired radiative recombination transition. Donor/acceptor levels are less significant as they have very small capture cross sections for holes/electrons[22]. Increasing non-radiative recombination due to defects in the $Ga_{0.45}In_{0.55}P$ quantum wells would certainly cause a reduction in output power through a reduction in the carrier lifetime

The carrier lifetime at threshold $\tau(N_{th})$ is given by:

$$\frac{1}{\tau(N_{th})} = A + BN_{th} + CN_{th}^2 \qquad (5\text{-}6)$$

where A, B and C are the non-radiative, radiative and Auger recombination coefficients respectively.

Equations 5-4 and 5-6 can be combined to express the pump threshold P_{th} as proportional to the ratio of the threshold carrier density N_{th} and carrier lifetime at threshold $\tau(N_{th})$:

$$P_{th} \propto \frac{\mathrm{N_{th}}}{\tau(\mathrm{N_{th}})} = N_{th}(A + BN_{th} + CN_{th}^2) \quad (5\text{-}7)$$

This supports the hypothesis that an increasing defect density in the quantum wells could be responsible for a decrease in output power by increasing the threshold. Equation 5-7 is used by Meneghini et al[23] to suggest that the degradation of InGaN laser diodes, with a consequent increase in threshold and decrease in efficiency, are caused by an increase in the defects of the active layer which increases the non-radiative recombination coefficient A. Stress is also shown to play a major role in the degradation.

5.2.1 Experimental Results

Photoluminescence measurements over time showed an initial increase in output before decay took over, as shown in Figure 5-3. This is likely due to recombination enhanced annealing[1], where non-radiative electron-hole recombination reduces the activation energy of defects to below the level of thermal energy present and enables defect diffusion. Note that the rise and subsequent decay in PL happens on a greatly increased timescale to that shown in Figure 4-19 due to the increased pump intensity used.

5.2.1.1 Non-Strain Compensated Structure

The output power through a high reflector output coupler was measured over time. To investigate if the decay was due to thermal build-up a further power decay measurement was taken where the pump beam was interrupted. After interruption the output power did not resume at its initial level indicating that the damage was structural. A normalised output power decay curve is presented in Figure 5-4.

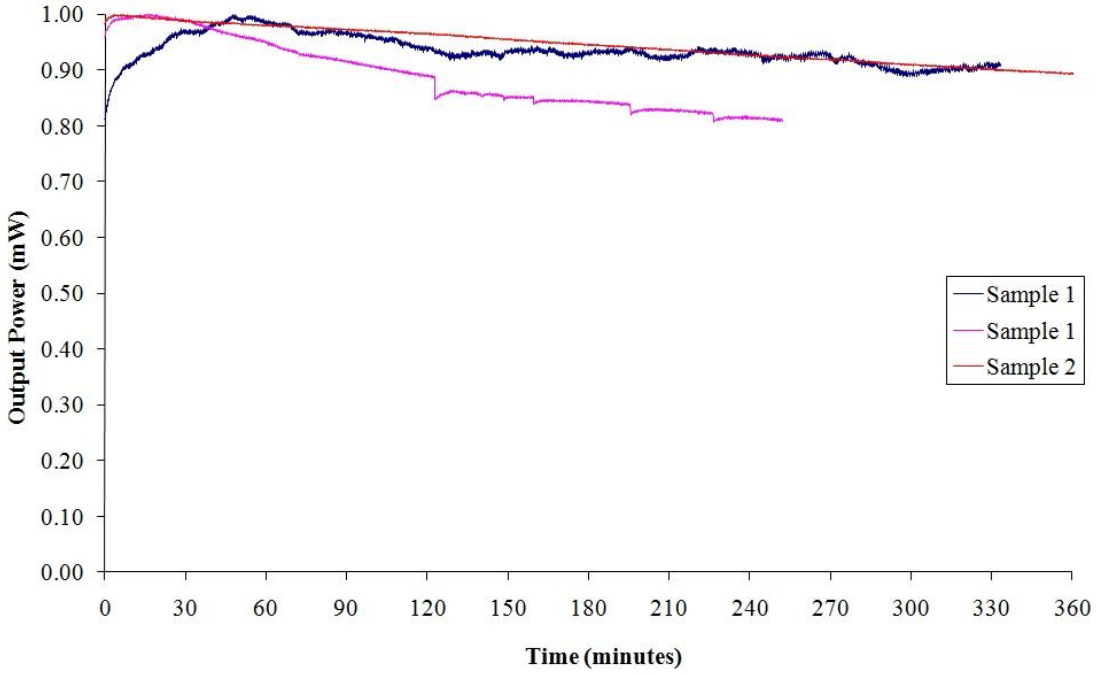

Figure 5-3: Normal PL measurements for two strain compensated diode-pumped red VECSEL samples

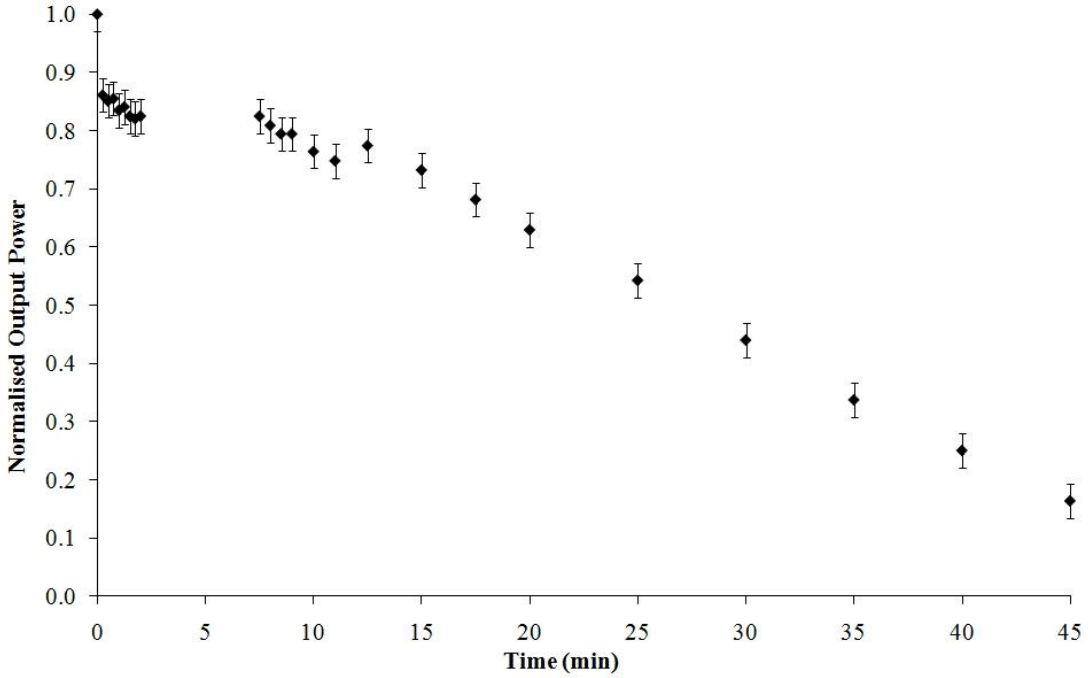

Figure 5-4: Normalised Output Power Decay Curve

Typical elapsed time between commencing and ceasing laser action was around 40 minutes. The decay appears to have three phases: an initial rapid exponential decline in output power, followed by a gentler decline which (usually) gives way to a gentle

exponential decay at a noticeable shoulder in the curve. These different phases imply that more than one decay mechanism is at work.

5.2.1.2 Strain Compensated Structure

The active region was lengthened in the strain compensated region to eliminate DBR degradation as a cause. The output power decay curves retain the same shape, indicating that the same mechanisms are still present.

A number of measurements of laser output power over time at different locations on the sample were made, including a pump interruption run, all of which show a sharp initial decline in power followed by more gentle decay. Normalised output power decay curves are presented in Figure 5-5.

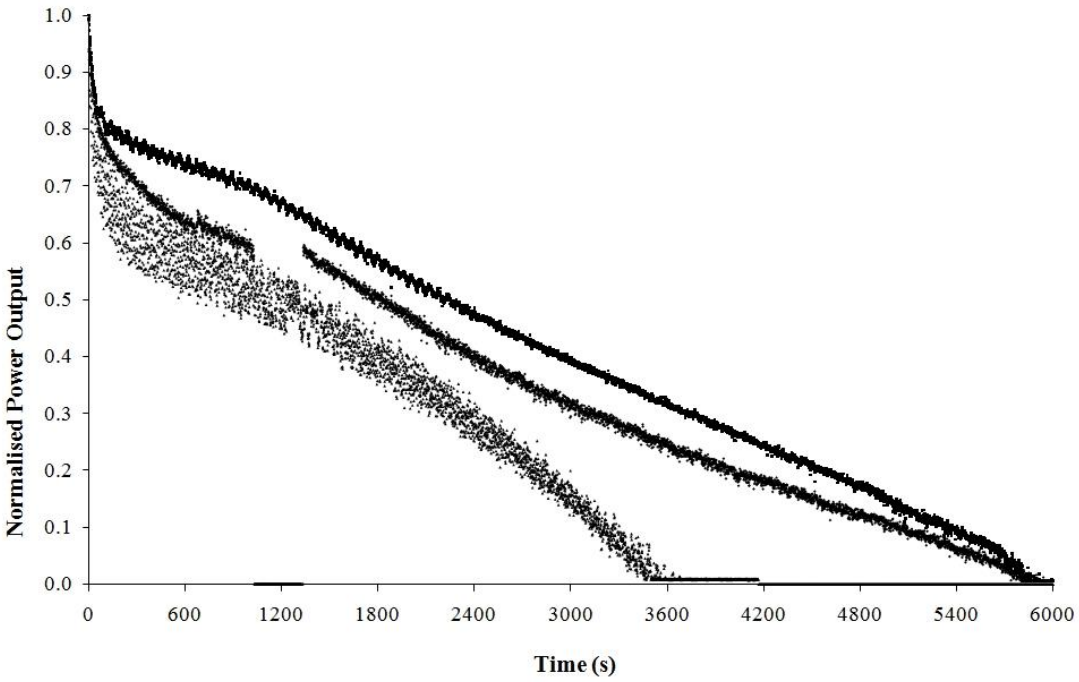

Figure 5-5: Normalised power decay curves for K2208

These output power curves for the strain compensated structure exhibit the same three phases in the decline in output power seen in the non strain compensated structure but on a longer timescale. It appears from this that decreasing the level of strain energy in the structure has reduced the rate at which the decay mechanisms

cause damage but not sufficiently reduced the activation energy to prohibit any of them.

5.2.2 Conclusion

Introducing strain compensation of the quantum wells increased the lifetime of the diode-pumped visible VECSEL structure from 40 to 100 minutes. The output power decline had the same character in both cases, a rapid drop followed by a more gentle decline, indicating that the changes reduced but did not eliminate the degradation mechanisms. Possible improvements to increase device lifetime will be suggested in Chapter 7.

References

1 D. V. Lang and L. C. Kimerling, "Observation of Recombination-Enhanced Defect Reactions in Semiconductors," Physical Review Letters **33** (8), 489 (1974).

2 O. Ueda, "Degradation of III--V Opto-Electronic Devices," Journal of The Electrochemical Society **135** (1), 11C-22C (1988).

3 S. Guha, J. M. DePuydt, M. A. Haase, J. Qiu, and H. Cheng, "Degradation of II-VI based blue-green light emitters," Applied Physics Letters **63** (23), 3107-3109 (1993).

4 G. H. Olsen, C. J. Nuese, and R. T. Smith, "Effect of Elastic Strain on Energy-Band Gap and Lattice-Parameter in III-V-Compounds," Journal of Applied Physics **49** (11), 5523-5529 (1978).

5 V. Kumar and B.S.R. Sastry, "Thermal Expansion Coefficient of Binary Semiconductors," Crystal Research and Technology **36** (6), 565-569 (2001).

6 "Kaye and Laby Online (Tables of Physical & Chenical Constants) http://www.kayelaby.npl.co.uk/general_physics/2_3/2_3_5.html", (1999).

7 S. K. Choi, M. Mihara, and T. Ninomiya, "Dislocation Velocities in GaAs," Jpn. J. Appl. Phys **16** (5), 737 (1977).

8 S. K. Choi, M. Mihara, and T. Ninomiya, "Dislocation Velocities in InAs and GaSb," Jpn. J. Appl. Phys **17** (2), 329 (1977).

9 H. Nagai, "Dislocation Velocities in Indium Phosphide," Jpn. J. Appl. Phys **20** (4), 793 (1981).

10 Kishino Seigo, Chinone Naoki, Nakashima Hisao, and Ito Ryoichi, "Dark-line defects induced by mechanical bending in GaAs-$Ga_{1-x}Al_xAs$ double-heterostructure wafers," Applied Physics Letters **29** (8), 488-490 (1976).

11 Mathias Ziegler, Tran Quoc Tien, Sandy Schwirzke-Schaaf, Jens W. Tomm, Bernd Sumpf, Gotz Erbert, Myriam Oudart, and Julien Nagle, "Gradual degradation of red-emitting high-power diode laser bars," Applied Physics Letters **90** (17), 171113 (2007).

12 A. Tukiainen, J. Dekker, T. Leinonen, and M. Pessa, "Characterization of deep levels in rapid-thermal-annealed AlGaInP," Materials Science and Engineering B **91-92**, 389-392 (2002).

13 V. Celli, M. Kabler, T. Ninomiya, and R. Thomson, "Theory of Dislocation Mobility in Semiconductors," Physical Review **131** (1), 58 (1963).

14 Lisa Sugiura, "Comparison of degradation caused by dislocation motion in compound semiconductor light-emitting devices," Applied Physics Letters **70** (10), 1317-1319 (1997).

15 K. Maeda and S. Takeuchi, "Recombination enhanced dislocation glide in InP single crystals," Applied Physics Letters **42** (8), 664-666 (1983).

16 Narihiko; Takeuchi Maeda, Shin, "Enhanced Dislocation Mobility by Electron-Beam Irradiation in GaP," Jpn. J. Appl. Phys **29** (6), 1151 (1990).

17 Koji Maeda, Miwa Sato, Akihisa Kubo, and Shin Takeuchi, "Quantitative measurements of recombination enhanced dislocation glide in gallium arsenide," Journal of Applied Physics **54** (1), 161-168 (1983).

18 M. Kuznetsov, F. Hakimi, R. Sprague, and A. Mooradian, "Design and characteristics of high-power (> 0.5-W CW) diode-pumped vertical-external-

cavity surface-emitting semiconductor lasers with circular TEM_{00} beams," IEEE J. Sel. Top. Quantum Electron. **5** (3), 561 (1999).

19 R. Vogelgesang, J. J. Liang, V. Wagner, H. J. Lugauer, J. Geurts, A. Waag, and G. Landwehr, "Wavelength-dependent optical degradation of green II--VI laser diodes," Applied Physics Letters **75** (10), 1351-1353 (1999).

20 Claus Ropers, Tran Quoc Tien, Christoph Lienau, Jens W. Tomm, Peter Brick, Norbert Linder, Bernd Mayer, Martin Muller, Sonke Tautz, and Wolfgang Schmid, "Observation of deep level defects within the waveguide of red-emitting high-power diode lasers," Applied Physics Letters **88** (13), 133513 (2006).

21 M. Y. A. Raja, S. R. J. Brueck, M. Osinski, and J. McInerney, "Laser-induced degradation of GaAs photoluminescence," Applied Physics Letters **52** (8), 625-627 (1988).

22 K. Sugiura, K. Domen, M. Sugawara, C. Anayama, M. Kondo, T. Tanahashi, and K. Nakajima, "Analysis of recombination centers in $(Al_xGa_{1-x})_{0.5}In_{0.5}P$ quaternary alloys," Journal of Applied Physics **70** (9), 4946-4949 (1991).

23 M. Meneghini, G. Meneghesso, N. Trivellin, E. Zanoni, K. Orita, M. Yuri, and D. Ueda, "Extensive Analysis of the Degradation of Blu-Ray Laser Diodes," Electron Device Letters, IEEE **29** (6), 578-581 (2008).

Chapter 6

II-VI VECSELs

As noted in previous sections, II-VI material systems offer the exciting prospect of being able to design VECSELs that will emit across the whole of the visible region. Here we carry out preliminary work on two different approaches, one utilising an epitaxial lift-off technique to transfer the active region to a new substrate and one using the highly flexible ZnCdMgSe material system.

6.1 ZnSe/ZnCdSe VECSEL

Our collaborators at Heriot-Watt University use a dedicated MBE system to grow II-VI materials lattice-matched to GaAs and novel semiconductors such as MgS in a zinc-blende structure. They have developed an interesting epitaxial lift-off process[1] where the structure is grown onto a sacrificial layer of MgS which is then dissolved in weak acid, thus also removing the original substrate, and enabling the active region to be floated onto another substrate. This has the advantage that the new substrate need bear no relation to the material system and can be chosen purely for its material properties, such as high thermal conductivity. It also forms a very strong bond as the thinness of the structure gives it great flexibility in conforming to the surface variation of the new substrate.

6.1.1 Structure

For this work we utilised an existing ZnSe/ZnCdSe growth in order to investigate diode-pumping the material and later lifting it off onto a diamond heatspreader, although fused silica was used initially.

A 5 quantum well structure (Table 6-1) grown on a GaAs substrate with a 20nm ZnSe buffer layer and a 5nm MgS sacrificial layer used in the epitaxial lift-off process. The structure was then floated onto a ~5mm square fused silica substrate which is transparent at the quantum well emission wavelength. The structure was not

Diode Pumped Visible Vertical External Cavity Surface Emitting Lasers designed for laser operation and the quantum wells were not situated to utilise resonant periodic gain. The quantum wells were compressively strained (~0.67%), the lattice constant for $Zn_{0.90}Cd_{0.10}Se$ being linearly interpolated from that of ZnSe (a=5.667Å) and CdSe (a=6.052Å) with an estimated room temperature direct bandgap difference of ~107meV[2].

ZnSe	8 nm
$Zn_{0.90}Cd_{0.10}Se$	8 nm
ZnSe	8 nm
$Zn_{0.90}Cd_{0.10}Se$	8 nm
ZnSe	8 nm
$Zn_{0.90}Cd_{0.10}Se$	8 nm
ZnSe	8 nm
$Zn_{0.90}Cd_{0.10}Se$	8 nm
ZnSe	8 nm
$Zn_{0.90}Cd_{0.10}Se$	8 nm
ZnSe	52.5 nm

Table 6-1: 5 quantum well ZnCdSe/ZeSe structure

6.1.2 Characterisation

Normal photoluminescence (PL) spectra were taken to measure the room temperature quantum well emission wavelength. The sample was held in a brass mount with no thermal management. Black backing was placed on the back of the fused silica substrate to eliminate back reflections from the mount. A 405nm GaN laser diode was used to pump the structure in the experimental set-up shown in Figure 6-1. A 405nm interference filter was used to remove longer wavelength spontaneous emission from the laser diodes which swamped the II-VI quantum well PL at low pump power levels. The PL was collected and collimated by a 2" f=49mm plano-convex lens and a 455nm long-pass filter removed the pump light before the collected light was focussed onto the fibre-tip leading to an optical spectrum analyser.

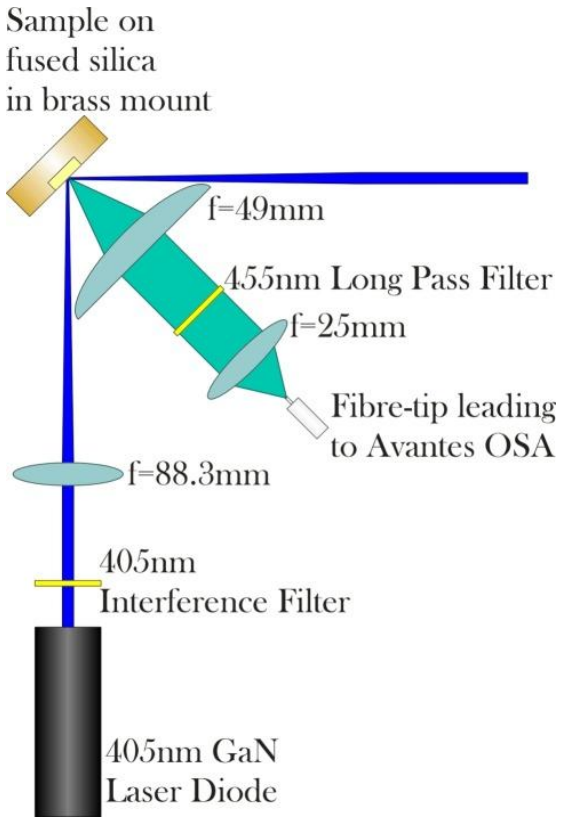

Figure 6-1: Schematic of normal PL experiment for II-VI Heriot-Watt structure

During the normal PL measurements it became clear that the level of PL declined over time. A series of PL intensity with time measurements were taken using the normal PL set-up to measure the timescale and character of the decay. The PL intensity was measured for four wavelength ranges (496-497nm, 498-499nm, 500-501nm, 502-503nm) and three levels of pump power (50mW, 91mW, 130mW).

The decay for all points on the sample and powers is well fitted by a curve of the form

$$P = P_0 + A_1 e^{-x/t_1} + A_2 e^{-x/t_2} + A_3 e^{-x/t_3} \quad (6\text{-}1)$$

(with an R^2 value of >0.99) indicating that more than one process is involved in the decay. Approximate time and decay strength constants are given in Table 6-2 and a typical set of decay curves in Figure 6-2.

Pump Power (mW)	t_1 (seconds)	t_2 (minutes)	t_3 (hours)	A_1	A_2	A_3
50	200	16.5	3.2	0.27	0.29	0.28
91	67	7.6	1.2	0.30	0.23	0.17
130	70	10.1	1.4	0.39	0.19	0.14

Table 6-2: Time constants for three PL decay runs

At higher pump powers the initial rapid decay is more severe, which is what would be expected for recombination enhanced mechanisms. The decay was consistent across the wavelength ranges measured indicating that the PL does not shift wavelength as it decays, although there is some minor variation between sample points due to growth variation or damage caused by the lift-off process.

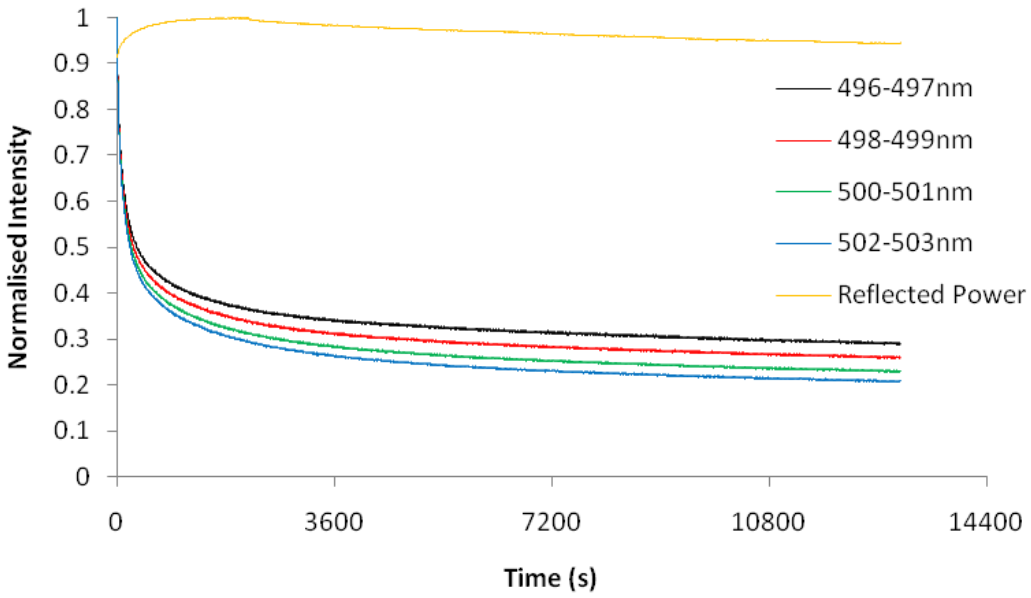

Figure 6-2: PL decay for 130mW pump power

Concerns have been expressed about the lifetime of II-VI materials as emission energy is typically greater than the bond strength[3], although device lifetime has been greatly improved by higher quality growth which results in lower defect densities[4] and lifetimes of hundreds of hours for II-VI laser diodes have been demonstrated.

The amount of pump power reflected from the sample surface was monitored simultaneously with the 130mW pump power decay run. This showed an initial increase in the level of reflected power followed by a slow decay. This appears to operate on a similar timescale to the PL decay, transitioning from increasing to decreasing reflectivity during the transition from rapid to gentle PL decay. The pump power remained stable over the duration of the experiment so the change on reflected power must be due to a change in the sample and, in view of the similar timescales, is probably caused by the same mechanism.

The PL did not recover after the pump had been blocked for some time, indicating the change is structural damage rather than thermal. Both the increase in reflectivity, irreversible decrease in PL and absence of wavelength shift are consistent with other experimental results for ZnCdSe/ZnSe multiple quantum wells, for instance Mogi et al[5] where fast photoluminescence decay times were observed to depend strongly on pump intensity at room temperature. The reduction in decay time was attributed to non-radiative recombination. The strongly irradiated samples also showed an increase in scattered light.

6.1.2.1 Fused Silica Substrate

As the sample was very thin and would allow some transmission of light we were able to take an absorption profile of the sample. The sample and substrate were temporarily bonded with water to a glass slide and placed in a Cary 50 Spectrometer to measure its absorbance with a 5nm resolution. The data in Figure 6-3 shows two clear steps at 460-465nm for the ZnSe barriers and ~495nm due to the $Zn_{0.90}Cd_{0.10}Se$ quantum wells. This matches well with the 493nm emission of the quantum wells and 2.7eV bandgap of ZnSe[6].

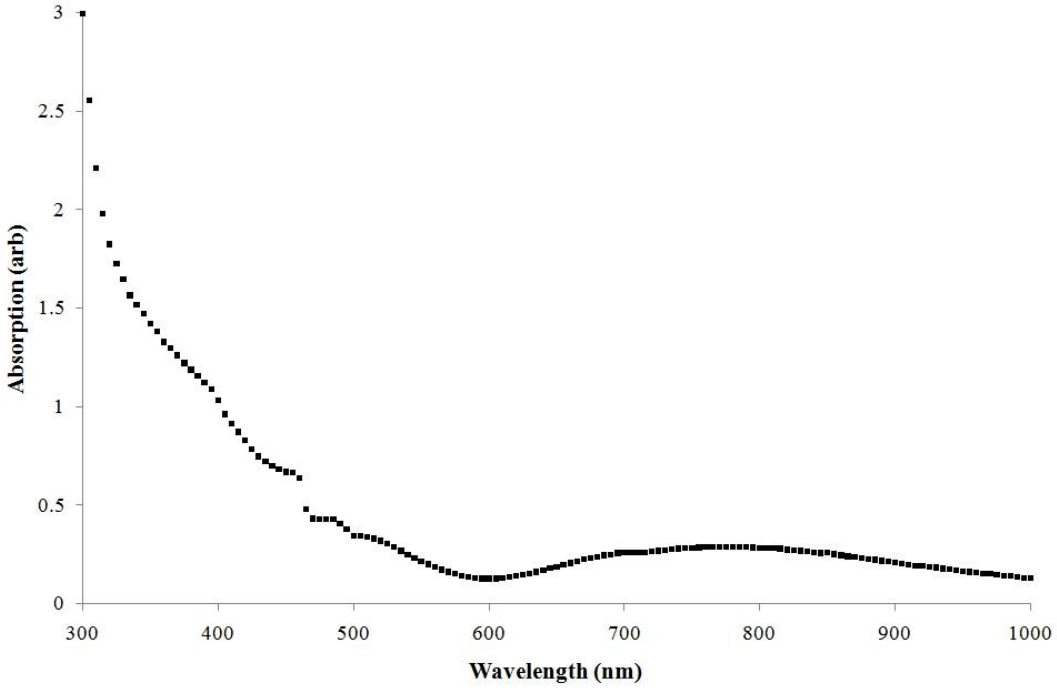

Figure 6-3: $Zn_{0.90}Cd_{0.10}Se/ZnSe$ structure absorbance spectrum

Spectra were taken at a range of pump powers to observe the shift in PL with pump power and shown in Figure 6-4 and Figure 6-5. The pump power shown is the amount which was not reflected by the sample: we were unable to measure the power transmitted through the sample and substrate due to the sample mounting arrangement.

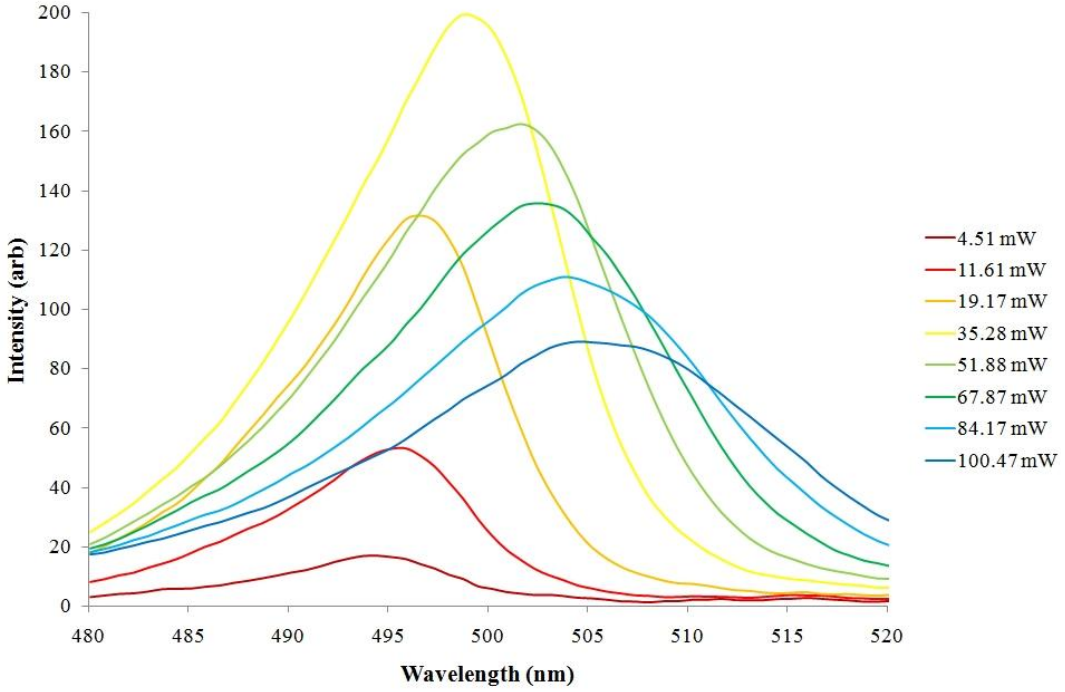

Figure 6-4: Normal PL for a range of pump powers for sample HWA1959

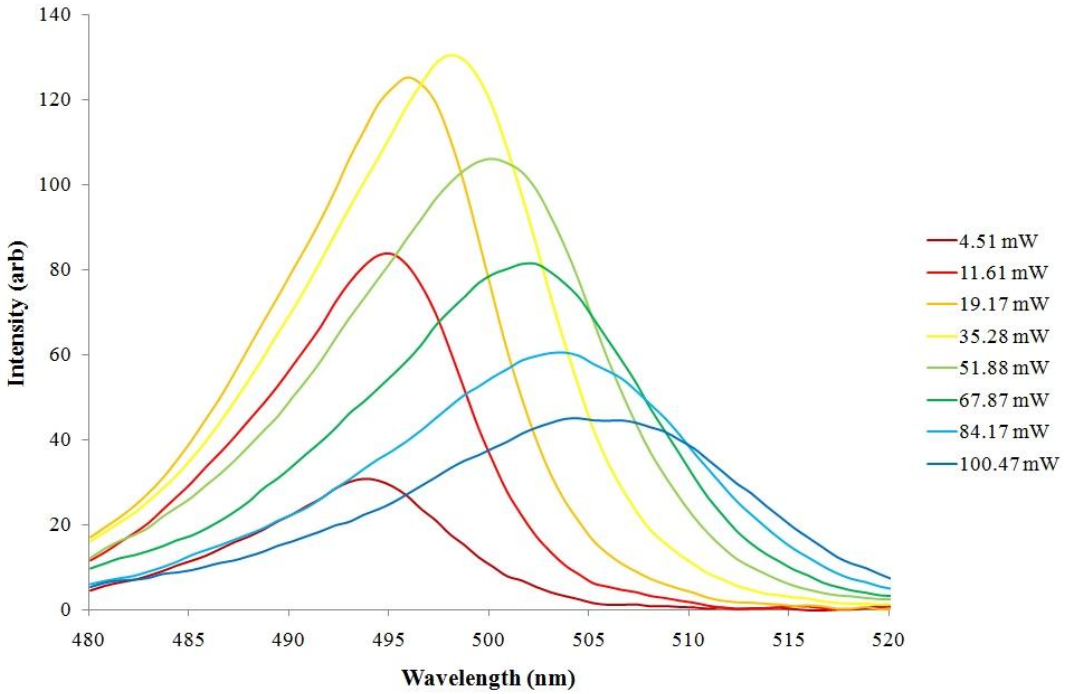

Figure 6-5: Normal PL for a range of pump powers for sample HWA1960.

The effect of heating due to optical pumping is evident in the shift of PL peak to longer wavelength at ~0.1nm/mW as the pump power increases, which was expected as no thermal management was used and the fused silica substrate has a very low thermal conductivity of ~1.4$Wm^{-1}K^{-1}$.

6.1.2.2 Diamond Substrate

Following the characterisation of the ZnCdSe/ZnSe structure on fused silica we provided a diamond heatspreader for improved thermal management to our collaborators at Heriot-Watt who performed the lift-off technique onto diamond for the first time. Diamond has a higher thermal conductivity than fused silica by three orders of magnitude and we could closely control the sample temperature and vary the temperature and pump power independently.

The sample was mounted in a brass mount, temperature-controlled by a peltier element. Normal PL spectra were taken by the same method as used for the sample on fused silica. The sample was illuminated with ~10mW from the 405nm GaN laser diode and the sample temperature raised from 10°C to 55°C in 5°C steps. As Figure 6-6 shows, as the sample temperature is raised, the PL intensity decreases and the peak wavelength shifts to longer wavelength at ~0.1nm/K.

To test the effectiveness of the thermal management, the sample mount was then held at a constant temperature of 10°C whilst the incident power was increased from 26mW to 162mW. As Figure 6-7 shows, the peak wavelength remained constant for the whole of the power range. This is in stark contrast to the earlier experiment with the sample on fused silica without thermal management where the wavelength changed by more than 10nm for a pump power increase of 100mW which suggests a local temperature increase of ~100K in the sample without thermal management.

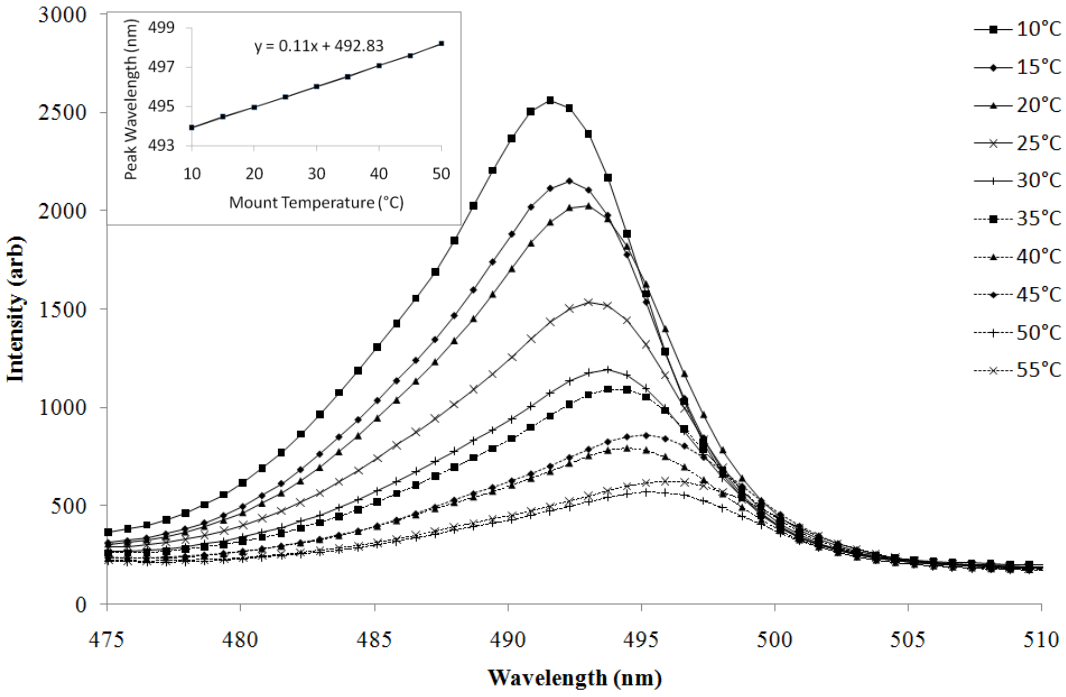

Figure 6-6: Variance of Normal PL at constant pump power for different temperatures Inset: Peak wavelength shift with temperature.

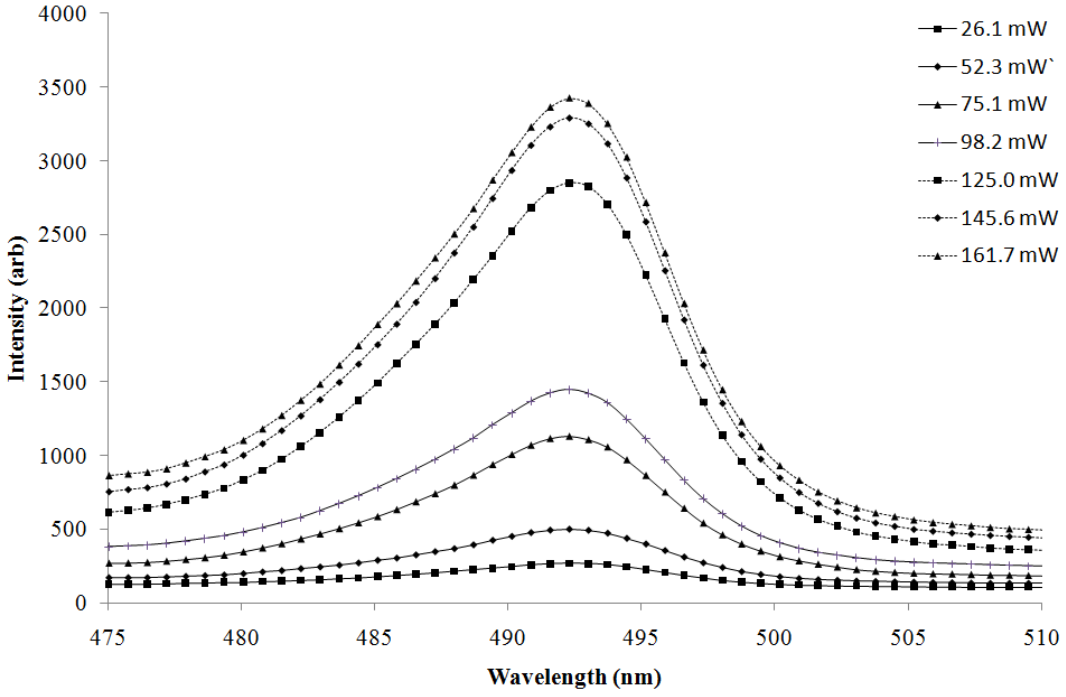

Figure 6-7: Spectra for constant temperature but varying pump power

6.2 ZnCdMgSe/ZnCdSe VECSEL

One II-VI material system with great promise is ZnCdMgSe. With the right composition it can be lattice-matched to InP with a direct bandgap covering the visible spectrum from orange to violet (and even just into the UV) as shown in Figure 6-8[7]. Professor Maria Tamargo, City University New York, has investigated the MBE growth of the wide-bandgap ZnCdMgSe system lattice matched to InP. They have demonstrated room temperature electroluminescence from ZnCdSe/ZnCdMgSe quantum well LEDs from blue through to red. This makes it an ideal and extremely flexible prospect for visible wavelength VECSELs.

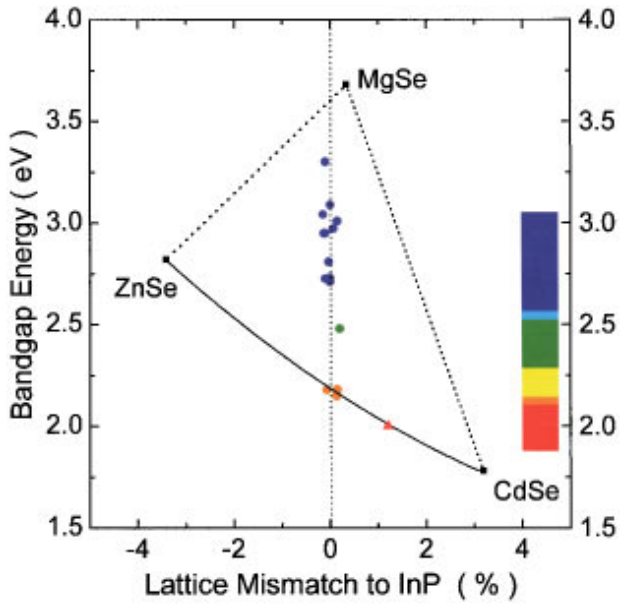

Figure 6-8: Spectral coverage of ZnCdMgSe Lattice Matched to InP

Edge-emitting optically-pumped quantum well structures based on the ZnCdMgSe material system have been successfully demonstrated at room temperature[7] and photoluminescence has been shown for quantum wells of different emission wavelengths fabricated together[8] on an InP substrate but multiple quantum well surface emitting laser devices have yet to be developed.

$Zn_xCd_{1-x}Se$ is a direct bandgap semiconductor and is lattice-matched to InP at $x=0.48$[9,10], which we have used as the quantum well material. Unlike the III-V designs, the quantum wells were not strained in this device as we were aiming for

structural stability in the first instance and incorporating strain for performance improvement in possible future iterations.

The barrier material $(Zn_{0.48}Cd_{0.52})_{0.65}Mg_{0.35}Se$ is lattice matched to InP[10], and a direct bandgap semiconductor at room temperature. II-VI materials absorb strongly at wavelengths near the band gap energy due to strong excitonic effects[11], although these are not expected to play a major role in emission[12], and this composition was chosen to have a bandgap near the intended pump wavelength of 445nm of the GaN laser diodes.

In order to show the potential of the II-VI VECSEL for applications we designed a device on the same principles used in the III-V visible VECSEL. The design for the structure does not include a DBR; hence the structure is used as a gain providing element within a cavity defined by the external mirrors.

The design incorporates a thin ZnSe top layer as the epi-surface of the structure to protect the active region. The wide bandgap range of the ZnCdMgSe material system allows us to use high bandgap carrier confinement layers of $(Zn_{0.48}Cd_{0.52})_{0.40}Mg_{0.60}Se$ near the epitaxial surface as a barrier to prevent carriers diffusing onto the epi-surface and recombining uselessly.

6.2.1 Structure

The structure incorporated the same design elements as the diode pumped III-V VECSEL and was similarly intended to be pumped at 445nm. A resonant and anti-resonant version were designed. The resonant design is shown in Table 6-3, the anti-resonant structure is the same except that the confinement layers are 160nm thick. All layers of the structure were designed to be lattice matched to InP.

Material	Thickness (nm)	Material
ZnSe	10	Cap
$(Zn_{0.48}Cd_{0.52})_{0.40}Mg_{0.60}Se$	100	Confinement
$(Zn_{0.48}Cd_{0.52})_{0.65}Mg_{0.35}Se$	104	Barrier
$Zn_{0.48}Cd_{0.52}Se$	4	QW
$(Zn_{0.48}Cd_{0.52})_{0.65}Mg_{0.35}Se$	101	Barrier x4
$Zn_{0.48}Cd_{0.52}Se$	4	QW x4
$(Zn_{0.48}Cd_{0.52})_{0.65}Mg_{0.35}Se$	423	Barrier
$(Zn_{0.48}Cd_{0.52})_{0.40}Mg_{0.60}Se$	100	Confinement
$Zn_{0.48}Cd_{0.52}Se$	10	Etch Stop
$In_{0.53}Ga_{0.47}As$	200	Buffer
InP [100]		Substrate

Table 6-3: Resonant II-VI VECSEL Design

It is possible to grow a II-VI DBR using ZnCdSe as the high refractive index material but the low index material of (ZnCd)MgSe presents problems due to the high concentration of Mg (MgSe has a rocksalt structure). Guo et al[13] achieved 95% reflectivity at 605nm with a 16 period $Zn_{0.52}Cd_{0.48}Se/Zn_{0.30}Cd_{0.28}Mg_{0.42}Se$ DBR. Kruse et al[14] achieved ~99.6% reflectivity using alternating layers of $ZnS_{0.06}Se_{0.94}$ and a $MgS/Zn_{0.67}Cd_{0.43}Se$ superlattice on GaAs, but both are a little short of the >99.9% required for a VECSEL DBR.

6.2.2 Characterisation

Initial characterisation of the samples was carried out using reflectivity and normal PL techniques in a similar arrangement to chapter 3. Normal PL measurements were taken using a 405nm GaN laser diode focussed to a spot coincident with the tungsten lamp spot. Incident pump power was less than 30mW. Five readings were taken for each sample, one at the centre (C0) and one 5.6mm towards each corner (C1-4). The sample was maintained at 20°C on a brass plate.

The structure does not include a mirror so reflectivity is weaker than for the III-V structures in chapter 3, which had an integral DBR, however the high refractive

index of the $In_{0.53}Ga_{0.47}As$ (n=4.21 at λ=560nm[15]) layer causes it to act as a weak mirror.

Two of the structures (A2796 & A2800) were grown to be resonant at operating emission wavelength and the normal PL data shows a well defined single peak (at ~ 570nm and 560nm respectively) with FWHM of ~10nm and ~13nm [Figure 6-9]

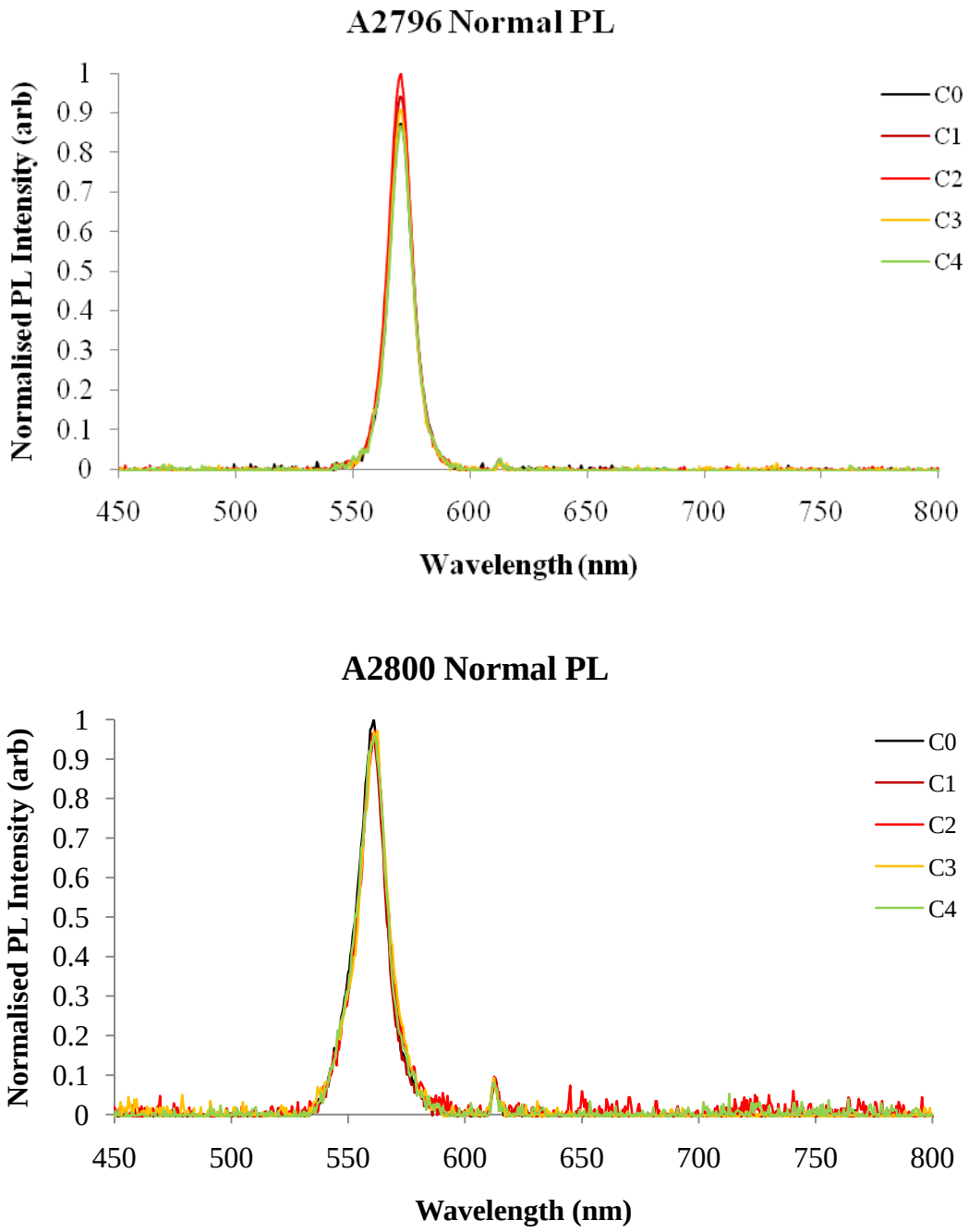

Figure 6-9: Normal PL of two resonant II-VI VECSEL structures

The peaks in the reflectivity measurements show the weak etalon due to the air/ZnSe $Zn_{0.48}Cd_{0.52}Se$/InGaAs interfaces [Figure 6-10], the spacing between the peaks increasing with increasing wavelength due to the increase in the refractive index (and thus optical depth) of the material. The noise below ~530nm is caused by the low intensity of the white light source at those wavelengths.

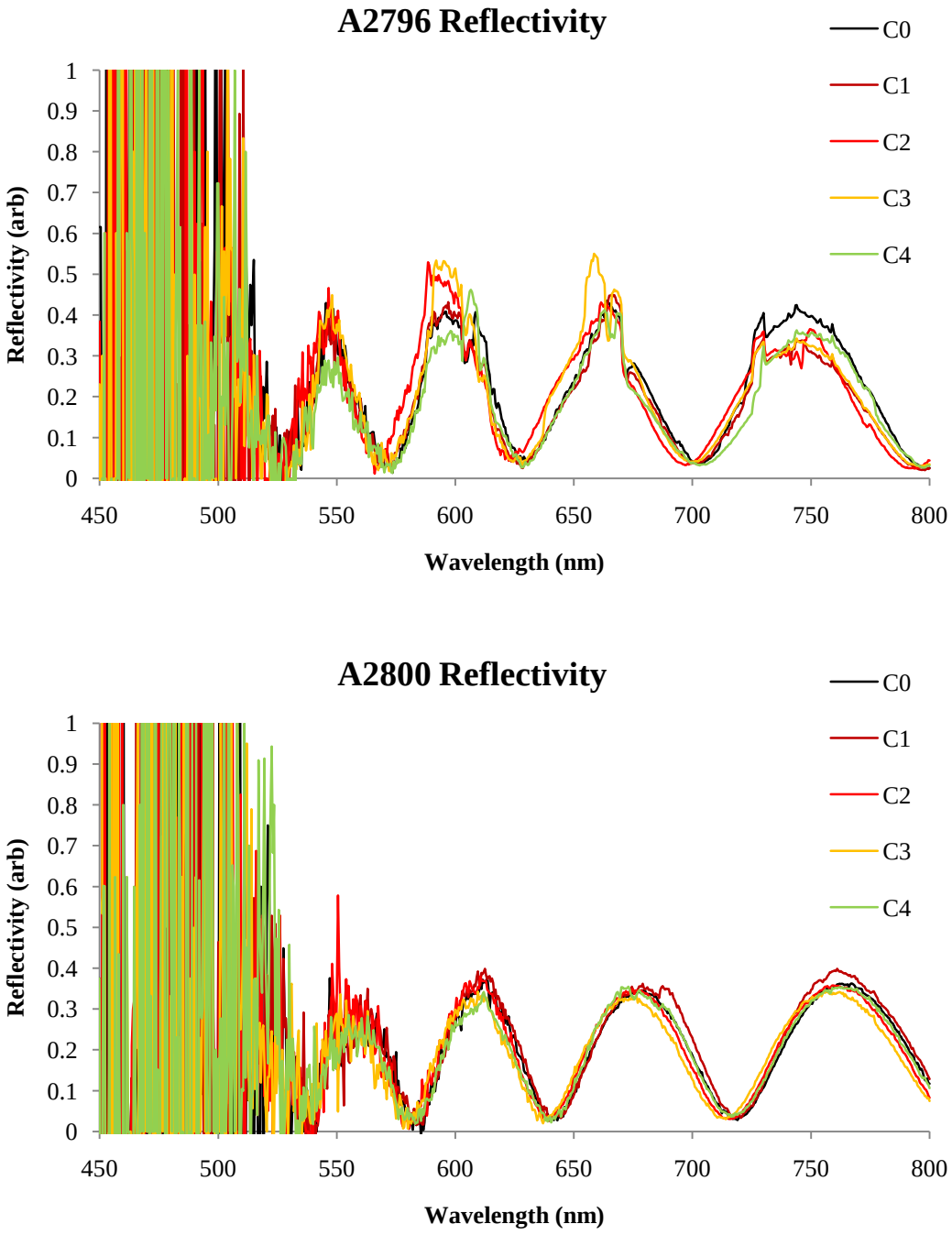

Figure 6-10: Reflectivity measurements of resonant II-VI VECSEL structures

The two anti resonant structures display more structure to their normal PL curves due to the subcavity resonances (Figure 6-11). The reflectivity measurements are very similar to those of the resonant structures and so are not shown here.

The change of device characteristics with temperature is of interest with regard to performance stability in operation, smaller variance with temperature being desirable. One of the wafers of the resonant design had been accidentally cleaved, providing a freshly cleaved edge at which we could take edge PL measurements in addition to the normal PL and reflectivity measurements temperatures between 10 and 81°C.

The normal PL and reflectivity curves were similar to those shown earlier for the resonant designs but with a small wavelength shift with temperature. The edge PL measurements are shown in Figure 6-12. Curves were fitted to the peaks of the normal and edge PL. The level of noise in the reflectivity measurements meant that a better fit was obtained to the reflectivity minima.

The normal and edge PL peaks shifted to longer wavelengths at ~0.1nm/K which is the same as observed in the $Zn_{0.90}Cd_{0.10}Se/ZnSe$ structure earlier. The reflectivity minima also shift at 0.04-0.05 nm/K which is also less than the ~0.1nm/K seen in the red VECSELs. These results imply at least comparable wavelength sensitivity to temperature as the III-V AlGaInP structure.

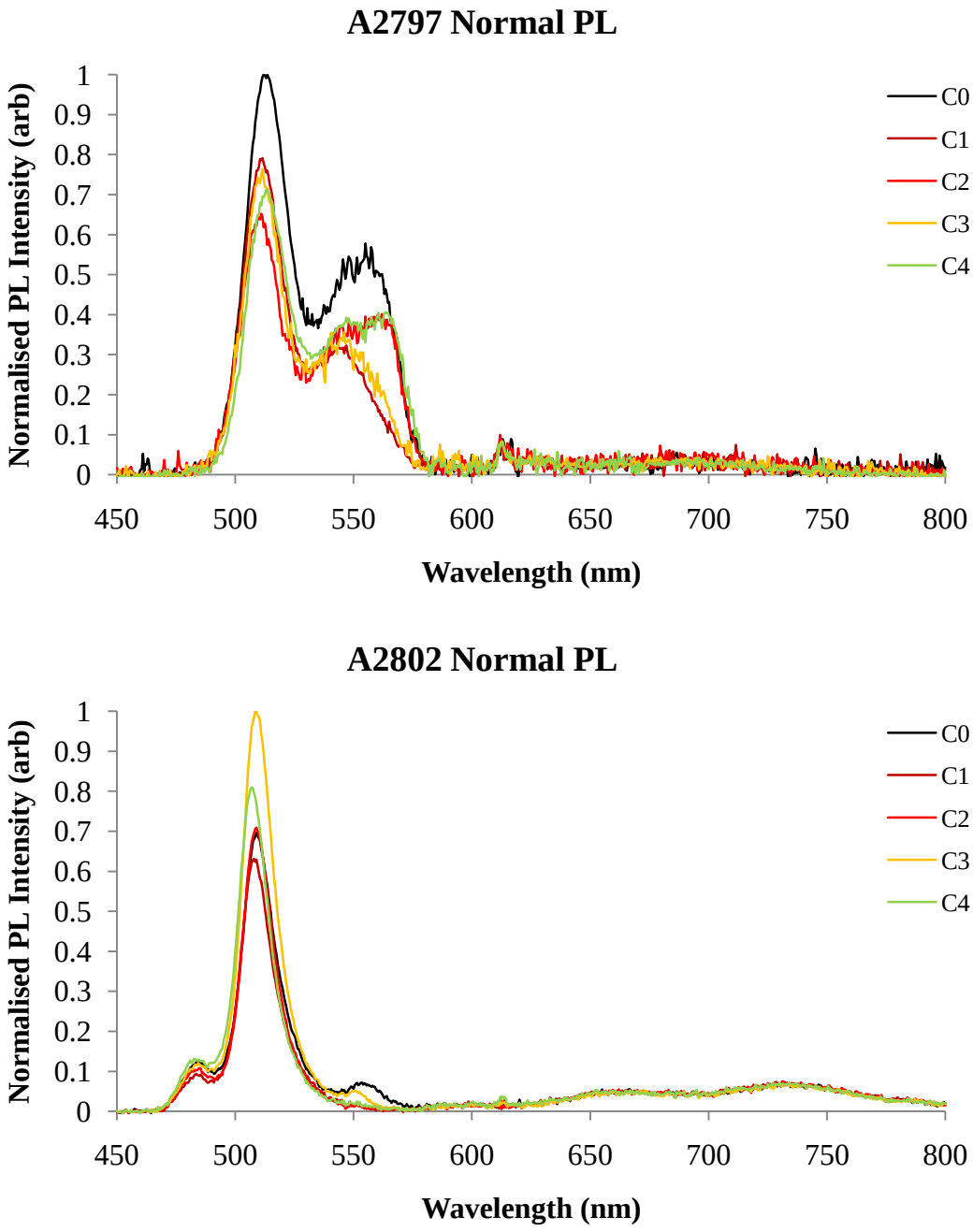

Figure 6-11: Normal PL of anti resonant II-VI VECSEL structures

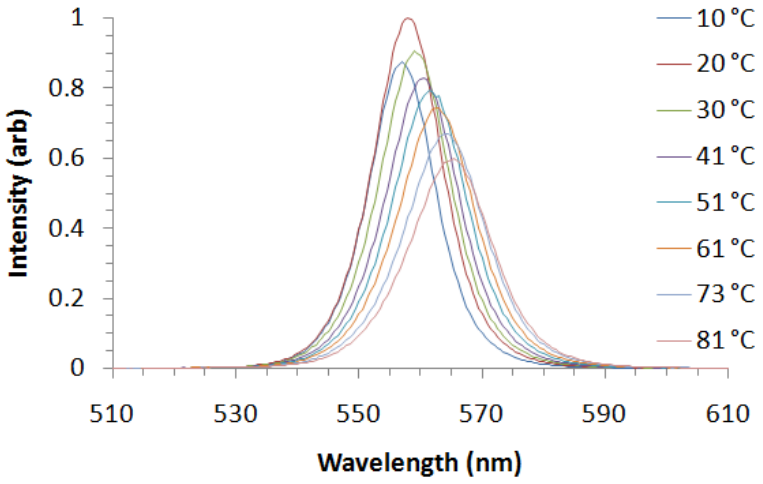

Figure 6-12: Edge PL curves for resonant structure

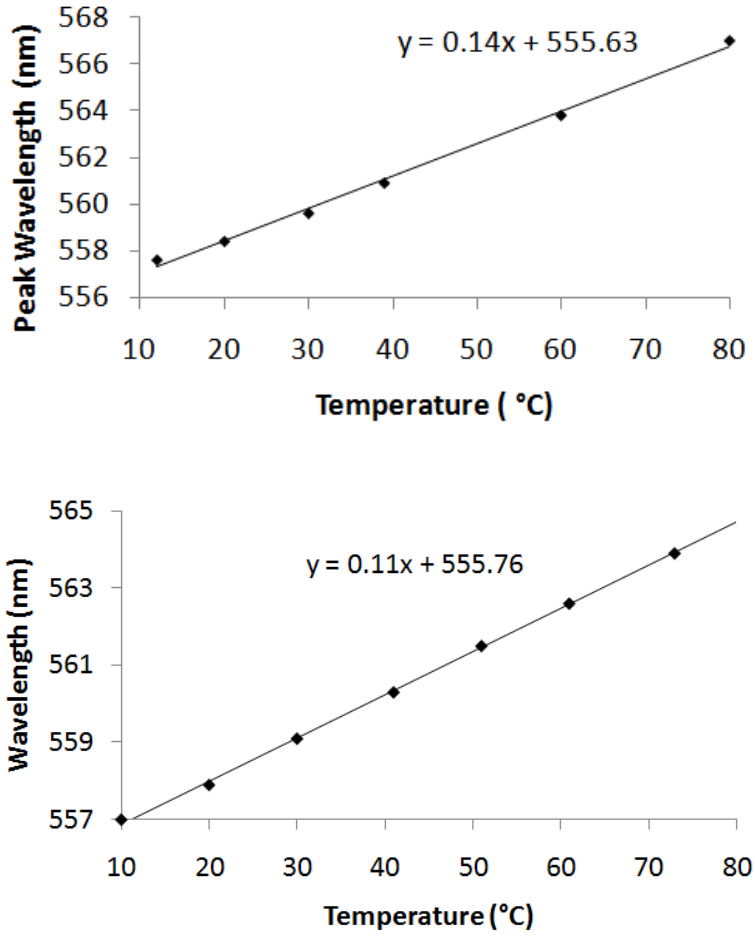

Figure 6-13: Peak wavelength shift of a)Normal PL and b) Edge PL

6.2.2.1 Edge PL Characterisation

As discussed in section 3.3.3.1, in order for a VECSEL to function well it is necessary for the edge emission to be TE polarised, i.e. the 1hh energy level to be the ground state. The two resonant and two anti-resonant samples were pumped at 405nm near the edge of each sample and the PL collected using the experimental set-up shown in Figure 6-14. If the quantum wells are unstrained then the 1hh and 1lh levels will be degenerate and the TE and TM emission will have the same wavelength. The sample mounts were maintained at ~20°C, and a chopper used in conjunction with a locking amplifier to reduce background noise. A 405nm long-pass filter was used to cut out the longer wavelength fluorescence from the pump source. A 532nm polarisation beamsplitter cube was placed on a rotation mount after the microscope objective was used to introduce polarisation sensitivity. Measurements were taken at 0°, 90°, 180° and 270°, with TM polarised light being transmitted at 0° and 180°, TE polarised light transmitted at 90° and 270°.

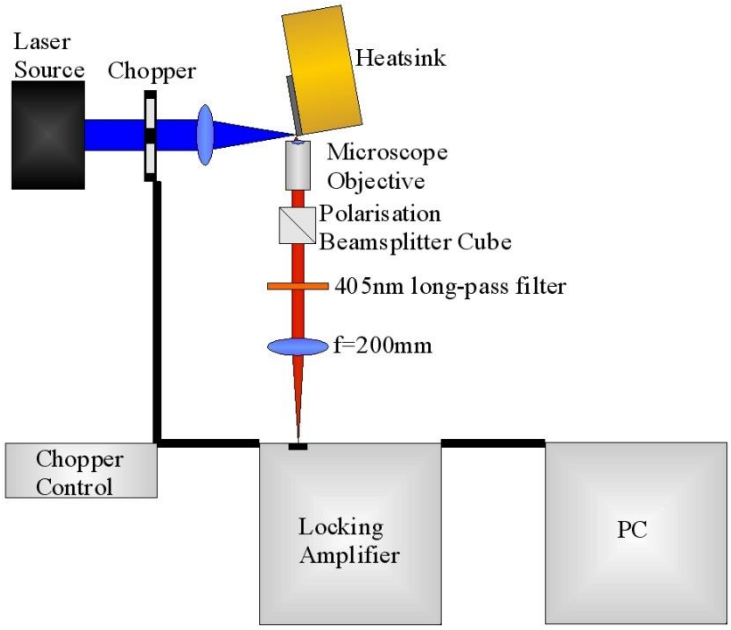

Figure 6-14: Schematic of the experimental set-up for polarised edge PL measurements

This arrangement was able to measure the wavelength difference between the TE and TM polarised emission but a comparison of the relative emission intensity could not be made as the orientation of the diffraction grating spectrometer was fixed.

Figure 6-15 and Figure 6-16 show polarisation edge PL spectra for a resonant and anti-resonant structure respectively. In both cases the TE emission is a slightly longer wavelength than the TM so the c-1hh transition is slightly lower energy than c-1lh and is the ground state, indicating that the quantum wells are slightly compressively strained.

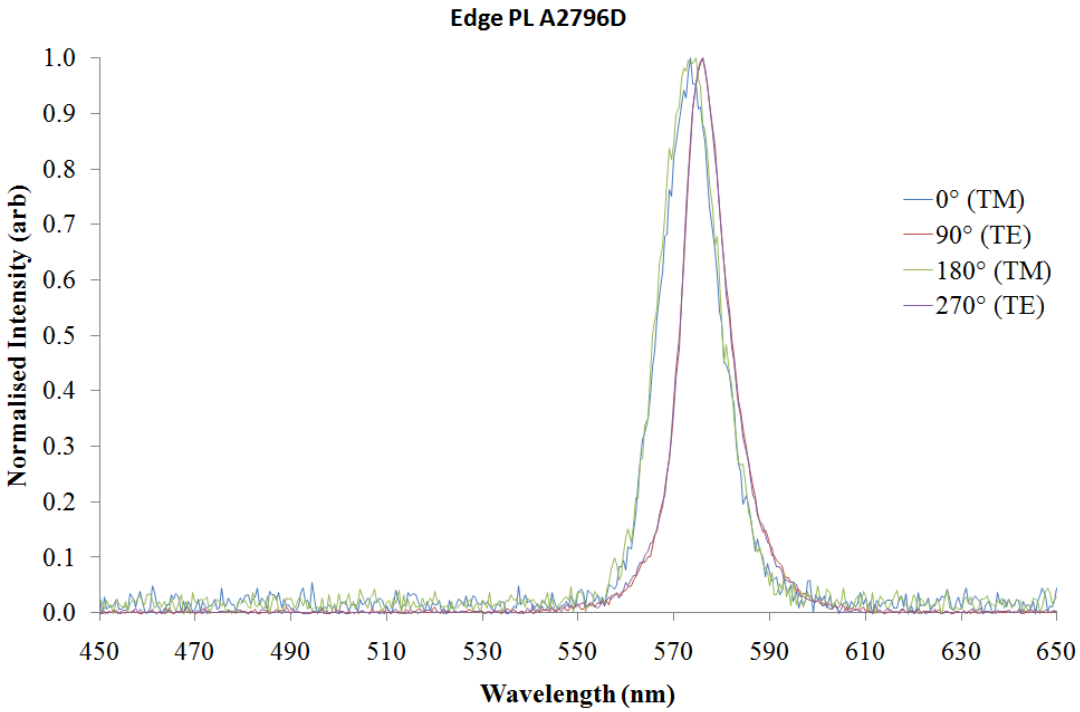

Figure 6-15: EdgePL polarisation spectra for resonant sample A2796D

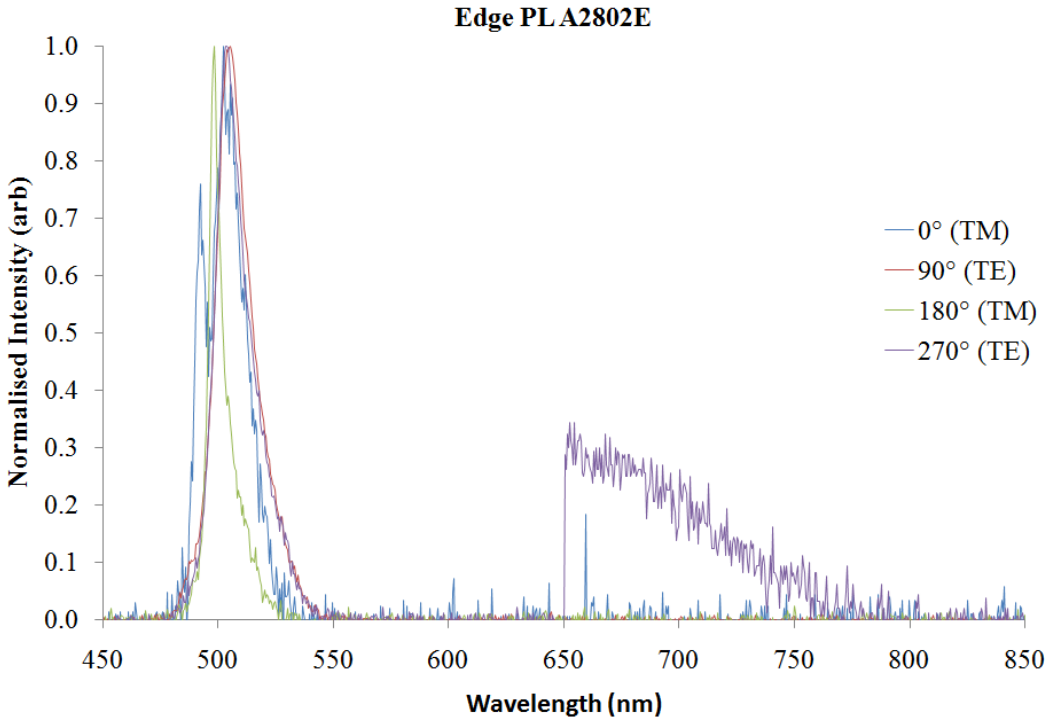

Figure 6-16: EdgePL polarisation spectra for anti-resonant sample A2802D

6.3 Conclusion

Samples of a five quantum well ZnSe/ZnCdSe structure were floated onto fused silica and diamond substrates by Heriot Watt using an epitaxial lift-off technique they developed. Measurements of normal PL intensity over time showed permanent degradation in intensity but not a shift in wavelength implying permanent structural damage. Both samples showed a wavelength shift of ~0.1nm/K for normal PL, but the diamond-mounted sample showed no variation in PL wavelength as the pump power was varied indicating excellent thermal contact between sample and substrate. We characterised four samples of ZnCdMgSe/ZnCdSe VECSEL structures (without DBR) grown by Professor Maria Tamargo. These structures also showed a wavelength shift of ~0.1nm/K for both normal and edge PL, showing at least comparable temperature sensitivity to the GaInP/AlGaInP structures discussed in earlier chapters. The polarisation of the edge PL showed the quantum wells were slightly compressively-strained. The wide wavelength range covered by this material system make it an excellent candidate for flexible II-VI visible emission VECSELs.

References

1 C. Bradford, A. Currran, A. Balocchi, B. C. Cavenett, K. A. Prior, and R. J. Warburton, "Epitaxial lift-off of MBE grown II-VI heterostructures using a novel MgS release layer," Journal of Crystal Growth **278** (1-4), 325-328 (2005).

2 N. Benosman, N. Amrane, and H. Aourag, "Calculation of electronic and optical properties of zinc-blende $Zn_xCd_{1-x}Se$," Physica B **275** (4), 316-327 (2000).

3 J. D. Weeks, J. C. Tully, and L. C. Kimerling, "Theory of recombination-enhanced defect reactions in semiconductors," Physical Review B **12** (8), 3286 (1975).

4 E. Kato, H. Noguchi, M. Nagai, H. Okuyama, S. Kijima, and A. Ishibashi, "Significant progress in Il-VI blue-green laser diode lifetime," Electronics Letters **34** (3), 282-284 (1998).

5 K. Mogi, H. Kobayashi, A. Ohki, Y. Kawaguchi, and H. Iwamura, "Fast photoluminescence decay and optical nonlinearity of a ZnCdSe/ZnSe multiple quantum well around an excitonic peak," Journal of Luminescence **68** (2-4), 193-198 (1996).

6 Samarth Agarwal, Kyle H. Montgomery, Timothy B. Boykin, Gerhard Klimeck, and Jerry M. Woodall, "Design Guidelines for True Green LEDs and High Efficiency Photovoltaics Using ZnSe/GaAs Digital Alloys," Electrochemical and Solid-State Letters **13** (1), H5-H7 (2010).

7 L. Zeng, B. X. Yang, A. Cavus, W. Lin, Y. Y. Luo, M. C. Tamargo, Y. Guo, and Y. C. Chen, "Red--green--blue photopumped lasing from ZnCdMgSe/ZnCdSe quantum well laser structures grown on InP," Applied Physics Letters **72** (24), 3136-3138 (1998).

8 Y. Luo, S. P. Guo, O. Maksimov, M. C. Tamargo, V. Asnin, F. H. Pollak, and Y. C. Chen, "Patterned three-color ZnCdSe/ZnCdMgSe quantum-well structures for integrated full-color and white light emitters," Applied Physics Letters **77** (26), 4259-4261 (2000).

9 N. Dai, A. Cavus, R. Dzakpasu, M. C. Tamargo, F. Semendy, N. Bambha, D. M. Hwang, and C. Y. Chen, "Molecular beam epitaxial growth of high quality $Zn_{1-x}Cd_xSe$ on InP substrates," Applied Physics Letters **66** (20), 2742-2744 (1995).

10 K. Kishino and I. Nomura, "II-VI semiconductors on InP for green-yellow emitters," IEEE J. Sel. Top. Quantum Electron **8** (4), 773-786 (2002).

11 G. N. Aliev, R. M. Datsiev, S. V. Ivanov, P. S. Kop'ev, R. P. Seisyan, and S. V. Sorokin, "Optics and magneto-optics of ZnSe heteroepitaxial layers," Journal of Crystal Growth **159** (1-4), 523-527 (1996).

12 S. K. Zhang, H. Lu, W. B. Wang, B. B. Das, N. Okoye, M. Tamargo, and R. R. Alfano, "Radiative and nonradiative recombination processes in ZnCdSe/ZnCdMgSe multi-quantum-wells," Journal of Applied Physics **101** (2), 023111 (2007).

13 S. P. Guo, O. Maksimov, M. C. Tamargo, F. C. Peiris, and J. K. Furdyna, "Distributed Bragg reflectors for visible range applications based on

(Zn,Cd,Mg)Se lattice matched to InP," Applied Physics Letters **77** (25), 4107-4109 (2000).

14 C. Kruse, S. M. Ulrich, G. Alexe, E. Roventa, R. Kröger, B. Brendemühl, P. Michler, J. Gutowski, and D. Hommel, "Green monolithic II-VI vertical-cavity surface-emitting laser operating at room temperature," physica status solidi (b) **241** (3), 731-738 (2004).

15 Sadao Adachi, *Optical Constants of Crystalline and Amorphous Semiconductors*. (Kluwer Academic Publishers, 1999).

Chapter 7

Conclusions

This thesis has described work in diode-pumped visible VECSELs. The design and characterisation of both of the diode-pumped III-V VECSELs and the preliminary design work on II-VI VECSELs has been examined. Red VECSELs designed to facilitate GaN diode-pumping are discussed. The first diode-pumped VECSEL with fundamental emission at visible wavelengths is demonstrated and improved. The effect of pump wavelength on device temperature, and thus emission wavelength, is measured and discussed.

7.1 VECSEL Thermal Issues

The methods used to characterise samples throughout this work were presented, with experimental examples and schematic experimental set-ups. Reflectivity spectra were taken to assess the quality and breadth of the high reflectivity stopband of samples and identify subcavity resonances which could impact on later laser performance. Photoluminescence techniques were used to measure the quantum well emission. PL taken from the edge of the sample showed the emission of the quantum wells, unmodified by modulation due to other structural elements and how close the emission was to the design wavelength. This technique was also used to measure the shift of emission wavelength with temperature, with shifts of ~0.2-0.3nm/K observed. Additionally this method was used to distinguish between the desired TE polarised emission and unwanted TM polarised emission in ZnMgCdSe samples. Photoluminescence emitted normal to the sample surface was measured, showing the effect of the structure on detected quantum well emission. Spectra were taken at various temperatures to measure the shift in emission wavelength with temperature, with shifts of ~0.1nm/K observed. The motivation for detuning the designed quantum well emission and subcavity resonance is seen in experimental results

where the emission intensity increases as the quantum well emission wavelength moves through a subcavity resonance despite the heat-related reduction in efficiency.

These techniques were used to map the characteristics of wafers grown by MOCVD at three different temperatures as an initial investigation into the effect of growth temperature. There appeared to be a correlation between lower growth temperature and red-shift of photoluminescence.

A red emission VECSEL, cooled only through the substrate by a peltier element, was demonstrated for a range of pump powers and spot sizes. Data of a red VECSEL pumped at different wavelengths was examined and a finite element analysis used to model the change in active region temperature, and thus emission wavelength, under different heat loading assumptions. Both modelling and experiment suggested the active region temperature actually increases with decreasing pump photon energy.

7.2 Diode-Pumped Visible VECSELs

In Chapter 4 the motivation for moving from optical pumping at 532nm to 405/445nm is discussed and design considerations in changing pump wavelength such as absorption length and quantum well placement, examined.

The structure was altered to take advantage of 445nm GaN laser diodes becoming available, with an additional quantum well being added at the first anti-node and the pump absorbing barrier lengthened to reduce pump absorption in the DBR, as well as removing the AlAs spacer layers to reduce the potential for oxidisation. Pump power limited output of 12mW at ~673nm was demonstrated with an M^2 of <1.2 and a tuning range of 11nm. Permanent degradation of laser output power was observed, with a typical lifetime of ~40 minutes. Strain compensation and lengthened active region were used in the next iteration of the structure to improve performance to 17mW at ~670nm with an M^2 of ~1.1. Degradation of laser output power was also slowed, extending the lifetime to ~100 minutes. The two 445nm pumped structures were compared and possible reasons for the aging effect examined

7.3 Structural Degradation

Investigation into the permanent structural damage seen in the diode-pumped red VECSEL structures is carried out in chapter 5. Structural defects are discussed, noting the factors which affect their movement and propagation such as strain, heat and non-radiative recombination.

Experimental results for stimulated emission are presented which rule out heat build-up as a cause of degradation. The Kuznetsov[1] model is used as an initial tool to investigate the effects on laser performance due to degradation. Experimental results from the strain and non-strain compensated structures are compared

Switching to an AlInP/GaInP DBR is suggested to strain-balance the structure and improve device lifetime and an anti-resonant design is proposed to increase the tuning range.

An additional option is to move to an anti-resonant structure to try to increase the tuning range. All the previous structures considered used a resonant cavity to maximise gain. However, the strong absorption of pump light in the active region may make a resonant cavity less desirable than for those designed for longer wavelength pumping. In the resonant cavities the first anti-node in the cavity is a half-wavelength from the epi-surface (~80nm). In that distance the pump intensity has declined by almost half and carrier generation in the vicinity of the wells is reduced.

In an anti-resonant structure, the first anti-node is much closer to the epi-surface (~40nm) and the pump intensity at that point is higher. Although the design would lose the benefit to threshold of a resonant cavity this would, at least in part, be compensated by having the quantum wells situated where there is greater carrier generation. In addition, the structure could be expected to have a greater tuning range than a resonant structure.

7.4 II-VI VECSELs

In chapter 6 we conduct preliminary work in the development of II-VI VECSELs. A transmission spectrum of the ZnCdSe structure is taken which shows step changes attributable to the pump-absorbing barriers and quantum wells. Photoluminescence intensity measurements are taken over time and fitted to a linear combination of exponential decay curves suggesting more than one mechanism damaging the structure.

Normal photoluminescence measurements were taken for a range of pump powers for both the fused silica and diamond mounted samples. The emission wavelength of the sample on fused silica shifted to longer wavelength by over 10nm for an increase in pump power of 100mW indicating sample heating, an effect which was not present in the diamond mounted sample, demonstrating the efficacy of diamond as a heatspreader material. When the diamond mounted sample was heated the photoluminescence shifted to longer wavelength at ~0.1nm/K which is the same change seen earlier in the III-V samples.

The ZnCdMgSe material system was presented as a good candidate for VECSELs covering most of the visible spectrum. Resonant and anti-resonant structures were designed, subsequently grown by our collaborators at the City University of New York, and characterised using normal photoluminescence and reflectivity. The resonant structures showed single peaks at 560 nm and 570nm. The anti-resonant structures emitted at shorter wavelengths but over a greater range with additional side peaks due to structure resonances. Normal and edge photoluminescence spectra were taken for a range of mount temperatures, both demonstrating a shift to longer wavelengths of ~0.1nm/K which compares well to the AlGaInP samples seen earlier. Edge PL was also used to measure the polarisation of the ground state transition.

7.5 Future Work

The work in this thesis is a first step in the journey towards commercial visible wavelength VECSELs.

Demonstrating successful diode-pumping of the visible VECSEL shows the potential for miniaturisation and savings required for a compact and cost-effective laser. Continuing development of GaN laser diodes will significantly affect the development of visible emission VECSELs. Progress to longer wavelengths and higher power will enable more powerful visible VECSELs through a lengthened active region allowing the inclusion of additional quantum wells. Power scaling will allow VESELs to take advantage of higher power laser diodes.

As the experimental results and FEA modelling showed, the thermal effect on laser performance of changing the pump wavelength is not limited to the quantum defect, but is strongly influenced by the temperature gradient determined by material absorption and heat removal paths. A better understanding of the mechanisms involved will help inform design decisions.

Understanding why the structures degrade is crucial to improving the performance and extending device lifetime. Strain within the structure appears to play a role in the rapidity of the aging effect and minimising this could significantly increase lifetime. Pump wavelength will also have an effect, in that shorter wavelengths deposit more energy into the lattice which facilitates defect migration and formation.

Although strain-compensating the quantum wells improved device performance and lifetime, there is still a need for improvement in the structure design to further increase performance and lifetime.

Whilst the quantum wells (and strain compensation layers) are the most highly strained element in the structures discussed earlier, they are not the biggest source of strain in the structure. Both the AlAs and $Al_{0.45}Ga_{0.55}As$ layers used in the DBR have slightly larger lattice constants than GaAs and are a little compressively strained as a result. Although the strain is low (-0.14% for AlAs and -0.06% for $Al_{0.45}Ga_{0.55}As$), the cumulative strain of over 4μm of slightly strained material is significant. If this cumulative strain could be removed by strain balancing the DBR it is expected that device performance and longevity would be enhanced.

It is not possible to significantly decrease the level of strain by reducing the amount of aluminium in the AlGaAs layer as the absorption edge of $Al_{0.45}Ga_{0.55}As$ is already close to the laser wavelength[2] so a change in DBR material is required.

One option is to replace the AlAs/AlGaAs DBR with one based on the (AlGa)InP material system. The ability to vary the lattice constant and bandgap of (AlGa)InP almost independently by varying the In and Al proportions is already utilised in designing the active region. This can be used to (near) strain-balance the DBR and the remaining source of strain (the quantum wells) may be balanced by tweaking the composition of the pump absorbing layers. Also, reducing the amount of aluminium in the structure reduces its susceptibility to oxidisation. The use of an (AlGa)InP DBR to an AlAs/AlGaAs DBR has previously been demonstrated by Schneider et al[3] with their optically-pumped VCSEL.

The low refractive index layers would be composed of $Al_{0.53}In_{0.47}P$. It has a lattice constant of a_0=5.6535Å[2] (and so is lattice-matched to the GaAs substrate which has a lattice constant of a_0=5.6533Å), a refractive index of n=3.1326 and direct bandgap of E0=2.36eV[4].

The high refractive index layers would be $(Al_{0.2}Ga_{0.8})_{0.52}In_{0.48}P$. It has a lattice constant of a_0=5.6528Å[2], refractive index of n=3.2928 and direct bandgap of E0=2.337eV[5].

A DBR of $(Al_{0.2}Ga_{0.8})_{0.52}In_{0.48}P$ / $Al_{0.53}In_{0.47}P$ would have a smaller refractive index contrast than the AlAs / $Al_{0.45}Ga_{0.55}As$ DBR used in the diode-pumped red VECSEL work. The refractive index contrast of the existing AlAs/$Al_{0.45}Ga_{0.55}As$ layers is 3.51-3.09=0.42. A DBR of $(Al_{0.2}Ga_{0.8})_{0.52}In_{0.48}P$ / $Al_{0.53}In_{0.47}P$ would have a refractive index contrast of 3.29-3.13=0.16 and so require 60 pairs of layers rather than the 40 in the existing AlAs/AlGaAs DBR. Although the increase in the thickness of the DBR is not ideal it is not the main heat flow path so the increased thermal resistance should not be an issue. As both layers are lattice-matched to GaAs, growing the additional thickness should not cause structural problems.

The misfit strain of each layer is $\varepsilon=(a_{GaAs}-a_{layer})/a_{layer}$. The cumulative misfit of layer α can be defined as $\Delta\alpha= \varepsilon_\alpha l_\alpha$ where l_α is the thickness and ε_α the misfit strain of layer α. The cumulative misfit of all layers Δ being the sum of the misfit of each layer. The closer Δ is to zero the better strain balanced the structure is.

Applying this to the seven quantum well structure with strain compensation layers in Table 7-1 we see that the cumulative misfit Δ=-4.51nm with an average misfit strain of ε=-0.10%.

Layer	Lattice Const (Å)	Dist (nm)	Misfit	Cumulative Misfit (nm)	Material	x	y
Substrate	5.6533				GaAs		
DBR High Index	5.6568	1880	-0.06%	-1.16	$Al_xGa_{1-x}As$	0.45	
DBR Low Index	5.6611	2160	-0.14%	-4.14	$Al_xGa_{1-x}As$	1	
Half Layer	5.6611	54	-0.14%	-4.21	$Al_xGa_{1-x}As$	1	
Barrier	5.6593	191	-0.11%	-4.42	$(Al_xGa_{1-x})_yIn_{1-y}P$	0.60	0.51
Barrier (Strain Comp)	5.6223	3.5	0.55%	-4.40	$(Al_xGa_{1-x})_yIn_{1-y}P$	0.60	0.60
QW	5.6813	7	-0.49%	-4.43	$Ga_xIn_{1-x}P$	0.45	
Barrier (Strain Comp)	5.6223	7	0.55%	-4.39	$(Al_xGa_{1-x})_yIn_{1-y}P$	0.60	0.60
QW	5.6813	7	-0.49%	-4.43	$Ga_xIn_{1-x}P$	0.45	
Barrier (Strain Comp)	5.6223	7	0.55%	-4.39	$(Al_xGa_{1-x})_yIn_{1-y}P$	0.60	0.60
QW	5.6813	7	-0.49%	-4.42	$Ga_xIn_{1-x}P$	0.45	
Barrier (Strain Comp)	5.6223	3.5	0.55%	-4.40	$(Al_xGa_{1-x})_yIn_{1-y}P$	0.60	0.60
Barrier	5.6593	51	-0.11%	-4.46	$(Al_xGa_{1-x})_yIn_{1-y}P$	0.60	0.51
Barrier (Strain Comp)	5.6223	3.5	0.55%	-4.44	$(Al_xGa_{1-x})_yIn_{1-y}P$	0.60	0.60
QW	5.6813	7	-0.49%	-4.47	$Ga_xIn_{1-x}P$	0.45	
Barrier (Strain Comp)	5.6223	7	0.55%	-4.43	$(Al_xGa_{1-x})_yIn_{1-y}P$	0.60	0.60
QW	5.6813	7	-0.49%	-4.47	$Ga_xIn_{1-x}P$	0.45	
Barrier (Strain Comp)	5.6223	7	0.55%	-4.43	$(Al_xGa_{1-x})_yIn_{1-y}P$	0.60	0.60
QW	5.6813	7	-0.49%	-4.46	$Ga_xIn_{1-x}P$	0.45	
Barrier (Strain Comp)	5.6223	7	0.55%	-4.43	$(Al_xGa_{1-x})_yIn_{1-y}P$	0.60	0.60
QW	5.6813	7	-0.49%	-4.46	GaxIn1-xP	0.45	
Barrier (Strain Comp)	5.6223	3.5	0.55%	-4.44	$(Al_xGa_{1-x})_yIn_{1-y}P$	0.60	0.60
Barrier	5.6593	63	-0.11%	-4.51	$(Al_xGa_{1-x})_yIn_{1-y}P$	0.60	0.51
Cap	5.6516	10	0.03%	-4.51	$Ga_xIn_{1-x}P$	0.52	
	Length ->	**4507**		-0.10%	**<- Average Strain**		

Table 7-1: AlAs/AlGaAs DBR with strain compensation layers in active region

Table 7-2 shows that strain balancing the DBR, with no changes to the active region, reduces the cumulative misfit to Δ=-0.13nm, and average misfit strain ε=0.002%.

Layer	Lattice Const (Å)	Dist (nm)	Misfit	Cumulative Misfit (nm)	Material	x	y
Substrate	5.6533				GaAs		
DBR - High Index	5.6528	3162	0.01%	0.28	$(AlxGa1\text{-}_{xy})In_{1-y}P$	0.2	0.52
DBR - Low Index	5.6535	3410	0.00%	0.16	$(AlxGa1\text{-}_{xy})In_{1-y}P$	1	0.53
Half Layer	5.6535	56	0.00%	0.16	$(AlxGa1\text{-}_{xy})In_{1-y}P$	1	0.53
Barrier	5.6593	191	-0.11%	-0.05	$(Al_xGa_{1-x})_yIn_{1-y}P$	0.60	0.51
Barrier (Strain Comp)	5.6223	3.5	0.55%	-0.03	$(AlxGa1\text{-}_{xy})In_{1-y}P$	0.60	0.60
Quantum Well	5.6813	7	-0.49%	-0.06	$Ga_xIn_{1-x}P$	0.45	
Barrier (Strain Comp)	5.6223	7	0.55%	-0.02	$(AlxGa1\text{-}_{xy})In_{1-y}P$	0.60	0.60
Quantum Well	5.6813	7	-0.49%	-0.06	$Ga_xIn_{1-x}P$	0.45	
Barrier (Strain Comp)	5.6223	7	0.55%	-0.02	$(AlxGa1\text{-}_{xy})In_{1-y}P$	0.60	0.60
Quantum Well	5.6813	7	-0.49%	-0.05	$Ga_xIn_{1-x}P$	0.45	
Barrier (Strain Comp)	5.6223	3.5	0.55%	-0.03	$(AlxGa1\text{-}_{xy})In_{1-y}P$	0.60	0.60
Barrier	5.6593	51	-0.11%	-0.09	$(Al_xGa_{1-x})_yIn_{1-y}P$	0.60	0.51
Barrier (Strain Comp)	5.6223	3.5	0.55%	-0.07	$(AlxGa1\text{-}_{xy})In_{1-y}P$	0.60	0.60
Quantum Well	5.6813	7	-0.49%	-0.10	$Ga_xIn_{1-x}P$	0.45	
Barrier (Strain Comp)	5.6223	7	0.55%	-0.06	$(AlxGa1\text{-}_{xy})In_{1-y}P$	0.60	0.60
Quantum Well	5.6813	7	-0.49%	-0.10	$Ga_xIn_{1-x}P$	0.45	
Barrier (Strain Comp)	5.6223	7	0.55%	-0.06	$(AlxGa1\text{-}_{xy})In_{1-y}P$	0.60	0.60
Quantum Well	5.6813	7	-0.49%	-0.09	$Ga_xIn_{1-x}P$	0.45	
Barrier (Strain Comp)	5.6223	7	0.55%	-0.06	$(AlxGa1\text{-}_{xy})In_{1-y}P$	0.60	0.60
Quantum Well	5.6813	7	-0.49%	-0.09	GaxIn1-xP	0.45	
Barrier (Strain Comp)	5.6223	3.5	0.55%	-0.07	$(AlxGa1\text{-}_{xy})In_{1-y}P$	0.60	0.60
Barrier	5.6593	63	-0.11%	-0.14	$(Al_xGa_{1-x})_yIn_{1-y}P$	0.60	0.51
Cap	5.6516	10	0.03%	-0.13	$Ga_xIn_{1-x}P$	0.52	
	Length ->	**7041**		-0.002%	**<- Average Strain**		

Table 7-2: AlInP/AlGaInP DBR with strain compensation layers in active region

Strain balancing the DBR would almost wholly remove the cumulative strain in the structure, leaving only local regions of strain in the quantum wells and strain compensation barriers. The quantum well-barrier interface can act as a seed for defects migrating into the quantum well so it may be a further improvement to reduce the shear stress at the interface by altering the composition of the pump absorbing barrier to strain balance the active region rather than using highly strained thin strain compensation layers as shown in Table 7-3. This would also have the advantage of simplifying growth by reducing the number of layers and have a cumulative misfit of Δ=0.05nm and average misfit strain ε=0.001%.

Layer	Lattice Const (Å)	Dist (nm)	Misfit	Cumulative Misfit (nm)	Material	x	y
Substrate	5.6533				GaAs		
DBR - High Index	5.6528	3162	0.01%	0.28	$(AlxGa1-_x)_yIn_{1-y}P$	0.2	0.52
DBR - Low Index	5.6535	3410	0.00%	0.16	$(AlxGa1-_x)_yIn_{1-y}P$	1	0.53
Half Layer	5.6535	55	0.00%	0.16	$(AlxGa1-_{xy}In_{1-y}P$	1	0.53
Barrier	5.6511	187	0.04%	0.23	$(Al_xGa_{1-x})_yIn_{1-y}P$	0.60	0.53
Quantum Well	5.6813	7	-0.49%	0.20	$Ga_xIn_{1-x}P$	0.45	
Barrier	5.6511	7	0.04%	0.20	$(Al_xGa_{1-x})_yIn_{1-y}P$	0.60	0.53
Quantum Well	5.6813	7	-0.49%	0.16	$Ga_xIn_{1-x}P$	0.45	
Barrier	5.6511	7	0.04%	0.17	$(Al_xGa_{1-x})_yIn_{1-y}P$	0.60	0.53
Quantum Well	5.6813	7	-0.49%	0.13	$Ga_xIn_{1-x}P$	0.45	
Barrier	5.6511	58	0.04%	0.15	$(Al_xGa_{1-x})_yIn_{1-y}P$	0.60	0.53
Quantum Well	5.6813	7	-0.49%	0.12	$Ga_xIn_{1-x}P$	0.45	
Barrier	5.6511	7	0.04%	0.12	$(Al_xGa_{1-x})_yIn_{1-y}P$	0.60	0.53
Quantum Well	5.6813	7	-0.49%	0.09	$Ga_xIn_{1-x}P$	0.45	
Barrier	5.6511	7	0.04%	0.09	$(Al_xGa_{1-x})_yIn_{1-y}P$	0.60	0.53
Quantum Well	5.6813	7	-0.49%	0.06	$Ga_xIn_{1-x}P$	0.45	
Barrier	5.6511	7	0.04%	0.06	$(Al_xGa_{1-x})_yIn_{1-y}P$	0.60	0.53
Quantum Well	5.6813	7	-0.49%	0.02	GaxIn1-xP	0.45	
Barrier	5.6511	65	0.04%	0.05	$(Al_xGa_{1-x})_yIn_{1-y}P$	0.60	0.53
Cap	5.6516	10	0.03%	0.05	$Ga_xIn_{1-x}P$	0.52	
	Length ->	7031			0.001% **<- Average Strain**		

Table 7-3: AlInP/AlGaInP DBR without strain compensating layers in active region

It would be possible to remove the cumulative strain from the DBR by not growing one at all, etching off the substrate, and applying a mirror coating to the polished bottom of the structure but that would negate one of the advantages of using a heatspreader: that it does not need significant post-processing.

Additionally there may be scope for improvement by changing the growth temperature. Whilst we have continued with the growth temperatures used for doped AlGaInP structures, the VECSEL is not restricted by a need to optimise growth conditions for doping and investigation into this area could be worthwhile.

Although this work has largely concentrated on the red VECSEL, the design principles used in the diode-pumped red VECSEL apply to the development of II-VI VECSELs. These have the potential to cover the whole of the visible spectrum[6] offering the exciting prospect of exploiting recent availability of GaN laser diodes to enter the multi-billion dollar display market. Particularly interesting is the possibility

of growing different wavelength VECSELs on the same wafer[7], simplifying integration into display devices.

Future work with the ZnCdSe/ZnSe material system will involve further testing of structures floated onto diamond as the preferred heatsink material. Once high quality repeatable results can be achieved a full VECSEL structure intended for laser action could be bonded to diamond using the epitaxial lift-off technique.

The ZnCdMgSe/ZnCdSe structure was designed for laser action using the same principles as our III-V red VECSELs, however it was grown without a DBR on an InP substrate which requires removal. Mechanical polishing to thin the substrate followed by wet etching a via hole through the InP, followed by wet etching through the InGaAs seems the most likely option. Whilst highly selective etchants, such as HCl:H_3PO_4 (3:1) which etches InP but not InGaAs[8] and H_3PO_4:H_2O_2:H_20 (1:1:8) which etches InGaAs but not InP used by Elias et al[8] to etch InP through an InGaAs mask, are known, we are currently investigating suitable etchants for high selectivity of InGaAs and InP over ZnCdSe. Once this has been overcome the first green II-VI VECSEL can be demonstrated, opening the way to further progress in visible VECSELs.

An important step in the fabrication of VECSEL structures is to widen the scope of the epitaxial lift-off technique[9] to other II-VI material systems such as ZnCdMgSe. This has recently been achieved by Dr Kevin Prior of Heriot-Watt and Professor Maria Tamargo of CUNY. This enabling process allows VECSEL structures to be floated directly onto a substrate, with entirely different properties to the VECSEL such as a mirror-coated diamond heatspreader, shown as an example in Figure 7-1.

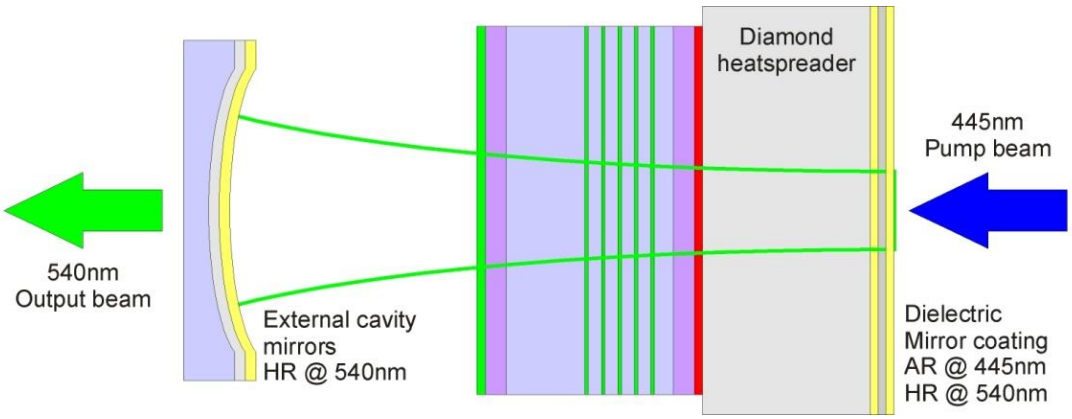

Figure 7-1: Schematic of a possible diode-pumped II-VI VECSEL floated onto a coated diamond heatspreader.

References

1 M. Kuznetsov, F. Hakimi, R. Sprague, and A. Mooradian, "Design and characteristics of high-power (> 0.5-W CW) diode-pumped vertical-external-cavity surface-emitting semiconductor lasers with circular TEM_{00} beams," IEEE J. Sel. Top. Quantum Electron. **5** (3), 561 (1999).

2 Sadao Adachi, *Optical Constants of Crystalline and Amorphous Semiconductors*. (Kluwer Academic Publishers, 1999).

3 R. P. Schneider, Jr., R. P. Bryan, E. D. Jones, and J. A. Lott, "Excitonic transitions in InGaP/InAlGaP strained quantum wells," Applied Physics Letters **63** (9), 1240-1242 (1993).

4 I. Vurgaftman, J. R. Meyer, and L. R. Ram-Mohan, "Band parameters for III-V compound semiconductors and their alloys," Journal of Applied Physics **89** (11), 5815-5875 (2001).

5 A. Hassine, J. Sapriel, P. Le Berre, P. Legay, F. Alexandre, and G. Post, "Acoustical and optical properties of $Ga_{0.52}In_{0.48}P$: A Brillouin scattering study," Journal of Applied Physics **77** (12), 6569-6571 (1995).

6 Maria C. Tamargo, Shiping Guo, Oleg Maksimov, Ying-Chih Chen, Frank C. Peiris, and Jacek K. Furdyna, "Red-green-blue light emitting diodes and distributed Bragg reflectors based on ZnCdMgSe lattice-matched to InP," Journal Of Crystal Growth **227**, 710-716 (2001).

7 L. Zeng, B. X. Yang, A. Cavus, W. Lin, Y. Y. Luo, M. C. Tamargo, Y. Guo, and Y. C. Chen, "Red--green--blue photopumped lasing from ZnCdMgSe/ZnCdSe quantum well laser structures grown on InP," Applied Physics Letters **72** (24), 3136-3138 (1998).

8 P. Eliás, J. Soltýs, and I. Kostic, "Study of ordinary facets revealed in (1 0 0) InP by etching in HCl," Materials Science and Engineering: B **138** (2), 172-179 (2007).

9 C. Bradford, A. Currran, A. Balocchi, B. C. Cavenett, K. A. Prior, and R. J. Warburton, "Epitaxial lift-off of MBE grown II-VI heterostructures using a novel MgS release layer," Journal of Crystal Growth **278** (1-4), 325-328 (2005).